



**SISSA**  
International School for Advanced Studies

**Scuola Internazionale Superiore di Studi Avanzati  
(SISSA, Trieste)**

International School for Advanced Studies

Department: Astrophysics and Cosmology

**Doctoral Thesis**

# **Nature of Dark Matter**

## from Astrophysics of

## High Redshift

## Star-forming Galaxies

Candidate: Gauri Sharma

Advisor: Prof. Paolo Salucci

**(2017-2021)**

**SISSA - Via Bonomea 265 – 34136 Trieste - Italy**

To,  
*My parents*  
*and*  
*Everyone who believed in me.*

“Where there is righteousness in the heart,  
there is *beauty in the character*.

When there is beauty in the character, there  
is *harmony in the home*.

When there is harmony in the home, there is  
*order in the nation*.

When there is order in the nation, there is  
*peace in the world*.”

-A.P.J. Abdul Kalam

“The life and death of a star teaches us a lot-  
*Live, Contribute and Impact* such that  
it enrich society & next generation.”

# Contents

<b>Acknowledgement</b>	vii
<b>Abstract</b>	xi
<b>Declaration</b>	xiii
<b>Glossary</b>	xv
<b>1 Introduction</b>	1
1.1 Discovery of Dark Matter . . . . .	4
1.2 Dark Matter Probes . . . . .	6
1.2.1 Galaxies & Galaxy Clusters . . . . .	6
1.2.2 CMB Power Spectrum . . . . .	7
1.2.3 Gravitational Lensing . . . . .	10
1.2.4 Other Dark Matter Probes . . . . .	12
1.3 Dark Matter Particles and Scenarios . . . . .	13
1.4 Problems in $\Lambda$ CDM Scenario . . . . .	16
1.4.1 Small Scale Problems . . . . .	17
1.4.1.1 Cusp-Core Problem . . . . .	17
1.4.1.2 Missing Satellite Problem . . . . .	20
1.4.1.3 Too Big to Fail . . . . .	20
1.4.1.4 Satellite Plane Problem . . . . .	21
1.4.2 Large Scale Problems . . . . .	22
1.5 Outline of Thesis . . . . .	23
<b>2 Kinematics &amp; Dynamics of Galaxies</b>	25
2.1 Galaxy Kinematics . . . . .	25
2.1.1 Conventional Spectroscopy . . . . .	25
2.1.2 Integral Field Spectroscopy . . . . .	29
2.2 Galaxy Dynamics . . . . .	32
2.2.1 Dynamical Models . . . . .	33
2.2.1.1 Stellar and Gas Disc . . . . .	33
2.2.1.2 Bulge Component . . . . .	34
2.2.1.3 Dark Matter Halo Component . . . . .	34

2.3	Star-forming Galaxies (SFGs) . . . . .	36
2.3.1	Kinematics and Dynamics of Local SFGs . . . . .	37
2.3.2	Kinematics and Dynamics of High Redshift SFGs . . . . .	41
2.4	Observational and Physical Uncertainties . . . . .	44
2.4.1	Beam Smearing . . . . .	44
2.4.2	Pressure Support . . . . .	46
2.5	Research Highlights . . . . .	47
<b>3</b>	<b>Dataset: Redshift One Star-forming Galaxies</b>	<b>49</b>
3.1	Observations . . . . .	49
3.1.1	KROSS Data . . . . .	50
3.1.2	Sample Selection . . . . .	50
3.2	Data Analysis & Processing . . . . .	51
3.2.1	Determining Physical Parameters . . . . .	51
3.2.1.1	Position and Inclination Angle . . . . .	51
3.2.1.2	Effective Radius . . . . .	51
3.2.1.3	Scale Length . . . . .	52
3.2.1.4	$H_{\alpha}$ Luminosity . . . . .	52
3.2.1.5	Stellar Masses . . . . .	52
3.2.1.6	Star Formation Rates . . . . .	53
3.2.1.7	Molecular Gas Masses . . . . .	54
3.2.1.8	Atomic Gas Masses . . . . .	55
3.2.2	Kinematic Modelling with ${}^3D$ BAROLO . . . . .	57
3.2.2.1	Basic Assumption . . . . .	57
3.2.2.2	Initial Requirements . . . . .	58
3.2.2.3	Limitations . . . . .	59
3.2.2.4	Results . . . . .	60
3.2.3	Pressure Gradient Correction (PGC) . . . . .	64
3.2.3.1	Case1: PGC with Constant and Isotropic Velocity Dispersion . . . . .	67
3.2.3.2	Case2: PGC with Non-constant and Anisotropic Velocity Dispersion . . . . .	67
3.2.3.3	Comparison of Case1 and Case2 . . . . .	68
3.3	Simulations . . . . .	70
3.3.1	Simulated Data . . . . .	70
3.3.2	Sample Selection & Analysis . . . . .	72
3.4	Summary . . . . .	72
<b>4</b>	<b>Rotation Curve Analysis</b>	<b>75</b>
4.1	Introduction . . . . .	75
4.2	Data Analysis & Results . . . . .	76
4.2.1	Characteristic Velocity . . . . .	76
4.2.2	Co-added Rotation Curves . . . . .	79

4.2.3	Comparison Sample . . . . .	82
4.3	Presenting Flat Rotation Curves . . . . .	84
4.4	Summary . . . . .	87
<b>5</b>	<b>Dark Matter Fraction</b>	<b>89</b>
5.1	Introduction . . . . .	89
5.2	Data Analysis . . . . .	90
5.2.1	Baryonic Mass Estimates . . . . .	90
5.2.2	Baryonic Mass Within the Characteristic Radii . . . . .	92
5.2.3	Dynamical Mass Estimates . . . . .	93
5.3	Dark Matter Fraction . . . . .	94
5.4	Results & Discussion . . . . .	98
5.5	Summary . . . . .	101
<b>6</b>	<b>Structural Properties of Dark Matter Halos</b>	<b>103</b>
6.1	Introduction . . . . .	104
6.2	Methodology . . . . .	106
6.2.1	Rotation Curve Modelling . . . . .	107
6.2.2	Fitting Details . . . . .	107
6.3	Results & Analysis . . . . .	112
6.3.1	Mass Modelled rotation curves . . . . .	112
6.3.2	Dark Matter Fraction . . . . .	112
6.3.3	Structural Properties of Dark Matter . . . . .	114
6.4	Point of View from Simulations . . . . .	116
6.4.1	Rotation Curves of Galaxy Simulations . . . . .	117
6.4.2	Comparison with Simulations . . . . .	122
6.5	Discussion & Conclusions . . . . .	123
6.6	Summary . . . . .	128
<b>7</b>	<b>Fundamental Scaling Relations</b>	<b>131</b>
7.1	Introduction . . . . .	131
7.2	Ensemble Data . . . . .	134
7.3	Methodology . . . . .	135
7.3.1	Circular Velocity and Stellar Mass Measurements . . . . .	136
7.3.2	Fitting Method . . . . .	137
7.4	Results and Analysis . . . . .	138
7.4.1	Mass-Size Relation . . . . .	138
7.4.2	Specific Stellar Angular Momentum . . . . .	140
7.4.3	Stellar Tully-Fisher Relation . . . . .	142
7.5	Discussion and Conclusions . . . . .	145
7.6	Summary . . . . .	146
<b>8</b>	<b>Synopsis</b>	<b>149</b>

<b>9 Conclusions &amp; Future Perspectives</b>	<b>157</b>
9.1 Concluding Remarks . . . . .	157
9.2 Future Prospects . . . . .	158

# Acknowledgement

"All that we are is the result of what we have thought".

---

*Gautama Budhha*

As with many other doctoral students, the journey of this work was made possible by the guidance and support of many people, who were either directly or indirectly involved in it. It is therefore my pleasure to express my deep gratitude to them. First and foremost, I would like to thank my Principal Investigator, Prof. Paolo Salucci, without his guidance this work would not have been possible. Paolo gave me all the freedom, needed to develop a problem and solve it scientifically. I thank him for his constant support throughout the work and the countless discussions, in fact, I feel that a "thank you" is not enough. I also thank Paolo's wife Brigitte for sending me lucky charms every year at Christmas. It has been an unique experience working with Paolo and learning from him.

I thank Prof. Andrea Lapi and Luigi Danese for several interesting discussions. In particular, Andrea has always been available for immediate discussion. Together with Andrea, I have made the basis of my thesis and learned numerous numerical tricks/skills. He has provided a significant contribution in enhancing my scientific skills.

I thank Dr. Christopher Harrison for giving me early access to the KROSS data, that became the basis of this thesis. Not to mention the countless discussions I had with him to understand the data and state-of-the-art observations. I cannot forget the day when he introduced me to Prof. Glenn van de Ven, who then became one of the main scientific advisors of this thesis work. I am so grateful to Glenn for giving me his time, irrespective of his busy schedule, working (and discussing) with me after office hours and sometimes even on weekends. If I learned so many things about Astrophysics and Cosmology from someone in a short period of time, that person is Glenn. I was not his responsibility, but he and his group accepted me like an integral part of them, and there I learned the value of- equality, inclusion and access in the field of research.

I am so grateful to Prof. Antonio Lanza for giving me a father figure far from home. He was always very easy to talk to about pretty much all the "extras" of life. I also thanks Prof. Alessandro Bressan, Prof. Carlo Baccigalupi, Prof. Francesca Perrotta, Dr. Davide Poletti and Dr. Darko Donevski, for keeping their doors open for me for any kind of short and long discussions.

Most of the time we forget about the infrastructure, that allows you to connect to the world, provide world-class facilities, and expose you to the latest techniques. So I would like to take this opportunity to thank SISSA and the SISSA-community for giving me

the opportunity to pursue my PhD in their environment. I am also grateful to INFN and IFPU for connecting me with them. How can I not mention *SISSA student Secretariat*, which deals with each and every problem of student in priori, so that students can focus on research. I bow to their immense support that they provide throughout the year to every student irrespective of their race and religion. I also thank the *SISSA canteen*, without you guys many research have gone hungry many times. And finally to *SISSA student representative* and *SISSA Club*, they are an integral part of the SISSA community and keep an eye out for all the basic needs of the students, and work collaboratively in the endeavours of the students.

I would like to thank my teachers: Prof. Anant Vinchurkar, Prof. Balveer Rathore, Prof. B.C. Bhatt, Prof. G.C. Anupama, Prof. D. K. Shau, Prof. Patrice Theule, Prof. Veronique Buat, Prof. Alfio Bonano, Dr. Stephane De Barros, Prof. Pascal Oesch, Prof. Daniel Schaerer, Dr. Antonino Marasco, and Dr. Kyle Oman for teaching me at different stages of my life, which has made me what I am today. I also thank for Prof. Gerhard Hensler for allowing me to attend his *galaxy formation evolution* lectures, and providing multiple discussion beyond the topic. I am truly grateful to Prof. Fabrizio Nesti for several discussions and bundles of letters he wrote to support my research plans.

I thank my dear fellow PhD students/friends, Hasti, Lara, Lumen and Sam for their immense support during this Phd Journey. I also thank my colleagues from the *Dynamics Group* in Vienna, Sabine, Tadeja, Prash, Francesco, and Alice for accepting me as if I were one of them. I had the best scientific discussions with you guys, our Dynamics JC, group meetings and seminars, I look forward to resume them soon after the PhD defence.

A special thanks to Prof. Corinne Charbonnel for being an inspiration in my academic career. Besides Corinne's academic achievements, she is full of compassion, I thank you for all you have given/passed to me. I carried your tears that had fallen on my hands (while last good-bye) and given them a meaning with this dissertation. Thank you for being my inspiration, you cherries still give me energy to do great things and with your pointer - I will win this world.

I am so thankful for my landlord in Trieste for providing me all the comforts (here in Trieste) like parents do for their kids. Thank you Antonio, Lilli, Monica, Tore, Julia, Jon-luca, katja, and all the amazing kids, for accepting as a part of their family. There is no doubt that your house is one of beautiful houses, but you all are the most beautiful folks in this world.

Life is incomplete without friends, and so is this acknowledgement. I thank all my friends who have become a part of my journey. I especially thank John and Mathew, my friends from the Masters, this life would have been so difficult without you guys, virtual hugs. I thank Anto, my flatmate and Indian buddy with whom I dare to share, we care and we fight. I thank Diksha, Priyanka dee, Arnab daa, Ranjan daa, Anjan daa, Ramit daa, RAJAT, Shubham, Abhinash, Ragini, and all the Indian friends in foreign for being part of my PhD journey. I thank Baldev Bhaishab for delivering the Indian food during my very busy time of writing the PhD thesis. I thank Philip, Gianni, and Ssandro for the morning coffees and breakfasts.

A friend in need is friend indeed: thanks to Sandeep, Viplove, Sabhya, Sramana dee,

Aritra daa, and Mihael for proofreading my thesis, providing various discussions, and really very useful comments. Chocolates and delicious Indian food is on the way. Thank you Anirban daa, without being here, despite the difference in time zone, you were always there to provide immediate support and discussions. I am so thankful for Aurora, my best friend in nature and physiotherapist in profession. I really thank her for all the efforts she made to heal my knee which I injured while skiing. She is caring, compassionate, and a great friend.

One always needs a proper push to begin their career, this happened to me when my friend Sasikumar sent me the link of Indian Institute of Astrophysics (IIA) job posting, which then made my way to IIA as a *Telescope Trainee*. I thank him for this initial push of my career, which led to me doing my Masters in France-Swiss, and PhD in Italy. Thank you for your support and for being part of this journey. To my IIA friends, Pramod, Venku (or Venku, Pramod, just don't fight), Chakradhari Bhiaya, Suresh bhai, and staya ranjan, thank you for always motivating and inspiring me to achieve great things. I have spent one of the most difficult times of my life with you guys. A part of this journey will always be dedicated to you guys. I just want to say that— your voices are still echoing in my ears.

A special thanks to Geeta, who is an integral part of me, and has supported me in every step I have taken so far. Thank you, Radha and Geeta, for supporting me throughout my life, despite the disrespect and difficulties you have had in supporting my dreams. You guys are so important. I thank Jeet and Raghu for being my true friends. This journey would have been so difficult without you guys (Geeta, Radha, Raghu and Jeet), thank you for everything you have given me, let's stay together and grow older.

Life is incomplete without family, thank you for my all family members. In India, family means a big Banyan tree, i.e. countless members. I thank my association to all of them. Especially, I thank Ankur Bhiaya, Shayam Bhiaya, Rahul Bhiaya, Arjun, and Bablu chacha, for hosting me for several months at their home in Delhi (after my undergrad) and taking care of my all needs. A special thanks to Manoj Tiwari, my Uncle, for taking care of my childhood when my father (an army man) could not stay with us for years-and-years due to on-going wars in India.

I remember my teenage years when my elder brother used to taught me science and mathematics, which was very useful in my academic journey. He was my first teacher and a guide. Not having you in life sucks, it is a great loss and that place will remain empty and you will always be remembered.

A very special thanks goes to Mihael who became an integral part of me. Thanks for all the intellectual discussions, whether its scientific or social. Hugs for all the happiness and adventures you shared with me. This life has reasons with you...

Thanks to my *roots*, we often forget to thank our parents for bringing us into life and giving us so much, to have all the opportunities in this world. Everything I have is for you guys. Mommas and Papa, you are so understanding and I am always so grateful to be your daughter. And last but not least, my childhood friend, partner in crime, best buddy, and brother "The Gourav :P", thank you. Let's grow old together, this life needs nothing more than to hear your idiocy.



# Abstract

“The Universe is infinite, on the shores of finite.”

---

In the late 1970s, Vera Rubin showed that the flat rotation curves are ubiquitous in local spiral galaxies, and concluded that “*galaxies are surrounded by a invisible matter, the so-called dark matter halo, that extends much farther than their visible matter*”. These observational results were later supported by theoretical models of structure formation. Since then, dark matter has become an essential building block of cosmological models. However, recent observations of high-redshift star-forming galaxies show declining rotation curves, and thus questioning the “faith of the dark matter halos” back in time. Therefore, there is an urgent need to perform the ‘classical’ study of Rubin et al. beyond the local Universe, probing directly the evolution of dark matter halos observationally.

With these line of thoughts and in search of dark matter and its astrophysical nature at high-redshift, I studied the shape of the rotation curves of  $z \sim 1$  star-forming disc-like galaxies. In doing so, I have explored the dark matter fraction, the structural properties of dark matter halo, and the fundamental scaling relations in the progenitors of local disc galaxies. In particular, I exploit 344 star-forming galaxies of KMOS Redshift One Spectroscopic Survey (KROSS) from publicly available data. I first aimed to disentangle the prevailing observational and physical uncertainties of high-redshift observations, namely beam smearing and pressure support. To this end, the kinematics of the KROSS sample is derived using 3D forward modelling with <sup>3D</sup>BAROLO, which accounts for beam smearing in 3D space and provide:  $H\alpha$  kinematic maps, surface density, rotation, and dispersion curves. For the purpose of this work, I analysed and investigated 256 rotation dominated disc-like galaxies from the main sample, covering the redshift range  $z = 0.57 - 1.04$ . The main entity, i.e. rotation curves, are then corrected for pressure support using the pressure gradient correction. I have found that only a combination of the three techniques (3D-kinematic modelling + 3D-beam smearing correction + pressure gradient correction) yields the accurate rotation curves of high-redshift galaxies. The rotation curves are then dynamically probed to determine the dark matter fraction. Then, in seek of the distribution of the dark matter profile, I dynamically mass modelled the rotation curves, employing Burkert and NFW halo profiles. The outcomes of the latter are cross-checked with previous studies, and state-of-the-art cosmological simulations: EAGLE and Illustris

TNG. In this way, I was able to gain new insights into the structural properties of dark matter halos and current state of fundamental scaling relations of star-forming galaxies at  $z \sim 1$ .

I confirm that the outer rotation curves of star-forming disc-like galaxies at  $z \sim 1$  are similar to the outer rotation curves of local star-forming disc galaxies. Statistically, the latter results indicate that the *total mass* within the outer region ( $\sim 5$  to  $20$  kpc) remains the same at  $z \sim 1$  and  $z \approx 0$ , while the *stellar mass* distribution, defined by the stellar disc radii, varies as a function of the *total mass* (or circular velocity). I show that star-forming galaxies at  $0.7 \leq z \leq 1$  have outer discs dominated by dark matter ( $\sim 5$  to  $20$  kpc). Only a small fraction ( $\sim 5\%$ ) of star-forming galaxies at  $z \sim 1$  have a low dark matter fraction within the effective radius. The dynamical mass modelling of rotation curves and their various comparisons show that the Burkert halo profile fits our sample best. The results of the dark matter structural properties ( $r_0$  and  $\rho_0$ ) show that the dark matter cores at  $z \sim 1$  are on average a factor of 0.3 smaller and more than an order of magnitude denser than those of local star-forming galaxies. As for the fundamental scaling relations, I find that star-forming disc-like systems at  $z \sim 1$  exhibit the same mass-size relations as local disc galaxies, as well as a similar scaling of the specific stellar angular momentum with stellar mass. On the other hand, I found a significant evolution in the slope of the stellar Tully-Fisher relation at  $z \sim 1$ , while its zero-point remains the same as that of the local disc galaxies.

To conclude, I have shown that dark matter is ubiquitous in star-forming disc-like galaxies at  $z \sim 1$ . A preliminary study of dark matter halo structures indicates smaller and denser dark matter cores at  $z \sim 1$ , which suggests that the predictions concerning the transformation of cusps into cores, which are observed in hydrodynamical simulations, indeed occur in nature. That is, the dark matter responds to the baryonic processes that dynamically heat-up the dark matter particles, leading to a disruption and displacement in its initial distribution. The latter can be interpreted as, transforming the original dense inner dark matter density (cusp) into a sparse distribution (core). Most importantly, with this study I attempted to provide the first empirical evidence of *gravitational potential perturbations* in the inner region of galaxies, linking the dark and luminous matter properties, and constraining the dark matter halo structural properties. If my results are verified with high quality data, they will have implications for theories of galaxy formation and evolution, as well as for the nature of dark matter particle itself.

# Declaration

The work described in this dissertation was carried out between October 2017 till August 2021, When I, Gauri Sharma, was a research student under the supervision of Prof. Paolo Salucci in the Department of Astrophysics and Cosmology at Scuola Internazionale Superiore di Studi Avanzati (SISSA). No part of this thesis has been submitted for any other degree at any other institution.

Some sections of this dissertation has been published and have appeared in peer-reviewed journals. These works are the following:

- Chapter 3 and Chapter 4: **Sharma, G.**, Salucci, P., Harrison, C. M., van de Ven, G., & Lapi, A. 2021, Monthly Notices of the Royal Astronomical Society, 503, 1753 ([DOI](#)): **Flat rotation curves of  $z \sim 1$  star-forming galaxies**
- Chapter 5: **Sharma, G.**, Salucci, P., & van de Ven, G., Astronomy & Astrophysics journal ([DOI](#)): **Dark matter fraction in  $z \sim 1$  star-forming galaxies**

The last two sections of this dissertation were recently accepted in Astronomy & Astrophysics journal and are currently in the review process:

- Chapter 6: **Sharma, G.**, Salucci, P., & van de Ven, G., Astronomy & Astrophysics journal: **Observational Evidence of Evolving Dark Matter Profiles since  $z \sim 1$** . A latest version of this article can be found [here](#), arXiv:2109.14224.
- Chapter 7: **Sharma, G.**, & Salucci, P., Astronomy & Astrophysics journal: **Scaling Relations of Star-forming Galaxies since  $z \sim 1$** . A latest version of this article can be found [here](#).

I have carried out all the work in this dissertation with the following exceptions: (1) photometric data reduction and analysis of  $z \sim 1$  star-forming galaxies was performed by Dr. Chris Harrison, (2) SED driven stellar masses were given by Dr. Alfie Tiley, and (3) simulated data of  $z \sim 1$  star-forming galaxies was given by Dr. Kyle Oman. All figures throughout this work are produced by myself, if not, then appropriate copyright is referenced.

In addition to the the work mentioned above I have also worked or has been the involved in the following work during the period of my PhD:

- Salucci, Paolo ; Esposito, Giampiero ; Lambiase, Gaetano ; Battista, Emmanuele ; Benetti, Micol ; Bini, Donato ; Boco, Lumen ; **Sharma, Gauri** ; Bozza, Valerio ; Buoninfante, Luca ; Capolupo, Antonio ; Capozziello, Salvatore ; Covone, Giovanni ; D'Agostino, Rocco ; De Laurentis, Mariafelicia ; De Martino, Ivan ; De Somma, Giulia ; Di Grezia, Elisabetta ; Di Paolo, Chiara ; et al. 2021, *Frontiers in Physics*, 8, 579 ([DOI](#)): **Einstein, Planck and Vera Rubin: relevant encounters between the Cosmological and the Quantum Worlds**
- **Sharma, G., & Salucci, P. ([arXiv:1807.10317](#)): The Dark Side Properties of Galaxies Requires (viable) Modifications to the Verlinde's Emergent Gravity Theory**

# Glossary

## KEYWORDS:

Below, I provide the information of non-standard keywords, which will be commonly used in this work:

- *Star-forming galaxies*: rotation dominated disc galaxies, also known as spirals.
- *Locals or local galaxies*: star-forming galaxies in the local ( $z \approx 0$ ) Universe.
- *High redshift star-forming galaxies*: rotation dominated **disc-like** galaxies.
- *Observed rotation curves*: after various corrections (inclination, beam smearing, and pressure support) observed rotation curves become close to circular velocity curves.
- *Simulated rotation curves*: exact circular velocity curves extracted from simulations.
- *Speed of light*: represented by character  $c$  having value  $3 \times 10^8$  m s $^{-1}$ .
- **3D BAROLO**: **3D-Based Analysis of Rotating Object via Line Observations** or **3D Barolo** is a tool for fitting 3D tilted-ring models to emission-line data-cubes. It can derive the kinematics of any disc-like object, including spiral galaxies, circum-nuclear accretion discs and proto-planetary discs, and can be used with any emission line data, like HI, molecular and recombination lines.

## ASSUMPTIONS:

- $z \sim 1$ : although sample contains the redshift range  $z = 0.57 - 1.04$  with median redshift  $z \approx 0.85$ , for simplicity we refer the sample as  $z \sim 1$  sample.
- *Dark Matter*: cold and collisionless.
- Throughout this work, I have assumed a flat  $\Lambda$ CDM cosmology with  $\Omega_{m,0} = 0.27$ ,  $\Omega_{\Lambda,0} = 0.73$  and  $H_0 = 70$  km s $^{-1}$ .

# Chapter 1

## Introduction

“In all the chaos there is cosmos, in all the disorders runs a secret order.”

---

Carl Gustav J. (edited)

Our Universe is roughly 13.7 billion years old and is full of extraordinary structures whose behaviour is well understood within the known laws of physics. However, the origin of the Universe and cosmic structures is still a mystery and remains an open question. Currently, cosmologists and astrophysicists are studying these open questions via theoretical predictions and modelling. The current model that is widely accepted to best represent the today’s Universe is the so-called *Standard Model* of the cosmology. According to this model, the Universe was initially homogeneous and isotropic and filled with a very high energy density characterized by high temperature and pressure. In the first fraction of seconds of its formation, the Universe is believed to rapidly expanded and cooled, which is popularly known as the ‘BIG BANG’ hypothesis. This epoch of the Universe is called the *plank epoch*. At this time, size of the Universe was the order of *plank length*:  $1.6 \times 10^{-35}$  m, and the temperature was nearly  $10^{32}$  Kelvin. Hypothetically, this is the time when four fundamental forces (electromagnetism, gravity, strong, and weak nuclear forces) of the Universe were unified as one (Klecze, 1988).

At nearly  $10^{-37}$  seconds, the Universe underwent a phase transition that triggered the *cosmic inflation* (e.g. Guth, 1981). During this time, the Universe expanded exponentially and the temperature dropped significantly. At about  $10^{-36}$  seconds, due to the low temperature, the strong nuclear force separated from the other three forces, while electromagnetism and the weak nuclear force remained unified, which is called the electro-weak interaction (e.g. Salam & Ward, 1959; Glashow, 1959; Weinberg, 1967; D’Onofrio & Rummukainen, 2016).<sup>1</sup> Inflation ended between roughly  $10^{-33}$  to  $10^{-32}$  seconds after the Big Bang, increasing the size of the Universe by at-least a factor of  $\sim 10^{60}$ . The rapid expansion stretched the initial quantum fluctuations to the extreme scales, exceeding the cosmological event horizon, which can be defined by speed of the light  $\times$  age of the Uni-

---

<sup>1</sup>About gravity we do yet know much, we are currently waiting for the quantum theory of gravity.

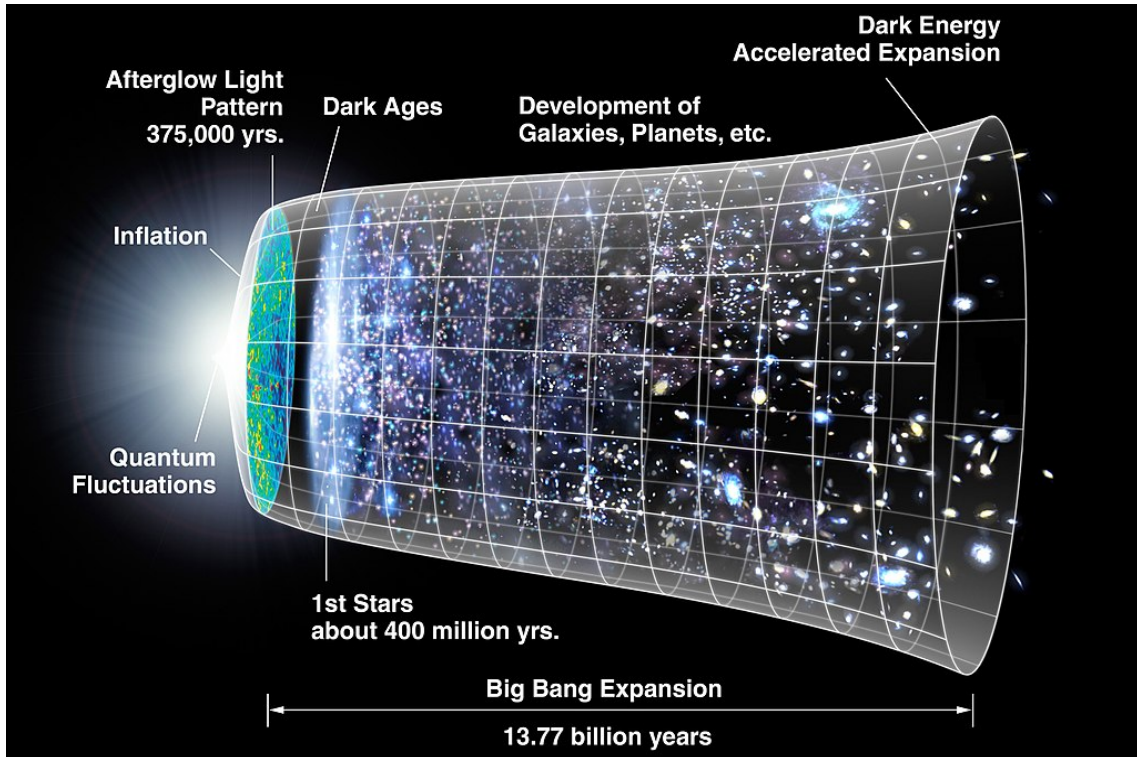


**Figure 1.1:** Cosmic history of the Universe (Image credit: NASA/WMAP Science Team).

verse. These fluctuations (inhomogeneities) later became the source of the present day Large Scale Structure (LSS) of the Universe.

One second after the Big Bang, when the Universe reached the temperature required for the formation of first nuclei, the primordial hydrogen, helium, and lithium started to form. This phase is called *primordial nucleosynthesis* (Kolb & Turner, 1990a), which lasted for roughly three minutes. At this point, the Universe was still very hot & dense, and any photons emitted were immediately captured by free electrons, leaving the Universe opaque. However, the Universe continued to expand in its size, consequently, the density and the temperature continued to decrease. About 380,000 years after the Big Bang, the Universe reached a sufficiently low temperature and density to form the first atom. In particular, the scattering rate between photons and nuclei reduced to the point where free electron could remain bound with nuclei. This era is called *epoch of re-combination*, which allowed photons to move freely and made the Universe transparent to us. The latter phenomenon is known as “decoupling of matter-radiation”. Theoretically, the radiation that emanated from the matter-radiation decoupling is a perfect black-body radiation emitted at  $T = 3000$  K and has continued to travel and cool due to the expansion of the Universe. Today, we observe this primordial radiation in form of *Cosmic Microwave Background* (CMB) having the temperature  $T \approx 2.7$  Kelvin (Penzias & Wilson, 1965).

After matter radiation decoupling, the Universe enter into *dark ages*, where no source of radiation remained, and the Universe was filled with diffused gas of hydrogen and helium. At this time, primordial inhomogeneities in the matter density field that occurred

during the inflationary phase continued to grow due to gravitational instabilities. In these inhomogeneities hydrogen and helium condensed to form the first stars, so-called pop- III stars<sup>2</sup>. The emergence of the first stars (sources) marks *the epoch of re-ionization* and ends the dark ages. Over time, due to gravitational instabilities, the inhomogeneities became larger and led to creation of ‘first galaxies’ and other astronomical structures (e.g., LSS), which we observe today. A schematic diagram of cosmic history of the Universe is shown in Figure 1.1, for the details of the early Universe, structure formation and cosmology, I refer the reader to [Kolb & Turner \(1990a\)](#); [Peebles \(1993\)](#) and [Padmanabhan \(1993\)](#).

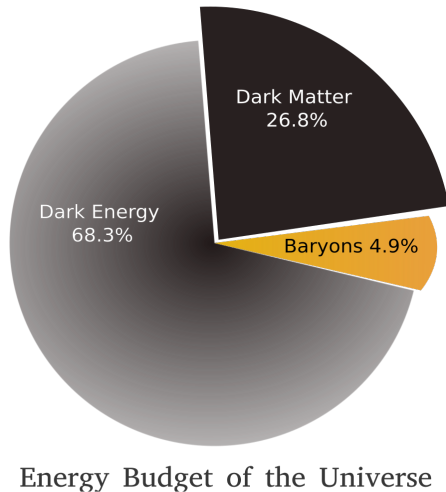


**Figure 1.2:** Constituents of the Universe: normal matter (baryons) that makes up stars and galaxies contributes only 4.9%, dark matter which is detected only via its gravity contributes 26.8%, and dark energy a hypothetical fluid/force, which leads to the accelerated expansion of the Universe, is responsible for most (68.3%) of the mass/energy budget in the Universe.

*particular attention paid to its observational evidence within the galaxies and the determination of its astrophysical nature. I will present the results of dark matter response to the baryonic processes in star-forming galaxies*

<sup>2</sup>Population III (Pop III) stars, which are composed entirely of primordial gas - hydrogen, helium, and very small amounts of lithium. This means that the gas from which the Pop III stars formed had not been ‘recycled’ (incorporated into, and then expelled ) from previous generations of stars, but was pristine material left over from the Big Bang.

<sup>3</sup>Dark Energy is the hypothetical form of energy that exerts a negative, repulsive pressure, behaving like opposite of gravity, thus leads to accelerated expansion of the Universe.

<sup>4</sup>Dark Matter is an invisible matter that does not emit electromagnetic radiation.

**Overview:** CMB and other cosmological observations (e.g. distribution of galaxies, voids and LSS) in the Universe suggest that the energy budget of the Universe is dominated by *Dark Energy*<sup>3</sup> . The next most significant contributor is *Dark Matter*<sup>4</sup> and only a small fraction is filled with ordinary matter, called *Baryons*, see Figure 1.2, for more details see Section 1.2.2. The current cosmological model, the so-called  $\Lambda$ CDM scenario, in which dark energy ( $\Lambda$ : representing the cosmological constant) and dark matter (CDM: Cold Dark Matter) are the theoretical constructors required for explaining the aforementioned observations, provides a good but not perfect explanation of the contemporary Universe. However, due to its various success and the lack of reliable alternatives, this framework is widely accepted in the scientific community, and has become the benchmark for current cosmological simulations. Although, we do not yet understand the true nature of dark energy and dark matter. ***This thesis will be focused on the phenomenon of DARK MATTER, with***

*from look-back time 6.5 Gyrs, as well as attempt to compare their kinematics and dynamics with their local counterparts, and state-of-the-art cosmological simulations.* In particular, I will answer the following questions:

1. What is the distribution and fraction of dark matter in  $z \sim 1$  star-forming galaxies?
2. Whether or not, interaction between dark and luminous matter impacts the structural properties of dark matter and fundamental scaling relations (e.g., Tully-Fisher relation)?
3. How dark matter plays an important role in galaxy evolution?

Before going into the details of my work, in this chapter I will briefly discuss the historical view on dark matter in Section 1.1; various dark matter probes in Section 1.2 covering the astrophysical and particle nature of dark matter, and other dark matter scenarios in Section 1.3. The small and large scale problems of widely accepted  $\Lambda$ CDM scenario are discussed in Section 1.4. Finally, in Section 1.5, I will provide an outline of this thesis.

## 1.1 Discovery of Dark Matter

The very first hints for the existence of invisible matter was obtained by Lord Kelvin in 1904, who argued that if we assume that the stars in the Milky Way behave like particles of gas and move under the influence of gravity then we can establish the relationship between the distance and the velocity distribution of the stars. He predicted that "*in the radius of  $3.09 \times 10^{16}$  km, there may be as many as  $10^9$  stars, but many of them are likely extinct and dark*" (Kelvin, 1904). Lord Kelvin's idea was taken up by Henri Poincaré. In 1906, Henri showed that the velocity dispersion predicted in Kelvin's estimates agreed with observations (Poincaré & Vergne, 1911), and he coined the term *Dark Matter* ('mattère obscure' in French).

Later investigations of the hypothetical dark matter began with the dynamical study of the solar neighbourhood by öpik (1915) and Kapteyn (1922). Both studies found that the sum of all stellar populations satisfies the velocity dispersion of the stars, i.e. they could not find any evidence for the existence of dark matter. In 1922, the British astronomer James Hopwood Jeans reanalysed the stellar motion near the Milky Way plane and recorded the presence of dark matter (Jeans, 1922). Later, in 1932, a student of Jacobus Kapteyn, Jan Hendrik Oort, revised Kapteyn's work. He improved upon the methods used by Kapteyn, in particular, relaxing the assumption of the 'isothermality' of the gas of stars, and determined the quantitative difference between the density of total matter and visible matter in the solar neighbourhood (see, Oort, 1932).

In 1933, the Swiss astronomer Fritz Zwicky estimated the velocity dispersion of galaxies in the Coma cluster using Virial estimates, taking the mass of galaxies from the study of Hubble (1926). He found that  $\sim 800$  galaxies of roughly  $10^9 M_\odot$  in a sphere of  $10^6$  light years should have a velocity dispersion of 80 km/s. In contrast, he observed that

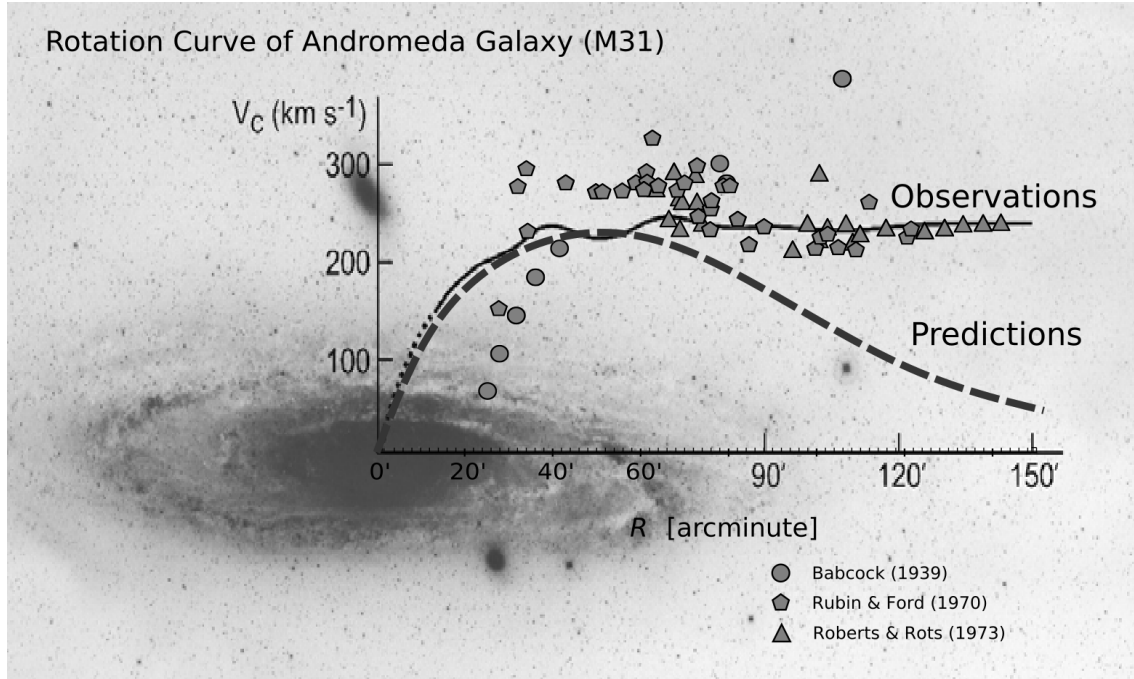


**Figure 1.3:** Historic rotation curve of Andromeda galaxy (M31). The rotation velocity data is taken from [Babcock \(1939\)](#), [Rubin & Ford \(1970\)](#) and [Roberts & Rots \(1973\)](#). The photographic image of M31 is taken from [Roberts \(2008\)](#) and improvised by G. Sharma for this work.

the velocity dispersion was  $\sim 1000$  km/s. He concluded that *if this is confirmed, then we would get the surprising results that the dark matter is present in a much greater amount than the luminous matter* (see, [Zwicky, 1933](#)). From an astrophysical point of view, this suggests that the total mass density of the Coma cluster is at-least an order of magnitude higher than what we would expect based on its light distribution. Zwicky's work was one of the most significant discoveries of the past century. A similar study of Virgo cluster galaxies by [Smith \(1936\)](#) confirmed Zwicky's discovery. Since then, dark matter has firmly been established in the field of astrophysics and has become a part of general interest (discussion). However, the hypothesis of dark matter was neither fully accepted nor denied. Rather, there were a consensus that more information is required to understand and clarify this "invisible" issue.

The first classical evidence for the existence of dark matter comes from the PhD thesis of [Babcock \(1939\)](#), who studied the rotational velocity of the Andromeda galaxy from the inner to the outer edge ( $\sim 20$  kpc) of the galactic disc, as shown in Figure 1.3. He found that the rotation velocity as a function of radius, the so-called rotation curve, does not show the Keplerian fall:  $1/\sqrt{R}$ , which is expected if the mass distribution follows the light. He concluded that the Andromeda galaxy is dominated by invisible matter. Later, [Oort \(1940\)](#) reported similar results for the galaxy NGC3115. After two decades, [van de Hulst et al. \(1957\)](#) confirmed Babcock's results using observations of neutral hydrogen (21cm wavelength). Later these results were again confirmed from optical observations by [Rubin & Ford \(1970\)](#) and radio observations by [Roberts & Rots \(1973\)](#), see Figure 1.3.

In another work of Rubin and collaborator (Rubin et al., 1978), they presented the flat rotation curves of 10 local spiral galaxies and concluded that-

*“To explain the observations we need to assume a more or less spherical distribution of dark matter, the so-called ‘dark matter halo’, which surrounds the galactic disc and extends much further out in the space than the visible part of the galaxy.”*

At the same time Albert Bosma (Bosma, 1981; Bosma, 1978) carried out the HI observations and measured the rotation curves of 25 spiral galaxies. This was an extension of the work started by Babcock and carried out by Van de Hulst, Roberts, Rubin and Ford. These observational findings were successfully incorporated into theoretical models of structure formation and became the building block of the current cosmological model (see, Ostriker & Peebles, 1973; Bertone & Hooper, 2018). Now, instead of denying the existence of dark matter, most of the scientific community look forward to discovering its nature, whether it is a particle, a fluid, or a force?

## 1.2 Dark Matter Probes

The most direct evidence for dark matter comes from observations where we dynamically study the gravitational interaction of dark and luminous matter, i.e. from the dynamics within galaxies and galaxy clusters. In addition to the classical probes, the two other most popular dark matter probes are the CMB power spectrum and the gravitational lensing effect. In this section, I will briefly discuss the determination of dark matter through these three and other dark matter probes in the chronological order of their discoveries.

### 1.2.1 Galaxies & Galaxy Clusters

The dynamical studies of individual galaxies and galaxy clusters have always been the classical laboratories of showing the presence of dark matter (Zwicky, 1933; Rubin & Ford, 1970; Sofue & Rubin, 2001; Allen et al., 2011; Salucci, 2019, and references therein). In particular, spectroscopic observations of emission (or absorption) lines of elements (e.g., hydrogen) gives us the circular velocity of stars and gas (for details see Chapter 2), which is a good proxy of total mass distribution in galaxies (or galaxy clusters). That is, by following Newtonian physics one can write:

$$M_{\text{enc}}(R) = \frac{V_c^2(R) R}{G}, \quad \text{or} \quad M_{\text{enc}}(R) = \frac{\sigma^2(R) R}{G}, \quad (1.1)$$

where  $M_{\text{enc}}(R)$  is the total mass enclosed in radius  $R$ , and  $G$  is gravitational constant. In general, local spirals, dwarf discs, and low surface brightness galaxies are rotation-dominated systems, i.e. they exhibit coherent circular motion which balances the gravitational force and hence allows us to determine the total enclosed mass. On the other hand, galaxy clusters are dispersion ( $\sigma$ ) dominated systems where gravitational collapse is circumvented by the velocity dispersion of its constituents, and hence the latter provides

a suitable proxy for the enclosed mass. While spectroscopic observations trace the total mass under the influence of gravity, the photometric observations of the light distribution of galaxies (or galaxy clusters), e.g. surface brightness, give us the total luminous matter distribution,  $M_L(R)$ , in galaxies (or galaxy clusters). In the absence of dark matter, the total enclosed mass  $M_{\text{enc}}(R)$  should be equal to the total luminous mass  $M_L(R)$ , i.e. if the mass follows the light, then  $M_{\text{enc}}(R) = M_L(R)$ , but what we observe is  $M_{\text{enc}}(R) > M_L(R)$ . For example see Figure 1.3, where we plot the **observations** of circular velocity of the Andromeda galaxy (M31), which gives  $M_{\text{enc}}(R)$ , and the **predictions** of the circular velocity (dashed line) coming from the light distribution  $M_L(R)$ . This immediately reveals the phenomenon of mass discrepancy in the galaxies, which is visible through the observed flat rotation curve/s contradicting the predictions obtained from light distribution. In case of galaxy clusters, the same problem is known as *missing mass problem*, which is studied by the velocity dispersion of the galaxies in the cluster.

In order to satisfy these observations, we need to assume that the enclosed mass of the system scales as  $M_{\text{enc}}(R) \propto R$ . That is, it suggests us to consider the dark matter halo component  $M_{\text{Halo}}(R)$  around a galaxy (or galaxy cluster), which can be computed from observations as:

$$M_{\text{Halo}}(R) = M_{\text{enc}}(R) - M_L(R), \quad (1.2)$$

where  $M_{\text{enc}}(R)$  is derived from observed circular velocity (see Equation 1.1) and luminous matter  $M_L(R)$  can be estimated from light distribution (e.g. photometry) of galaxies. In some case, such as in scalar estimates<sup>5</sup>, it is also useful to consider Equation 1.2 in terms of logarithmic derivative of total enclosed mass:

$$\frac{\partial \log M_{\text{enc}}(R)}{\partial \log R} = \frac{M_L(R)}{M_{\text{enc}}(R)} \frac{\partial \log M_L(R)}{\partial \log R} + \frac{M_{\text{Halo}}(R)}{M_{\text{enc}}(R)} \frac{\partial \log M_{\text{Halo}}(R)}{\partial \log R}, \quad (1.3)$$

which tells us the infinitesimal relative change in  $M_{\text{enc}}$  as a function of radius  $R$  of the galaxy. This also implies that precise measurements of gravitating matter (from luminosity and velocity) are capable of deriving the dark matter content of galaxies (or galaxy clusters). We recall again, that these type of studies are straightforward in rotation dominated systems, since their dynamics and kinematics can be easily derived (Persic et al., 1996; Salucci & Burkert, 2000a; Sofue & Rubin, 2001; de Blok et al., 2001; Karukes & Salucci, 2017; Di Paolo et al., 2019). In this thesis, starting from Chapter 3, I will treat only the rotation-dominated systems in the local and at the high-redshift Universe. However, the study of dispersion-dominated systems, such as elliptical galaxies and galaxy clusters, is somewhat difficult, but not impossible. Indeed, the seminal studies of dark matter came from the coma cluster studied by Zwicky (1933) and later followed by many others (e.g. Allen et al., 2011, and references therein).

### 1.2.2 CMB Power Spectrum

The observation of the CMB is a milestone in our current understanding of the origin of the Universe. It is constituted of isotropic electromagnetic radiation (close to perfect

---

<sup>5</sup>Scalar estimates, e.g. finding inner slope of dark matter and luminous matter.

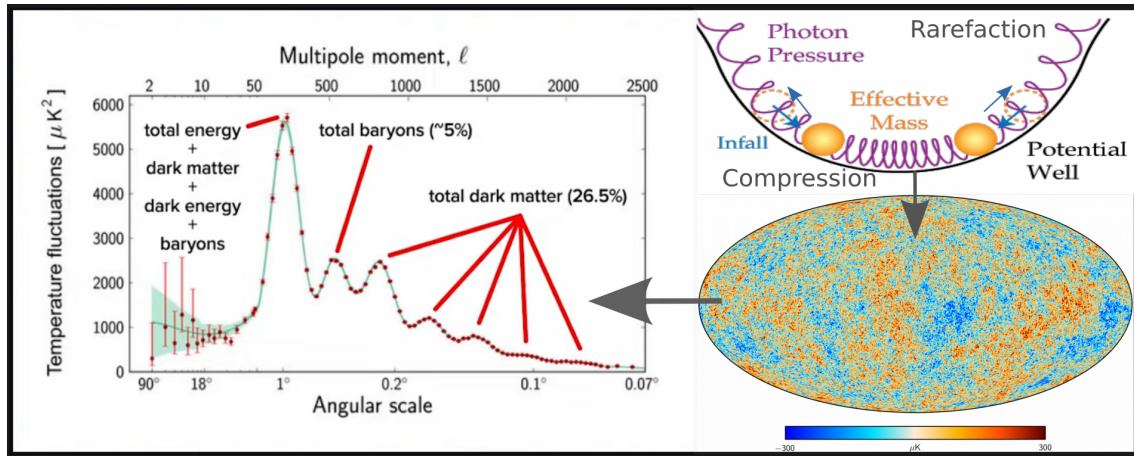


**Figure 1.4:** Observations of Cosmic Microwave Background explanation. *Right top panel*: cartoon image of the acoustic oscillation in the potential well of baryons (yellow balls), photons (springs) and dark matter (invisible), this leads to the temperature fluctuation in the matter density field at the time of recombination, which we measured today in form of CMB, shown in *Right bottom panel*. An examination of the CMB map by cross-correlating the temperature and size of all the regions in the sky yields the CMB power spectrum (*left panel*). Image credit [Planck Collaboration et al. \(2016\)](#), improvised by G. Sharma for the purposes of this thesis. Note that a relative difference of second peak with first gives the baryon fraction, while the dark matter fraction is inferred via relative difference of higher order peaks with the first and the second peaks.

blackbody), emitted during the period of recombination in the early Universe, which is why it is also known as '*relic radiation*'. A careful study of this radiation has allowed us to accurately measure the energy content of the Universe, and established the Standard Model of Cosmology.

As mentioned earlier, between the Big Bang and recombination, the young Universe was filled with ordinary matter, radiation, and hypothetical dark matter. During that epoch, characterized by high-density and temperature, the ordinary matter was strongly coupled with radiation and formed a fog of hydrogen plasma that made the Universe opaque to us. On the other hand, under the same conditions dark matter did not interact with either of these substances, which allowed primordial dark matter density perturbation to grow forming the dark matter potential wells. This forms the basis of the perturbation theory ([Peebles, 1993](#); [Ma & Bertschinger, 1995](#); [Bashinsky & Bertschinger, 2002](#)), according to which the gravitational instabilities continue to increase in the dark matter density, while baryons oscillate in the corresponding gravitational wells. These oscillations are commonly known as acoustic oscillations and arise due to the significant radiation pressure within the hydrogen plasma. A simple analogy for this behaviour is the motion of a mass on a spring, as depicted in Figure 1.4, where spring plays the role of radiation pressure.

When recombination occurred, the photons decoupled from the hydrogen plasma, making the Universe transparent, which enabled us to detect the photons that were produced

at that time, and even today, i.e. giving us the *first image* of the young Universe. In this image, we see a frozen plasma field (of that time), in which matter is either collapsing due to gravity (i.e. maximum baryon density) or expanding due to the radiation pressure (i.e., minimum baryon density), or somewhere in between of these two states. The maximum density situation is called maximum compression and the minimum density situation is called maximum rarefaction, which is represented by the red and blue (hot and cold) spots on the CMB map (see Figure 1.4, right panel), respectively. A study of size and temperature of these spots provide us with the CMB temperature power spectrum, shown in left panel of Figure 1.4, which gives us a clear picture of the sound wave oscillation in the baryon density field. In particular, we plot the number of spots of all possible sizes (in angular units) as a function of the temperature fluctuations. Theoretically, the temperature (so the density) of these spots, tells us whether they belongs to maximum-compression or rarefaction. All spots of angular size  $\sim 1^\circ$  belong to the first peak, and they are the regions in the sky that can collapse only once (maximum compression) before the recombination. The second peak corresponds to a complete compression and a complete rarefaction. The third peak corresponds to compression-rarefaction-compression and so on. These peaks of the power spectrum provide us with the basic ingredients of our contemporary Universe, namely the energy budget.

In detail, the first peak shows the areas (angular sizes) in the sky where the baryons collapsed only once before the recombination occurred. Theoretically, the physical size corresponds to these areas are roughly half a million light years ( $= 0.58c^6 \times 380,000^7$  years  $\times$  scale-factor<sup>8</sup>). From simple geometry ( $angle = arc/radius$ ), we can deduce that if light-rays travel from an area (or spot) of size ‘half a million light years’ from the time of recombination to the present day without converging or diverging, then the area associated to light-rays should form an angle of  $1^\circ$ . The latter is only possible if light-rays travel in straight line, i.e. in a geometrically flat space<sup>9</sup>. Here, the phenomenon of convergence or divergence of light-rays can also be related to the total energy which derives the curvature of the Universe:  $\Omega_K = [-ve, 0, +ve]$ , for a closed, flat, and open Universe, respectively. In particular, the Universe leads to a positive curvature  $\Omega_K > 0$  due to its positive gravitational effect. On the other hand, an expanding Universe without energy would have negative curvature. That is, a flat Universe will have just the right amount of energy to flatten the geometry of the Universe. Since we observe that most spots in the CMB maps have an angular size of  $1^\circ$ , as shown by the first peak in the CMB power spectrum (see Figure 1.4 left panel), and a detailed analysis of it by the Planck team (Planck Collaboration et al., 2016, 2020a) have shown that the curvature of the Universe,  $\Omega_K = 0.001 \pm 0.002$ . That is, *the location of first peak in the CMB power spectrum tells us that the Universe is flat*, and thus gives us the total amount of energy in the Universe.

<sup>6</sup>sound speed at the time of recombination is  $0.58 \times$  speed of light.

<sup>7</sup>age of the Universe at the time of recombination is 380,000 years.

<sup>8</sup>the relative expansion of the Universe at the time of recombination.

<sup>9</sup>Geometrically flat space means, where parallel line stays parallel and angles of a triangle add up to 180 degrees.

The second peak represents the situation when the baryons has collapsed once and then expanded. That is, the ratio of the first peak to the second gives us the total baryon fraction ( $\Omega_b$ ) in the Universe. The result of [Planck Collaboration et al. \(2016, 2020a\)](#) shows that the  $\Omega_b \approx 0.044$ . The third and the higher-order peaks is a consequence of multiple compression and rarefaction. That is, we can argue that when baryon over densities expanded to its maximum, photons will continue to redshift with the Universe. As a consequence gravitational potential will decay, this would allow the temperature perturbation to be of much greater than it would be otherwise, and hence will enhance the third peak. In contrast, non-relativistic matter (hypothetical dark matter) redshift very minimally and slowly, so for other consecutive peaks the gravitational potential produced by it will remain there. This would lead to a relatively smaller temperature perturbations, i.e., smaller peaks. This is how, *studying a relative difference of higher order peaks with first and second peaks tells us the amount of non-relativistic matter, i.e., dark matter*. The  $\Lambda$ CDM model that best fit the CMB data gives us only 4.9% baryons, 26.5% dark matter and rest 63.3% is dark energy ([Planck Collaboration et al., 2020a](#)), see Figure 1.2, for more relevant details on this topic we refer the reader to [Hu & Dodelson \(2002\)](#); [Wang & Huang \(2020\)](#) and references therein. This energy budget is also independently measured from the modern galaxies ([Cappi, 2015](#); [Wang & Zhao, 2020](#), and references therein) and large scale structure surveys of the Universe ([Bahcall, 1988](#); [Tröster et al., 2020](#), and references therein).

### 1.2.3 Gravitational Lensing

The light rays coming from a distant object in the Universe are sometimes intervened by the presence of massive structures such as clusters of galaxies. This intervention generally occurs as a bending of light due to the gravitational deformation of space-time. This phenomenon of *light bending* is known as *Gravitational Lensing* ([Refsdal, 1964](#); [Sauer, 2008](#)). The matter distributed between the distant object (also called the source) and the observer is called *Gravitational Lens*, for details see Figure 1.5. The light bending on space-time is also one of the predictions of Einstein's general theory of relativity, which has been confirmed by the observations of gravitational lensing.

In some peculiar conditions source, observer, and lens found to be aligned in a straight line, consequently, the source appears as a ring around the lens in the sky, referred to as *Einstein ring*, as shown in Figure 1.5 bottom (second/middle) left panel. The latter gravitational lensing phenomena, in which light rays are distorted into the Einstein rings, long arcs, and multiple images, fall into the category of *Strong Lensing*. The first image of a strongly lensed system 'twin quasars' was discovered by [Walsh et al. \(1979\)](#). This discovery opened a completely new avenue for the study of the dark matter, since the lensed source allows us to reconstruct the total mass distribution of gravitational lens purely from observations of baryonic matter using general relativity ([Blandford & Narayan, 1992](#); [Kochanek, 1995](#)). These measurements typically lead to a more accurate dark matter estimate than the use of the virial theorem. In recent decades, numerous strongly lensed systems have been discovered, where the gravitational lens is typically a galaxy cluster

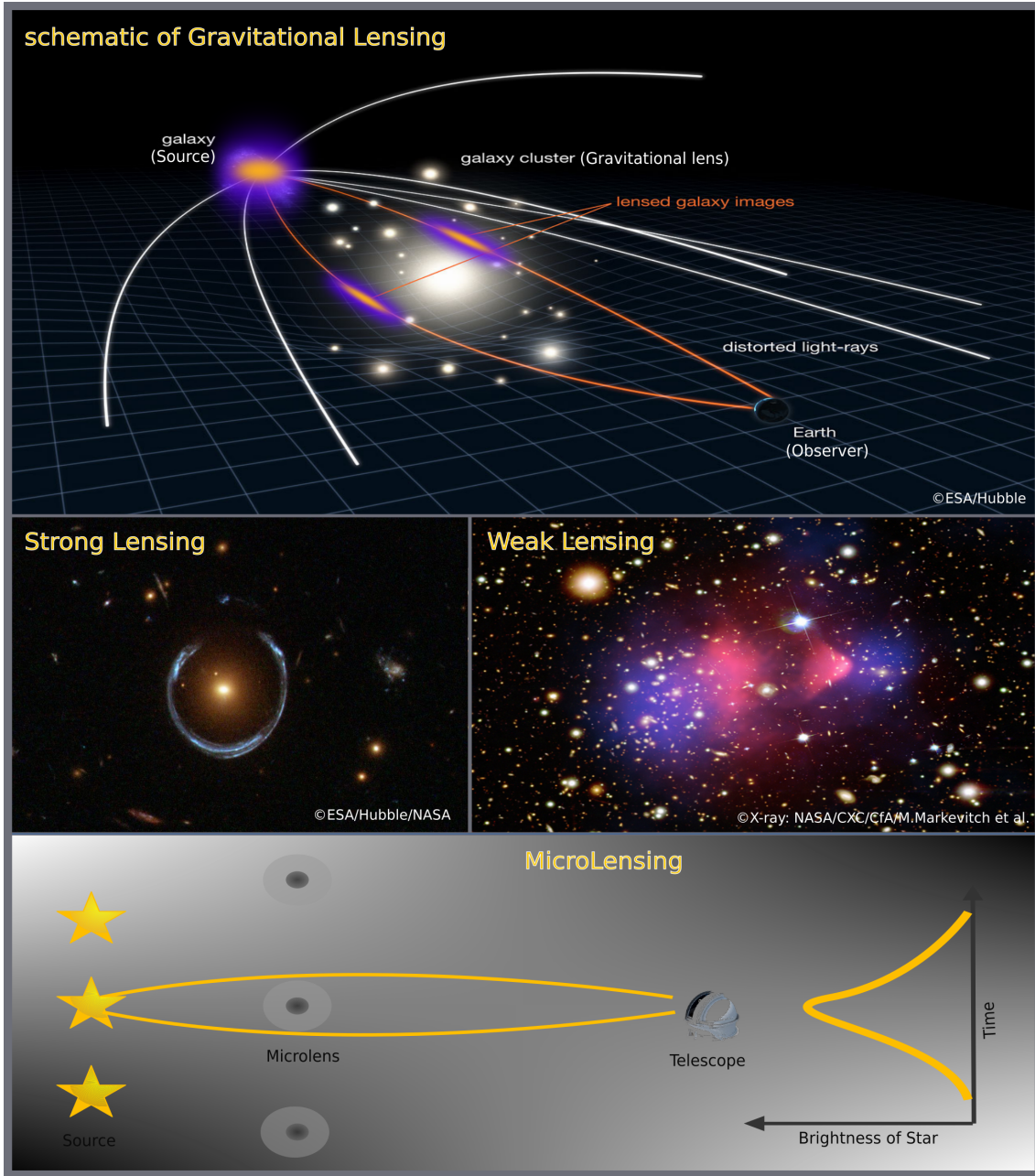


**Figure 1.5:** Gravitational lensing in the Universe. *Top:* schematic representation of gravitational lensing phenomenon occurring on the fabric of space-time. *Middle left:* strong lensing phenomenon when the source (galaxy), lens (galaxy cluster), and observer are aligned in a straight line, forming a horseshoe-shaped Einstein ring, captured by Hubble Space Telescope (HST). *Middle right:* weak lensing phenomenon visible in the collision of galaxy clusters known as *bullet cluster*. The background is constructed from HST and Magellan Telescope images, the pink region in the centre is imaged with the Chandra X-ray telescope, and the blue region represents the mass distribution of the clusters artificially drawn by calculating the gravitational effect. *Bottom:* schematic representation of microlensing happening on the Galactic scale. Note that this image was constructed to illustrate the phenomenon of gravitational lensing and its types using different images, the copyrights are printed on each image (improvised by G. Sharma).

and the source varies from galaxies to quasars or distant galaxy clusters. While strong lensing provides an unique and accurate estimate of dark matter in the local Universe (Treu, 2010, and references therein) and at high-redshift (van der Wel et al., 2013; Wong et al., 2014; Díaz-Sánchez et al., 2021), these phenomena are relatively rare.

A common type of lensing is the *Weak Lensing*, in which the trajectory of the light source is only slightly distorted either due to less accurate source-lens alignment or less massive gravitational lens. By statistically studying the shear deformation in the broad galaxy surveys (or large-scale structures), we can infer the global distribution of dark matter (Refregier, 2003; Hoekstra & Jain, 2008). Indeed, again weak lensing indicates the mass discrepancy between gravitating and luminous matter (More et al., 2015; Hildebrandt et al., 2017). For example, *Bullet cluster* is a phenomenal example where weak lensing is widely observed. The bullet cluster is a system of two colliding clusters those are mapped with ultraviolet, optical and X-ray telescopes. A multi-wavelength image of this cluster, shown in the middle right panel of Figure 1.5, shows a clear segregation of hot, ionized, interacting gas lagging behind the dark matter dominated centre of mass and galaxies causing the weak lensing of background sources (Clowe et al., 2006).

Besides, the strong and weak lensing, there is also the phenomenon called *Microlensing Lensing* (Alcock et al., 1993), which is gaining a lot of attention in connection with the determination of the nature of dark matter (Fedorova et al., 2016). Microlensing occurs at galactic scale, presumably when a substructure, i.e. a lens, passes in front of the light source, as shown in bottom panel of Figure 1.5. In the case of microlensing, the mass of the gravitational lens is small ( $10^{-8}$  to  $10^2 M_{\odot}$ ) and it can move from the front of the light source in seconds-to-years. As a consequence, the apparent brightness of the light source changes, which can be observed with regular photometry of the source (i.e., the light curve), but cannot be imaged as in case of strong & weak lensing. As already mentioned, this is a galactic-scale phenomenon, where the source is usually a star and potential candidates for lens are faint brown dwarfs, low-mass black holes, primordial black holes, and massive compact halo objects (MACHOs); for a detailed overview on this topic, I refer the reader to Alcock et al. (1993); Aubourg et al. (1993); Gates et al. (1995); Gaudi (2012); Fedorova et al. (2016) and Croon et al. (2020).

#### 1.2.4 Other Dark Matter Probes

Beyond the study of galaxies and galaxy clusters, dark matter can also be studied using the dynamics of globular clusters<sup>10</sup>, ‘the oldest structures’ in the Universe, (e.g. Tallet et al., 1995; Forbes et al., 2016). Recently, Hassani & Milad Ghaffarpour Mousavi (2021) has shown that the dark matter affects the stellar population in globular clusters, and Wirth et al. (2020) has shown that the globular clusters are the laboratory for detecting the annihilation of the dark matter particle. In addition, the bound structures such as globular clusters or satellite galaxies, while orbiting the host galaxy get disrupted or create the tidal streams. This phenomena is capable of testing the dark matter hypothesis,

<sup>10</sup>Globular clusters are spheroidal gravitationally bound systems containing 100,000 to a million stars, and orbiting in the halos of all large galaxies.

as well as constraining its particle nature (Erkal & Belokurov, 2015; Banik et al., 2018; Peñarrubia, 2019). The particle nature of dark matter can also be constrained by a careful study of dark matter interaction rate in astrophysical processes such as cooling rate of neutron stars (Ding et al., 2019). Moreover, recent studies show that the dark matter capture within the white dwarf may also lead to the premature ignition of supernova (Graham et al., 2018; Acevedo & Bramante, 2019). Besides this, it is also thought that a supernova explosion can act as particle accelerator and possibly be interesting to constrain the new particles beyond the standard model of particle physics, and so the particle nature of dark matter (DeRocco et al., 2019; Sung et al., 2019).

Besides the CMB, the other cosmological probes of the dark matter are the Lyman- $\alpha$  forest (McQuinn, 2016) and the 21-cm emission line of neutral hydrogen (Pritchard & Loeb, 2012). These two observables are sensitive to the distribution of neutral hydrogen at different redshifts. This allows us to reconstruct the matter power spectrum, which is a consequence of hydrogen overdensities, this concept is explained in great detail in Kovetz et al. (2019) and Ouchi et al. (2020). Thus, these two probes are able to constrain the dark matter clustering properties, that will allow us to see the possible deviation from the standard cold dark matter scenario.

Furthermore, the detection of gravitational waves open-up a whole new window for astrophysicists and cosmologists to explore the Universe and its constituents (for details see, Miller & Yunes, 2019). Although gravitational wave physics is a relatively new field, it has already provided several ways to study the nature of the dark matter. For example, collisions of black holes and neutron stars place tighter constraints on the abundance of primordial black holes, which are one of the potential candidates for dark matter (Bartolo et al., 2019; Frampton, 2019). With the anticipated advancement of this field, we will soon be able to trace the physics of the early Universe, as well as from astrophysics of small to large scales (Bailes et al., 2021), i.e. making gravitational waves a valuable cosmological and astrophysical probe.

### 1.3 Dark Matter Particles and Scenarios

Although observations of astrophysical processes, gravitational effects, and cosmological parameters have strongly demonstrated the presence of dark matter, its particle nature remains elusive. From the aforementioned observational probes, it can be inferred that the dark matter is non-baryonic matter, and effectively behaves like collisionless non-relativistic particles, which has to be stable (or metastable) on the timescale of  $>> 10$  Gyr. If one adopt the particle definition, it can be shown that none of the standard model particle can form a significant fraction of dark matter. However, observational constraints allows many theoretical possibilities, and give us a great scope to constrain the dark matter particle. In particular, a parameter space of more than 50 orders of magnitude for the interaction cross-section ( $\sigma_{\text{int}}$ ) and mass range is allowed, see Figure 1.6, which actually gives us a feeling of "looking for a needle in a haystack".

Some of the most prominent particle candidates for dark matter are ultra-light bosons

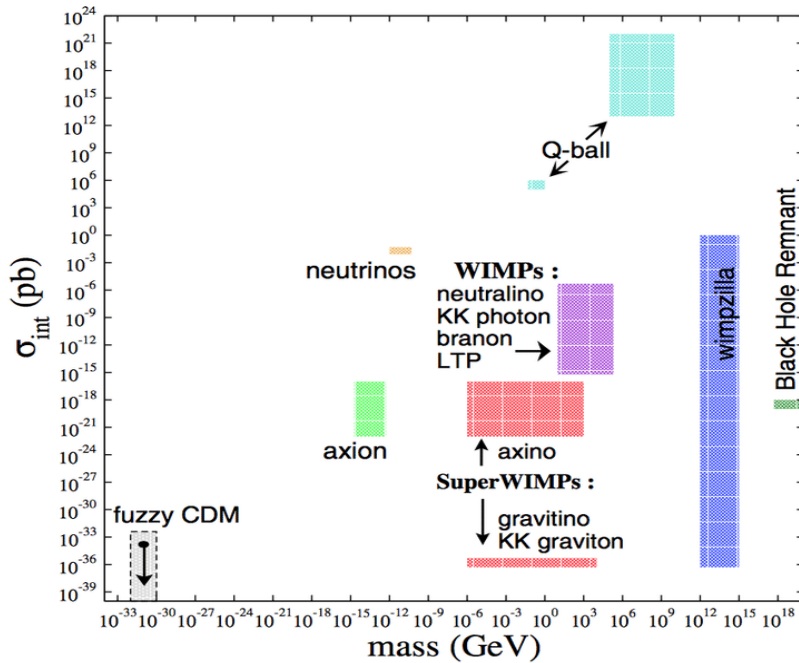


**Figure 1.6:** The locus of various dark matter particle candidates in mass and interaction cross section plain, image credit: [DMSAG](#).

(e.g. axions), sterile neutrinos, weakly interacting massive particles (WIMPs), gravitationally interacting massive particles (GIMPs), etc. Theoretically, depending on the free streaming length<sup>11</sup> (FSL) of these particles, we can divide dark matter into three scenarios: hot, warm, and cold. The *hot dark matter* candidates are mainly neutrinos, they interact with ordinary matter only via gravity, they are dark and difficult to detect. The FSL of these particles is larger than those of proto-galaxies ([Vittorio & Silk, 1984](#); [Umemura & Ikeuchi, 1985](#)). That is, the hot dark matter scenario predicts giant super-clusters in the early Universe, that then fragmented into small galaxies. In contrast, deep field observations show that galaxies formed first ([Dayal & Ferrara, 2018](#), and references therein). Therefore, the hot dark matter scenario is not motivated by observations. On the other hand, *warm dark matter* has FSL of the order of proto-galaxies, so it allows for small density perturbations as observed. The sterile neutrinos are known to be warm dark matter particles, but this scenario predicts the low abundance of dwarf galaxies, and reduces the dark matter density in the inner region of galaxies. On the other hand, *cold dark matter* scenario is similar to warm dark matter, but the FSL of its particles is smaller than that of proto-galaxies, which promotes/predicts the right amount of sub-structures in the Universe. For this reason, the cold dark matter scenario is the most favorable and widely accepted in the community. The possible candidates of cold dark matter are WIMP like particles, but they are not discovered yet. Currently, experiments

<sup>11</sup>The free streaming length is the distance traveled by a particle (or photon) in a medium without scattering.

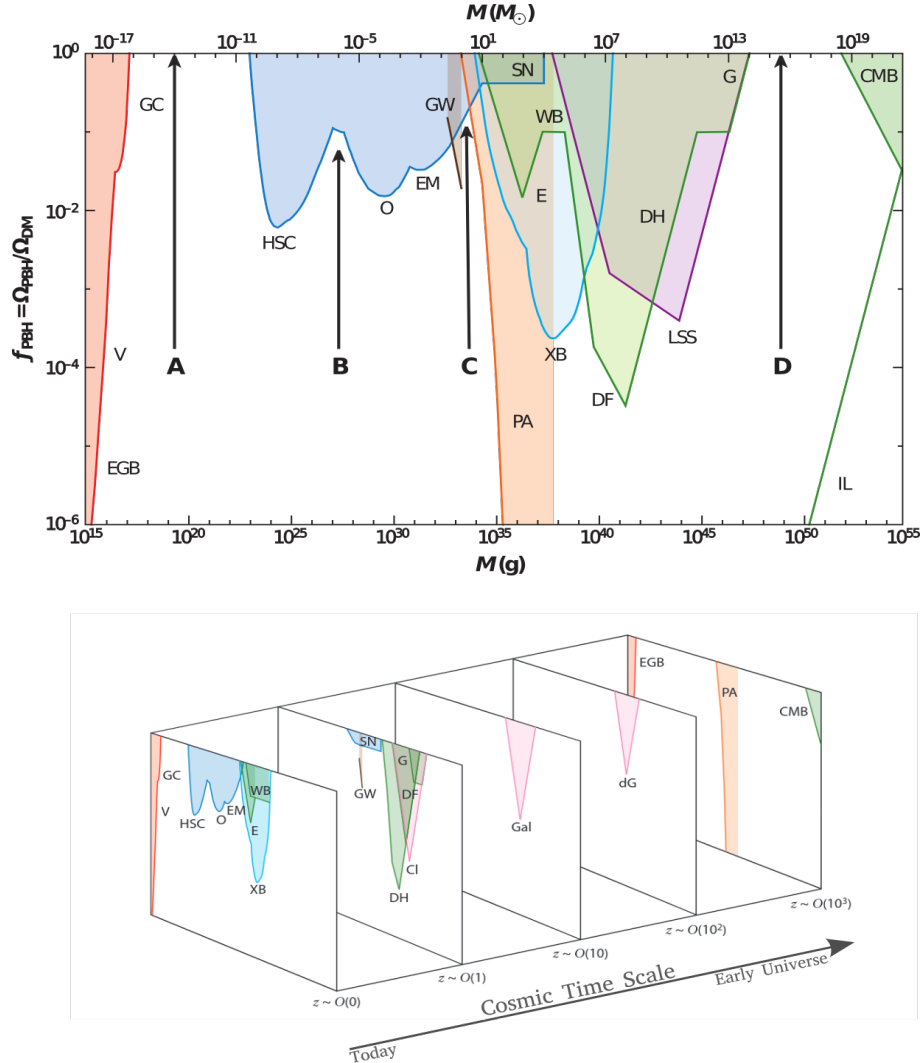


**Figure 1.7:** Constraints on  $f_{\text{PBH}}(M)$  for a monochromatic mass function from evaporation (red), lensing (dark blue), gravitational waves (GW) (brown), dynamical effects (green), accretion (light blue), CMB distortions (orange), and large-scale structure (purple). Evaporation limits come from the extragalactic -ray background (EGB), the Voyager positron flux (V), and annihilation line radiation from the Galactic center (GC). Lensing limits come from microlensing of supernovae (SN) and of stars in M31 by the Subaru Hyper Suprime-Cam (HSC), the Magellanic Clouds by EROS and MACHO (EM), and the Galactic bulge by OGLE (O). Dynamical limits come from wide binaries (WB), star clusters in Eridanus II (E), halo dynamical friction (DF), galaxy tidal distortions (G), heating of stars in the Galactic disc (DH), and the CMB dipole (CMB). Large-scale structure constraints derive from the requirement that various cosmological structures do not form earlier than observed (LSS). Accretion limits come from X-ray binaries (XB) and Planck measurements of cosmic microwave background distortions (PA). The incredulity limits (IL) correspond to one primordial black hole (PBH) per relevant environment (galaxy, cluster, the Universe). There are four mass windows (A, B, C, D) shown by black arrows in which PBHs could have an appreciable density. The bottom panel shows the chronological order of the PBHs constraint as they appear over cosmic time (at various redshift ranges). The image and its description is adopted from Carr et al. (2020); Carr & Kühnel (2020).

based on the Large Hadron Collider, as well as direct and indirect dark matter searches, are working exhaustively to find the properties of dark matter and its coupling strength. However, no success has been achieved so far. Since my this thesis work is mainly centred on the astrophysical properties/nature of dark matter; hence, the more detailed discussion on its particle nature is beyond the scope of this work. However, we refer the reader to some great reviews in the field such as [Gaitskell \(2004\)](#); [Feng \(2010\)](#); [Porter et al. \(2011\)](#); [Bergström \(2012\)](#); [Kawasaki & Nakayama \(2013\)](#); [Gaskins \(2016a\)](#); [Roszkowski et al. \(2018\)](#); [Dutta & Strigari \(2019\)](#); [Profumo et al. \(2019\)](#); [Billard et al. \(2021\)](#) and [Arbey & Mahmoudi \(2021\)](#).

Besides the particle(s) being the candidate of dark matter, it has also been suggested that black hole that were emerged in the early Universe, the ‘Primordial Black Holes (PBHs)’, may constitute the dark matter. The formation of PBHs is often associated with enhanced small-scale curvature perturbations which can arise in various models of inflation (e.g. [Inomata et al., 2017](#)). They behave like non-relativistic matter on large scales and if their mass is above  $\sim 10^{-17} M_\odot$  they should be sufficiently long-lived to provide a viable dark matter candidate. In Figure 1.7, I show the recent constraints on the fraction of dark matter in the form of PBH as a function of PBH mass ( $M$ ). As can be seen from the plot, a significant portion of the PBH mass range is strongly constrained by various observations. However, there are still very narrow mass windows, shown by **A**, **B**, **C**, and **D**, where PBHs can potentially constitute all of the dark matter ([Carr & Kühnel, 2020](#), and references therein). For PBHs, not only the exclusion limits but also their detection is challenging. However, microlensing discussed in Section 1.2.3, or gravitational wave experiments can be very useful to detect PBHs in the near future ([Paczynski, 1986](#); [Niikura et al., 2019](#)).

Given the lack of tangible signals from particle and PBH dark matter candidates, there have been efforts to provide an alternative explanations to the dark matter phenomenon through modified theories of gravity, such as: Modified Newtonian Dynamics (MOND: [Milgrom, 1983](#)),  $f(R)$  theories ([Capozziello et al., 2007](#)). For details on modified theories of gravity, we refer the reader to [Ferreira \(2019\)](#). The alternative theories to particle dark matter are able to reproduce the rotation curves of local spiral galaxies (e.g. [McGaugh, 2020](#)), but observations of other classes of galaxies consistently argue against them. In particular, the gravitational lensing and cosmological probes are difficult to reconcile with the theories of modified gravity (e.g. [Clowe et al., 2006](#)).

## 1.4 Problems in $\Lambda$ CDM Scenario

In this work, I primarily focus on the standard  $\Lambda$ CDM scenario, which we have already discussed in detail in introductory section and in Section 1.2. Thus, I have assumed that the  $\Lambda$ CDM model is capable of describing the early Universe, the various elements of matter and energy, and the formation and evolution of large-scale structures in the Universe. However, we often find discrepancies between the physics going on at the galactic and extragalactic scales and the observations reproduced with the current state-

of-the-art simulations under the  $\Lambda$ CDM scenario, commonly referred to as *small-scale problems*. Moreover, with precision cosmology, we recently began to see several tensions between the observations of the early Universe and the  $\Lambda$ CDM scenario, referred to as *large-scale problems*. In this section, I will discuss some of the important small- and large-scale problems. It should be emphasised that these problems have a very minor (or no) impact on the work conducted in this thesis.

### 1.4.1 Small Scale Problems

It is the small-scale problems that often highlight the conflicts between observations of galactic to extragalactic scales and simulations. Recently, [Del Popolo & Le Delliou \(2017\)](#) discussed these small-scale problems in detail and provided some reasonable solutions. In this section, I will discuss some of these problems that are relevant to this work.

#### 1.4.1.1 Cusp-Core Problem

The cusp/core problem hinges on finding the Universal dark matter density profile of galaxies: spirals, ellipticals, dwarfs, low surface brightness galaxies, etc. Most observations of local dwarfs and ultra-faint galaxies show that the dark matter density is constant in the inner region of galaxies, i.e. the density scales with radius as  $\rho_c \propto r_c^0$ , the so-called *core* profile ([Burkert, 1995](#)). This is in contrast to the otherwise highly successful predictions of cosmological N-body simulations, the so-called *dark matter only* simulations, which lead to a central *cusp*  $\rho_s \propto r_s^{-1}$  ([Navarro et al., 1996b](#)).<sup>12</sup> This discrepancy between the observations and the simulations is known as the cusp-core problem.

In the past two decades, several investigations have been carried out on various types of local galaxies in order to solve the core-cusp problem. In particular, earlier studies of rotation curves of late-type and low surface brightness galaxies (hereafter LSBs) showed that the observed dark matter density profile is inconsistent with the theoretically preferred cuspy structure of dark matter ([Palunas & Williams, 2000](#); [Salucci & Burkert, 2000a](#); [de Blok et al., 2001](#); [de Blok et al., 2003](#); [Gentile et al., 2004](#); [Simon et al., 2005](#); [Salucci et al., 2007](#)). On the other hand, some studies support that the galaxies have diverse dark matter density profiles depending on their luminous matter distribution ([van den Bosch & Swaters, 2001](#); [Swaters et al., 2003](#)), while [Hayashi et al. \(2004\)](#) showed that rotation curves of LSBs, which are known to be dark matter dominated systems, agree with the N-body simulations. Later, it was suggested that the discrepancies might be due to poor resolution, systematics, and observational uncertainties (beamsmearing, slit misplacement). Therefore, the investigation of the same problem went in the direction of updating the observational techniques and careful systematic corrections, such as beamsmearing stellar and gas pressure, adiabatic contraction, etc.

Using modern integrated field spectrographs (IFS) accounting various systematics,

---

<sup>12</sup>N-body simulations are an accurate prediction of structure formation models. These simulations do not include baryonic physics (e.g. radiative transfer). They only include the physics of gravity affecting the collisionless cold dark matter particles

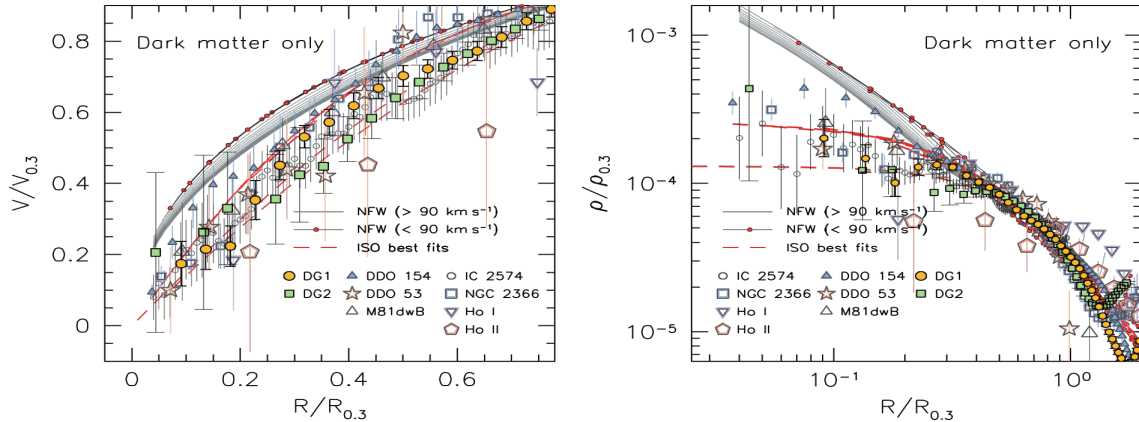


**Figure 1.8:** Illustration of the cusp-core problem using observations and simulations. In particular, we show the local dwarf galaxies using various symbols (with errors), N-body simulations (small red dots), and supernovae feedback included simulations in the gray thin lines. *Left* and *Right* panel, respectively, shows the rotation curves and density profile normalized at  $R_{0.3}$ , representing the distance at which  $\frac{d \log V}{d \log R} = 0.3$ . As we can see, most of the observed rotation curves in the inner region of the galaxies differ from the simulations and show a flat inner density distribution, i.e. a cored dark matter profile. This image is reproduced from the review paper of [Del Popolo & Le Delliou \(2017\)](#), which uses simulations of [Governato et al. \(2010\)](#) and observations of [Oh et al. \(2011b\)](#).

e.g., [Kuzio de Naray et al. \(2008\)](#) and [Kuzio de Naray & Kaufmann \(2011\)](#) observed the LSBs with IFS and they showed that the core observed in local galaxies is consistent with the new observation of high-resolution velocity fields. Similarly, [Oh et al. \(2011b,a\)](#) observed nearby dwarf galaxies using the 21-cm emission line (in radio wavelength) of neutral hydrogen and concluded that the rotation curves of local dwarf galaxies rise very slowly, which cannot be explained by the cuspy dark matter distribution. However, a study by [Oman et al. \(2015a\)](#) has again shown the diversity in the rotation curve profiles of local dwarf galaxies, i.e. some agree with the core and some do not. Nevertheless, it is worth noting that the majority of local dwarfs fit the cored dark matter profile better than the cusp profile, as shown in Figure 1.8. Some other important studies in favour of the core profile are [Martinsson et al. \(2013\)](#); [Karukes & Salucci \(2017\)](#); [Di Paolo et al. \(2019\)](#) and [Hayashi et al. \(2020\)](#). However, the cusp-core problem is still an open question, which nowadays is slowly changing its name to *inner density problem* or *diversity conundrum*. Being ambitious, we anticipate to solve this problem by studying:

- high-resolution observations of galaxy rotation curves over wide a redshift range, which is one of the goals of this thesis, mostly covered in Chapter 6.
- hydrodynamical simulations that take into account the effect of baryons (e.g., supernova feedbacks, dynamical frictions).
- the detailed galactic physics using semi-analytical modelling of galaxy formation and evolution.

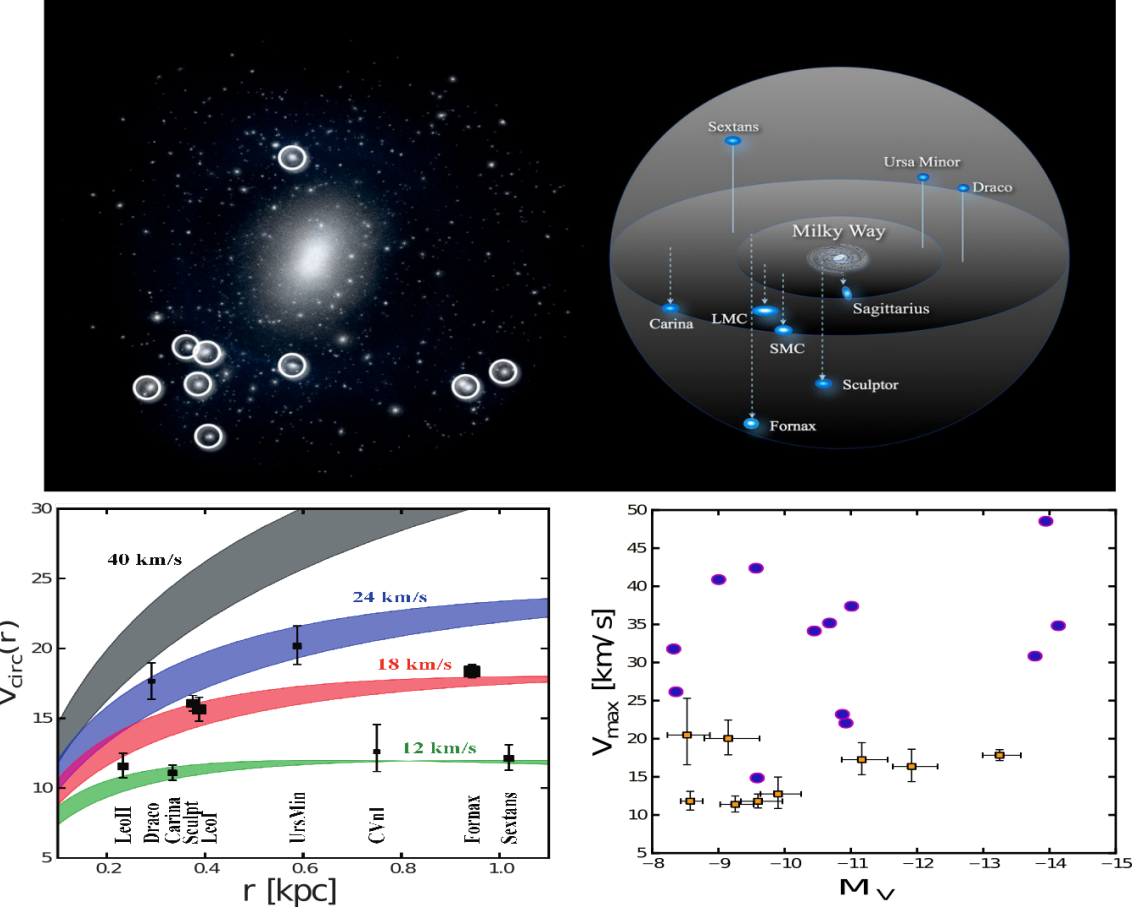


**Figure 1.9:** The ‘missing satellite problem (MSP) and ‘too big to fail (TBTF)’ problem. *Upper panel:* missing satellite problem, left hand side Milky Way like system and its satellites observed in GHALO simulations, and right hand side observed cartoon image of Milky Way and its satellites, image credit: F. Governato. As we can notice in left side of the upper panel Milky Way satellites are isotropically distributed. The white highlighted bright halos show the massive dense satellite halos that are not observed around the actual Milky Way shown in right. *Bottom panel:* TBTF problem, on the left we show the maximum circular velocities (black squares) of the Milky Way satellites, plotted with the rotation curves of DM only simulation (colored stripes). On the right side, we show the maximum circular velocity as a function of V-band magnitude (orange squares with error bars). The dark matter only simulations are shown in blue filled circles. We see in both panels that the satellites with similar brightness in the simulations predict the higher circular velocity of the galaxies and fast rising rotation curves, which is not observed. This bottom panel is reproduced from [Boylan-Kolchin et al. \(2012\)](#) and [Del Popolo & Le Delliou \(2017\)](#).

### 1.4.1.2 Missing Satellite Problem

N-body simulations predict a very steep sub-halo mass function of Milky Way like galaxies, i.e., the Milky Way must have thousands of satellite halos with masses  $\geq 10^6 M_\odot$ . In the late 1990s, the observed sub-halo mass function of the Milky Way galaxy was much shallower, i.e., very few satellite galaxies (here onwards satellites) were observed (Klypin et al., 1999; Moore et al., 1999), an illustration is given in Figure 1.9 (upper panel). At the time, this discrepancy led to the *missing satellite problem*. Since the 2000s, with the beginning of Sloan Digital Sky Survey (SDSS), many ancient faint satellites (Dalal & Kochanek, 2002) have been discovered. With this discovery and a detailed investigation of these satellites, such as their stellar population and dynamical state, we now lead to *too many satellite* problem (Dalal & Kochanek, 2002; Willman et al., 2005; Tollerud et al., 2008; Vegetti et al., 2014; Kim et al., 2018; Kelley et al., 2019). However, (Kim et al., 2018; Kim & Peter, 2021) has recently argued that the traditional missing-satellite problem was posed in the velocity plane, while in our observations we study the luminosity plane. In this context, Kim et al. provided the completeness correction for the Milky Way satellites in velocity space using the stellar velocity dispersion, which encodes the information related to total density profile and abundance. They claim that now there is neither ‘missing satellites’ nor ‘too many satellites’.

### 1.4.1.3 Too Big to Fail

The N-body simulations of the Milky Way, in particular the Aquarius, Via Lactea, and GHALO simulations (Springel et al., 2008; Kuhlen et al., 2008; Stadel et al., 2009, respectively), show that  $\sim 10$  Milky Way satellites have massive dense halos, as shown in Figure 1.9 (upper panel). These simulations are in contrast with the brightest satellites observed around the Milky Way, see Figure 1.9 (lower panel). This discrepancy between observations and simulations is called the *too big to fail* (TBTF) problem, that was first reported by Boylan-Kolchin et al. (2011, 2012). In Figures 1.9, we show the TBTF problem in observations and simulations using typical rotation curves and luminosity information of galaxies. Similar to the Milky Way satellites, TBTF is also observed in nearby isolated galaxies (e.g., Kirby et al., 2014; Papastergis et al., 2015). Ferrero et al. (2012) have also found the same problem while analysing the dwarf irregular galaxies around the Milky Way.

It is proposed that this discrepancy may be due to incorrect estimates of dark matter density profile (Chan et al., 2015), i.e., this problem is closely related to the cusp-core issue. While, Sawala et al. (2016) suggests that re-ionization, star-formation feedback and ram-pressure stripping affect the growth of low-mass halos, which may cause such mismatch, and are not precisely constrained in N-body simulations. In addition to these suggestions, it is also claimed to be an observational uncertainty (Dutton et al., 2016). The up-to-date solution to this problem is baryons plus dark matter driven simulations, i.e. hydrodynamical simulations that take into account Active Galactic Nucleic (AGN) & supernova feedbacks, radiative transfer, dynamical effects of the baryonic disc, etc., for more details on this topic we refer reader to Weinberg et al. (2015); Kohler (2016) and

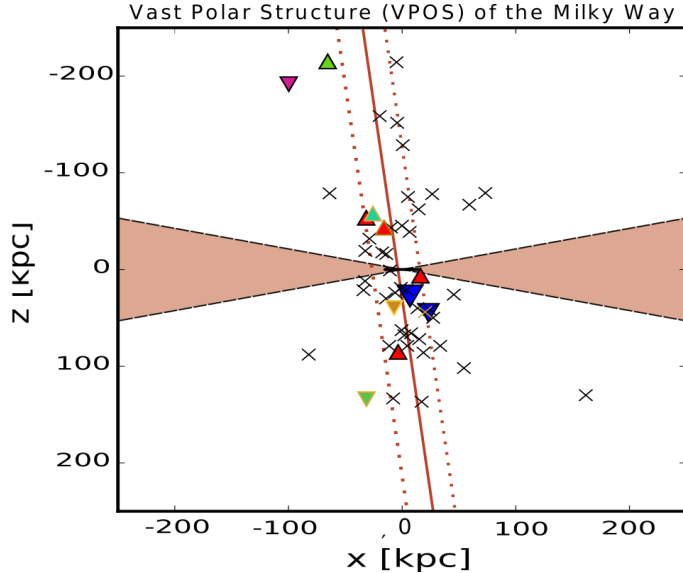


**Figure 1.10:** The planar alignment of the Milky Way satellites on Vast Polar structure. The markers represent the position of the Milky Way satellites and the brown shaded area is representing the plane of the Milky Way. The upward and downward triangles are showing approaching and receding satellites, respectively. The satellites with unknown proper motion are shown by crosses. This image is reproduced from [Pawlowski & Kroupa \(2019\)](#).

[Verbeke et al. \(2017\)](#).

#### 1.4.1.4 Satellite Plane Problem

Another important issue receiving attention in disfavouring the  $\Lambda$ CDM model is the *satellite plane problem*. In 1976, [Lynden-Bell \(1976\)](#) showed that the classical satellite galaxies of the Milky Way (observed at that time): Large Magellanic Cloud and Small Magellanic Cloud, Draco, Ursa minor, Sculptor, Fornex, LeoI, LeoII, and globular clusters, appear to lie in one place. This plane is commonly referred to as ‘Vast Polar Structure’ ([Kroupa et al., 2005](#); [Metz et al., 2008](#); [Pawlowski & Kroupa, 2013](#)). The satellites of the Andromeda galaxy also show a similar inhomogeneous distribution, but are more aligned in the ‘Great Plane of Andromeda’ ([Ibata et al., 2013](#); [Conn et al., 2013](#)). A similar planar alignment is also observed in local isolated dwarfs ([Galianni et al., 2010](#); [Pawlowski et al., 2013](#); [Pawlowski & McGaugh, 2014](#)) and distant galaxies ([Bellazzini et al., 2013](#); [Duc et al., 2014](#); [Karachentsev et al., 2014](#)). These observations strongly challenge the  $\Lambda$ CDM model in which satellites are isotropically distributed around Milky Way like galaxies as shown in upper left panel of Figure 1.9 (also see [Weinberg et al., 2015](#)).

Several ideas have been proposed to investigate (and solve) this problem, but no great success has been achieved ([Pawlowski & Kroupa, 2013](#); [Deason et al., 2011](#)). And again, the consensus seems to be to include baryons in dark matter only simulations ([Sawala et al., 2016](#)). However, for this problem, even the inclusion of baryons does not seem to help because the scales on which baryon physics act is smaller than those on which

satellites lies (Pawlowski et al., 2015); so the problem remains open. A contemporary solution is to accurately study the 3D motion of galaxies in the galactic and the extra-galactic Universe. In fact, now the study of the 3D motion of Milky way satellites is possible with the Gaia proper motion survey (Pawlowski & Kroupa, 2019). In addition, a study of dynamical friction and retain angular momentum can also be a useful tool in this context.

### 1.4.2 Large Scale Problems

With the rapidly growing science & technology, it is now possible to make more precise and deeper observations (e.g., WMAP → Planck), as well as the amount of data and its sensitivity is also growing day by day. By implementing this data with standard physics, mathematics, and computational power, we are now able to get a much better look at the early Universe than we could in the 1990s or early 2000s, i.e. we are now in the era of precision cosmology. So far, we knew that the  $\Lambda$ CDM possess no problems in defining the early Universe and large scale structures. However, with aforementioned advancement in the field, we now see the serious problems in explaining the large-scale structures under  $\Lambda$ CDM scenario, which we call large-scale problems. In this section I will highlight these problems. We remind the reader, that most of the large-scale problems fall in the regime of cosmology; therefore, I will only briefly mention these problems with their possible references.

- The Hubble tension is one of the widely known tension of large-scale problems. The Hubble constant ( $H_0$ ) measured from local galaxies, supernovae, and Cepheid variable stars are nearly in  $4\sigma$  tension with indirect measurements of the CMB, i.e. the  $\Lambda$ CDM model (Verde et al., 2019; Di Valentino et al., 2021a).
- The growth rate of cosmological perturbations, responsible for structure formation, observed from weak-lensing (or redshift space distortion) and the CMB using the  $\Lambda$ CDM are in  $2 - 3\sigma$  tension (Joudaki et al., 2018).
- CMB anisotropy anomalies: cosmological parameters inferred from the observations, such as galaxies, large-scale structures and CMB (under assumption of  $\Lambda$ CDM ), are different and appear to be in  $2 - 3\sigma$  tension, for details and other CMB anomalies I refer reader to Planck Collaboration et al. (2020b).
- The one of the key entity ‘the age of the Universe’, which we measure from the oldest stars of the Milky Way is at odds with the age inferred from the CMB observations accounting the  $\Lambda$ CDM model (Verde et al., 2013).
- Big Bang Nucleosynthesis (BBN) anomaly: We can now measure the CMB data independently of the BBN by using the cosmic baryon density. This gives us a new window to test the indirect measurements of the CMB (under  $\Lambda$ CDM ). Recently, we have learned that cosmic deuterium agrees well with the BBN+CMB predictions, while the  $^7\text{Li}$  abundance is an order of magnitude lower than that derived from

CMB, typically with a tension of  $4 - 5\sigma$ , for details we refer the reader to [Fields \(2011\)](#).

- Recently [Asencio et al. \(2021\)](#) studied the collision of two massive ( $M_{200} \approx 3 \times 10^{15} M_{\odot}$ ) clusters at  $z \sim 0.87$ . They reported that these clusters are colliding with the speed of  $2500 \text{ km s}^{-1}$ , such a rapid collision of massive cluster is not possible under  $\Lambda$ CDM model. Thus showing a serious issue of  $\Lambda$ CDM scenario.

Besides these key issues there are also other large scale facts that are in tension with  $\Lambda$ CDM scenario, such as: cosmic dipole problem, quasar Hubble diagram, low baryon temperature at epoch of re-ionization. For a detailed discussion on large scale problems, we refer the reader to [Di Valentino et al. \(2021b\)](#) and [Perivolaropoulos & Skara \(2021\)](#).

## 1.5 Outline of Thesis

In this thesis, I will focus on the study of dark matter using galaxies in the local and the distant (high-redshift) Universe. While the structure of the local galaxies has already been meticulously studied by many authors, the main contribution of this work is a careful analysis of the dark matter distribution in high-redshift galaxies. This requires the precise determination of their kinematics and dynamics from the inner to the outermost regions, which can also be referred to as the resolved study of galaxies. In Chapter 2, I introduce the reader to traditional and modern techniques of determining the rotational velocity and velocity dispersion, i.e., kinematics of galaxies, as well as recent updates in the field.

At high-redshift, determining the kinematics of galaxies is nontrivial due to their extreme distance and faintness. Therefore, the data analysis requires special attention, which I discuss in the last sections of Chapter 2 and provide further details in Chapter 3. The Chapter 4 presents the results of accurate kinematics of galaxies from 6.5 billion years ago. The obtained kinematics of high-redshift galaxies are then analysed in Chapter 5 to determine their dark matter content at different radii, as well as compared with previous studies of local and high-redshift galaxies. In Chapter 6, I model the dynamics of high-redshift galaxies based on their kinematics. Thereby, I attempt to study the internal structure of their dark matter halos, and subsequently compare the results with local galaxies and hydrodynamical galaxy simulations. In chapter 7, I analysed and scaled the fundamental physical properties (mass, size, and angular momentum) of galaxies, that provide an independent verification of the results obtained in the previous chapters. Finally, in Chapter 8, I comprehensively summarise the thesis, and it is ended by providing concluding remarks and future prospects with Chapter 9.



# Chapter 2

## Kinematics & Dynamics of Galaxies

Galaxy kinematics is a way to measure the motion of stars and gas that allows us to obtain fundamental information about the formation of galaxies and their current dynamical state. For example, kinematics derived from gas, which is collisional in nature, and stars, which are assumed to be collisionless (to a good approximation), allows us to disentangle various physical processes that occur on the galactic scale, such as: mass accretion and dynamical instabilities caused by supernovae (or AGN) feedbacks. The motion of the stars and gas also gives us the total amount of mass and its distribution within the galaxy as  $V_c^2 = GM_{\text{dyn}}/R$ , so does the shape of its potential under the Poisson's equation of gravitational potential, for details see [Binney & Tremaine \(2008\)](#). That is, the galaxy dynamics derived from the observed kinematics is a portal to constrain the baryons and dark matter reside in the galactic potential wells. The latter line of thought is the main focus of this work, which I will discuss and interpret in several chapters of this thesis. In this chapter, I will briefly introduce the basics of determining the kinematics & dynamics of galaxies, and recent progress in the field.

### 2.1 Galaxy Kinematics

In this section, I present the conventional and state-of-the-art techniques of obtaining galaxy kinematics.

#### 2.1.1 Conventional Spectroscopy

A conventional method of determining the motion of stars and gas in a galaxy is slit spectroscopy<sup>1</sup>. Depending on the scientific goal, one can use a long narrow slit or a wide slit. For studying extended objects (such as galaxies), a long narrow slit is recommended ([Mathewson et al., 1992](#); [Sofue & Rubin, 2001](#), and references therein). The light rays coming from an object as they pass through the slit are exposed to the spectrograph<sup>2</sup>,

---

<sup>1</sup>Spectroscopy is the technique of splitting electromagnetic radiation (i.e., light) into its constituent wavelengths, based on the same principle as a prism splits light into a colorful rainbow.

<sup>2</sup>Spectrograph is an instrument that performs spectroscopy and records the information.

which produces the spectrum<sup>3</sup> along the horizontal axis of the slit, where the vertical axis of the slit gives the spatial information, see Box 1 & 2. The spectrum of a galaxy generally contains absorption, emission and the continuum, see Box 1.<sup>4</sup> For details of spectroscopy, we refer the reader to [Kakkari \(2015\)](#). These absorption and emission features in the spectrum of galaxy (or any object) are the key to unlock its composition, element abundance, temperature, pressure and motion plus distribution of stars and gas ([Massey & Hanson, 2013](#)). To derive the galaxy kinematics, we generally study the *Doppler-shift* in the peak (or dip) of the emission (or absorption) lines. The Doppler shift connects the line-of-sight velocity ( $V_{\text{los}}$ ) of the object with its emitted wavelength (or frequency):

Box 2.1

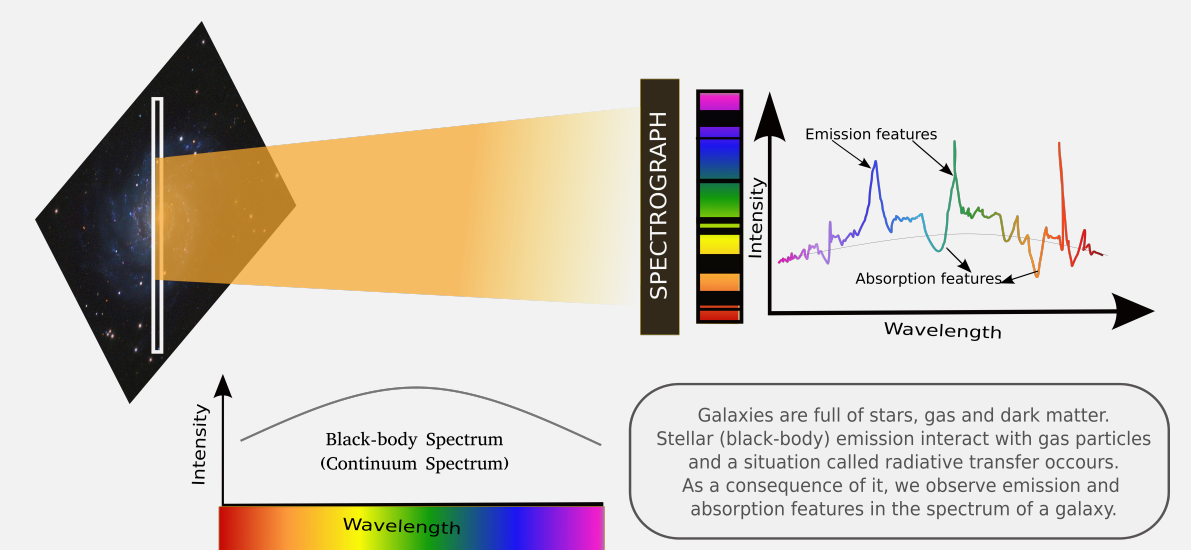


Illustration of a conventional method of recording the spectrum of galaxies and its properties. In principle, the light rays coming from the stars in the galaxies should form a continuum spectrum (blackbody), but because of the presence of gas particles, some of the light is absorbed and a part of it radiates even with higher intensity. The former corresponds to absorption and the latter is called an emission feature. For example, a continuum feature can be represented by a rainbow slab, where dark lines on this rainbow slab represent absorption and bright lines represent emission. Astronomers study these features to determine the kinematics and dynamics of a galaxy (or galaxies, also stars and gas).

<sup>3</sup>The spectrum is the distribution of characteristic wavelengths of electromagnetic radiation when absorbed or emitted by a particular object or particle.

<sup>4</sup>In the absence of a medium, most objects emit a blackbody spectrum, also known as a continuum. In the presence of a medium, when an electron gains energy from the surrounding medium by absorbing photons, it jumps from a lower energy level to a higher one, and therefore we see an absence of light (wavelength) equal to the energy difference of the levels ( $\Delta E = h\nu$ , where  $\nu = c/\lambda$ ). This situation is called absorption. On the other hand, when the electron falls back to the lower energy level, it emits the light with a wavelength corresponding to the energy difference of the levels, which we refer to as emission.

$$\frac{V_{\text{los}}}{c} = \frac{\lambda_{\text{obs}} - \lambda_{\text{emit}}}{\lambda_{\text{emit}}} = \frac{f_{\text{emit}} - f_{\text{obs}}}{f_{\text{obs}}}, \quad (2.1)$$

where  $\lambda_{\text{obs}}$  and  $\lambda_{\text{emit}}$  are the observed and emitted (at rest frame of the source) wavelengths, respectively. Equation 2.1 also provides the cosmological redshift ( $z$ ) of the objects, as  $z = V_{\text{los}}/c$ . At this stage, it is important to pinpoint that the galaxy as a whole 1) is moving away from us due to the expansion of the Universe, this motion is called the *recession velocity* ( $V_{\text{res}}$ ) of the galaxy, and 2) have local motion due to local gravitational effects, so-called *peculiar velocity* ( $V_{\text{pec}}$ ). The sum of peculiar and recession velocity of a galaxy can be termed as galaxy's *systemic velocity*, i.e.,  $V_{\text{sys}} = V_{\text{res}} + V_{\text{pec}}$ , which is measured in Sun's rest frame, that is by accounting the heliocentric velocity<sup>5</sup>. In addition to  $V_{\text{sys}}$ , the gas and stars of the galaxy rotate around the centre of the galaxy at a certain speed, called the *rotational velocity*  $V_{\text{rot}}$ . In principle, the line-of-sight velocity inferred from the Doppler effect is the sum of  $V_{\text{rot}} + V_{\text{sys}}$ , i.e., to determine the true observed rotation velocity, we need to separate these two velocities. In general, an average velocity of stars within the galaxy or velocity about its centre of mass equals to the systemic velocity. Providing this information, the observed rotation velocity of the galaxy is  $V_{\text{obs}} = (V_{\text{los}} - V_{\text{sys}})$ . Moreover, a galaxy is often inclined with respect to an observer's line-of-sight, with some *inclination angle*<sup>6</sup> ( $i$ ), which lowers the *intrinsic* rotation velocity. Therefore, the observed rotation velocity needs to be corrected for the inclination as follows:

$$V_{\text{rot}}(R) = \frac{V_{\text{obs}}(R)}{\sin i} = \frac{(V_{\text{los}}^{r_i} - V_{\text{sys}})}{\sin i} \quad (2.2)$$

where  $V_{\text{rot}}$  is intrinsic rotation velocity and  $V_{\text{los}}^{r_i}$  is the line-of-sight velocity measured at different radii of the galaxy. The rotation velocity as a function of radius,  $V_{\text{rot}}(R)$ , is referred to as the *rotation curve* of the galaxy. Further systematic corrections to the rotation curve, such as asymmetric drift (or pressure support), bring the rotation curve very close to the circular velocity curve, that follows  $V_c(R) \approx GM_{\text{dyn}}/R$ . An example of rotation curve derived from slit-spectroscopy is shown in Box 2.

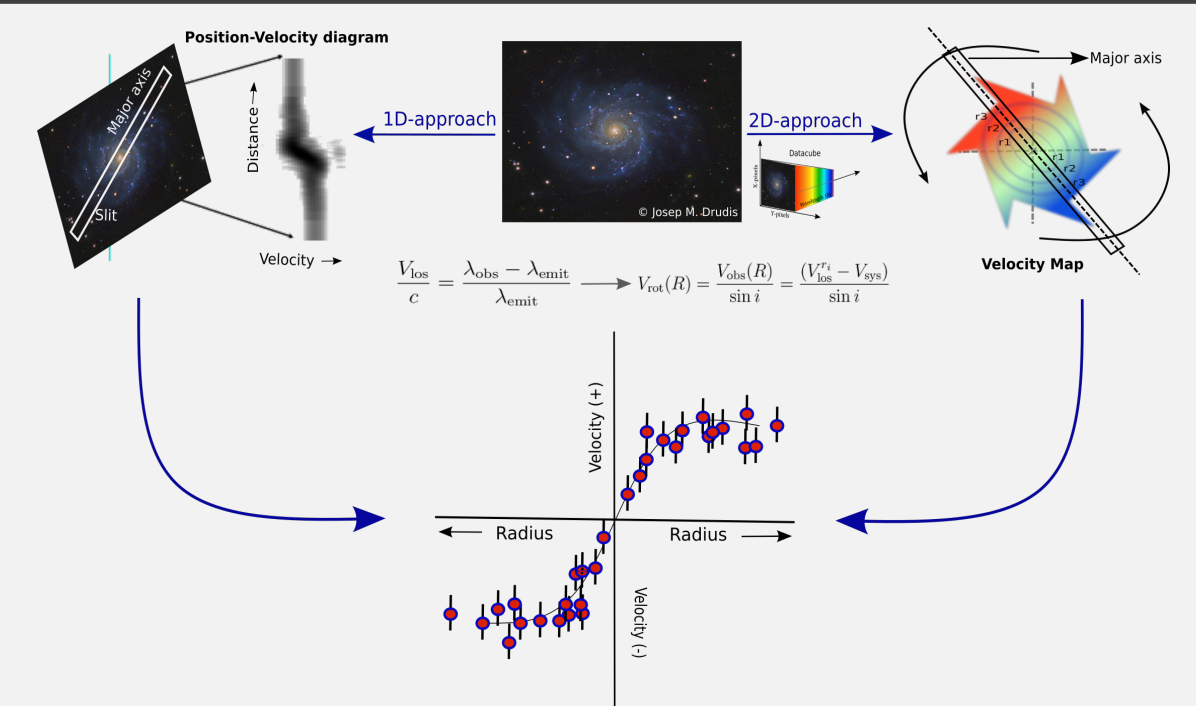
Deriving the rotation curves from slit spectroscopy is quite simple and fast, but it has several drawbacks: 1) the spatial information perpendicular to the slit is indeterminate; 2) light outside the slit is always lost; 3) to study the kinematics in the whole galaxy, we need to repeat the observation several times, which is time-consuming and expensive; 4) to obtain the rotation curve, the slit is generally placed along the major axis, since this gives us the averaged rotational velocity of a galaxy. However, if the angular size of the object is small, especially for high-redshift objects, then it is difficult to guess the axis information; 5) the triaxial component of the velocity field and the line strength distribution of a galaxy provide rich information about its present dynamical state, which is difficult to measure with slit spectroscopy. To overcome these problems, it was important to come up with advanced techniques. At the end of the last century (1980-2000), considerable efforts were

<sup>5</sup>The Heliocentric velocity is the velocity defined with respect to a frame in which the Sun is at rest.

<sup>6</sup>The angle between the normal to the disc plane and the observer's line-of-sight is called the *inclination angle* ( $i$ ) of the galaxy. A galaxy is called face-on when  $i = 0^\circ$  and edge-on if  $i = 90^\circ$ .

made to develop high resolution spectroscopy (Woodgate et al., 1998; Dekker et al., 2000) and integral field spectroscopy (Courtes, 1982; Bacon et al., 1995; Bacon et al., 2001a). In which integral- field spectroscopy has proven remarkably successful in terms of resolved study of galaxies and conducting large galaxy surveys. In the last decade, the scientific community has made significant progress in the development of second generation integral field spectrographs (Bacon et al., 2010, 2015; Eisenhauer et al., 2003; Sharples, 2014), one of which was used in the observation of the data used in this work.

### Box 2.2



One- and two-dimensional approaches to deriving rotation curves. In the one-dimensional (1D) approach, we place the slit along the major axis of the galaxy and obtain the spectrum using the step-up shown in Box 1. In the two-dimensional (2D) approach, we first obtain the spectrum using integral field spectrographs, as shown in Figure 2.1, which comes in the form of a datacube. This datacube is then reduced to the velocity map (the velocity map can also be derived using slit spectroscopy, but this process is time consuming). In both the 1D and 2D approaches, the Doppler effect is used as the basis for deriving the observed velocity. As can be seen from the figure, the main difference between the two studies is that in the 1D-approach the velocity is observed along the major axis of a galaxy, while in the 2D-approach the velocity is observed over the entire galaxy, which is then averaged along the major axis, resulting in the rotation curve similar to the 1D approach. Finally, we can note that the rotation curve has two arms, one indicating the positive velocity and the other the negative velocity, representing respectively the receding and approaching parts of the galaxy with respect to the observer's rest frame.

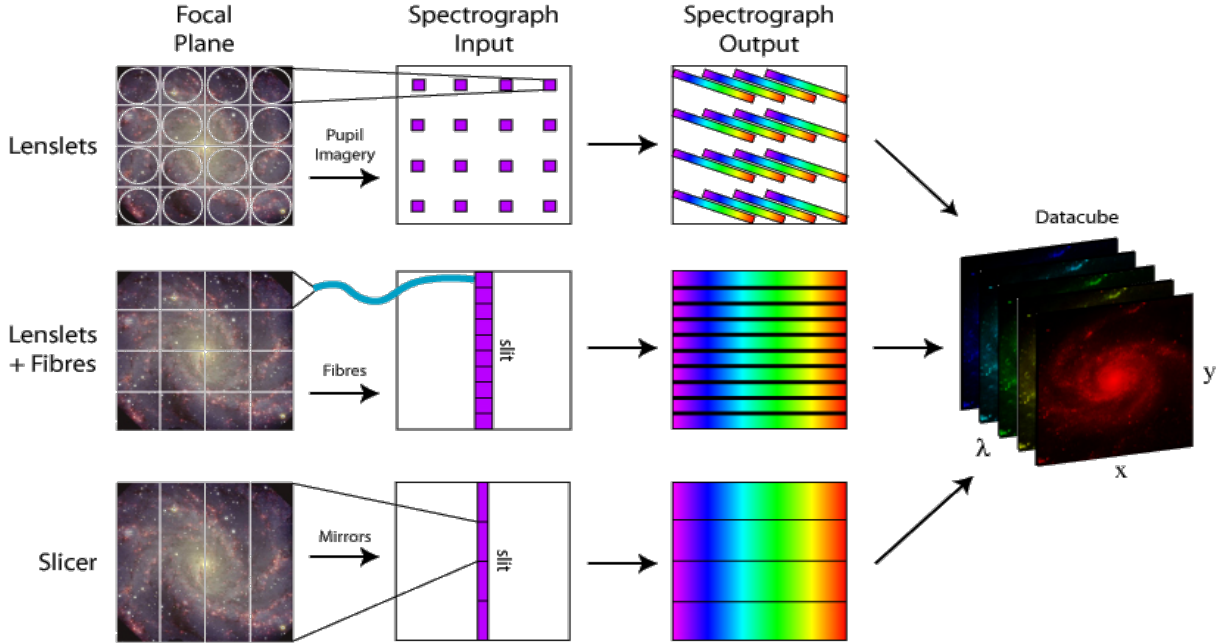


**Figure 2.1:** Types of Integral Field Units, image credit [Westmoquette \(2007\)](#).

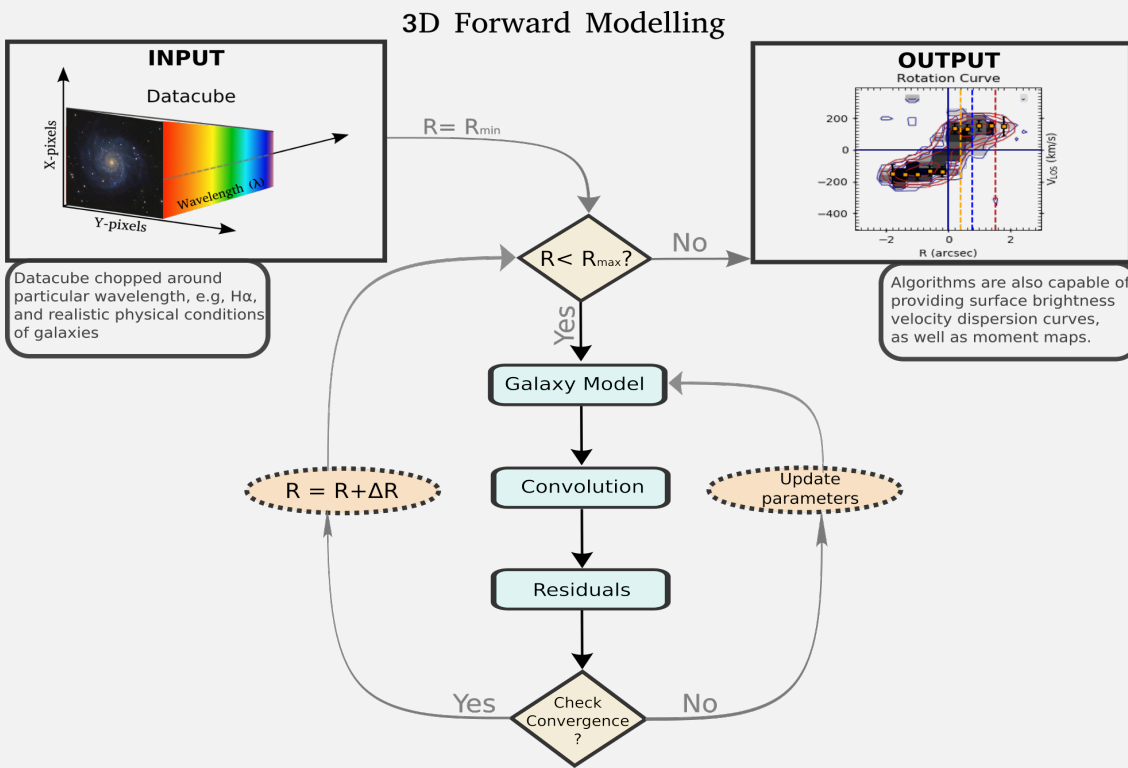
### 2.1.2 Integral Field Spectroscopy

Integral Field Spectrograph (IFS) came with the goal of studying triaxial motion, resolved kinematics, and extended objects (e.g. galaxies). IFS uses the Integral Field Units (IFUs), which collects light from each pixel and transmits it to the spectrograph without any loss. Many advanced IFUs have been developed since the 2000s, and they can be designed in many different ways. In Figure 2.1, I have shown three commonly used IFU+IFS designs. (1) *Lenslets* uses microlens arrays that split the image into small light sources, then each light source is placed in the spectrograph entrance (same slit plane) and exposed to the disperser, resulting in a spectrum. The system is tilted to avoid the overlap of each lenslet spectrum. The spectrograph like SAURON ([Bacon et al., 2001b](#)) and SPHERE ([Claudi et al., 2008](#)) uses Lenslet IFU. (2) *Lenslets plus fibers* IFU is very similar to lenslet IFU, but in this case each lenslet focuses the light beam on the optical fiber and behaves like a pseudo-slit, which is then transmitted to the disperser to produce the spectrum. The surveys like CALIFA ([Sánchez et al., 2012](#)), SAMI ([Konstantopoulos et al., 2013](#)) and MANGA ([Law et al., 2015](#)) use lenslets plus fibers technique. (3) *Image Slicer*: As the name suggests, the image is sliced and then each slice is reformatted into a pseudo-slice, then the light is exposed to the disperser to obtain the spectrum. An image slicer uses mirrors to form and reform the image. Therefore, it is achromatic and can be cooled at cryogenic temperature (which allows low noise level while integrating the data for longer hours). This makes the Image Slicer suitable for observation in the infrared, thus for high redshift too.<sup>7</sup> The second generation IFS uses image slicers such as MUSE ([Bacon et al.,](#)

<sup>7</sup>The most prominent optical emission line, i.e.  $\text{H}\alpha$ , when emitted at high-redshift get redshifted due to the expansion of the Universe, and often seen in near infrared or infrared regime. That is, near infrared

2010), SINFONI (Eisenhauer et al., 2003), and KMOS (Sharples et al., 2003).

Box 2.3



Schematic representation of the 3D forward modeling algorithm. In 3D forward modelling, we input the entire data along with some initial guesses about the physical conditions of the galaxy. In particular, we provide 1) three geometrical parameters of galaxy: position & inclination angle, central  $x$  &  $y$  coordinates, which are estimated from photometry; 2) guess on kinematic parameters rotation velocity and velocity dispersion; 3) instrument response: Point Spread Function (PSF) and the Line Spread Function (LSF); and 4) depending on the distance of galaxy, one also needs to provide redshift information. For a given geometrical and kinematical parameters, the algorithm generates a mock datacube. This mock datacube is then convolved for the instrumental response. Then, the flux in the observed and mock datacubes is compared using some statistics (e.g., Bayesian), which allows to modify the initial guesses until the convergence occurs. In the end, the observed rotational velocity, velocity dispersion, and surface brightness is calculated ring by ring. Note, here I have briefly covered the algorithm used in 3D-BAROLO. With different software/algorithm, technical details (e.g., galaxy model) may differ, but the general structure and idea remains the same. In Chapter 3, we expand this discussion in great detail. The flow-chart is reproduced from [Teodoro & Fraternali \(2015\)](#).

or infrared facilities are required for high-redshift observations.

The spectrum of an IFU is always rearranged in the  $x - y$  position of the galaxy as a function of wavelength, creating a *datacube* =  $f(x, y, \lambda)$  that gives the 2D observations a three-dimensional appearance. These datacubes are then used for multiple purposes, for example we can retrieve both, the object image and the spectrum. In particular, the datacubes are very useful to derive the spatial distribution of stars, gas, star formation rate, and metallicity. IFU data, i.e. datacubes, can also be used to obtain various velocity moments (intensity, rotation, and dispersion), which are relevant to extract the galaxy dynamics. The major advantage of IFUs has been seen in large galaxy surveys at low and high-redshift. Those earlier were taking years but now take only a few months to observe 1000s of resolved galaxies.

In our work, we mainly use the datacubes to derive the rotation curves; however velocity moments can also been used. I would like to emphasize that there is no rule of thumb for deriving the rotation curves from datacubes, but there are a few standard methods that are commonly used within the community 1) Physically motivated models that take into account the potential well of the galaxy through the information of the mass distribution (Förster Schreiber et al., 2009; Wisnioski et al., 2015; Swinbank et al., 2017). 2) phenomenological model incorporating a known parametric function (e.g.,  $V(R) = \frac{2}{\pi} \arctan(r/R_{\text{scale}})$ ) to reproduce observed rotation curves that are flat in outskirts (e.g. Epinat et al., 2010; Swinbank et al., 2012; Stott et al., 2016; Harrison et al., 2017). Both 1 & 2 uses two-dimensional velocity maps extracted from datacubes (pixel-wise fitting of the emission line profile), to derive the rotation curves. These type of studies have serious drawbacks like beamsmearing, especially for high-redshift galaxies (Di Teodoro et al., 2016; Sharma et al., 2021b). Recently, scientific community have made progress in developing 3D algorithms for inferring rotation curves (and other properties) from datacubes, for example GALPAK-3D (Bouché et al., 2015), 3D-BAROLO (Teodoro & Fraternali, 2015), and BLOBBY-3D (Varidel et al., 2019). These algorithms are capable of directly fitting the flux of datacube, generating mock datacube, and comparing the data and models using robust statistics that take into account the instrumental response (line and point spread function). As a result, they proved to be relatively robust in determining the accurate rotation curves. A schematic diagram of the 3D approach to derive the rotation curves is shown in Box 3.

Furthermore, we use either stellar or gas kinematics to derive the rotation curves. With current instrument capabilities, both stellar and gas kinematics are accurately measured for local galaxies. However, for high-redshift galaxies, it is still impossible to obtain a spectrum with a high signal-to-noise ratio in the stellar continuum due to the extreme distance and faintness of the galaxies. Therefore, currently we can only study the gas kinematics of high-redshift galaxies (Stott et al., 2016; Lang et al., 2017; Turner et al., 2017; Tiley et al., 2019b; Sharma et al., 2021b). In addition to optical and near-infrared (NIR) observations, we can also infer rotation curves from radio observations of neutral hydrogen (HI) gas, which is easily observed in the local Universe but appears to be very challenging at high-redshift. Currently, we cannot observe HI above  $z > 0.3$ ; however, with next-generation radio telescopes such as ASKAP (Johnston et al., 2008; McConnell et al., 2016; Bonaldi et al., 2021), MeerKat (Jonas & MeerKAT Team, 2016; Baker et al.,

2018; Maddox et al., 2021), it will soon be possible to detect resolved HI kinematics from distant ( $z \simeq 1$ ) sources.

## 2.2 Galaxy Dynamics

A gravitationally bound system, such as galaxy, is characterized by its gravitational potential  $\Phi(r) = -GM(< r)/r^2$ , in which the individual constituents experience a conservative force  $F = -m\nabla\Phi(r)$ . For particles on circular orbits the gravitational force is equivalent to the centripetal force  $F = mV_c^2/r$ . Thus, in a spherical system the radial change of the potential is related to the circular velocity as:

$$\frac{d\Phi}{dr} = \frac{V_c^2}{r} \quad (2.3)$$

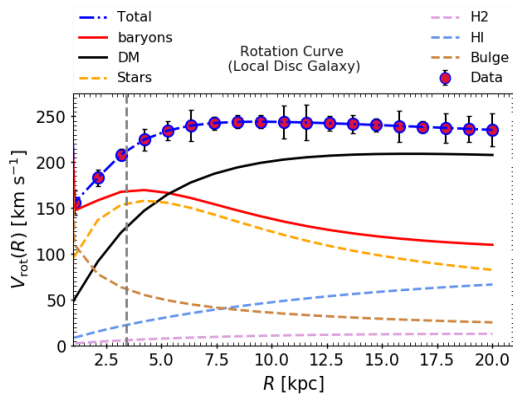


**Figure 2.2:** An example of mass modelled rotation curve. This is a mock rotation curve of galaxy having stellar disc length: 2 kpc, HI disc scale length: 20 kpc, stellar mass:  $3 \times 10^{10} M_\odot$ , bulge-to-total ratio: 0.1, molecular gas mass:  $3.2 \times 10^9 M_\odot$ , atomic gas mass:  $8 \times 10^{10} M_\odot$ , virial mass of halo:  $6.6 \times 10^{11} M_\odot$ , and virial radius: 180 kpc. The rotation curve is mass modelled using Burkert dark matter halo which has core radius: 5 kpc, and core density:  $10^5 M_\odot \text{ kpc}^{-3}$ , and baryons are assumed to be distributed in exponential disc.

to determine the mass distribution within the galaxy. Technically, this can be done by decomposing the components that make up the rotation curve, i.e. disentangling the various mass components using an appropriate mass modelling technique called *dynamical*

Another useful relation is Poisson's equation, which relates the gravitational potential of the system to its mass density:

$$\Delta\Phi = 4\pi G\rho \quad (2.4)$$

where  $\rho$  is the total mass density of the system, i.e. it includes baryons and dark matter. The Poisson's equation for spherical system Equation 2.4 can be expressed as:

$$\frac{1}{r^2} \frac{d}{dr} \left( r^2 \frac{d\Phi(r)}{dr} \right) = 4\pi G\rho(r) \quad (2.5)$$

which yields:

$$V_c^2(R) = \frac{4\pi G}{R} \int_0^R \rho(r)r^2 dr. \quad (2.6)$$

Equation 2.6 relates the circular velocity to the total mass density, i.e. the total mass enclosed within the radius  $R$ . From the observed kinematics of the galaxy, we can get the rotation curve which is very close to the circular velocity profile (when corrected for systematics). Thus, the rotation curve of a galaxy can be used as a proxy

*mass modelling.* Let me remark, mass modelling techniques vary from one galaxy class to another and also depend on the information that we have about the baryons. In this work, I focus on disc (or disc-like) star-forming galaxies, for which the baryon distribution (e.g., stellar disc radius, stellar mass) can be derived from photometry. As mentioned above, the rotation curve of a galaxy gives us the circular velocity of the system as a function of its radius. This  $V_c(R)$  is composed of the contribution of baryons (stars and gas) and dark matter. Therefore,  $V_c(R)$  can be described as a sum of quadratures:

$$V_c^2(R) = V_D^2(R) + V_{\text{bulge}}^2(R) + V_{\text{H}_2}^2(R) + V_{\text{HI}}^2(R) + V_{\text{DM}}^2(R), \quad (2.7)$$

were  $V_D(R)$ ,  $V_{\text{bulge}}(R)$ ,  $V_{\text{H}_2}(R)$  and  $V_{\text{HI}}(R)$  are the terms associated with circular velocity profiles of the stellar disc, bulge, molecular ( $\text{H}_2$ ) and atomic ( $\text{HI}$ ) gas discs, providing the baryonic contribution to the circular velocity and  $V_{\text{DM}}(R)$  is the dark matter contribution. Here, we neglect the black-hole's contribution to the circular velocity (as a first order approximation). In the following sections, we present an approach to disentangle the aforementioned contributions from observed rotation curves. An example of decomposed rotation curve is shown in Figure 2.2.

## 2.2.1 Dynamical Models

Here I explain the various components of our mass modelling.

### 2.2.1.1 Stellar and Gas Disc

The stellar and gaseous components of local star-forming discs, dwarf-discs and low surface brightness galaxies are well described by [Freeman \(1970a\)](#) exponential disc model (e.g., [Persic et al., 1996](#); [Karukes & Salucci, 2017](#); [Di Paolo et al., 2019](#)). Therefore, here also we assume that the distribution of stars and gas in local and high-redshift star-forming galaxies are in exponential discs, so that the surface densities can be written as (up to a geometric factor):

$$\Sigma_i(R) \propto \frac{M_i}{R_{\text{scale},i}} \exp(-R/R_{\text{scale},i}), \quad (2.8)$$

where,  $M_i$  and  $R_{\text{scale}}$  are the total mass and the scale length of the different components (stars,  $\text{H}_2$ ,  $\text{HI}$ ), respectively. The definition of latter quantities are given in Chapter 3, where we derive these quantities from photometry. Note that stellar mass in the disc (without bulge) is denoted by  $M_D$ , while the contribution of the total stellar mass is represented by  $M_*$  or  $M_{\text{star}} = M_D + M_{\text{bulge}}$ . Assuming the above density distribution of the stars and the gas, their contribution to the circular velocity of the disc can be expressed as follows:

$$V_i^2(R) = \frac{1}{2} \left( \frac{GM_i}{R_{\text{scale},i}} \right) (x^2) [I_0 K_0 - I_1 K_1], \quad (2.9)$$

where,  $x = R/R_{\text{scale}}$  and  $I_n$  and  $K_n$  are modified Bessel functions computed at  $1.6x$  for stars and  $0.53x$  for gas (c.f. [Persic et al., 1996](#); [Karukes & Salucci, 2017](#)).

If the surface density distribution is not an exponential disc, but it instead follows an arbitrary distribution  $\Sigma_{-}(x, y)$ , then radial gravitation force on mass element  $\Sigma'_{-}(x)dx dy$  is:

$$\frac{d\Phi(R)}{dr} = G \int_{-\infty}^{+\infty} \int_{-\infty}^{+\infty} \frac{\Sigma'_{-}(x)(R - x)}{\sqrt{(R - x)^2 + y^2}} dx dy \quad (2.10)$$

Thus the circular velocity can be determined using Equation 2.3 (see also, [Binney & Tremaine, 2008](#)).

### 2.2.1.2 Bulge Component

The most commonly used bulge profile for modelling the central spheroidal component of galaxy is [de Vaucouleurs \(1958\)](#) profile:

$$\Sigma_{\text{bulge}}(R) = \Sigma_0 \exp \left( -\beta \left[ \left( \frac{R}{R_{\text{bulge}}} \right)^{1/4} - 1 \right] \right) \quad (2.11)$$

where  $\Sigma_0$  is the surface mass density at the scale radius  $R_{\text{bulge}}$ , and  $\beta = 7.695$ . Then the total bulge mass is given by:

$$M_{\text{bulge}} = 2\pi \int_0^{+\infty} R \Sigma_{\text{bulge}}(R) dR \quad (2.12)$$

The other alternative bulge profiles are Sérsic profile ([Sersic, 1968](#)) and exponential spherical model ([Sofue, 2016](#)). For local star-forming disc galaxies (spirals) bulge is often assumed to be point mass. Especially, at high-redshift due to limited resolution in the inner region of the galaxy we assume bulge as a point mass. In any case, the bulge contribution to the circular velocity is computed as:

$$V_{\text{bulge}}^2(R) = \frac{G M_{\text{bulge}}}{R}, \quad (2.13)$$

where,  $M_{\text{bulge}}$  is total bulge mass computed by fitting the aforementioned bulge profiles to the photometric data, or it can be estimated dynamically by fitting the bulge-to-total ratio  $B/T = M_{\text{bulge}}/M_{\text{star}}$ .

### 2.2.1.3 Dark Matter Halo Component

In chapter 1, we established that the baryons fall in the dark matter halos to form the galaxies. After the galaxies are formed, the baryons can be easily detected in electromagnetic radiation, however, dark matter is invisible and can only be studied via its gravitational influence on baryons. Thus the dark matter distribution, i.e. its radial profile, is unknown, and various predictions have to be tested dynamically against the observations of baryons. Note that similar tests can be performed using simulations. One of the simplest dark matter halo models is the semi-isothermal sphere ([Kent, 1986; Begeaman et al., 1991](#)). The generalized form of the latter is Burkert profile ([Burkert, 1995](#)).

On the other hand, the N-body simulations generically predict the NFW profile (Navarro et al., 1996b), whereas current hydrodynamical simulations are showing more complex dark matter distribution, e.g. Einasto profile (Einasto, 1965), Di Cintio profile (Di Cintio et al., 2014) and Dekel-Zhao profile (Freundlich et al., 2020a). In this work, I will discuss two widely used and observationally motivated dark matter halo models, namely Burkert (Burkert, 1995) and NFW (Navarro et al., 1996b) profiles.

Burkert Halo: Local spirals and low surface brightness galaxies indicate the existence of central dark matter *cores*, i.e.  $\rho_{inner} \propto const$  (Salucci & Burkert, 2000a; de Blok et al., 2001). These observations are well fitted by the Burkert (1995) halo, which assumes a double power law for the DM-density, namely at small radii  $\rho \propto r^0$  and at larger radii  $\rho \propto r^{-3}$ . Therefore, the Burkert dark matter density profile is as follows:

$$\rho(r) = \frac{\rho_0}{\left(1 + \frac{r}{r_0}\right)\left(1 + \frac{r^2}{r_0^2}\right)}, \quad (2.14)$$

where  $\rho_0$  and  $r_0$  are the central dark matter core density and core radius, respectively. Assuming spherical symmetry, the mass profile of Burkert dark matter halo follows as:

$$M_{DM}^{\text{Burk}}(r) = 4\pi\rho_0 r_0^3 \left[ \ln\left(1 + \frac{r}{r_0}\right) - \arctan\left(\frac{r}{r_0}\right) + 0.5 \ln\left(1 + \frac{r^2}{r_0^2}\right) \right], \quad (2.15)$$

NFW Halo: In the standard collisionless cold dark matter paradigm, the current cosmological simulations predict a *cuspy* dark matter distribution in the center, i.e.,  $\rho_{inner} \propto r^{-\alpha}$  where  $\alpha \sim 1$ . This type of dark matter profile is well approximated by NFW halo, which is again a double power law but it has  $\rho \propto r^{-1}$  at small radii and  $\rho \propto r^{-3}$  at larger radii:

$$\rho(r) = \frac{\rho_s}{\left(\frac{r}{r_s}\right) \left(1 + \frac{r}{r_s}\right)^2} \quad (2.16)$$

where  $\rho_s$  and  $r_s$  are, respectively, the characteristic density and scale radius of the dark matter distribution. Again, assuming spherical symmetry, the corresponding mass profile is given by:

$$M_{DM}^{\text{NFW}}(r) = 4\pi\rho_s r_s^3 \left[ \ln\left(1 + \frac{r}{r_s}\right) - \frac{\frac{r}{r_s}}{1 + \frac{r}{r_s}} \right], \quad (2.17)$$

The circular velocity of the above dark matter profiles can be written as:

$$V_{DM}^2(R) = G \frac{M_{DM}(< R)}{R}, \quad (2.18)$$

where  $M_{DM}(< R)$  is enclosed dark matter mass within radius  $R$  given in Equations 2.15 & 2.17. Above formalism allow us to compute the various structural properties of dark matter halo. For the purpose of this work, we define virial radius ( $R_{vir}$ ), virial mass ( $M_{vir}$ ), and concentration ( $c$ ) parameter of halo. The virial radius is the distance within

which the average halo density is 200 times the cosmological critical density ( $\rho_{\text{crit}} = 9.3 \times 10^{-30} \text{ gm cm}^{-3}$ ) of the Universe and can be easily computed numerically for a given pair of dark matter halo parameters. The virial mass is defined as:

$$M_{\text{vir}} = \frac{4}{3}\pi R_{\text{vir}}^3 200 \rho_{\text{crit}}, \quad (2.19)$$

In case of NFW halo, the ratio of virial radius to scale radius gives the halo concentration,  $c = R_{\text{vir}}/r_s$ . Furthermore, once the various components of rotation curve are disentangled, then, given the information on  $V_{\text{DM}}(R)$  and  $V_c(R)$ , one can also estimate:

$$f_{\text{DM}}(< R) = \frac{V_{\text{DM}}^2(R)}{V_c^2(R)}, \quad (2.20)$$

which gives us the dark matter fraction within the radius  $R$ .

## 2.3 Star-forming Galaxies (SFGs)

The galaxies in the local Universe are often classified based on their colour and magnitude (brightness), resulting in the "red sequence" and "blue cloud" bi-modality, shown in Box 4 (see, [Strateva et al., 2001](#); [Baldry et al., 2004](#); [Gavazzi et al., 2010](#)). Most elliptical galaxies, i.e. early-type galaxies (ETGs), belong to the red- sequence. These galaxies are generally free of dust & gas, usually contain old, massive stars, and are often dominated by stellar pressure. The blue cloud, on the other hand, contains young dust & gas rich galaxies, that are actively star forming and keep old and young stellar populations. These are called late-type galaxies, often referred to as LTGs.

The conversion of gas into stars is one of the fundamental characteristics of every galaxy in the Universe, the time-scale with which this process occurs is called the star-formation rate. The stellar mass and star formation rate of galaxies are the basic quantities that can be measured at any cosmic time (assuming a certain astrophysics). In LTGs, also known as star-forming galaxies, these two quantities, stellar mass and star formation rate, are tightly co-related, and this correlation is often referred to as the "Main Sequence" of star-forming galaxies. Recently, [Speagle et al. \(2014\)](#) have shown that the main-sequence of star-forming galaxies persists up to  $z \sim 4$ . On the other hand, local star-forming galaxies are rotation supported disc systems and have a geometrically simple morphology. Therefore, the dynamics of these systems can be easily modelled using Jeans hydrodynamical equations, ignoring the pressure support. These two main factors of star-forming galaxies 1) similar baryonic physics throughout cosmic time ( $z \sim 0-4$ ) and 2) simple dynamical modelling, make them compelling to use as a *cosmic ladder* to study the evolution of local properties of galaxies (e.g. stars and gas distribution) and global properties related to dark matter halo (e.g., dark matter fraction and its distribution). This is one of the main reasons, I am investigating star-forming galaxies to understand the astrophysical nature of dark matter over cosmic time. To bring or understanding on the same level, in section [2.3.1](#) & [2.3.2](#) I give an overview of the current state of kinematic and dynamical studies of local and high-redshift star-forming galaxies.

## Box 2.4

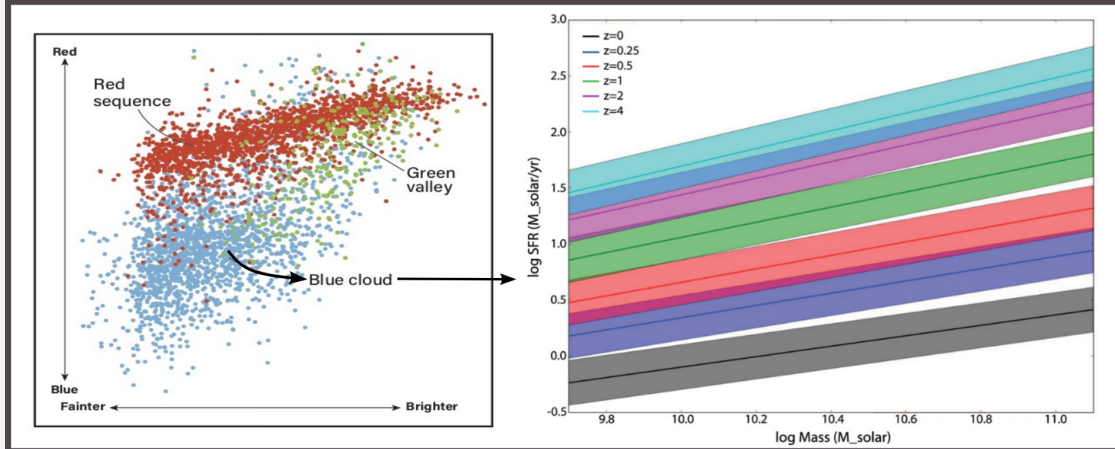
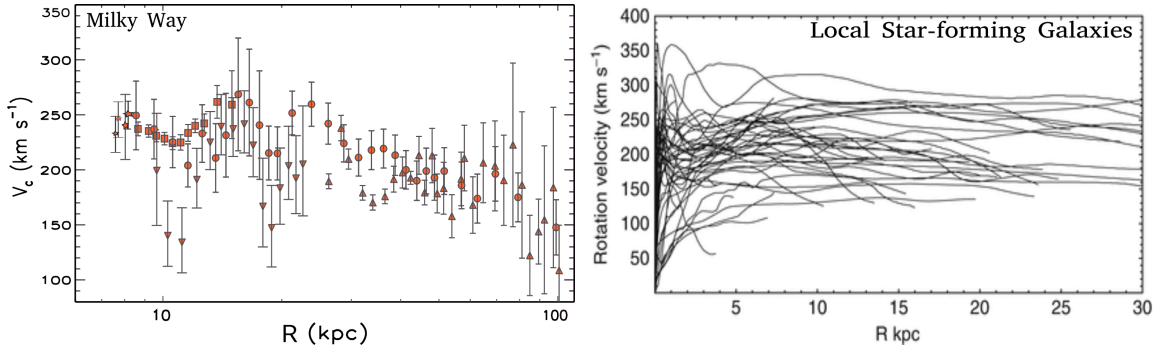


Illustration of the classification scheme of local star-forming galaxies. *Left panel:* Color-magnitude diagram of galaxies in the local Universe showing bimodality in the form of the ‘red sequence’ and the ‘blue cloud’. The red sequence galaxies represent the early-type galaxies (passive in star formation), and the blue cloud shows the late-type galaxies (star-forming galaxies: spirals). There is also an unusual population of red spirals that form the ‘green valley’. *Right panel:* The stellar mass and star formation rate of late-type galaxies (blue cloud) are tightly co-related, forming the so-called ‘Main Sequence’ of star-forming galaxies, which persist from  $z = 0$  to  $z = 4$ , shown by colored strips. The black arrow in the left panel followed by blue cloud galaxies indicating towards right panel, shows that the blue cloud galaxies are the star-forming galaxies and contributing to the main sequence. Image source: Roen Kelly (Astronomy blog), [Gavazzi et al. \(2010\)](#) and [Speagle et al. \(2014\)](#).

### 2.3.1 Kinematics and Dynamics of Local SFGs

I begin by mentioning the kinematics and dynamics of our own galaxy "Milky Way", which is one of the star-forming galaxies. As defined in Section 2.1, we measure the Galactic rotation curve through the spectroscopy of the gas kinematics (e.g. HI disc thickness: [Honma & Sofue 1997](#), HII regions: [Blitz 1979](#), CO emission: [Luna et al. 2006](#), HI terminal velocities: [McClure-Griffiths & Dickey 2007](#), and giant molecular gas clouds: [Hou et al. 2009](#)), stellar kinematics (e.g., classical Cepheids: [Pont et al. 1997](#), planetary nebulae: [Durand et al. 1998](#), carbon stars: [Battinelli et al. 2013](#)) and masers ([Reid et al., 2014](#)). Due to the particular location of the Sun in the Milky Way, it is difficult to measure the intrinsic circular velocity of Galactic objects. In this context, several sophisticated techniques have been developed to determine the circular velocity, such as the tangential velocity method, disc thickness, trigonometric method, etc. The circular velocity determined by these methods is generally rescaled to the Local Standard



**Figure 2.3:** Example of kinematics of local star-forming galaxies. *Left panel:* Rotation curve of Milky Way galaxy from 8-100 kpc radius derived from stellar and gas kinematics using various observations (image credit: [Huang et al. 2016](#)). *Right panel:* Rotation curves of several star-forming galaxies in the local Universe (image credit [Sofue, 2016](#)). Often rotation curves are derived from  $H\alpha$  (optical: stellar kinematics) or HI observation (radio: gas kinematics), and in some special cases the inner rotation curves are constrained with CO-line emission (radio observations) .

of Rest (LSR) frame, given by the Galactic constants  $[R_0, V_0]$ <sup>8</sup>, where  $R_0$  is the distance from the Galactic centre and  $V_0$  is the rotation velocity around the Galactic centre. In left panel of Figure 2.3, I show an average study of the Milky Way rotation curve out to 100 kpc, taken from various studies (for details see [Pato et al., 2015](#); [Huang et al., 2016](#)). The Milky Way rotation curve is very useful to study the local density of dark matter and its velocity distribution. The latter studies are crucial for testing direct and indirect searches for dark matter particles. In the last 20 years, several teams have dynamically studied the Milky Way rotation curve, in particular the inner rotation curve ( $\leq 20$  kpc), to determine the dark matter density in the solar neighbourhood ([Dehnen & Binney, 1998](#); [Sofue et al., 2009](#); [Catena & Ullio, 2010](#); [Nesti & Salucci, 2013](#); [Iocco et al., 2015](#)). For more details on the latter topic, we refer to [Sofue \(2020\)](#), where the author performed a kinematic and dynamical study of the Milky Way rotation curve to determine the local dark matter density. Using a very similar approach described in Section 2.2, [Sofue \(2020\)](#) reports that the local dark matter density is about  $\rho_{\text{DM}} \sim 9.5 \times 10^6 \text{ M}_\odot \text{ kpc}^{-3}$  ( $\rho_{\text{DM}} = 0.359 \pm 0.017 \text{ GeV cm}^{-3}$ ). We also refer the reader to [Wang et al. \(2020\)](#), who has reviewed extensive literature on the mass and velocity distribution of the Milky Way.

Moving on towards the local extragalactic Universe<sup>9</sup>, the most of the star-forming galaxies are spirals and disc like rotation supported systems. Often kinematics of these galaxies are derived from the optical and near infrared observations by detecting  $H\alpha$  (or [NIII]) emission coming from HII regions (stars surrounded by diffuse molecular gas clouds), and HI (or CO) emission detected in radio observations (neutral hydrogen and molecular hydrogen region). These observations are capable of yielding the rotation curves of local star-forming galaxies up-to 20-30 kpc radius, see right panel of Figure 2.3, for details I refer the reader to [Sofue \(2016\)](#). Moreover, [Salucci \(2019\)](#), and references therein)

<sup>8</sup>Galactic constant  $[R_0, V_0] = [8.0 \text{ kpc}, 238 \text{ km s}^{-1}]$  Sofue2017

<sup>9</sup>The local extragalactic Universe is referring the galaxies beyond the Milky Way and its satellites.

suggested that the dynamical study of these rotation curves is a portal to study the nature of dark matter in the local Universe.

In fact, the rotation curve mass modelling approach described in Section 2.2 is robust in constraining the baryon and dark matter distribution in local spirals, dwarf discs, and low surface brightness galaxies (Persic et al., 1996; Salucci et al., 2007; Sofue, 2016; Karukes & Salucci, 2017; Di Paolo et al., 2019). A best example of such studies and also a pioneering work is Persic et al. (1996), where authors have tested and verified this approach on a large number of local star-forming disc galaxies. The data for this study was collected from  $H\alpha$  kinematics (Mathewson et al., 1992) and radio observation (Gentile et al., 2004, added in later years). Persic et al. (1996) binned (grouped) the rotation curves of local spiral galaxies according to their absolute I-band magnitude (brightness or luminosity) and combined them into a single rotation curve, the so-called *co-added* rotation curve. In binning, the individual rotation curves are normalized at the optical radius<sup>10</sup> ( $R_{\text{opt}}$ ) and its corresponding velocities ( $V_c(R_{\text{opt}})$ ). These co-added rotation curves are then modeled using the same approach defined in Section 2.2.1 (see also Salucci et al., 2007). In particular, the stars are assumed to be distributed in an exponential disc and the dark matter follows the Burkert profile, while bulge and gas contribute negligibly to the circular velocity of the galaxy. An example of four mass-modelled rotation curves is shown in upper panel of Figure 2.4. As can be seen, simple models given by Equations 6.1, 2.9, 2.15 & 2.18 are able to fit the observed nature of the rotation-cum-circular velocities of galaxies, as well as disentangle the stellar and dark matter distribution. Moreover, we notice that the rotation curves of local spiral galaxies are flat up to twice the optical radius, and the dark matter turns out to be dominant over the entire magnitude (luminosity) range. However, at high luminosities, the stellar disc begins to prevail and we often see slightly declining rotation curves. With this study we have learned that the rotation curve of local spirals are one parameter family, i.e. they can be described as a function of luminosity (or stellar mass or circular velocity). This has given them the name *Universal Rotation Curves*.

The Universal Rotation Curves (URCs) are an observationally derived theoretical framework, which is capable of linking the local properties of galaxies (observed from luminous matter) to the global properties of dark matter halo, see Figure 2.4 bottom panel. In particular, URCs provide the gravitational potential of galaxies at any radius by simply using the luminosity of the system (see Persic et al., 1996). Despite some caveats (e.g., Bosma, 1999; Verheijen, 1997; Oman et al., 2015b), which are obvious in the infinite Universe given the finite capabilities, URCs provides a benchmark scheme that has been considered in various theoretical models. Moreover, URCs also predict the cored inner dark matter density profile, which has been confirmed by several studies of galaxies in the local Universe (e.g. Palunas & Williams, 2000; Salucci & Burkert, 2000a; de Blok et al., 2001; de Blok et al., 2003; Gentile et al., 2004; Simon et al., 2005; Salucci et al., 2007; Karukes & Salucci, 2017; Di Paolo et al., 2019). Moreover, URCs successfully reproduce the local scaling relations (e.g. Tully-Fisher relation, mass-size relation) and physical

<sup>10</sup>An optical radius encompasses the 83% of the galaxy's total luminosity

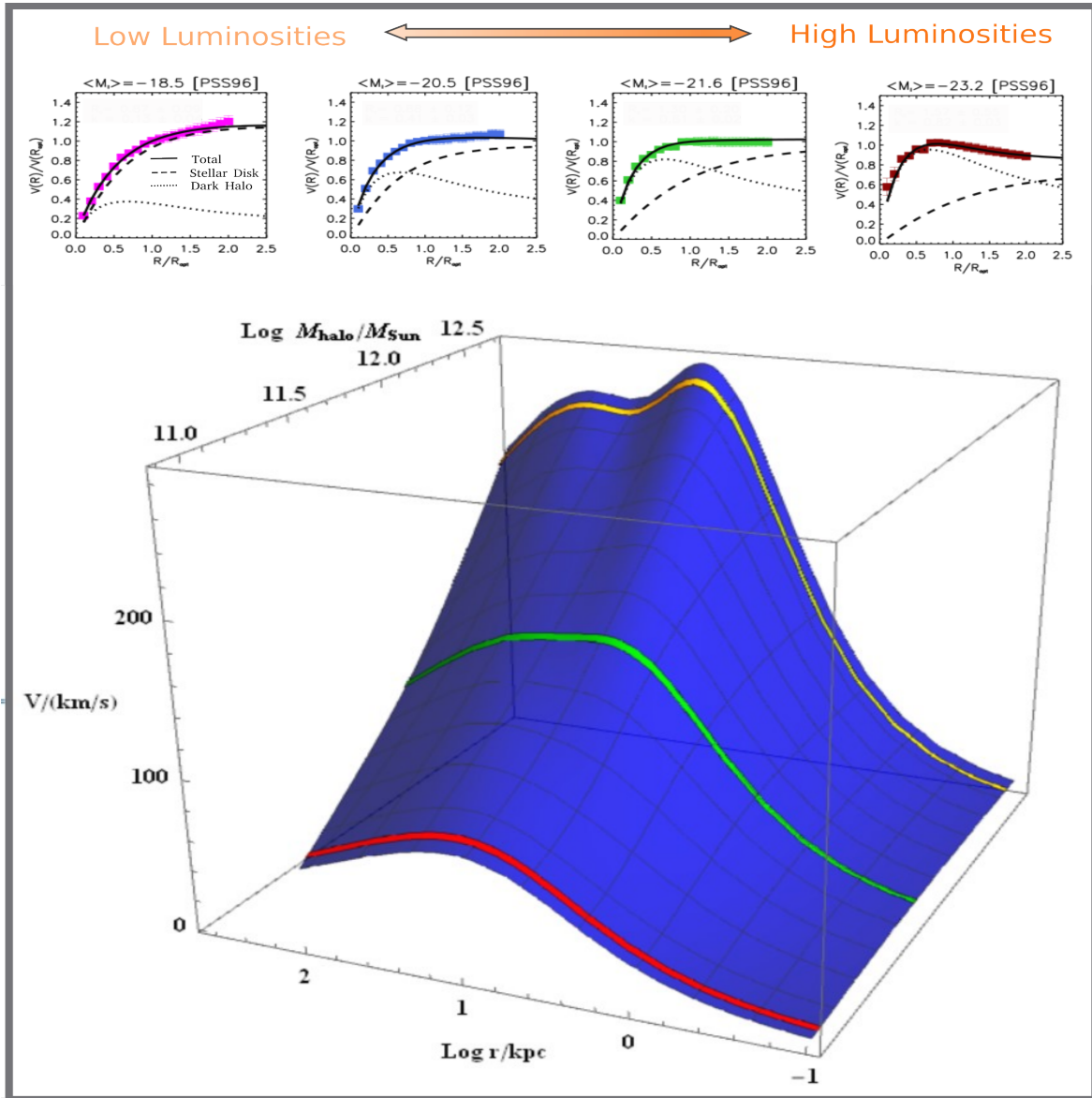


**Figure 2.4:** Universal rotation curves (URCs) of local star-forming disc galaxies. In *Upper panel*, I show a sub sample of URCs from high to low I-band absolute magnitude ( $M_I$ ), i.e. we are looking at the galaxies from fainter to brighter end (low to high luminosities). These rotation curves are dynamically modelled assuming that stars are distributed in exponential disc and dark matter follows the cored profile. The contribution of gas and bulge is minimal towards circular velocity; therefore neglected. As we can notice, simple models defined in Section 2.2.1 are capable of disentangling the stellar and dark matter distribution (component) of galaxies. The main figure shows the classical URCs surface plot in blue sheet, and few example rotation curves of circular velocity  $V(r; M_{vir})$  is plotted out to  $R_{vir}$  as a function of log radius and  $\log M_{vir}$ . The three rotation curves plotted as yellow, green, and red bands correspond to the cases  $\log M_{vir}/M_\odot = 11 \pm 0.03, 11.9 \pm 0.03, 12.3 \pm 0.03$ , respectively. A full description and details of figure can be obtained from [Persic et al. \(1996\)](#) and [Lapi et al. \(2018b\)](#).

parameters (e.g. angular momentum and star-formation efficiency), which are successfully implemented in semi-analytical models of galaxy evolution (Lapi et al., 2018a; Lapi et al., 2020). This gave me a strong motivation to discover such a theoretical framework of galaxies (using galaxy kinematics and dynamics) over cosmic time. For a comprehensive study on this topic, we refer the reader to Reyes et al. (2011); Read et al. (2016); Sofue (2016); Salucci (2019); Salucci et al. (2020).

### 2.3.2 Kinematics and Dynamics of High Redshift SFGs

In the last decade, advanced use of integral field units (IFUs) in galaxy surveys has opened the several possibilities of studying the spatially resolved kinematics and the dynamics of galaxies. For example, surveys with the Multi-Unit Spectroscopic Explorer (MUSE: Bacon et al. 2010), K-band Multi-Object Spectrograph (KMOS: Sharples 2014), and the Spectrograph for INtegral Field Observations in the Near Infrared (SINFONI: Eisenhauer et al. 2003). In general, the kinematics of galaxies is inferred from the IFU datacube using the spatially resolved emission lines (e.g., H $\alpha$ , [OIII], [NII]). In particular, the H $\alpha$  emission is the most promising tracer for inferring the kinematics of high-redshift galaxies (e.g. Di Teodoro et al., 2016; Burkert et al., 2016; Harrison et al., 2017; Lang et al., 2017; Förster Schreiber & Wuyts, 2020, and references therein).

From this kinematic information, it is easy to derive global and resolved properties of galaxies. The current study of global properties of high-redshift star-forming galaxies shows a relatively high fraction of molecular gas and star formation rate (Tacconi et al., 2010; Glazebrook, 2013; Speagle et al., 2014; Turner et al., 2017; Johnson et al., 2018; Tacconi et al., 2018), as well as they have a large variety of kinematics in terms of rotating disc, velocity dispersion, and mergers (Förster Schreiber & Wuyts, 2020, and references therein). We also find that, the rotational velocity of high-redshift galaxies at turn over radii (and at flattened part) is about 100-300 km s $^{-1}$  (see Chapter 3), which is very similar to local star-forming galaxies (shown in the right panel of Figure 2.3). The velocity dispersion, on the other hand, tends to increase, and is roughly between < 50 – 100 km s $^{-1}$  (Genzel et al., 2008; Förster Schreiber et al., 2009). In fact, some recent studies have shown that average gas velocity dispersion evolves with redshift as well as the disc fraction (Kassin et al., 2007, 2012; Wisnioski et al., 2015; Simons et al., 2017; Wisnioski et al., 2019). These studies are very interesting in the context of galaxy evolution scenarios, for example, the high velocity dispersion could be triggered by (1) cosmic gas accretion or feedback processes (Green et al., 2010), and (2) gravitational instabilities (Übler et al., 2019). However, there is still the possibility that the high velocity dispersion in the high-redshift star-forming galaxies could be an artifact of the low spatial resolution in the data (Di Teodoro et al., 2016), leading to ‘beam smearing’ that could overestimate the velocity dispersion (see Section 2.4.1).

The global kinematics also allows us to study the fundamental scaling relations, such as: the mass-size relation, the Tully-Fisher relation, and the angular momentum. These scaling relations are important to report because they form the foundation of our current understanding of the interplay between dark and luminous matter, galaxy formation, and

their evolution. Often, the mass-size relation of galaxies is studied using photometry because it can be easily derived using high-resolution photometric data. For example, [van der Wel et al. \(2014a\)](#) analysed extensive data from the CANDELS survey, which showed an evolution of the mass-size relation of high-redshift star-forming galaxies as a function of stellar mass ( $R_{\text{eff}} \propto M_{\text{star}}^{0.22}$ ) and redshift ( $R_{\text{eff}} \propto (1+z)^{-0.75}$ ).

The Tully-Fisher relation (TFR) is the most fundamental empirical scaling relation that correlates the properties of luminous matter with the dark halo. In the traditional TFR, dating back to the seminal work of [Tully & Fisher \(in 1977\)](#), the luminosity of galaxies scales with their characteristic velocity (i.e., the circular velocity  $V_c$ ) via a power-law  $L \propto \beta V_c^\alpha$ , which remarkably relates the halo potential (determined by  $V_c$ ) to luminous matter. Some studies [Ziegler et al. \(2002\)](#); [Böhm et al. \(2004\)](#); [van Starkenburg et al. \(2006\)](#) have shown that the slope of TFR at intermediate redshift ( $z \sim 0.5$ ) is shallower in comparison to locals and lead the discussion of selection bias. However, other studies have shown that the slope of TFR hardly changes from  $z \sim 1$  to  $z \approx 0$  ([Conselice et al., 2005](#); [Kassin et al., 2007](#); [Miller et al., 2011](#); [Miller et al., 2012](#)). Some recent studies of Integrated Field Unit (IFU) observations ([Puech et al., 2008](#); [Cresci et al., 2009](#); [Gnerucci et al., 2011](#); [Tiley et al., 2016](#); [Übler et al., 2017](#); [Harrison et al., 2017](#); [Tiley et al., 2019a](#)), claim that the zero point of TFR varies while the slope remains almost the same. Therefore, currently these studies do not seem to converge for high-redshift star-forming galaxies.

In terms of angular momentum which is a conserved quantity, this means that any change (or no change) in this quantity will directly reflects the current dynamical state of a galaxy, when studied for its various constituents (gas, stars, and dark matter). For example, [Burkert et al. \(2016\)](#) and [Swinbank et al. \(2017\)](#) suggest that the for high-redshift star-forming galaxies angular momentum scaling relation with stellar mass remains the same as locals ( $j_* \propto M_*^{2/3}$ ) but seems to reflect a redshift evolution that scales as  $j_* \propto M_*^{2/3}(1+z)^{-n}$ , where  $n = 0.5 - 1.5$ . This slight evolution in the stellar angular momentum with redshift indicates a transfer of angular momentum, which has also been suggested by [Lagos et al. \(2017\)](#) using the hydrodynamical simulations. A recent study of the specific angular momentum, in particular, the stellar specific angular momentum sequence ( $J_* - M_*$  plane) provided by [Gillman et al. \(2020\)](#), shows a strong correlation with the morphology of high-redshift galaxies (see also [Swinbank et al., 2017](#)). In particular, galaxies with high  $J_*$  tend to have a disc-like morphology. However, the work of [Gillman et al. \(2020\)](#) is not yet confirmed by any other independent study and dataset.

Recently, the study of resolved kinematics, i.e., rotation curves, have been extended to higher redshifts (e.g., [Di Teodoro et al. 2016](#) and [Genzel et al. 2017](#)). In particular, [Genzel et al. \(2017\)](#) and [Lang et al. \(2017\)](#) analyzed the rotation curves of star-forming galaxies at high-redshift and found a declining behavior with increasing radius (see Figure 2.5), such behavior is only seen in very massive local star-forming galaxies, while the rotation curves of normal star-forming galaxies are remarkably flat and rarely decline (e.g., [Rubin et al. 1980](#) and [Persic et al. 1996](#)). The study of [Genzel et al. \(2017\)](#) investigate the individual rotation curves of six massive ( $\log(M_*/[\text{M}_\odot]) = 10.6 - 11.1$ ) star-forming galaxies at redshift  $0.9 \leq z \leq 2.4$  in more detail. They showed declining rotation curves in two

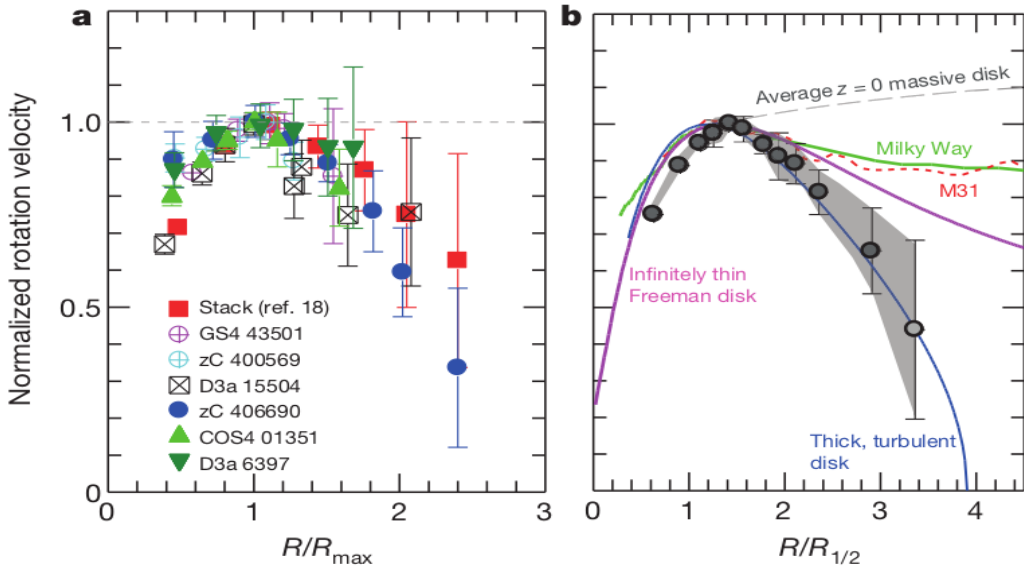


**Figure 2.5:** Rotation curves of high-redshift star-forming galaxies. *Left panel:* Individual rotation curves normalized at their maximum velocity. *Right Panel:* Stacked rotation curve where individual rotation curves are normalized at effective radius. This figure is copied from [Genzel et al. \(2017\)](#). A similar study is also presented by [\(Lang et al., 2017\)](#).

cases: first, when the individual rotation curves were normalized at  $R_{max}$ , where the amplitude of the rotational velocity is maximal; and second when the binned average of the six individual galaxies were normalized at the effective radius ( $R_e$ ). Based on these results, [Genzel et al. \(2017\)](#) concluded that the fraction of dark matter within  $R_e$  is below 20%. Later, these results were confirmed by [Lang et al. \(2017\)](#), who obtained the stacked normalized rotation curves of 101 star-forming galaxies at  $0.6 \lesssim z \lesssim 2.2$  with stellar masses  $9.3 \lesssim \log(M_* [\mathrm{M}_\odot]) \lesssim 11.5$ , where the normalization of rotation curves was performed at a ‘turnover radii’, where  $R_{turn} \sim 1.65 R_e$  (for details see [Lang et al. 2017](#)). Both studies suggest that the declining behavior of rotation curves can be explained by a combination of high baryon fraction and extensive pressure support (see Section 2.4.2). Some other high-redshift studies of late-type and early-type galaxies also report similar low dark matter fractions within the effective radii (e.g., [Burkert et al., 2016](#); [Wuyts et al., 2016](#); [Price et al., 2016](#); [Übler et al., 2018](#)).

On the other hand, [Tiley et al. \(2019b\)](#) studied the shape of rotation curves in  $\approx 1500$  star-forming galaxies at high-redshift ( $0.6 \lesssim z \lesssim 2.2$ ) that have stellar masses  $8.5 \lesssim \log(M_* [\mathrm{M}_\odot]) \lesssim 11.7$ . These authors used a similar stacking approach as [Lang et al. \(2017\)](#) and confirmed that the rotation curves are similar to those in Lang et al. (i.e., declining) if they are normalized at turnover radii. However, if instead the normalization was performed at  $3 \times R_D$  ( $\approx 1.77 R_e$ ) they found flat or rising rotation curves. Moreover, [Tiley et al. \(2019b\)](#) reported a more than 50% dark matter fraction within  $3.5 R_e$ , which is similar to local star-forming disc galaxies ([Persic et al., 1996](#); [Martinsson et al., 2013](#); [Courteau & Dutton, 2015](#)). Finally, another study by [Drew](#)

et al. (2018) analyzed a massive star-bursting galaxy at  $z = 1.55$ , which showed strong evidence of a flat rotation curve between  $6 - 14$  kpc with a 44% dark matter fraction within the effective radius. One of the recent study of Genzel et al. (2020) reports that the that "at least two-thirds of massive star forming disc like galaxies at the peak of cosmic galaxy/star formation ( $z > 1 - 2.5$ ) had strongly baryon-dominated discs up-to 1020 kpc radius". Thus the interpretation of high-redshift star-forming galaxies and their dark matter content remain ambiguous and still need to be investigated until we converge on some concrete conclusions.

## 2.4 Observational and Physical Uncertainties

Differences in rotation curve shapes may also arise due to different kinematic modelling approaches, different treatment of observational uncertainties e.g., low spatial resolution and small angular size lead to the beam smearing (Teodoro & Frernali, 2015; Di Teodoro et al., 2016) and the underlying physical effects, e.g., pressure support/gradient (Valenzuela et al., 2007; Read et al., 2016; Wellons et al., 2020; Johnson et al., 2018). To provide the contribution in a similar context, I analysed the KROSS data, a subset of Tiley et al. (2019b) sample. The kinematics of this data were primarily studied by Harrison et al. (2017). When the KROSS data were not publicly available (in 2018-2019), I analysed the rotation curve data handed over by Harrison et al. to understand the intrinsic shape of high-redshift rotation curves and their comparison with local galaxies (hereafter "locals"), as well as corresponding scaling relations (e.g. Tully-Fisher relation). In my first PhD progress report, I have demonstrated that due to (1) the limited spatial resolution which causes the so-called *Beam Smearing*, and (2) the extremely turbulent interstellar medium at high-redshift causing the *Pressure Gradient*, the determined rotational velocity profile ( $V(R)$ ) of galaxies were underestimated at all radii. This has affected the inferred dynamical quantities (circular velocity, dynamical mass, dark matter fraction, Virial mass) as well as impacted upon the scaling relations. For these reasons, I have re-analysed KROSS data from scratch (see Chapter 3). I proposed to improve the spatial resolution problem by using 3D forward modelling of datacubes (Bouché et al., 2015; Teodoro & Frernali, 2015). To decouple the physical uncertainty of turbulent interstellar medium, I incorporate the pressure gradient correction derived from the collisionless Boltzmann equation (Subrahmanyan, 1960; Aoki, 1985; Weijmans et al., 2008), where the velocity dispersion (or pressure) is anisotropic and a function of the radius (or position). Below, I briefly describe the problem of beam smearing and the pressure gradient problem, and how these processes affect the kinematics of galaxies. In Chapter 3 I have given a detailed diagnosis to resolve these problems.

### 2.4.1 Beam Smearing

Although IFUs brought remarkable progress in the field, due to the small angular size of the high- $z$  galaxies, the attained spatial resolution is limited. Without Adaptive Optics

(AO), an IFU achieves only  $0.5 - 1.0$  arcsec spatial resolution, whereas, a galaxy from  $z \sim 1$  has a typical angular size of  $2 - 3$  arcsec. The finite beam size causes the line emission to smear on the adjacent pixels, shown in Box 5. This effect is referred to as ‘Beam Smearing’, which under estimates the rotation velocity and overestimates the velocity dispersion. The same beam smearing scenario happens in HI observations (Bosma & Van der Kruit, 1979; Begeman, 1989) of local spiral galaxies. Although the previous IFU studies of high- $z$  galaxies have applied beam-smearing corrections in different ways, these have usually been applied to the derived two-dimensional velocity maps or the one-dimensional rotation curves. An alternative approach is to apply dynamical models and beam-smearing corrections simultaneously directly to the 3D datacube. For example,  $3D$ BAROLO (Teodoro & Fraternali, 2015; Di Teodoro et al., 2016) (hereafter BBarolo or Barolo) uses a tilted ring approach, which allows the reconstruction of intrinsic kinematics closest to the observations. Then the model is compared with data ring by ring in 3D-space, and, at the same time, beam smearing corrections are accounted. This is the approach that we employ in this work and the details are discussed in Section 3.2.2.

### Box 2.5

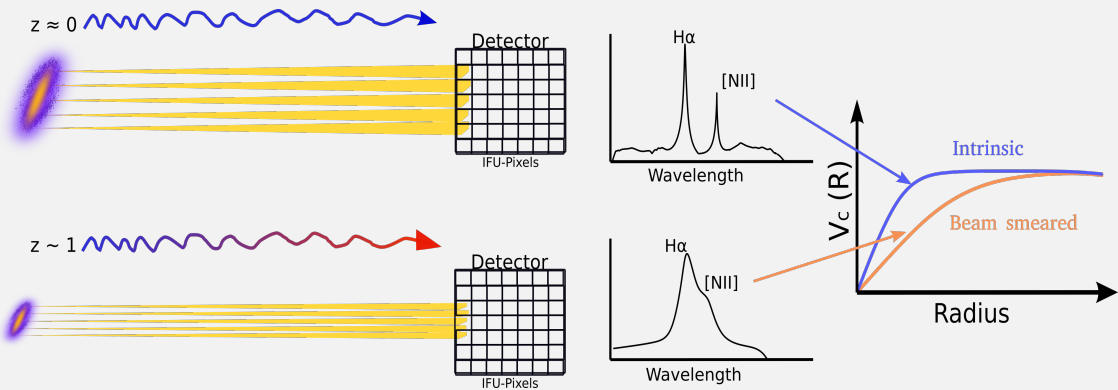


Illustration of beam smearing problem. When the object is situated in the local Universe, where our instruments are accurately calibrated, the spectroscopic observations are precise and capable of resolving adjacent emission lines, as shown in upper left column. This leads to an accurate intrinsic circular velocity estimates. However, spectroscopy of distant objects is challenging due to their small angular size and finite light beam, which tends to spread on the neighbouring pixels (show in lower left panel) and blends the nearby emission lines as shown in middle column. This problem in spectroscopy is known as ‘beam smearing’, which underestimates the rotation velocity and overestimates the velocity dispersion. In particular, this effect reflects as a shallow rise in the rotation curve, and mostly affects the inner region, see right column. The slow rise in rotation curves mislead the dark matter content and show minimal stellar disk scenario.

Box 2.6

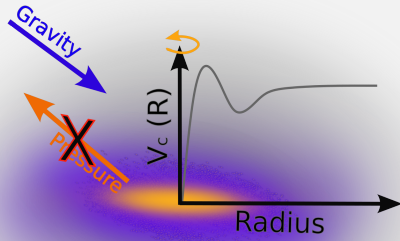
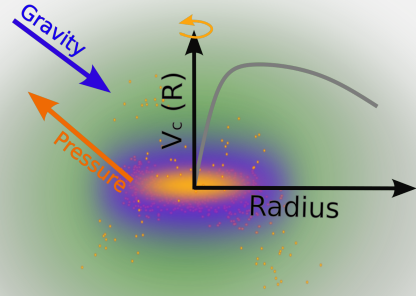
 $z \approx 0$  Disc Galaxies $z \sim 1$  Disc-like Galaxies

Illustration of the pressure support problem. All galaxies experience gravitational force (inward) and radiation pressure (outward), along with these forces, the stars and gas rotate and thus experience a centrifugal force. It is known that disc galaxies in the local universe contain only a small amount of molecular gas and form stars very slowly. Consequently, their Inter-Stellar Medium (ISM) is quiet and the radiation pressure is therefore negligible. In this situation, the gravitational force is only supported by rotation. In contrast, disc-like galaxies at high-redshift are known to be dominated by gas (high star formation rate), and consequently their ISM is turbulent. The turbulent interstellar medium of high-redshift star-forming galaxies makes the velocity dispersion anisotropic and function of radius, leading to the ‘pressure gradient’ problem. In these extreme situations, pressure, centrifugal force and gravity support each other to maintain equilibrium, consequently, the galactic disc starts to rotate slowly. Therefore, we observe somewhat declining rotation curves, although the dark matter is still present, and providing its full potential or gravity. This is why, we need to disentangle pressure support while studying rotation curves and dark matter.

### 2.4.2 Pressure Support

As mentioned earlier in the section, the kinematics of the galaxies are derived using the emission lines like  $H_\alpha$  or [OIII]. These emission lines arise from the gaseous disc around the stars or the ISM. If the ISM is highly turbulent, then the emission also experiences a turbulence, i.e. radial force against gravity. This turbulence/force scales with the gas density and velocity dispersion. Since the density and velocity dispersion both decrease with increasing radius, this creates a pressure gradient, i.e.  $F_P \propto -dP/dr$  (where  $P \propto \rho\sigma^2$ ). In these dramatic situations, the resulting radial force supports the disc against the gravity and keep it in equilibrium such that the disc starts rotating slower than its actual circular velocity for given total mass. The latter result in declining the rotation curves

and potentially underestimate the dynamical masses (Valenzuela et al., 2007; Dalcanton & Stilp, 2010a), for an illustration see Box 6. This effect is generally minimal in the local rotation-dominated star-forming galaxies but significant in the local dwarfs and early-type galaxies (e.g. Valenzuela et al. 2007; Read et al. 2016; Weijmans et al. 2008). Since, high-redshift star-forming galaxies are gas dominated (Glazebrook, 2013; Tacconi et al., 2018, references therein), and the ISM is relatively turbulent (Förster Schreiber & Wuyts, 2020, references therein), which in principle modifies the kinematics of the galaxies (Burkert et al., 2010; Glazebrook, 2013; Turner et al., 2017; Johnson et al., 2018; Übler et al., 2019; Wellons et al., 2020) and may result in different shapes of the rotation curves derived from the kinematics of high-redshift galaxies. Thus, also impacts upon the accurate determination of dark matter content and its distribution. Therefore, it is essential to take into account the pressure support. In this work, we apply the ‘Pressure Gradient Correction (PGC)’ on rotation curves to disentangle the pressure support, for details I refer the reader to Section 3.2.3.

## 2.5 Research Highlights

In this work I undertake the challenging task of understanding the controversial issues of high-redshift star-forming galaxies in more detail and provided several novel conclusions. I established a robust framework for analysing the high redshift spectroscopic surveys, which improves upon the standard techniques that have been commonly used in the past studies of high-redshift galaxies (particularly in large galaxy surveys). Using this framework, I have analysed one of the 3D-spectroscopic surveys data of  $z \sim 1$  galaxies, which is described in Chapter 3. Following a similar methodology as described in Section 2.1 & 2.2, I obtained new insights regarding their kinematics and dynamics. My current results, provide a robust statistical study of  $z \sim 1$  star-forming galaxies, their rotation curves, mass budget, scaling relations, and structural properties of dark matter halos. Apart from this, I have also analysed cosmological hydrodynamical simulations to provide the consistency check between observational and numerical studies of galaxies and their dark matter halos. These results are explained in great details in Chapter 3, 4, 5 6 & 7.



# Chapter 3

## Dataset: Redshift One Star-forming Galaxies

In this chapter, I describe the photometric and kinematic dataset used and analysed in this thesis to determine the physical properties of galaxies (e.g., effective radius, stellar mass) and their kinematics (i.e., circular velocity and rotation curves). In Chapter 2, I mentioned the prevailing observational and physical uncertainties, or say complexities, associated with the determination of intrinsic kinematics (see Section 2.4). In this chapter, I have presented state-of-the-art solutions to overcome these complexities, which have enabled me to present one of the most accurate and robust statistical studies of star-forming galaxies and their matter distribution over the last  $\sim 6.5$  billion years, see Chapter 4. In addition, I have also provided the simulated dataset that I will use to compare the observations with the theoretical predictions, see Chapter 6.

***Preamble:*** *The majority of the work presented in this chapter has been published as a first author paper in [Sharma et al. \(2021b\)](#) and [Sharma et al. \(2021c\)](#). To highlight certain aspects with more clarity, here, I have included some additional illustrations and descriptions.*

### 3.1 Observations

KMOS-Redshift One Spectroscopic Survey (KROSS) was aimed to observe the  $z \sim 1$  star-forming galaxies ([Stott et al., 2016](#)). In this work, we have analysed a sub-sample of the publicly available KROSS data to determine the ‘intrinsic rotation curves’ of high-redshift rotation dominated star-forming galaxies (most likely disc-type galaxies). The minor and major details of observations and physical properties of the full sample can be found in [Stott et al. \(2016\)](#) and other first and foremost papers by the KMOS team (e.g., [Harrison et al., 2017](#); [Johnson et al., 2018](#); [Tiley et al., 2019b](#)). Nevertheless, in the section below, I have given a short overview of KROSS observations and our sample selection criteria.

### 3.1.1 KROSS Data

KROSS is an Integrated Field Spectroscopic (IFS) survey using the KMOS instrument on ESO/VLT. The KMOS consists of 24 Integrated Field Units (IFUs); those can be placed within 7.2 arcmin diameter field. Each IFU covers the  $2.8 \times 2.8$  arcsec in size with 0.2 arcsec pixels. The targets for the survey are selected from extragalactic deep field covered by multi-wavelength photometric and spectroscopic data: 1)Extended Chandra Deep Field Survey (E-CDFS: Giacconi et al. 2001; Lehmer et al. 2005), 2)Cosmic Evolution Survey (COSMOS: Scoville et al. 2007), 3)Ultra-Deep Survey (UKIDSS: Lawrence et al. 2007), 4)SA22 field Steidel et al. (1998). Some of the targets were selected from CF-HiZELS survey (Sobral et al., 2015). The targets were selected such that the  $H_{\alpha}$  emission is shifted into J-band. The median redshift of parent sample (KROSS full sample) is  $z = 0.85^{+0.11}_{-0.04}$ . The median J-band seeing of observations was 0.7 arcsec, with 92% of the objects were observed during seeing  $< 1$  arcsec. Individual frames have exposure times of 600 sec, and a chop to the sky was performed every two science frames. The data were reduced using ESOREX/SPARK pipeline (Davies et al., 2013), and flux calibration is performed using standard stars which have been observed during the same night as science data. The end product of the process is 3D datacube consists of two spatial axes and one spectral axis of 2048 channels (e.g., 3D datacube =  $f(x, y, \lambda)$ ). These datacubes are capable of producing spectrum, the line and the continuum images and the moment maps (see: Stott et al. 2016). Since mid-2019, this data is publicly available at KROSS-website<sup>1</sup>.

### 3.1.2 Sample Selection

We are focusing on 586 KROSS galaxies studied by Harrison et al. (2017, hereafter H17), we refer it as parent sample. We have selected 344 objects out of 586, on the basis of integrated  $H_{\alpha}$  flux cut ( $F_{H_{\alpha}} > 2 \times 10^{-17}$  [erg s $^{-1}$  cm $^{-2}$ ]) and inclination angle ( $25^{\circ} \leq \theta_i \leq 75^{\circ}$ ). The chosen flux and inclination cuts ensure the sufficient signal-to-noise data (S/N) and reduces the impact of extinction <sup>2</sup> during the kinematic modelling procedure (see Section 3.2.2). The intrinsic characteristic of the selected sample (referred to as ‘analysed sample’) is the following (given with respect to TableA1 of H17): 1)AGN-flag is zero i.e., no evidence for an AGN contribution to the  $H_{\alpha}$  emission-line profile; 2)H17 Quality-flag 1, 2, and 3, i.e., only  $H_{\alpha}$ -emission line detected objects ( $S/N > 3$ ). We adopted the values of effective radii ( $R_e$ ), photometric position angle ( $PA$ ), photometric inclination angle ( $\theta_i$ ), absolute H-band magnitude ( $M_H$ ), K-band AB magnitude ( $K_{AB}$ ), z-band AB magnitude ( $z_{AB}$ ),  $H_{\alpha}$  luminosity ( $L_{H_{\alpha}}$ ),  $H_{\alpha}$  flux ( $F_{H_{\alpha}}$ ),  $H_{\alpha}$  star-formation rate ( $SFR_{H_{\alpha}}$ ), and redshift ( $z$ ).

<sup>1</sup><http://astro.dur.ac.uk/KROSS/data.html>

<sup>2</sup>In the highly inclined system ( $\theta_i > 75^{\circ}$ ) observed flux extinct due to extinction, which suppress the rotation velocity upto a few times  $R_e$  (see Valotto & Giovanelli, 2003). On the other hand, in face-on galaxies ( $\theta_i < 25^{\circ}$ ) the rotation signal drops below the observational uncertainties. Therefore, to be conservative we down-select the sample for  $25^{\circ} \leq \theta_i \leq 75^{\circ}$ .

## 3.2 Data Analysis & Processing

The physical parameters of KROSS galaxies namely position & inclination angle, effective radius,  $H_{\alpha}$  luminosities, H-band absolute magnitude, star-formation rate, and stellar masses are adopted from [Harrison et al. \(2017\)](#). Note that for accuracy I have corrected the star-formation rates for dust reddening. Moreover, I compute the gas mass of the sample using scaling relations. For details on the determination of physical parameters of sample see Section [3.2.1](#).

To the kinematics, i.e. the intrinsic shape of the rotation curves, we follow the 3D-forward modelling and a relatively rigorous approach is considered for handling the observational and the physical uncertainties. Under 3D-forward modelling, a simulated datacube is populated for given initial conditions and then compared with the observed datacube. I keep on populating/reconstructing the simulated datacube by changing the initial guess until convergence between data and model occur. This yields the PV-diagrams and moment maps. For implementing such 3D-forward kinematic modelling of datacubes, I have used  ${}^3D$ BAROLO code ([Teodoro & Fraternali, 2015](#)), it is discussed in the Section [3.2.2](#) below. In the end, I implement the pressure support correction on  ${}^3D$ BAROLO generated rotation curves, which are discussed in the Section [3.2.3](#).

### 3.2.1 Determining Physical Parameters

For the details of adopted quantities we refer the reader to [Harrison et al. \(2017\)](#) and [Stott et al. \(2016\)](#), while next we briefly discuss some of the requisite quantities.

#### 3.2.1.1 Position and Inclination Angle

The position angle ( $PA$ ) and inclination angle ( $\theta_i$ ) are estimated by fitting a two-dimensional Gaussian model to the broadband images. [Harrison et al. \(2017\)](#) compared their  $PA$  and  $\theta_i$  with [van der Wel et al. \(2012\)](#) which fits Sérsic models to the *HST* near-infrared images using GALFIT that incorporates PSF modelling. Their calculations were in agreement with the GALFIT results and those derived using a two-dimensional Gaussian fitting method. Moreover,  $PA$  and  $\theta_i$  for COSMOS targets with  $I$ -band images were cross-checked with [Tasca, L. A. M. et al. \(2009\)](#) who derived the  $PA$  and  $\theta_i$  using the axis ratios.

#### 3.2.1.2 Effective Radius

The effective radius ( $R_e$ ) is measured from the broadband images by deconvolving the PSF and semi-major axis of the aperture, which contains half of the total flux. Since the broadband images are observed in  $I$ ,  $z'$ ,  $H$ , and  $K$  bands (depends on the surveys goal and instrument facility) therefore, the targets where the images are in  $I$ , and  $z'$  band, a systematic correction factor of 1.1 is applied in  $R_e$  to account the colour gradient. The simple approach of colour correction applied because HST images were not available for all the targets (for details see [Harrison et al. 2017](#)).

### 3.2.1.3 Scale Length

In general the scale lengths are associated with various quantities that decrease exponentially such as the surface brightness. The concept of scale-length has emerged from the local star-forming disc galaxies (given in, [Freeman 1970b](#) and [Persic et al. 1996](#)). According to which, the effective radius (half-light radius)  $R_e$  of a galaxy is defined to encompass the 50% of total integrated light. For an exponential surface brightness distribution  $I(r) \propto \exp(-R/R_s)$ ,  $R_s$  can be one of the various scale lengths, each of which is proportional to the stellar Freeman disc length  $R_D$ <sup>3</sup> ([Freeman, 1970b](#)); for example,  $R_e = 1.69 R_D$ . Under the same assumption, the optical radius  $R_{opt}$  containing 83% of the integrated light becomes  $R_{opt} = 3.2 R_D$ . In our sample, the median effective radius is  $\sim 3.1$  kpc and the median optical radius is  $\sim 5.9$  kpc. This means that the effective radius of the majority of the sample falls below the resolution limit ( $\sim 4.0$  kpc), since the median seeing is 0.5 arcsec at  $z \sim 0.9$ , while the optical radius is of the same order. Therefore, to be conservative and trace the physical quantities (e.g. circular velocity) to the furthest point where we have data, we define the outer radius  $R_{out} = 5 R_D$ , which stays above the resolution limit in majority ( $\approx 99\%$ ) of the sample.<sup>4</sup>

### 3.2.1.4 $H_\alpha$ Luminosity

To obtain the galaxy integrated  $H_\alpha$  luminosity ( $L_{H_\alpha}$ ), [Harrison et al. \(2017\)](#) first grade the  $H_\alpha$  sources on the basis of signal-to-noise (S/N: average over two times derived velocity full width at half-maximum (FWHM) of  $H_\alpha$  line). If the S/N  $\leq 3$ , then sources are discarded. Secondly, the emission line width is corrected for instrumental dispersion, which is measured from unblended skylines near the observed wavelength of the  $H_\alpha$  emission. Then, the  $H_\alpha$  flux was measured using 2.5 arcsec aperture (with an uncertainty of 30%) and hence the integrated  $H_\alpha$  luminosity<sup>5</sup> obtained.

### 3.2.1.5 Stellar Masses

We adopt the stellar masses given by [Harrison et al. \(2017\)](#). These stellar masses were calculated using a fixed mass-to-light ratio following  $M_* = \Upsilon_H \times 10^{-0.4 \times (M_H - 4.71)}$ , where  $\Upsilon_H$  and  $M_H$  are the mass-to-light ratio and absolute magnitude in the H band (rest frame), respectively. Here  $\Upsilon_H = 0.2$ , which is the median value of our sample obtained using the HYPERZ ([Bolzonella et al., 2000](#)) spectral energy distribution (SED) fitting tool; this tool uses a suite of spectral templates from [Bruzual & Charlot \(2003\)](#) and optical to near-infrared (NIR) photometry (U, B, V, R, I, J, H, and K)<sup>6</sup>.

The stellar masses calculated from a fixed mass-to-light ratio are slightly different from other studies of the same KROSS sample (e.g., [Stott et al. 2016](#) and [Tiley et al.](#)

<sup>3</sup> $R_D$  is a typical characteristic radius of local star-forming disc galaxies.

<sup>4</sup>Scale lengths in terms of the effective radius:  $R_D = 0.59 R_e$ ;  $R_{opt} = 1.89 R_e$ ;  $R_{out} = 2.95 R_e$ .

<sup>5</sup>Notice, we do not account for extinction due to lack of required data (e.g., Balmer line ratios) to measure the extinction. However, these luminosities are not used for the bulk of our analyses.

<sup>6</sup>In some cases, mid-infrared IRAC bands were also used; [Harrison et al. \(2017\)](#) provide details.

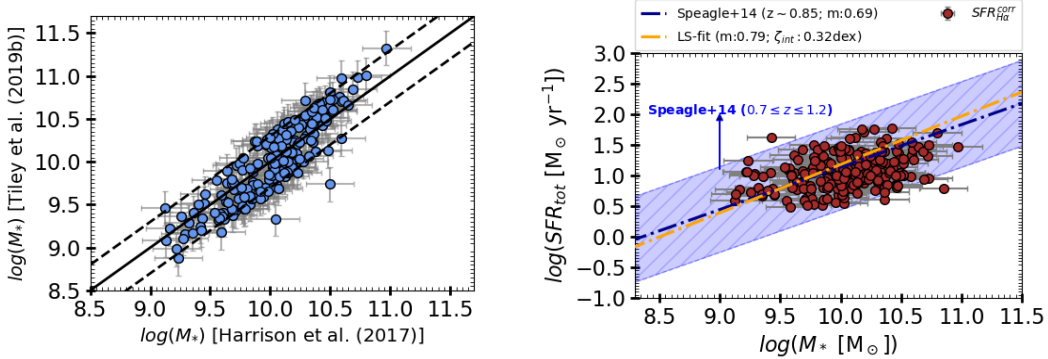


**Figure 3.1:** *Left panel:* Comparison of stellar masses derived from SED fitting (Tiley et al., 2019a) and fixed mass-to-light ratio (Harrison et al., 2017). The black solid and dashed line shows the one-to-one relation and 0.2 dex scatter, respectively. *Right panel:* Star formation rate (SFR) vs. total stellar mass ( $M_*$ ), tracing the MS of galaxies, where  $SFR_{\text{tot}} = SFR_{H\alpha}$  corrected for dust reddening. The brown filled circles represent the data used in this work. The dashed-dotted orange line shows the least-squares fit to our data, and the blue line shows the Speagle et al. (2014) MS relation at  $z \sim 0.85$ . The shaded blue region represents the MS limit between redshift  $0.7 \leq z \leq 1.2$ , which includes 0.3 dex uncertainty at each redshift.

2019a), in which different SED fitting procedures were used. For example, Tiley et al. (2019a) stellar masses are derived using the LE PHARE (Arnouts et al., 1999; Ilbert et al., 2006) SED fitting tool. The LE PHARE compares the suites of modeled SED of objects from the observed SED. Where the observed SED of our sample is derived from optical and NIR photometric bands (U, B, V, R, I, J, H, and K), in some cases we also used the IRAC mid-infrared bands. In modeling, the stellar population synthesis model is derived from Bruzual & Charlot (2003), and stellar masses are calculated using Chabrier (2003) initial mass function (IMF). The LE PHARE routine fits the extinction, metallicity, age, star formation, and stellar masses and allows for a single burst, exponential decline, and constant star formation histories. Details of stellar-mass computation are available in Tiley et al. (2019a). In left panel of Figure 3.1, we show that the Tiley et al. (2019a) and Harrison et al. (2017) stellar masses are in full agreement with an intrinsic scatter of 0.2 dex. Therefore, we assigned a homogeneous uncertainty of  $\pm 0.2$  dex on  $M_*$ , which is motivated by the aforementioned studies, as well as accounts for the typical uncertainty owing to low and high signal-to-noise photometry. Our sample covers the stellar mass range  $9.0 \leq \log(M_* [\text{M}_\odot]) < 11.0$ . We note that we do not have very massive ( $\log(M_* [\text{M}_\odot]) > 11.0$ ) galaxies in our sample.

### 3.2.1.6 Star Formation Rates

In general, SFRs in the ultra-violet, optical, or NIR ( $0.1\text{-}5 \mu\text{m}$ ) probe the direct star light of galaxies, while SFRs in mid- or far-infrared ( $5\text{-}1000 \mu\text{m}$ ) probe the stellar light reprocessed by dust. Therefore, the total SFR of any galaxy can be obtained by the linear combination of stellar and IR luminosities (Kennicutt Jr, 1998; Calzetti et al., 2007; Kennicutt & Evans, 2012), for example,

$$\text{SFR} [\text{M}_\odot \text{ yr}^{-1}] = C_{H\alpha} L_{H\alpha} + C_{24\mu\text{m}} L_{24\mu\text{m}}, \quad (3.1)$$

where  $C_{H\alpha}$  and  $C_{24\mu\text{m}}$  are the calibration constants, depends on star formation histories and IMFs. We can also derive the total SFR solely from stellar light (e.g.,  $L_{H\alpha}$ ), but then it requires an additional dust attenuation (or extinction) correction, which is defined as  $\text{SFR}^{tot} = \text{SFR}^{obs} \times 10^{A_\nu}$ , where  $A_\nu$  is the attenuation correction at given wavelength.

In our sample we do not have possibility to trace the luminosities from UV to the mid- or far-infrared. However, we have access to  $H_\alpha$ , H-, and K-band luminosities. Therefore, we estimated the SFR from  $H_\alpha$  using [Kennicutt Jr \(1998\)](#) relation given as

$$SFR_{H\alpha} [\text{M}_\odot \text{ yr}^{-1}] = 4.677 \times 10^{-42} L_{H\alpha} [\text{erg s}^{-1}], \quad (3.2)$$

where calibration constants,  $C_{H\alpha} = 4.677 \times 10^{-42} M_\odot \text{ yr}^{-1} \text{ erg}^{-1} \text{s}$ , include the correction factor of 1.7 due to the [Chabrier \(2003\)](#) IMF and [Salpeter \(1955\)](#) IMF used by [Kennicutt Jr \(1998\)](#). Furthermore, we correct for dust reddening (extinction), based on the average value ( $A_{Vgas} = 1.43$ ) derived in [Stott et al. \(2016\)](#) using the SED fitting. The  $A_{Vgas} = 1.43$  is corrected for stars using  $A_{Vgas}/A_{Vstar} \approx 1.7$  ([Calzetti et al., 2000](#); [Pannella et al., 2015](#)). In the right panel of Figure 3.1, we show the results and compare them with SFR- $M_*$  relation given by [Speagle et al. \(2014\)](#), MS of star-forming galaxies. In particular, we derive the [Speagle et al. \(2014\)](#) MS relation between  $0.7 \leq z \leq 1.2$  including 0.3 dex error (shown by blue shaded area), and the best fit is given for  $z = 0.85$ , which has a slope 0.69. For our sample we derive the best fit using the least-squares method, which includes the errors in both axis. We obtain a slope of  $0.79 \pm 0.1$  with intrinsic scatter 0.32 dex. Using a similar approach for the SFR determination, [Stott et al. \(2016\)](#) also observed a similar scatter in the SFR- $M_*$  relation, which reassures our measurements.

### 3.2.1.7 Molecular Gas Masses

To estimate the molecular gas mass ( $M_{\text{H}_2}$ ) of our galaxies, we adopt the relation given by [Tacconi et al. \(2018\)](#). These authors used a large sample of 1309 star-forming galaxies in the redshift range  $z = 0 - 4.4$  with stellar masses  $\log(M_* [\text{M}_\odot]) = 9.0 - 11.9$  and star formation rates (SFRs)  $10^{-2} - 10^2 \text{M}_\odot \text{ yr}^{-1}$ . We stress that [Tacconi et al. \(2018\)](#) combined the three different methods to determine the molecular gas mass, each of which is related to one of the following: 1) CO line flux, 2) far-infrared dust SED, and 3) 1 mm dust photometry. Based on their composite findings, they established a single multidimensional unified scaling relation given by

$$\log(M_{\text{H}_2}) = [A + B \times (\log(1 + z) - F)^2 + C \times \log(\delta MS) + D \times (\log M_* - 10.7)] + \log(M_*), \quad (3.3)$$

where,  $A$ ,  $B$ ,  $C$ ,  $D$ , and  $F$  are proportionality constants reported in Table(3b) of [Tacconi et al. 2018](#),  $MS$  is the main sequence (MS) relation of star-forming galaxies (see, [Speagle et al., 2014](#)), and  $\delta MS$  is the offset from  $MS$  line. In detail,  $\delta MS = sSFR/sSFR(MS; z, M_*)$ , where  $sSFR$  is total specific SFR that is computed as  $sSFR = (SFR_{H\alpha}^{int})/M_*$ , where

$SFR_{H\alpha}^{int}$  is the dust reddening-corrected  $H\alpha$  SFR. In this work the quantity  $SFR_{H\alpha}^{int}$  is derived by following the procedure of [Stott et al. \(2016\)](#); for details see Section 3.2.1.6. The quantity  $sSFR(MS; z, M_*)$  is the specific SFR defined by [Speagle et al. \(2014\)](#) and can be computed as follows:

$$\log(sSFR(MS; z, M_*)) = (-0.16 - 0.026 \times t_c) \times (\log M_* + 0.025) - (6.51 - 0.11 \times t_c) + 9, \quad (3.4)$$

where  $t_c$  is the cosmic time, given by

$$\log(t_c [Gyr]) = 1.143 - 1.026 \times \log(1+z) - 0.599 \times \log^2(1+z) + 0.528 \times \log^3(1+z). \quad (3.5)$$

The full derivations of  $M_{H2}$  and  $MS$  of galaxies at different redshifts are explained in greater detail in [Tacconi et al. 2018](#) and [Speagle et al. \(2014\)](#), respectively. The galaxies in our sample follow the relation between star formation rate and stellar mass given by [Speagle et al. \(2014\)](#), the so-called main sequence, with the following range of the relevant quantities: redshifts  $0.77 \leq z \leq 1.04$ , stellar masses  $9.0 \leq \log(M_* [M_\odot]) \leq 10.97$ , and SFRs  $0.49 \leq \log(SFR [M_\odot \text{ yr}^{-1}]) \leq 1.77$  (see Figure 3.1). Therefore, using the equation [3.3], we estimated the molecular gas mass of our galaxies.

### 3.2.1.8 Atomic Gas Masses

Observation of atomic hydrogen (HI) is challenging and can only be done in the radio wavelength by mapping the 21 cm fine-structure emission line produced by the spin-flip transition of the electron in the H atom. Currently, we cannot observe the 21 cm line at high-redshift, but with next-generation radio telescopes (e.g., ASKAP: [Johnston et al. 2008](#); [McConnell et al. 2016](#) and [Bonaldi et al. 2021](#)) this should become possible in the near future. At present, the HI gas mass is typically inferred through the spectra of quasars ([Péroux et al., 2003](#); [Prochaska et al., 2005](#); [Rao et al., 2006](#); [Guimarães et al., 2009](#); [Noterdaeme et al., 2012](#); [Krogager et al., 2013](#); [Moller et al., 2018](#), and reference therein), and scaling relations based on these observations and simulations. In our work, we use the scaling relation given by [Lagos et al. \(2011\)](#) for the atomic gas mass as follows:

$$M_{HI} = \frac{M_{H2}}{0.01} \left( \frac{10^{10} h^{-1} M_\odot}{M_*} \right)^{0.8} (1+z)^{-3.3}. \quad (3.6)$$

The above relation agrees well with the global density of atomic and molecular hydrogen derived from damped Ly- $\alpha$  observations ([Péroux et al., 2003](#); [Rao et al., 2006](#); [Noterdaeme et al., 2009](#)) and predicts the H<sub>2</sub> and HI mass function in the local Universe ([Zwaan et al., 2005](#); [Martin et al., 2010](#)). Moreover, the Equation 3.6 agrees very well with the scaling relation provided by a recent study of [Calette et al. \(2018\)](#) and DustPedia late-type galaxies ([Casasola et al., 2020](#)). Therefore, we use this relation to determine the HI masses of our sample. However, we emphasize that the  $M_{HI}$  computed using Equation 3.6 gives the mass of the atomic gas, which corresponds to the scale of the molecular gas. In the outskirts of galaxies,  $M_{HI}$  is most likely different.

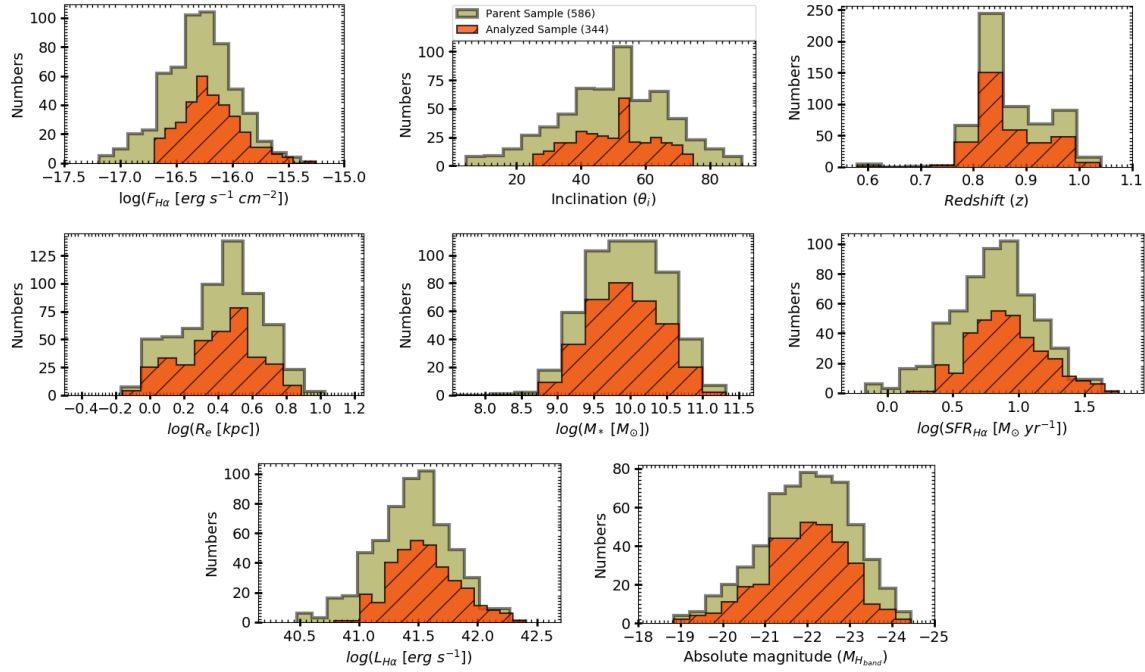


**Figure 3.2:** The distributions of physical quantities of parent and analysed sample. The color code is same in all the panels and given as follows, the parent KROSS sample (given by Harrison et al. 2017) shown by the green histograms and the analysed sample by orange hatched histogram. The *upper row* first & second panel represents the  $F_{H\alpha}$  and  $\theta_i$  distribution, which verifies our sample selection cuts, the *third panel* shows the redshift ( $z$ ) distribution, which justify that we are working with  $z \sim 1$  galaxies. The *middle row* first panel demonstrate the size distribution of our analysed sample, and second and third panel shows the distribution of stellar masses and  $H\alpha$  based star-formation rate (SFR), these distributions are informative of main sequence at  $z \sim 1$ . The *bottom row* shows the brightness distribution of the sample in terms of  $H\alpha$  luminosities ( $L_{H\alpha}$ ) and H-band absolute magnitude ( $M_H$ ).

**Resume:** The parent sample is selected in such a way that it does not preferentially contain galaxies in a merging or interacting state, and include good representatives of main sequence star-forming galaxies at  $z \sim 1$  (see Stott et al., 2016, and references therein). To reaffirm, we present the distributions of the physical quantities of parent sample and analysed sample, shown in Figure 3.2. The final analysed sample selected for this study is representative of the parent sample from Harrison et al. (2017) and, therefore, is representative of main sequence, star-forming galaxies at this redshift. Quantitatively, our analysed sample of star-forming galaxies covers the following range of physical parameters:  $H\alpha$  flux:  $-16.70 \leq \log(F_{H\alpha} [\text{erg s}^{-1} \text{cm}^{-2}]) \leq -15.26$ , the inclination angle:  $25^\circ \leq \theta_i \leq 75^\circ$ , the redshift:  $0.75 \leq z \leq 1.04$ , the effective radii:  $-0.16 \leq \log(R_e [\text{kpc}]) \leq 0.89$ , the stellar mass:  $8.79 \leq \log(M_* [\text{M}_\odot]) \leq 11.32$ , the star formation rate:  $0.15 \leq \log(SFR_{H\alpha} [\text{M}_\odot \text{yr}^{-1}]) \leq 1.76$ , the molecular gas mass:  $8.97 \leq \log(M_{\text{H}_2} [\text{M}_\odot]) \leq 10.34$ , and the atomic gas masses:  $8.20 \leq \log(M_{\text{HI}} [\text{M}_\odot]) \leq 9.45$ .

### 3.2.2 Kinematic Modelling with ${}^3D$ BAROLO

We have modelled the kinematics of our sample using the  ${}^3D$ BAROLO code (Teodoro & Fraternali, 2015). The main advantage of modelling the datacube with  ${}^3D$ BAROLO (3DBarolo): (1) it allows us to reconstruct the intrinsic kinematics in 6-domain (three spatial and three velocity components) for given initial conditions; (2) the 3D projected modelled datacube is compared to the observed datacube in 3D-space; (3) it simultaneously incorporates the instrumental and the observational uncertainties (e.g., spectral-smearing<sup>7</sup> and beam-smearing<sup>8</sup>) in 3D-space. For details, we refer the reader to Teodoro & Fraternali (2015) and Di Teodoro et al. (2016). This 3-fold approach of deriving kinematics is designed to overcome the observational and instrumental effects and hence allows us to stay close to the realistic conditions of the galaxy. Therefore, it gives us somewhat improved results than the 2D-approach of kinematic modelling on the datacubes, specifically, in the case of small angular sizes and moderate S/N of high-redshift galaxies (see Di Teodoro et al. 2016). In the section below, we have discussed the 3DBarolo's underlying assumptions, its initial requirements for performing the kinematic modelling, and the very first results/tests on a large dataset.

#### 3.2.2.1 Basic Assumption

3DBarolo is based on the ‘tilted ring model,’ i.e. the motion of the gas and stars are assumed to be in the circular orbits. It does not assume any functional evolution of the kinematic quantities (e.g.  $v_{rot}(R) \propto \arctan(R)$ ). Therefore, free parameters in 3DBarolo are not forced to follow any parametric form, rather estimated in the annuli of increasing distance from the galaxy centre without making any assumption on their evolution with the radius. However, 3DBarolo uses the radial binning for the velocity measurement, because in the ‘tilted ring model’, a galaxy is divided into several rings and parameters are calculated within each ring. The number of pixels used per bin depends on the choice of NRADII<sup>9</sup> and RADSEP<sup>10</sup> in the fitting. Therefore, each position-velocity (PV) diagrams contains  $\sim 3 - 6$  rotation velocity measurements (and similarly for the velocity dispersion). The errors on velocity measurement per radial bin (inside 3DBarolo) are estimated using Monte Carlo sampling.

A non-parametric approach of calculating kinematic parameters, makes 3DBarolo robust and reliable to use, and this is one of the reasons we are using it for kinematic modelling. As mentioned earlier in Chapter 2, there are other high-redshift 3D-kinematic modelling codes, e.g., GalPak 3D (Bouché et al., 2015), which has been successfully tested on  $z \sim 0.5$  galaxies observed from the Multi-Unit Spectroscopic Explorer (MUSE) but it follows the parametric approach and BLOBBY3D (Varidel et al., 2019), which has been tested on 20 local star-forming galaxies from the SAMI Galaxy Survey. It is a useful tool to study the gas dynamics of high-redshift low-resolution data. However, it comes with

<sup>7</sup>line spread function (LSF) which corresponds to spectral broadening

<sup>8</sup>the point spread function (PSF) which determines the spatial resolution

<sup>9</sup>Number of rings used in fitting the galaxy

<sup>10</sup>Separation between rings in arcsec

a long list of free parameters, which one may not know without a detailed study of the system and will be particularly degenerate for lower S/N data available for high redshift systems.

### 3.2.2.2 Initial Requirements

The kinematic modelling with 3DBarolo requires three geometrical parameters, i.e. the coordinates of galactic centre in the datacube ( $x_c, y_c$ ), the inclination angle ( $\theta_i$ ), the position angle ( $PA$ ), and three kinematic parameters, i.e. the redshift ( $z$ ), the rotation velocity ( $v_{rot}$ ) and the velocity dispersion of ionized gas ( $\sigma_{H\alpha}$ ). In our modelling, we fix the geometrical parameters and redshift (with an exception for  $PA$ , discussed below) and leave the two kinematic parameters free. Notice,  $(x_c, y_c)$  are the photometric galactic centre positions adopted from H17. 3DBarolo comes with several useful features particularly necessary/useful for high-redshift low S/N data (see 3DBarolo documentation<sup>11</sup>). We are using 3DFIT TASK for performing the kinematic modelling. First, 3DBarolo produces the mock observations on the basis of given initial conditions in the 3D observational space  $(x, y, \lambda)$ , where  $(x, y)$  stands for the spatial axes and  $\lambda$  is spectral axis coordinate. These models are then fitted to the observed datacube in the same 3D-space accounting for the beam smearing simultaneously. A successful run of 3DBarolo delivers the beam smearing corrected moment maps, the stellar surface brightness profile, the rotation curve (RC), and the dispersion curve (DC) along with the kinematic models. Notice, rotation curves (PV-diagrams) are not derived from the velocity maps, instead they are calculated directly from datacubes by minimizing  $V_{LOS} = V_{rot} \sin \theta_i$  (of model and data). 3DBarolo is well tested on the local systems (e.g., [Teodoro & Fraternali, 2015](#); [Korsaga et al., 2019](#)) as well as on high-redshift galaxies including the KMOS data (see: [Di Teodoro et al., 2016](#); [Loiacono et al., 2019](#)).

The position angle ( $PA$ ) is usually fixed to the photometric  $PA$  adopted from the H17 catalog, but for  $\sim 44\%$  of objects,  $PA_{phot}$  doesn't allow to extract position-velocity diagram. This might be a consequence of misaligned morphological and kinematic major-axis, that result in unalike photometric and kinematic position angles,  $PA_{phot}$  and  $PA_{kin}$ , respectively. In this situation, if we use  $PA_{phot}$  to infer the kinematics, we spot an asymmetry in PV-diagram. Therefore we decided to free the  $PA$  parameter in 3DBarolo-run particularly for these 44% objects. An example of kinematic modelling using  $PA_{phot}$  (when it is wrong) and  $PA_{kin}$  is shown in Figure 3.3. *upper panel* shows the kinematics and rotation curve derived using  $PA_{kin}$ , whereas *lower panel* shows the kinematics and rotation curve derived from fixed  $PA_{phot}$ . We can see that PV-diagrams derived from fixed  $PA_{phot}$  are asymmetric around  $x$  and  $y$ -axis, while this problem resolved if the  $PA$  is set to free in 3DBarolo run. We are not keeping  $PA$  free for all objects because 3DBarolo documentation suggests to 'keep the number of free parameters low, specifically in low-resolution data'.

<sup>11</sup><https://bbarolo.readthedocs.io/en/latest/>

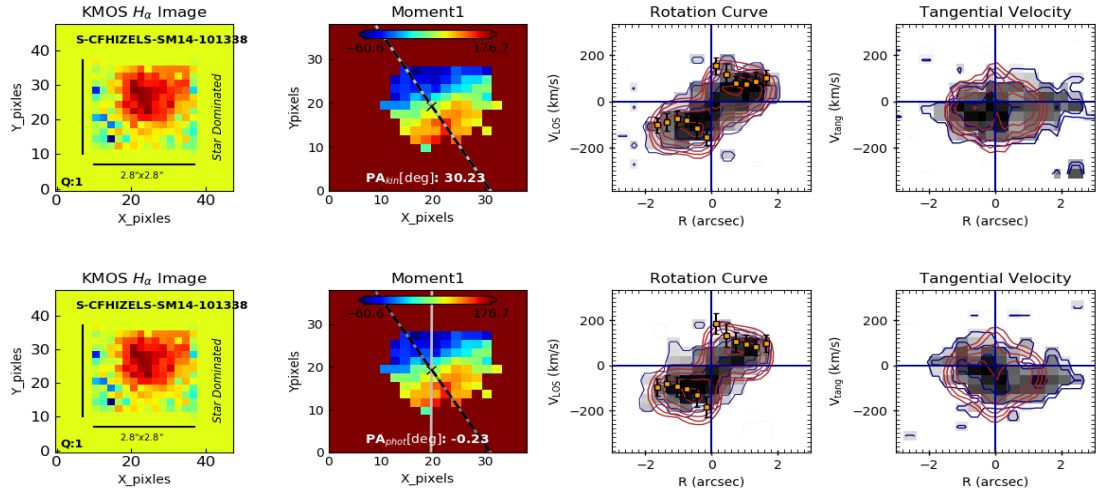


**Figure 3.3:** *Upper Panel:* Kinematic modelling using  $PA_{kin}$ . *Lower Panel:* Kinematic modelling performed using  $PA_{phot}$ . *COL 1:* Integrated  $H_{\alpha}$ -image from 3D datacube; *COL 2:* Rotation velocity map, where  $PA_{kin}$  is shown by dotted dashed black-grey line, and  $PA_{phot}$  is shown by solid grey line; *COL 3:* LOS rotation velocity curve; *COL 4:* Tangential velocity profile. In the PV-diagrams, the black shaded area with blue contour represents the data, the red contour is model, and orange squares with error bars are best-fit velocity measurements.

### 3.2.2.3 Limitations

To obtain a good fit 3DBarolo requires a mask to identify the true emission region and to ignore the noisy pixels. For this purpose, we use the in-built **MASK** task with an input of either **SEARCH** or **NEGATIVE** masking. In particular, the **SEARCH** mask uses the source finder algorithm **DUCHAMP** (Whiting, 2012) and hence builds a mask on the identified emission regions based on 3D reconstructed sources. This mask works very well on high S/N (clean) data if noise is Gaussian distributed among the channels. However, when the noise does not follow a Gaussian distribution, then the **SEARCH** task is unable to find the source. In this situation, we have used the **NEGATIVE** mask. It computes the noise statistics ( $\sigma_{noise}$ ) channel by channel, using only pixels with negative values, then build the mask in regions of  $flux > (1.5 - 2.5) \sigma_{noise}$ . Notice, noise in negative pixels are often more Gaussian-distributed than positive pixels, especially in low S/N KMOS data, and hence returns a better estimate of noise properties.

Notice that fully exploiting the 3<sup>rd</sup> (velocity) dimension is still a caveat in the 2D/3D kinematic modelling of high-redshift galaxies. However, we suggest that 3D-forward modelling has a potential to provide better results than applying models to fit to 2D or 1D projections of the datacube, because it uses the full information available inside the datacube. We remark (see also Teodoro & Fraternali, 2015) 3DBarolo corrects well for beam smearing whenever a galaxy is resolved with at least 2-3 resolution elements across and has a  $S/N \gtrsim 3$ . The relative errors are within 20% for the rotation curve and within a factor 2 for the velocity dispersion, in the worst cases.

The errors on the data are estimated during the fitting procedure, the algorithm

weights pixels based on their S/N, i.e. a pixel with a high S/N is considered more reliable and given more weight than a pixel with low S/N. The noise level is calculated directly from emission-free regions of the datacube using robust statistics (median and absolute deviation from the median). Notice, 3DBarolo's current error-estimation algorithm does not account for intrinsic uncertainties in the data. However, we minimised the impact of these effects by a careful selection/analysis of sub-sample (see Section 3.2.1 & 3.2.2.4).

Finally let us remark, extinction is complex to account in the 3D modelling therefore, it is not accounted in 3DBarolo. However, extinction is important in inner region of galaxies, where high-z galaxies are not resolved. At least in our sample, we do not have resolution within  $\sim 2$  kpc, where extinction dominates. In particular we do not draw any conclusions about the inner parts of the rotation curves (see Section 4.2.2). Nevertheless, 3DBarolo's performance has been extensively tested on optical/NIR data (e.g. KROSS, KMOS<sup>3D</sup> [Teodoro & Fraternali 2015](#); [Di Teodoro et al. 2016](#); [Korsaga et al. 2019](#); [Loiacono et al. 2019](#)), where it delivers remarkable results. Therefore, we expect 3DBarolo to perform well on our sample too; however, results are critically analysed and discarded whenever required (see Section 3.2.2.4).

### 3.2.2.4 Results

The analysed sample was selected on the basis of the  $H_{\alpha}$  emission line flux cut ( $F_{H_{\alpha}} > 2 \times 10^{-17}$  [erg s<sup>-1</sup> cm<sup>-2</sup>]), the inclination angle cut ( $25^{\circ} \leq \theta_i \leq 75^{\circ}$ ), and the S/N ( $> 3$ ) of the  $H_{\alpha}$  detection. After executing 3DBarolo, we have visually inspected the 3DBarolo-outputs for quality assessment. We noticed that the best quality outputs correspond to objects with the inclination  $45^{\circ} \leq \theta_i \leq 75^{\circ}$  where kinematics is derived using the **SEARCH** mask. On the other hand, worse quality is often spotted for relatively low inclination ( $\theta_i < 45^{\circ}$ ) along with use of the **NEGATIVE** mask. Moreover, as per the limitations of 3DBarolo, objects with low S/N and  $\theta_i < 45^{\circ}$  might be being considered as background galaxy emission, which may lead to over/underestimated rotation velocity or velocity dispersion. Therefore, to classify the quality of the galaxies, we have taken into account the S/N per pixel in the masked region, limitations of 3DBarolo and the participation of the mask (which gives us a direct indication of the noise level). Hence, we have assigned the quality of 3DBarolo outputs as the following:

1. **Quality-1:**  $45^{\circ} < \theta_i \leq 75^{\circ}$  with **SEARCH** mask and  $S/N > 3$  in masked region.
2. **Quality-2:**  $30^{\circ} \leq \theta_i \leq 75^{\circ}$  with **SEARCH** or **NEGATIVE** mask and  $S/N \geq 3$ .
3. **Quality-3:** the remaining objects.

An example of a visual representation of the Quality-1, 2, & 3 objects is shown in Figure 3.4. In total, we have 120 Quality-1, 194 Quality-2 and 30 Quality-3 objects. The Quality-3 galaxies are discarded from the rotation curve analysis. We would remark, [Teodoro & Fraternali \(2015\)](#) have tested the performance of 3DBarolo on simulate data in terms of S/N, spatial/spectral resolution, and galaxy properties. They have shown that the code works well when most of the emission has  $S/N \gtrsim 3$  and for inclination

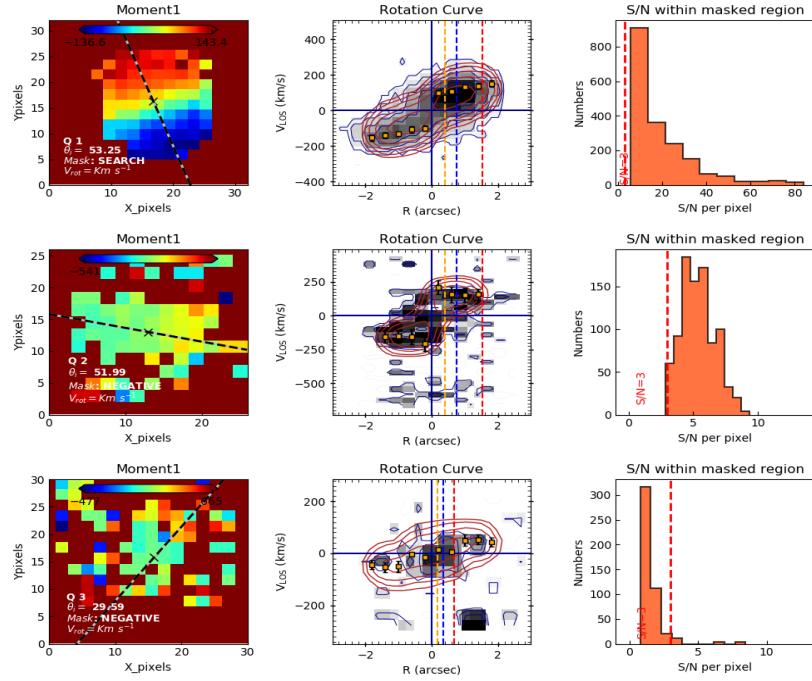


**Figure 3.4:** A visual representation of the quality assessment of 3DBarolo outputs. The Upper, middle and bottom row represents the Quality-1, Quality-2 & Quality-3 galaxies respectively. *COL 1:* First moment map, black-grey dashed line is showing the position angle, and the black cross shows the galactic centre  $(x_c^p, y_c^p)$ . *COL 2:* Rotation curve, the black shaded area with blue contour shows the data while the red contour refers to the model and the orange squares with error bars are the best-fit velocity measurements. The yellow, blue and red vertical dashed lines are representing the effective radius ( $R_e$ ), optical radius ( $R_{opt} = 1.89 R_e$ ), twice optical radius ( $R_{out}$ ) respectively. *COL 3:* Distribution of S/N in masked region of datacube. The vertical red dashed line shows the  $S/N = 3$ .

$30^\circ \leq \theta_i \leq 75^\circ$ . All of our Quality-1 & Quality-2 objects (Q12 sample) abide these criteria, except nine galaxies those inclined between  $25^\circ < \theta_i < 30^\circ$  but contain  $S/N > 3$  per pixel. For the satisfaction of reader (and cross check), we attach the plots of S/N per pixel of the analysed sample in the external appendix of [Sharma et al. \(2021b\)](#).

As we mentioned in the Section 3.2.2.2, nearly 44% of analysed sample have  $PA_{phot} \neq PA_{kin}$ . This discrepancy in the position angles can affect our results in two ways: (1) uncertain inclination angle because inclination is derived using photometric axis ratio, which is used in computing  $PA_{phot}$  too (see Section 3.2.1) and (2) presumably misaligned systems are not in disc configuration, which is worrisome. Therefore, we quantitatively explored the misalignment in the Q12 sample. Following [Wisnioski et al. \(2015\)](#) we define the misalignment between photometric and kinematic position angle as:

$$\sin \psi = |\sin(PA_{phot} - PA_{kin})| \quad (3.7)$$

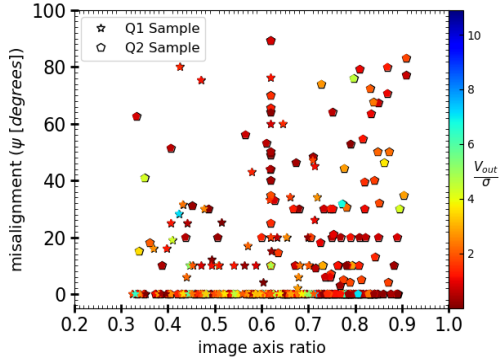


**Figure 3.5:** The difference between the photometric and kinematic position angles ( $\psi$ ) as a function of broad-band image axis ratio. The stars and hexagons represents the Q1 and Q2 sample respectively, color coded for  $v/\sigma$ . Nearly 3.5% Q1-sample and 13.3% Q2-sample have misalignment more than  $\psi > 30^\circ$ . Overall 83% Q12-sample have good position angles measures (i.e.,  $PA_{\text{phot}} \simeq PA_{\text{kin}}$ ) which places confidence on our measurements.

by misalignment.

In Figure 3.6, we have shown a few examples of 3DBarolo outputs. From left to right, the broad-band high-resolution image, the  $H_\alpha$ -image, the first-moment (rotation velocity) map, the second-moment (dispersion velocity) map, the rotation curve, and the dispersion curve. In detail, COL 1: the broad-band image is constructed from the ground and the space-based photometric observational data (discussed in Section 3.1.1). The central photometric coordinate (galactic centre:  $(x_c^p, y_c^p)$ ) of the object is shown by a black cross, which is calculated by fitting the 2D Gaussian to the 2D distribution of the data. The size of each image can be inferred in terms of  $10 \times 10$  pixel size, converted to arcsec (displayed on the bottom left of the image). The size of the broad-band images varies from image-to-image due to the multi-wavelength data and different photometric surveys. COL 2: the integrated  $H_\alpha$ -image constructed from the KMOS datacube. The size of the image is displayed in arcsec by drawing the horizontal and the vertical black line. The name of the galaxy is displayed in the upper-left corner, and the quality displayed in the lower-left corner. COL 3,4: Moment-1 map and Moment-2 map, these maps are the output of the 3DBarolo kinematic modelling. The black-grey dashed line shows the position angle of the image. The black cross represents the galactic centre positions adopted from the work of Harrison et al. (2017). COL 5,6: the rotation curve (RC) & the dispersion curve (DC), constructed after a comparison of the data and the model in 3D-space (an output of 3DBarolo). In the rotation curve, the red contour is the model and the black shaded area with the blue contour represents the data. The orange squares

where  $\psi$  gives the misalignment and lies between  $0^\circ$  to  $90^\circ$ . If  $\psi > 30^\circ$  than morphologies are considered irregular. Figure 3.5, shows the  $\psi$  as a function of image axis ratio, where axis-ratios are derived using broad-band images (for details see Harrison et al. 2017). We notice,  $\sim 40\%$  objects of Q12-sample are misaligned, in which only  $\sim 17\%$  objects have  $\psi > 30^\circ$  (which includes  $\sim 3.5\%$  Q1-sample and  $\sim 13.3\%$  Q2-sample). We notice low  $v/\sigma$  galaxies are highly misaligned, most likely due to lack of well defined kinematic axis. Despite the different kinematic modelling approaches, our misalignment results are similar to Harrison et al. (2017). Moreover, majority ( $\sim 83\%$ ) of our sample used in rotation curve analysis (Q12 sample), have  $PA_{\text{phot}} \simeq PA_{\text{kin}}$  which places confidence on our measurements. Besides this, we provide a statistical study of rotation curves which encompass any uncertainties caused

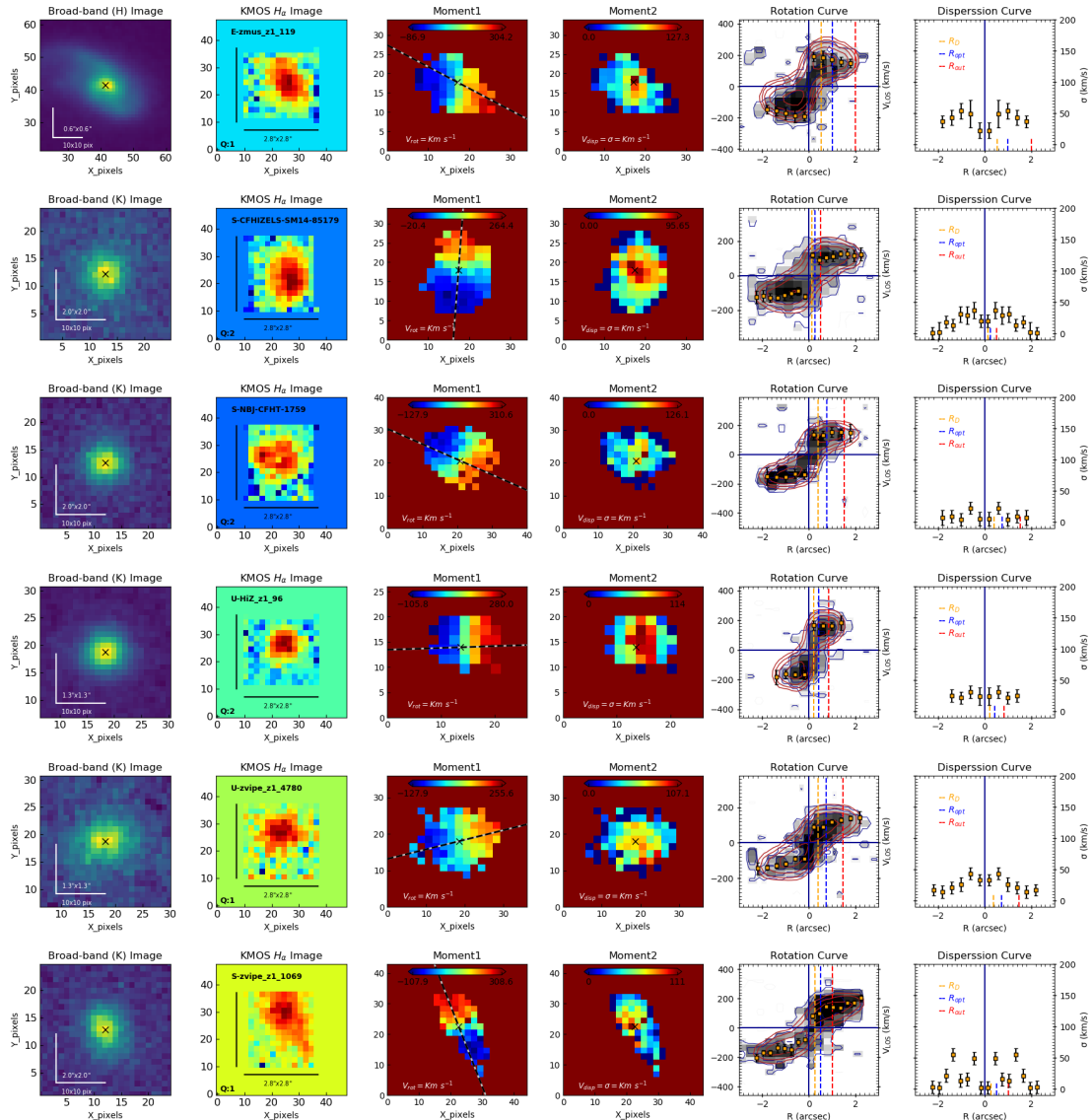


**Figure 3.6:** The outputs of the kinematic modelling using  $^{3D}$ BAROLO. *COL 1*: Broad-band image, where black cross shows the central coordinates of the photometric image. The horizontal and the vertical white lines in the lower-left corner are showing the  $10 \times 10$  pixel size in arcsec (an estimator of image-size). *COL 2*: Integrated  $H_{\alpha}$ -image from datacube, the size of the image is shown by the black horizontal and the vertical lines. The name of the galaxy is shown in the upper-left corner, and quality is mentioned in the lower-left corner. *COL 3-4*: the first and second-moment map, the black-grey dashed line is showing the position angle, and the black cross represents the galactic centre. *COL 5*: Rotation curve, the black shaded area with blue contour represents the data while the red contour shows the model and the orange squares with error bars are the best-fit rotation velocity measurements. *COL 6*: the best-fit velocity dispersion. The yellow, blue, and the red vertical dashed lines are representing the effective radius ( $R_e$ ), the optical radius ( $R_{opt} = 1.89 R_e$ ), twice the optical radius ( $R_{out} = R_{2opt} = 3.78 R_e$ ) respectively. Notice that the first data point in rotation curves and dispersion curves is within resolution limit, therefore excluded from the analysis.

with error bars are the best-fit rotation velocity (referred to as ‘rotation curve data’) and velocity dispersion. The yellow, blue, and red vertical dashed lines are representing the effective radius ( $R_e$ ), the optical radius ( $R_{opt} = 1.89 R_e$ ), and twice the optical radius ( $R_{out} = R_{2opt} = 3.78 R_e$ ) respectively. The size of the  $H_\alpha$ -image is always  $2.8 \times 2.8$  arcsec, so are the spatial length of the moment maps, rotation and the dispersion curve. In some cases, even though  $R_e$  is  $1.6 \text{ kpc}$  (i.e.  $0.2 \text{ arcsec}$ ), rotation curves are extended more than  $16 \text{ kpc}$  (i.e.  $2.0 \text{ arcsec}$ ) due to the fact that  $H_\alpha$ -emission can trace the light up to large radius in comparison to broad-band filters. A full version of Figure 3.6 is attached in the external appendix of paper [Sharma et al. \(2021b\)](#). Notice, 3DBarolo estimates the errors using Monte Carlo sampling, which are plotted on rotation curves and DCs in Figure 3.6. In further analysis we consider symmetric errors on RC/DC data, since parameter space is very much Gaussian distributed. However, to be precise, we take root mean square of upper and lower bounds of 3DBarolo estimated errors.

### 3.2.3 Pressure Gradient Correction (PGC)

A significant amount of the 3DBarolo generated rotation curves show a strong asymmetry and rapid fall in the inner region as well as in the outskirts of the galaxy, see Figures 3.7 & 3.8 orange data-points (also check left panel of Figure 4.4). Such a rise and fall could be either due to the low dark matter fraction or, it could be an impact of pressure support (e.g., [Genzel et al. 2017](#)). The latter is observed in local dwarfs and early-type galaxies (e.g., [Valenzuela et al. 2007](#); [Weijmans et al. 2008](#); [Read et al. 2016](#)), which noticeably suppresses the rotation velocity of the gas. In short, if the ISM is highly turbulent (like in high-redshift galaxies [Burkert et al. 2010](#); [Turner et al. 2017](#); [Johnson et al. 2018](#); [Übler et al. 2019](#); [Wellons et al. 2020](#)), then the pressure gradient induces a force against gravity, which supports the disc against gravity and keeps it in kinematic equilibrium by hampering its rotation velocity. This situation is negligible in local rotation-dominated systems, but the same is not valid for high-redshift galaxies. Mainly, in the case of the dynamical mass modelling of high-redshift galaxies, it is very crucial to disentangle the pressure support; otherwise, one might lead to wrong estimates of baryonic and dark matter components.

To correct the rotation velocities for the pressure support, we consider a spherically symmetric rotating galaxy. We assume that along the radial direction stars is in jeans equilibrium and gas is in hydrostatic equilibrium ([Jeans, 1915](#); [Binney & Tremaine, 2008](#)). Under this assumption, circular velocity ( $V_c$ ) of the galaxy at any radius ( $R$ ) can be written as:

$$V_c^2(R) = V_\phi^2(R) - \frac{d(\ln \rho(R) \sigma_R^2(R))}{d \ln R} + \left(1 - \frac{\sigma_\phi^2}{\sigma_R^2}\right) \quad (3.8)$$

where  $V_c(R) = \sqrt{GM(< R)/R}$ . The first term in the right hand of the equation is observed rotation velocity  $V_\phi$  (corrected for inclination). The middle term is giving the pressure support (which could be due to stars and gas or both ), where  $\rho(R)$  is the 3D density, and  $\sigma_R(R)$  is intrinsic radial velocity dispersion. The last term includes the velocity anisotropies, where  $\sigma_\phi(R)$  is intrinsic azimuthal velocity dispersion. The

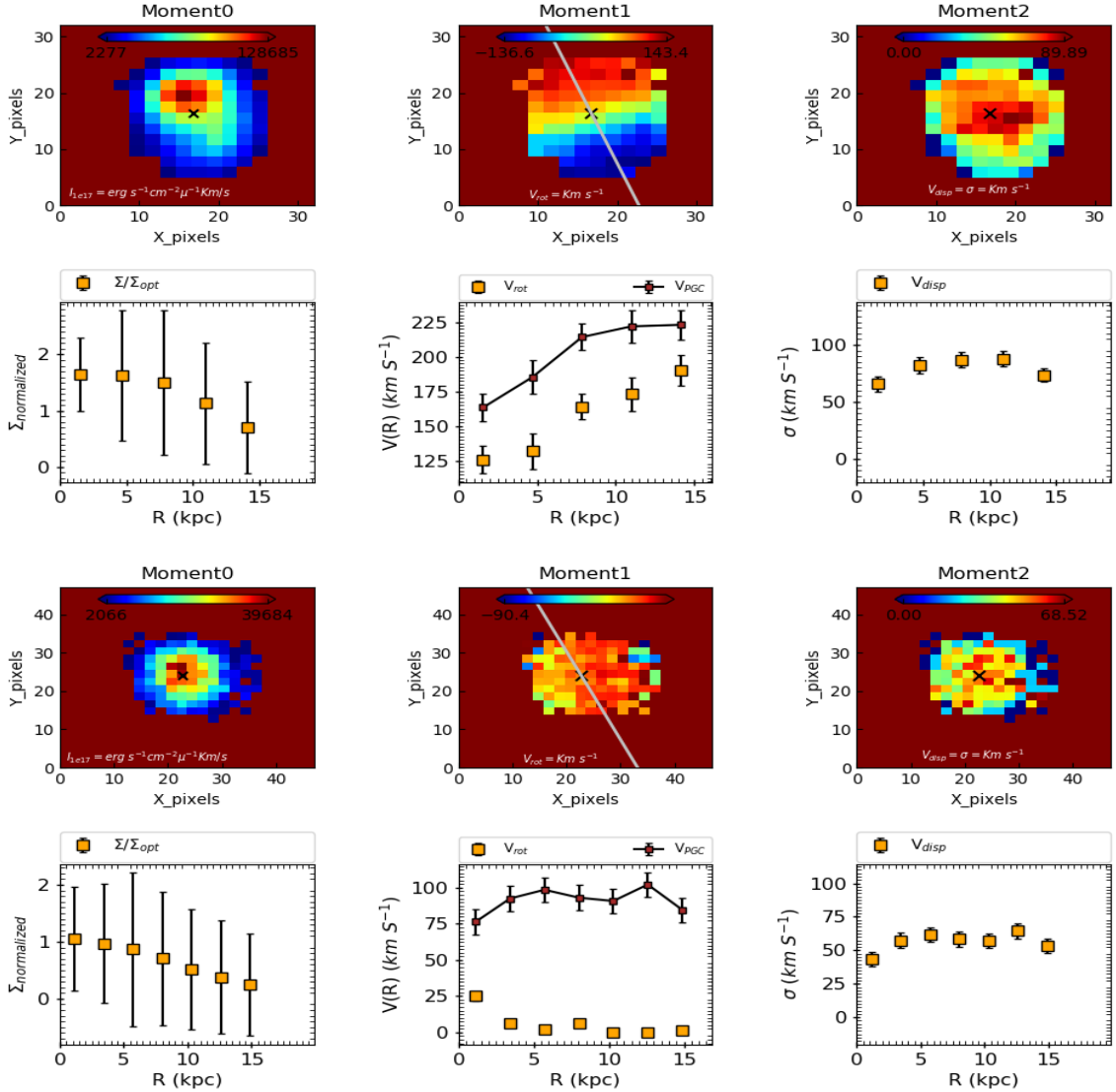


**Figure 3.7:** An example of PGC. *Upper panel:* left-to-right, zeroth, first, and second moment maps. *Lower panel:* left-to-right, the surface brightness, the rotation velocity, and the velocity dispersion. In the moment-1 map, the grey line is the photometric position angle and the black cross are the galactic kinematic center  $(x_c^k, y_c^k)$ . In the surface brightness profile and the P-V diagrams, the orange squares with error bars are best fit data. In the rotation curve profile, brown squares connected with the black line is PG corrected rotation velocity profile.

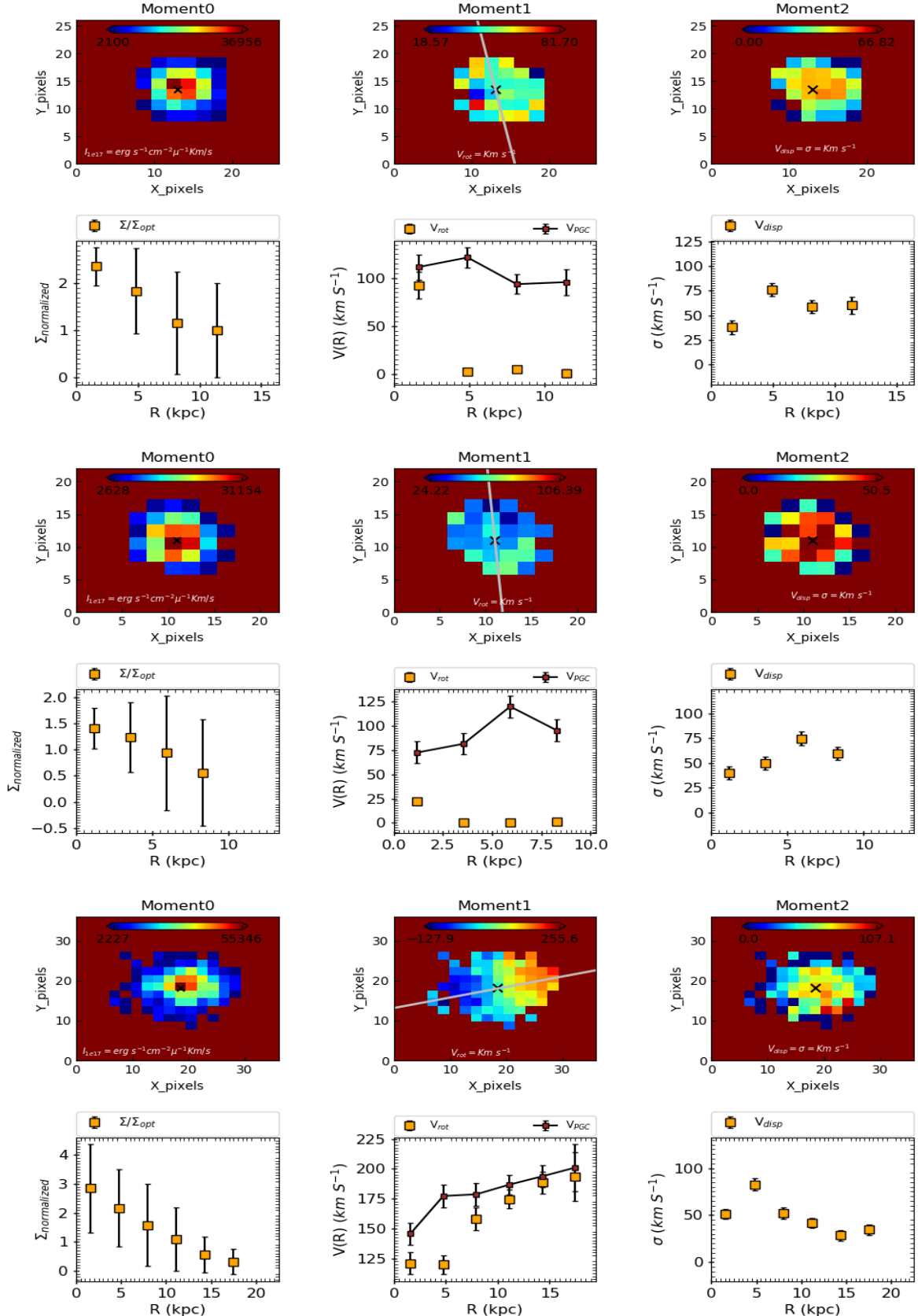


Figure 3.8: PGC examples continue..

Equation 3.8 is true for both, stellar and gas pressure, separately. In this work, we are employing Equation 3.8 for gas pressure support because stellar component of our dataset is not determined due to low signal-to-noise on stellar continuum. Moreover, in our work, we have generalized the Equation 3.8 for two special cases of self gravitating exponential disc (1) constant and isotropic velocity dispersion (see Section 3.2.3.1), and (2) non-constant and anisotropic velocity dispersion (see Section 3.2.3.2).

### 3.2.3.1 Case1: PGC with Constant and Isotropic Velocity Dispersion

Following Burkert et al. (2010), for a self-gravitating exponential disc in case of constant and isotropic velocity dispersion Equation 3.8 reduced to:

$$V_c^2(R) = V_\phi^2(R) - \sigma_0^2 \frac{d \ln \Sigma(R)}{d \ln R} \quad (3.9)$$

where velocity anisotropies are vanished and 3D density is reduced to surface density (Binney & Tremaine, 2008):

$$\rho(R) \rightarrow \Sigma(R) = 2 \rho_0(R) h(R) \quad (3.10)$$

where,  $\rho_0(R)$  is the density in the mid-plane ( $z = 0$ ) that can be derived from vertical hydrostatic Spitzer solution (Spitzer, 1942; Binney & Tremaine, 2008, section4), which is given as  $\rho_0(R) = \pi G \Sigma^2 / 2 \sigma_0^2$ . The  $h(R)$  is disc-scale height, for an exponential disc height increase exponentially with radius, given by:

$$h(R) = \frac{\sigma_0^2}{\pi G \Sigma_0} \exp\left(\frac{R}{R_D}\right) \quad (3.11)$$

where  $R_D = 0.59 R_e$  is the disc-scale length. On substituting Equation 3.10 & 3.11, Equation 3.9 give the Pressure Gradient Corrections (PGC) on rotation velocity as:

$$V_c^2(R) = V_\phi^2(R) - \sigma_0^2 \left( -2 \frac{R}{0.59 R_e} \right) \quad (3.12)$$

where last term in right hand side of the equation corrects for the pressure support, which we refer to as  $\alpha_{\text{self}} = 2\sigma_0 R / 0.59 R_e$ . For simplicity, the pressure corrected circular velocity in this case is denoted as  $V_{\text{PGC}}^{\text{B10}}$ .

### 3.2.3.2 Case2: PGC with Non-constant and Anisotropic Velocity Dispersion

For non-constant and anisotropic velocity dispersion, we follow Weijmans et al. (2008) by adopting their following Pressure Gradient Corrections (PGC):

$$V_c^2 = V_\phi^2 + \sigma_R^2 \left[ -\frac{\partial \ln \rho \sigma_R^2}{\partial \ln R} + \left(1 - \frac{\sigma_\phi^2}{\sigma_R^2}\right) \right] \quad (3.13)$$

where  $V_\phi$  is the inclination-corrected<sup>12</sup> rotation velocity,  $\rho$  is the density of gas,  $\sigma_R$  and  $\sigma_\phi$  are the intrinsic radial and vertical velocity dispersion respectively. Under the common assumption of a constant disc scale height the slope of the intrinsic 3D-density ( $\rho$ ) and 2D-surface density are the same; therefore,  $\rho$  can be replaced with  $\Sigma$ , where  $\Sigma$  is 2D-density<sup>13</sup> proportional to  $H_\alpha$  mass surface density. From the kinematic modelling of the datacubes (discussed in Section 3.2.2), we have required information about  $\Sigma$ ,  $\sigma_R$  and  $V_\phi$  to employ into the PGC. Let us remark, all the quantities (namely:  $V_\phi$ ,  $\sigma_R$ , and  $\Sigma$ ) are function of radius ( $R$ )<sup>14</sup>, and they are derived from  $H_\alpha$  datacubes.

In Equation 3.13, the second term ( $-\partial \ln \rho \sigma_R^2 / \partial \ln R$ ) gives the pressure gradient and the third term ( $1 - \sigma_\phi^2 / \sigma_R^2$ ) gives the velocity anisotropy. Often, it is assumed that the velocity dispersion is isotropic, so that  $\sigma_\phi = \sigma_R$ . However, here, we follow [Weijmans et al. \(2008\)](#) in which velocity anisotropy ( $1 - \sigma_\phi^2 / \sigma_R^2$ ) is given as  $(1 - \alpha)/2$ , where  $\alpha$  is the radial slope of the rotation velocity ( $\alpha = \partial \ln V_\phi / \partial \ln R$ ). Therefore, we do not need to limit our formalism to isotropic velocity dispersion. Finally, Equation 3.13 takes the form of:

$$V_c^2 = V_\phi^2 - \sigma_R^2 \left[ \frac{\partial \ln \Sigma}{\partial \ln R} + \frac{\partial \ln \sigma_R^2}{\partial \ln R} + \frac{1}{2}(1 - \alpha) \right] \quad (3.14)$$

where  $V_c$  is the pressure gradient corrected circular velocity, which for this case is denoted as  $V_c^{\text{W08}}$ . Although, we assume velocity anisotropy but this term has a small effect as it is sub-dominant with respect to the combined slope in the density and dispersion. However, the slope in neither density nor in dispersion can be ignored, especially, for high-redshift star-forming galaxies where interstellar medium is highly turbulent.

### 3.2.3.3 Comparison of Case1 and Case2

For local galaxies [Valenzuela et al. \(2007\)](#) presented a similar pressure gradient formalism as discussed in Case2 (section 3.2.3.2). However, simplistic form of pressure gradient given in Case1 (Section 3.2.3.1) also work very well for local galaxies [Dalcanton & Stilp \(2010b\)](#); [Read et al. \(2016\)](#); [Valenzuela et al. \(2007\)](#). Moreover, the latter is also used several times for high-redshift galaxies ([Genzel et al., 2017](#); [Lang et al., 2017](#)). Therefore, we decide to do a quantitative and qualitative comparison of Case1 and Case2 on BBarlo derived rotation curves.

Firstly, we compare the Shape of rotation curves, shown in Figure 3.9. Recalling that the circular velocity corrected for PGC in Case1 is denoted as  $V_{\text{PGC}}^{\text{B10}}$  and in Case2  $V_{\text{PGC}}^{\text{W08}}$ . In Case1 rotation curve are successively rising, and corrections are always applied even when they are not required. This is due to the constant  $\sigma$  and  $r/R_D$  pressure correction factor ( $\alpha_{\text{self}}$ ), which imposes the circular velocity to increase as a function of radius. On the other hand, Case2 uses the full information available in the datacubes, including the

<sup>12</sup>Inclination correction is required, to go from observed to intrinsic rotation velocity as well as to convert the observed velocity dispersion into the intrinsic radial dispersion in the general case of an anisotropic velocity distribution (see eq. A13 of [Weijmans et al. 2008](#)).

<sup>13</sup>In fact,  $\rho = \kappa \Sigma$ , where  $\kappa$  is constant with radius.

<sup>14</sup>i.e.,  $V_\phi = V_\phi(R)$ ,  $\sigma_R = \sigma_R(R)$ ,  $\Sigma = \Sigma(R)$ , and  $\alpha = \alpha(R)$

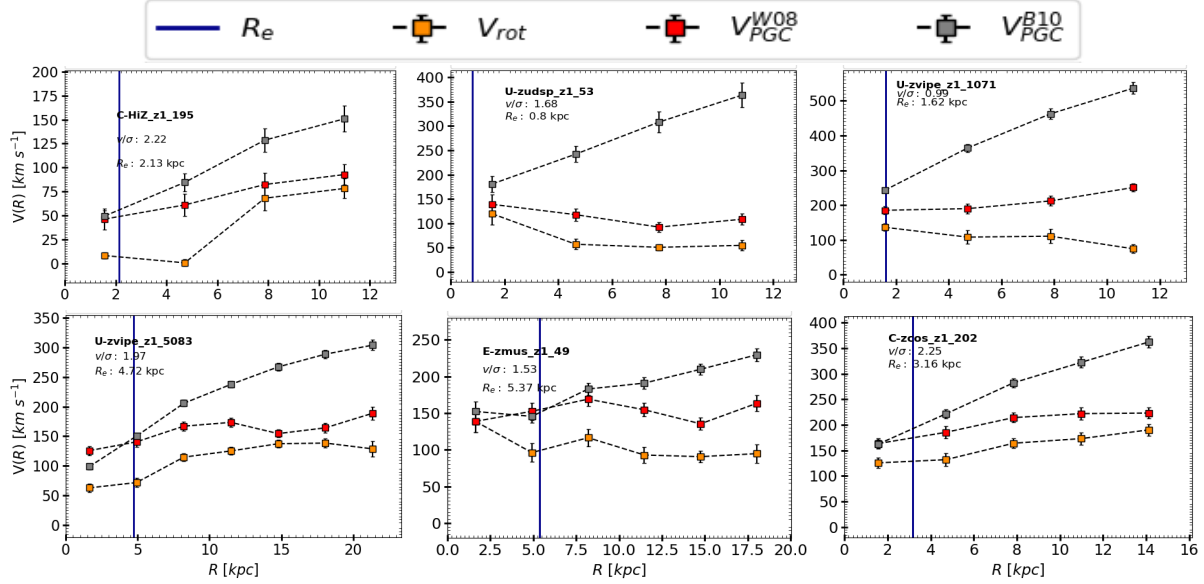


**Figure 3.9:** The Rotation curves before and after PGC using [Weijmans et al. \(2008\)](#) and [Burkert et al. \(2010\)](#) method. The yellow square represents the intrinsic rotation curve without PGC (denoted by  $V_{rot}$ ). The red and gray square shows the PG corrected rotation curves using [Weijmans et al. \(2008\)](#) and [Burkert et al. \(2010\)](#) method, denoted by  $V_{PGC}^{W08}$  and  $V_{PGC}^{B10}$  respectively. The vertical blue line shows the effective radius of the galaxy. The name,  $v/\sigma$  and  $R_e$  of galaxies are printed at upper-left corner of each plot.

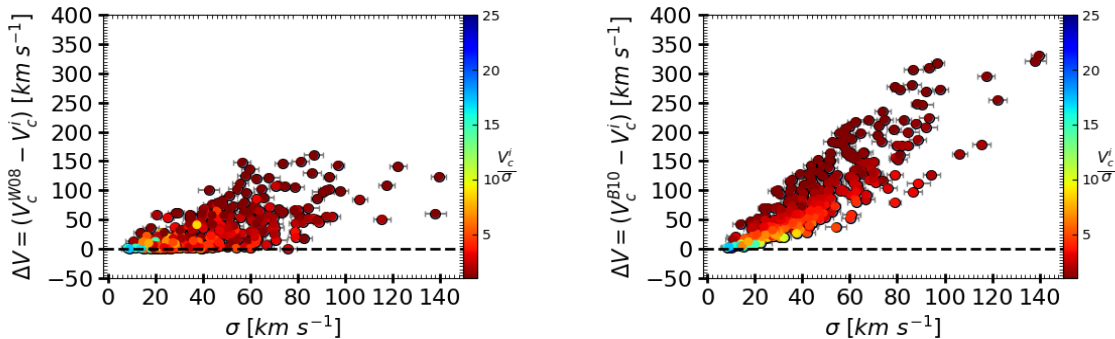


**Figure 3.10:** The comparison of correction factor ( $\Delta V = V_c^{PGC} - V_c^i$ ) on rotation velocities before and after the PGC, using [Weijmans et al. \(2008\)](#) and [Burkert et al. \(2010\)](#) method (left and right panel respectively). The correction factor is plotted as a function of velocity dispersion and data-points are color coded for  $V_c^i/\sigma$  (i.e.,  $v/\sigma$ ). The notation of circular velocities are given as follows,  $V_c^{W08}$  and  $V_c^{B10}$  denotes the PGC using W08 and B10 method respectively. Whereas  $V_c^i$  is the inclination corrected rotation velocity without PGC, computed at  $R_{out}$ . We notice, pressure correction using B10 method are on an average a factor of 2 higher than W08 method, which is also shown by [Kretschmer et al. \(2020\)](#).

radially varying surface-brightness, rotation velocity and velocity dispersion. This avoids the un-necessary radially growing circular velocity, as well as, the corrections are only applied if needed. Furthermore, In Figure 3.10, we have shown the amount of pressure support correction  $\Delta V = V_c^{PGC} - V_c^i$  (computed at  $R_{out} = 2.95 R_e$ ) in both cases as a function of velocity dispersion. We can see that the corrections are twice higher in Case1 method than case2, and unrealistically high in low  $v/\sigma$  galaxies.

Recently, based on high-resolution zoom-in cosmological simulation, [Kretschmer et al. \(2020\)](#) compared the pressure term of jeans/hydrostatic equilibrium ([Weijmans et al., 2008](#)) given by:

$$\alpha_{true} = -\frac{\partial \ln \rho \sigma_R^2}{\partial \ln R} + \left(1 - \frac{\sigma_\phi^2}{\sigma_R^2}\right) + \Delta Q$$

where, all the symbols have their usual meaning (as given in Section 3.2.3) and  $\Delta Q$  is non-spherical potential term, which we neglect in our work. On the other hand, pressure term in self-gravitating exponential disc ([Burkert et al., 2010](#)), given by:

$$\alpha_{self} = 2\sigma_0^2 \frac{r}{0.59 R_e}$$

[Kretschmer et al. \(2020\)](#) concluded that 1)  $\alpha_{self} = 2 \alpha_{true}$ , 2) pressure correction from non-isotropic and non-constant velocity dispersion are not negligible for gas within  $R = R_{e,gas}$ , and 3) pressure support correction derived from self-gravitating disc assuming constant velocity dispersion is not valid for high-redshift galaxies. In Figure[3.10], we clearly verify their findings. Moreover, since we do not know the exact distribution of gas in high-redshift. Therefore, we encouraged to avoid any prior assumption on gas component, whether it is related to turbulent pressure or effective radii of gaseous disc ( $R_{e,gas}$ ). Thus we followed pressure gradient correcting given by [Weijmans et al. \(2008\)](#), i.e. Case2. In Figures 3.7 & 3.8, we have shown a few examples of PGC in case-2 on rising and falling rotation curves. Notice, 3DBarolo generated rotation curves are corrected for pressure support while moment-1 maps are not.

### 3.3 Simulations

In addition to observations, we also analyse recent state-of-the-art hydrodynamical simulations. In the section below, I briefly describe the simulated dataset and sample selection as it studied at limited extent.

#### 3.3.1 Simulated Data

In last phase of my thesis, I have also analysed state-of-the-art galaxy simulations, EAGLE ([Schaye et al., 2015](#)) and IllustrisTNG ([Pillepich et al., 2018](#)). For the purpose of this paper, we select central galaxies from the simulations using friends-of-friends halo finder approach ([Davis et al., 1985](#)) and the SUBFIND algorithm ([Springel et al., 2001](#); [Dolag et al., 2009](#)). Gas and star particles are associated to the galaxy of their nearest

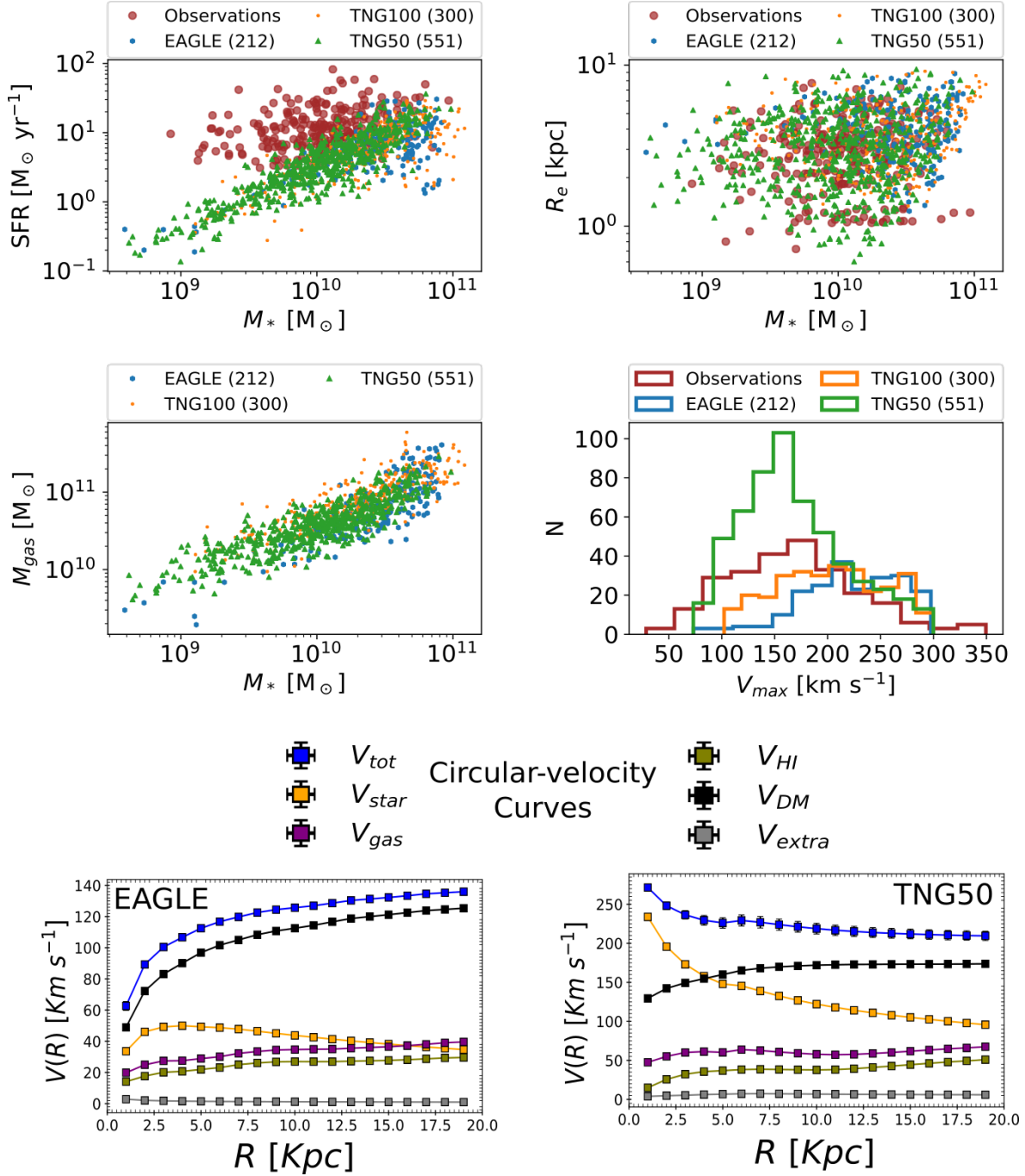


**Figure 3.11:** Comparison of physical parameters of simulations (EAGLE: blue dots; TNG100: orange stars; TNG50: green triangles) with observations (brown filled circles). The first row, *left panel*: Star formation rate as a function of stellar mass, so-called main sequence of star-forming galaxies; *right panel*: Effective radii of galaxies as a function of stellar mass, so-called mass-size relation. The second row, *left panel*: gas and stellar mass relations; *right panel*: Distribution of the maximum circular velocity of the simulated sample compared to  $V_{\text{out}} = V_c$  of the observations. The third (bottom row) shows the example of circular velocity curves from EAGLE and TNG50 simulation, left and right panel, respectively.

neighbouring dark matter particle if belongs to one, and if they are gravitationally bound to the object. The centre of a galaxy is defined as the location of its particle/cell (of any type) with the minimum gravitational potential energy evaluated over the particles belonging to the galaxy- we take this as the origin of the profiles assumed in Chapter 6.

### 3.3.2 Sample Selection & Analysis

To match the observed and simulated galaxies, we further filter the central galaxies using following selection criteria:  $z = 0.85$ ,  $M_* = 10^8 - 10^{11.6} M_\odot$ ,  $\text{SFR} = 0.1 - 100 M_\odot \text{yr}^{-1}$ ,  $R_e = 0.03 - 30 \text{ kpc}$ ,  $V_c = 75 - 300 \text{ km s}^{-1}$  and  $V_{\text{rot}}/\sigma > 1$ . Here,  $V_c$  is maximum circular velocity of the galaxies within the radius of 100 kpc radius. The  $V_{\text{rot}}/\sigma$  is ratio between maximum rotation (azimuthal) velocity to the velocity dispersion. With this selection criteria, we obtained 212 EAGLE, 300 TNG100, and 551 TNG50 galaxies. We present this selected sample together with the observed data in Figure 3.11, where we show the main-sequence of star-forming galaxies, the mass-size relation, gas-to-stellar mass relation, and the velocity distribution. As we can notice that our observed sample agrees very well with the simulations in terms of their effective radii, stellar masses, gas masses, and circular velocities. However, the SFR of the simulated sample is lower by a factor of 0.37 dex, which is one of the well-known problems in current simulations (Whitaker et al., 2014; Donnari et al., 2019). In spite of this mismatch, we consider the selected simulated galaxy sample as an optimal sample for a detailed comparison with our data, as it is a representative for the population of typical star-forming, rotation-dominated galaxies at  $z \sim 1$  in the  $\Lambda$ CDM Universe. To compare the simulations with observed rotation curves, we extract the mass profile of simulated galaxies expressed as circular velocity curve ( $V_c(R) = \sqrt{GM/R}$ ) and its constituent components, i.e. stars, gas, and dark matter, see bottom panel Figure 3.11. The rotation curve analysis of galaxy simulations is explained in details in Chapter 6, Section 6.4.

## 3.4 Summary

In this chapter, I have analysed the KROSS parent sample (Stott et al., 2016; Harrison et al., 2017). These are IFU based (i.e., 3D data)  $H_\alpha$  detected star-forming galaxies at redshift  $0.57 \leq z \leq 1.04$ . On the bases of the  $H_\alpha$  flux cut ( $F_{H_\alpha} > 2 \times 10^{-17} [\text{erg s}^{-1} \text{cm}^{-2}]$ ), signal-to-noise of the  $H_\alpha$  detection ( $S/N > 3$ ) and the inclination angle cut ( $25^\circ \leq \theta_i \leq 75^\circ$ ), I have selected 344 galaxies for analysis. I have used the  ${}^3\text{D}\text{BAROLO}$  (3DBarolo) for kinematic modelling of these galaxies, see Section 3.2.2, which is also capable of extracting the corresponding rotation curves. The main advantage of this tool is that, it incorporate the beam smearing corrections simultaneously with kinematic modelling in 3D-space. Thus it allows us to determine the unbiased rotation velocity and intrinsic velocity dispersion even in the low spatial resolution data. Moreover, I have corrected the rotation curves for the pressure support applying the pressure gradient correction (PGC), which is discussed in detail in Section 3.2.3. A 3-fold approach of deriving rotation curves

(3D-kinematic modelling + beam smearing corrections in 3D-space + pressure support corrections), delivers the true intrinsic shape of the rotation curves which I have analysed in the Chapter 4. This rotation curve data is then further investigated and interpreted in Chapter 5 6 & 7 for determining the dark matter fraction, its structural properties, and fundamental scaling relations, respectively. Furthermore, simulated data established in Section 3.3, is utilized in Chapter 6 to compare the dark matter fraction and density profile of dark matter halo.



# Chapter 4

## Rotation Curve Analysis

***Preamble:*** *The majority of the work presented in this chapter has been published as a first author paper in [Sharma et al. \(2021b\)](#). To highlight certain aspects with more clarity, here, I have included some additional illustrations and descriptions.*

### 4.1 Introduction

In the late 1980s, [Rubin et al. \(1980\)](#) and [Bosma \(1981\)](#) published the most explicit observational evidence of non-Keplerian rotation curves of spiral galaxies. These findings have made far-reaching changes in the field of Astronomy, Astrophysics as well as Cosmology, introducing an elusive component that astrophysicist dubbed as Dark Matter, thought to be made of a dark particle necessarily beyond the standard model of elementary particles. Since then, Dark Matter (DM) became a building block of the current cosmological model so as the formation and evolution of all the structures in the Universe ([Padmanabhan, 1993](#); [Springel et al., 2005](#)). It contributes  $\approx 24\%$  to the energy budget of the Universe ([Freedman & Turner, 2003](#)), despite ‘no success’ in the discovery of its particle nature.

In the local Universe, by studying the shape of the rotation curves, we established a fair understanding about the presence of dark matter and its contribution in the mass distribution (e.g. [Salucci & Burkert, 2000b](#); [Sofue & Rubin, 2001](#); [Salucci et al., 2007](#); [Courteau & Dutton, 2015](#); [Salucci, 2019](#), and references therein), see also Section 1.1. The rotation curve studies not only constrain the mass budget but has also strengthened our understanding of galaxy formation and evolution in the local Universe (e.g. [Reyes et al., 2011](#); [Read et al., 2016](#); [Karukes & Salucci, 2017](#); [Lapi et al., 2018b](#)). As mentioned earlier in Section 2.3.2, with the development of advance spectrographs equipped with integral field units (IFUs), rotation curve study has been extended to high-redshift ([Di Teodoro et al., 2016](#); [Genzel et al., 2017](#); [Lang et al., 2017](#); [Harrison et al., 2017](#); [Tiley et al., 2019b](#)). However due to poor treatment of either observational uncertainty (precisely beam smearing) or physical conditions of high-redshift galaxies (pressure gradient corrections), the rotation curve study at high-redshift is still a matter debate, see Section 2.3.2. Therefore, I begin my thesis work by analysing the high-redshift rotation

curves. In particular, I exploited KROSS data (Stott et al., 2016; Harrison et al., 2017) by employing different techniques than used in Genzel et al. (2017); Lang et al. (2017) and Tiley et al. (2019b). In brief, the key differences between our findings and previous studies lie in the modeling of the kinematics and the consideration of pressure support. We performed 3D forward modeling of datacubes using the 3DBarolo code (Teodoro & Fraternali, 2015), which improves the quality of resulting kinematics with respect to 2D kinematic modeling approaches. For pressure support, we employed the pressure gradient correction (hereafter PGC) method using Weijmans et al. (2008), which makes use of the full information available in the datacube and therefore gives better results than pressure support correction assuming isotropic and constant velocity dispersion (which have been used in Genzel et al. 2017 and Lang et al. 2017). For details, we refer reader to Chapter 3 (Section 3.2.2 & 3.2.3). In this chapter, I have analysed the rotation curve data established in Chapter 3, which I briefly described in Section 4.2. Then, I straight forward begin to investigate the rotation velocity of galaxies (Section 4.2.1) and shape of their rotation curves (Section 4.2.2). In the end, I discuss the results in Section 4.3 and conclude them in Section 4.4.

## 4.2 Data Analysis & Results

Recalling the dataset established in Chapter 3. I ran 3DBarolo on 344 star-forming galaxies selected from KROSS survey, having the  $H_{\alpha}$  flux ( $F_{H_{\alpha}} > 2 \times 10^{-17}$  [erg s<sup>-1</sup> cm<sup>-2</sup>]), the inclination ( $25^\circ \leq \theta_i \leq 75^\circ$ ), the redshift range ( $0.75 \leq z \leq 1.04$ ), and the stellar masses ( $8.83 \leq \log(M_* [\mathrm{M}_\odot]) \leq 11.32$ ). Thereby, we have 344 beam smearing corrected rotation curves, dispersion curves, and the corresponding moment maps. After quality assessment of 3DBarolo outputs, we have selected 314 Quality-1 & Quality-2 objects; this sample is referred to as the Q12 sample in the analysis (see Section 3.2.2.4). In this sample, we have 256 rotation-dominated ( $v/\sigma > 1$ ) and 57 dispersion-dominated ( $v/\sigma \leq 1$ ) systems, where  $v/\sigma$  is calculated before the PGC. A distribution of re-sampled data is shown in Figure 4.1. This sample has objects with the effective radii  $-0.16 \leq \log(R_e [\mathrm{kpc}]) \leq 0.89$  and the circular velocities  $1.42 \leq \log(V_{out}^{PGC} [\mathrm{km s}^{-1}]) \leq 2.57$ . In the section below, I analyse the rotation curves of rotation dominated Q12 sample and their circular velocities.

### 4.2.1 Characteristic Velocity

We begin by analysing the global circular velocity of galaxies computed at various scale lengths. Recalling the definition of scale-lengths defined in Section 3.2.1.3, for an exponential thin disc, the stellar component of a galaxy follows surface density:  $\Sigma_D(R) = \frac{M_D}{2\pi R_D^2} \exp\left(\frac{-R}{R_D}\right)$  (Freeman, 1970b), where  $M_D$  is the disc mass and  $R_D$  is the disc radius. Under this assumption, one can relate the scale length ( $R_e$ ) determined from the light profile of the galaxy to compute the characteristic radius e.g. the disc length ( $R_D = 0.59 R_e$ ). In our work, we calculate velocities at three different characteristic radii: 1) the optical

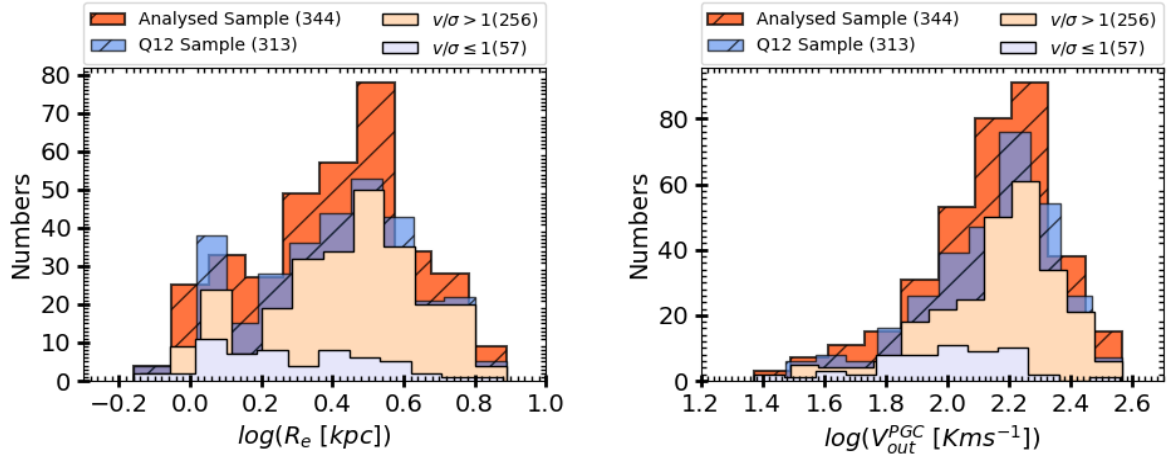


**Figure 4.1:** *Left:* The effective radii distribution and *Right:* the circular velocity distribution of the analysed sample. The colour codes are same in both panel and given as following: the dark orange hatched distribution is the 3DBarolo analysed sample, blue hatched distribution is Q12 sample (i.e. Quality-1 & 2 objects only). The peach-puff histogram represents the rotation dominated (i.e.  $v/\sigma > 1$ ) Q12 sample, and the light blue distribution shows to the the dispersion dominated (i.e.  $v/\sigma \leq 1$ ) Q12 sample. The digits in the bracket of legend represent the total number of the objects in each sub-sample. In the rotation curve analysis, we have used only rotation-dominated Q12 sample.

radius ( $R_{opt} = 3.2R_D$ ); **2**) twice the optical radius ( $R_{out} = 6.4 R_D$ )<sup>1</sup> and **3**)  $R_{80}$ <sup>2</sup> i.e. the radius where the rotation curve is presumably flat (notice that at the different radii, rotation curves can be rising and falling). The  $R_{opt}$  and  $R_{out}$  are the photometric measurements (derived from effective radii:  $R_e$ ), whereas,  $R_{80}$  is the kinematic measurement. Referring to each radii  $R_{opt}$ ,  $R_{out}$ , and  $R_{80}$ , we define the corresponding velocities  $V_{opt}$ ,  $V_{out}$ , and  $V_{80}$  respectively. In this work we have used velocities computed at  $R_{out}$ . The observed dispersion curves (of ionized gas) are nearly flat, therefore, we have calculated the overall velocity dispersion ( $\sigma$ ) of the galaxy using weighted mean statistics (see: Equation 4.1). Note, the characteristic velocities measured from a PG-corrected rotation curves are referred to as  $V_{opt}^{PGC}$ ,  $V_{out}^{PGC}$ , and  $V_{80}^{PGC}$  respectively. In left panel of Figure 4.2, we have shown a comparison of the PGC and the non-PGC circular velocities computed at  $R_{out}$  ( $V_{out}^{PGC}$  and  $V_{out}$  respectively). We can see that if the system does not have sufficient rotation, i.e. if  $V_{out}/\sigma$  ( $= v/\sigma$ )  $\lesssim 5$  then the pressure gradient is dominant, which is also noticeable in PG correction factor:  $\Delta V_c = V_{out}^{PGC} - V_{out}$  (shown in right panel of Figure 4.2). On the other hand, if the system is rotation-dominated, then the PGC does not increase the rotation velocity and hence we notice a strong correlation between  $V_{out}^{PGC}$  and  $V_{out}$  for  $v/\sigma > 5$ .

Furthermore, we conclude that the pressure gradient is a more dominant effect in the high-redshift systems than the beam smearing. For a quantitative measurement,

<sup>1</sup>In this chapter we use  $R_{out} = 2 R_{opt}$  but from Chapter 5 onward  $R_{out} = 1.5 R_{opt}$ .

<sup>2</sup> $R_{80}$  is the radius which covers the 80% of the rotation velocity curve

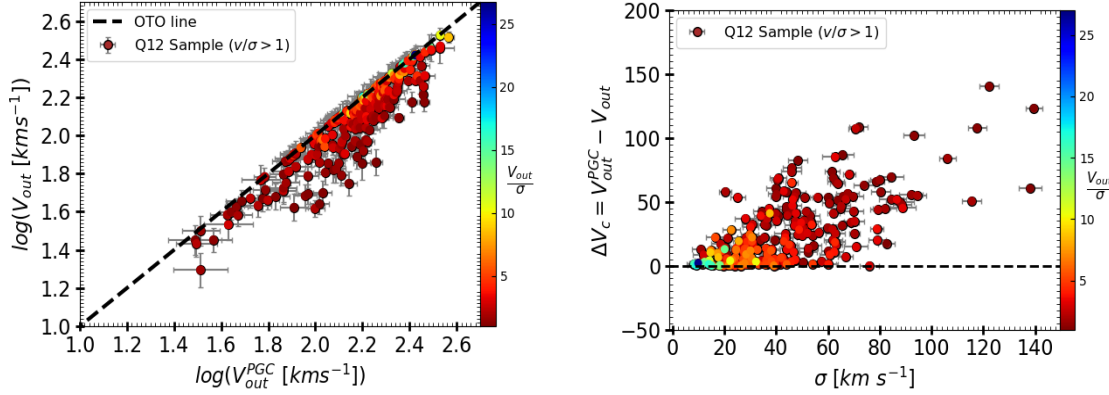


**Figure 4.2:** *Left panel:* The correlation between rotation velocities before and after pressure gradient correction (PGC), i.e.  $V_{out}$  and  $V_{out}^{\text{PGC}}$  respectively. The black dashed line shows the one-to-one relation. The objects are color coded by  $V_{out}/\sigma$  ( $= v/\sigma$ , computed before PGC). *Right panel:* The pressure gradient correction factor:  $\Delta V_c = V_{out}^{\text{PGC}} - V_{out}$  as a function of velocity dispersion ( $\sigma$ ), color coded for  $V_{out}/\sigma$ . The corrections are significant in  $V_{out}/\sigma \lesssim 5$  galaxies.

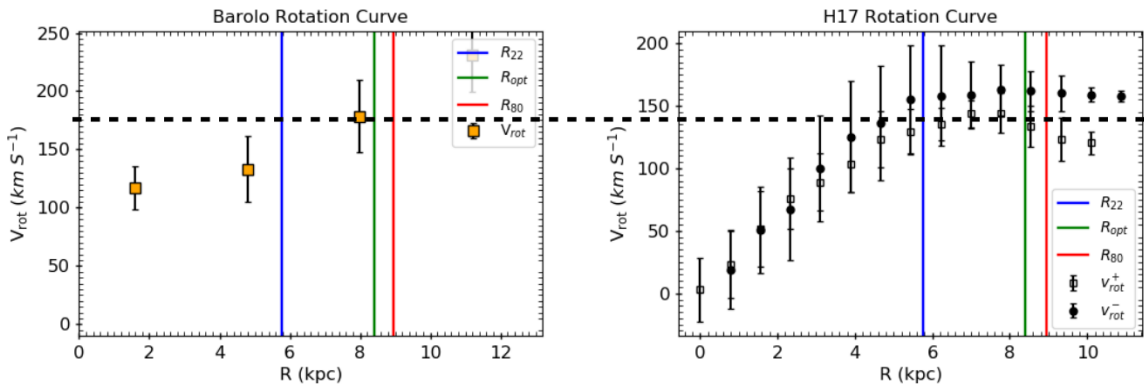


**Figure 4.3:** Comparison of beam smearing corrected and non-corrected rotation curves. *Left panel:* 3DBarolo generated rotation curve corrected for beam smearing. The orange square with error-bars represents rotation curve. *Right panel:* rotation curve derived from 2D approach not corrected for beam smearing (Harrison et al., 2017). The open and close square with error-bars represents rotation curve data of receding and approaching arm of the galaxy. The vertical lines in both panels are scale radii:  $R_{22} = 2.2R_D$ ,  $R_{opt} = 3.2R_D$ , and  $R_{80}$ , the blue, green, and red, respectively. The black horizontal line is giving a measuring scale to estimate the circular velocity at different radii, before and after beam smearing corrections.

we matched rotation curves of our analysed sample with [Harrison et al. \(2017\)](#) rotation curves, those are not corrected for beam smearing, and calculated the rotation velocity at  $3.2R_D$  in both samples, see Figure 4.3. We found beam smearing has increased the median rotation velocity of sample by  $\sim 10 - 15 \text{ km s}^{-1}$  (similarly observed by [Johnson et al. 2018](#)), whereas PGC increases the median rotation velocity by more than  $30 - 50\%$  relative to the initial value. Although pressure support is dominant than beam smearing, to obtain the ‘intrinsic shape of rotation curves’, we need to correct for both effects.

### 4.2.2 Co-added Rotation Curves

Here, we present the five co-added and binned rotation curves constructed from the 256 individual rotation curves. We have performed co-addition on both PGC and non-PGC rotation curves. The technique of co-adding and binning is the following; first, we batch the rotation curves according to their circular velocity calculated at  $R_{out}$ , where the dark matter is expected to be dominating. Then we treat each batch of the rotation curves as a single co-added rotation curve. Second, we bin the galaxies radially per  $2.5 \text{ kpc}$  corresponding to the binning scale of 3DBarolo. For the binning, we have used standard weighted mean statistic given by:

$$\bar{X} = \frac{\sum_{i=1}^n x_i \times w_i}{\sum_{i=1}^n w_i} \quad (4.1)$$

where,  $x_i = \text{data}$ ;  $w_i = 1/\text{error}^2$ ;  $\bar{X} = \text{binned data}$ . The errors on binned data are root mean square error, computed as  $\delta_v^{r_i} = \sqrt{\sum[(\delta_{v_i}^r)^2 + (\sigma_{v_i}^{r_i})^2]/N}$ , where  $\delta_{v_i}^r$  is the individual error on the velocities per radial bin and  $\sigma_{v_i}^{r_i}$  scatter per radial bin. We are using such a statistical approach because it has plausible advantages on the rotation curve studies e.g. **a)** it gives us a smooth distribution of rotation curves ignoring the random fluctuations arising from bad data points, i.e. it allows to enhance the S/N in the data; **b)** it allows the mass decomposition of similar velocities but having different spatial sampling. This kind of approach in rotation curve studies has been used for decades, pioneered by [Persic & Salucci \(1991\)](#) later developed in several other works ([Persic et al., 1996](#); [Salucci & Burkert, 2000b](#); [Salucci et al., 2007](#); [Catinella et al., 2006](#); [Yegorova et al., 2011](#); [Karukes & Salucci, 2017](#); [Lapi et al., 2018b](#)). To be more precise, we have constructed the five co-added rotation curves (selected according to the circular velocities at  $R_{out}$ ), where each co-added rotation curve is divided into six radial bins. The statistics, including the number of sources included per radial and velocity bin of the co-added & binned rotation curves are tabulated in Table 4.1.

In the Figure 4.4, we have shown the co-added & binned rotation curve before and after PGC. We notice that the some of the individual rotation curves are subjected to large fluctuations before the PGC. In particular, the individual rotation curves of the lower velocity bins (*bin\_50 – 100* & *bin\_100 – 150*) falls to zero (or stay close to zero) at  $R > 4 \text{ kpc}$  (left panel). This might be interpreted as the galaxies not being in the disc-like configuration. However, it could also be an effect of heavy turbulence (i.e. large pressure gradient), which provides a substantial pressure support, and keeps the disc in

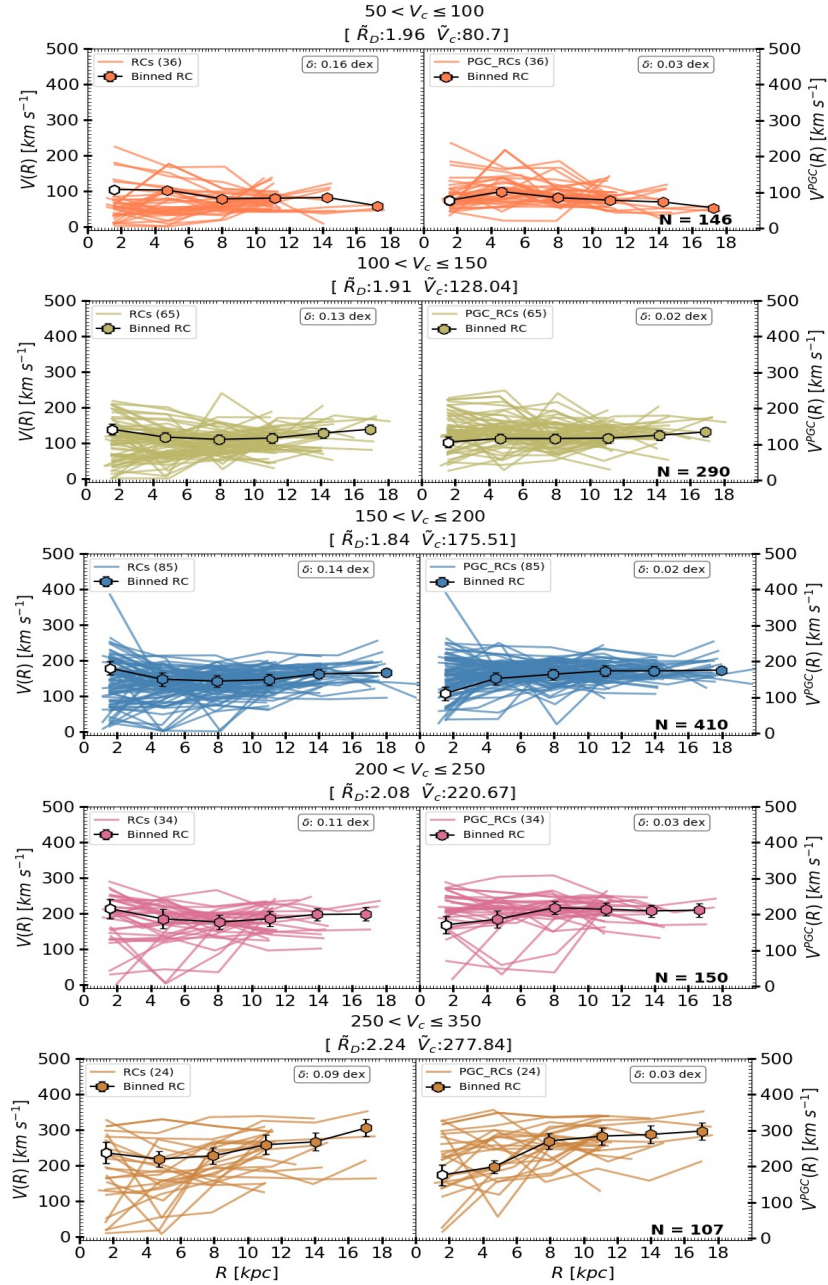


**Figure 4.4:** The comparison of non-PGC and PGC co-added rotation curves (left and right panel respectively). From top to bottom- bin\_50-100: orange colour, bin\_100-150: khaki colour, bin\_150-200: blue colour, bin\_200-250: pink colour and bin\_250-350: dark-orange colour. The color code is same for individual rotation curves (solid curves/lines) and Co-added rotation curves (black line/curve connected with hexagons). The median disc radii ( $\tilde{R}_D$  in  $kpc$ ) and the median circular velocity ( $\tilde{V}_c$  in  $km\ s^{-1}$ ) of each bin is displayed in the title of each bin. The digits in the bracket of each legend represent the number of rotation curves co-added in each bin, and total number of co-added data points per bin are printed in the lower right corner of each plot. The variance in the individual rotation curves data is given by  $\delta$ , shown in the rectangular box in the upper-right corner of the each plot. Notice, binned data point of first radial bins is within the resolution limit. Hence, to make it clearer to the reader, we show it by open/white hexagon, and discarded in the further analysis of rotation curves.

Bin Name bin_ $V_{min}$ - $V_{max}$	$N_v$ [dpts]	$N_{v,r}$ [dpts]	$\tilde{R}_{out}$ [kpc]	$\tilde{V}_{out}^{PGC}$ [km s $^{-1}$ ]
bin_50-100	36	36, 36, 36, 35, 3	12.56	80.70
bin_100-150	65	65, 65, 65, 65, 25, 5	12.24	128.04
bin_150-200	85	85, 85, 85, 85, 45, 25	11.79	175.51
bin_200-250	34	34, 34, 34, 32, 13, 3	13.31	220.67
bin_250-350	24	24, 24, 24, 24, 9, 2	14.33	277.83

**Table 4.1:** The statistics of the co-added and binned rotation curves. *Col1*: shows the name of each velocity bin, e.g. bin\_a-b, here  $a$  is lower velocity limit and  $b$  is higher velocity limit. *Col2*:  $N_v$  gives the number of objects per velocity bin. *Col3*  $N_{v,r}$  gives the number of objects per radial bin. *Col4* & *Col5*: gives the average  $R_{out}$  and  $V_{out}$  respectively for the each velocity bin.

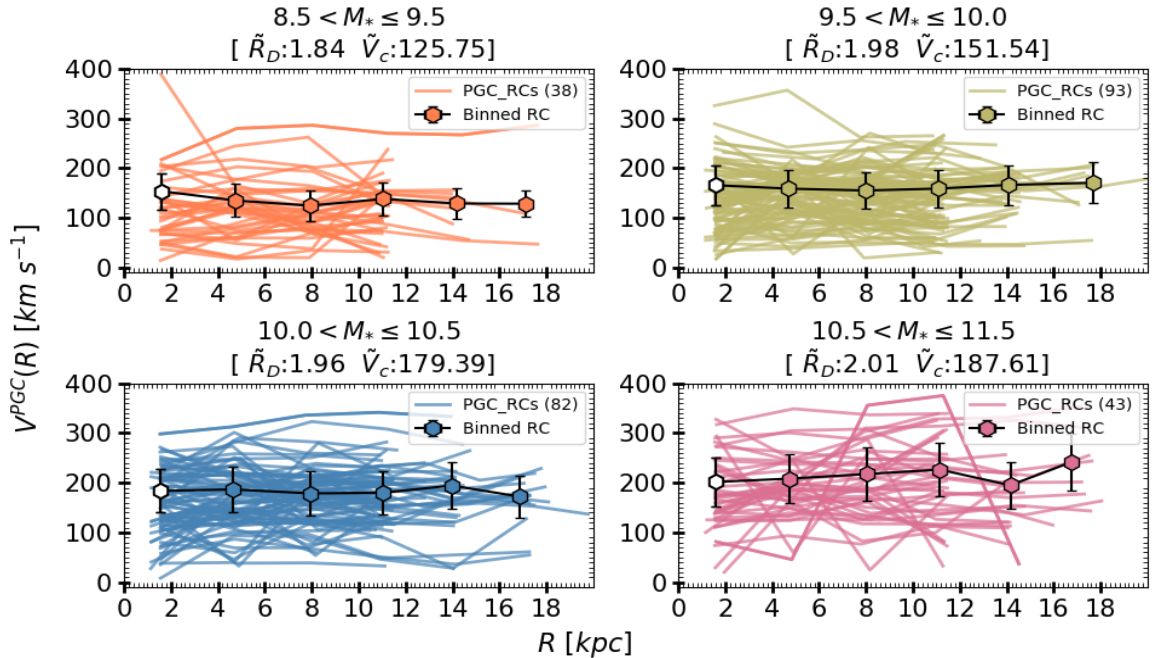


**Figure 4.5:** The co-added and binned rotation curves in the stellar mass bins. The color code of  $M_*$  bins is the following, the orange: bin\_8.5-9.5, green: bin\_9.5-10, blue: bin\_10.0-10.5, and pink: bin\_10.5-11.5. The solid lines represents the individual rotation curves and hexagon connected black curve shows the binned rotation curves.

kinematic equilibrium without the need for strong rotation. We suggest that it is most likely the latter case, because after the PGC, we do not see any rotation curve lie close to zero circular velocity (right panel). This effect is also noticeable in characteristic velocity measurements (see left panel of Figure 4.2) and PG correction factor (see right panel of Figure 4.2) of low  $v/\sigma(< 5)$  galaxies, where the corrections are  $\sim 100 - 150 \text{ km s}^{-1}$ . Here, we would like to emphasize the importance of our PGC, which makes use of complete information about the galaxy available in the datacube (namely density, dispersion, and rotation) and hence is able to correct for the strongly turbulent pressure conditions. The PGC also gives an usual shape to all rotation curves (as we can see in the right panel of Figure 4.4). In addition, we notice that the variance ( $\delta$ ) in the PG corrected rotation curves decreased by a median factor of  $\sim 5$ .

Furthermore, we also show the co-added rotation curves in the stellar mass bins in Figure 4.5. As one can notice, we ye again find the similar scenario as velocity bins but with relatively larger intrinsic scatter. This indicates that the star-forming galaxies at  $z \sim 1$  have diverse dark matter halo properties connected with baryons. Notice, due to low spatial resolution in the inner region ( $R < 2.5 \text{ kpc}$ ), we do not draw any conclusion within the effective radii. Moreover, due to the lack of knowledge on gaseous components and the fact that stellar disc scale-lengths show no dependency on the circular velocity, we leave the presumably complex process of rotation curve normalization for future work. Hence, in this work, all the rotation curves are presented in physical units, i.e.  $\text{km s}^{-1}$  opposed to  $\text{kpc}$ . Let us finally remark, the model and techniques employed in this work may be subject to some uncertainties, mostly because high-redshift galaxies may not be fully rotation supported disc galaxies. However, this is a problem for any high-redshift study and can be mitigated only by acquiring better data, e.g. JWST/NIRSpec and ELT/HARMONI as providing more sensitive and higher spatial resolution observations of high-redshift galaxies.

#### 4.2.3 Comparison Sample

We compare our binned rotation curves of  $z \sim 1$  with the Universal Rotation Curves (URCs) of local star-forming disc-type galaxies. The URCs sample is one of the largest (contains 2300 galaxies) and deeply investigated samples, which have been used several times to show the interplay of dark and luminous matter in the local Universe (e.g. [Persic & Salucci, 1991](#); [Persic et al., 1996](#); [Salucci & Burkert, 2000b](#); [Salucci et al., 2007](#); [Catinella et al., 2006](#); [Yegorova et al., 2011](#); [Lapi et al., 2018b](#)). For comparison, we have used the rotation curves of the same velocity bins drawn from the URC sample (particularly used in [Lapi et al., 2018b](#)). The distribution of the circular velocities of both samples is shown in Figure 4.6. We notice that the circular velocities of both samples trace a similar *total potential* or *total mass* within  $R_{out}$ . In the Figure 4.7, we have shown the distribution of stellar masses of both samples. Notice, for  $z \sim 1$  galaxies stellar masses are derived from SED fitting while for locals (URC sample) they are derived from rotation curve analysis given in [Lapi et al. \(2018b\)](#). We found that the stellar masses show a relatively broad distribution for a given velocity bin, and are noticeably lower in comparison with

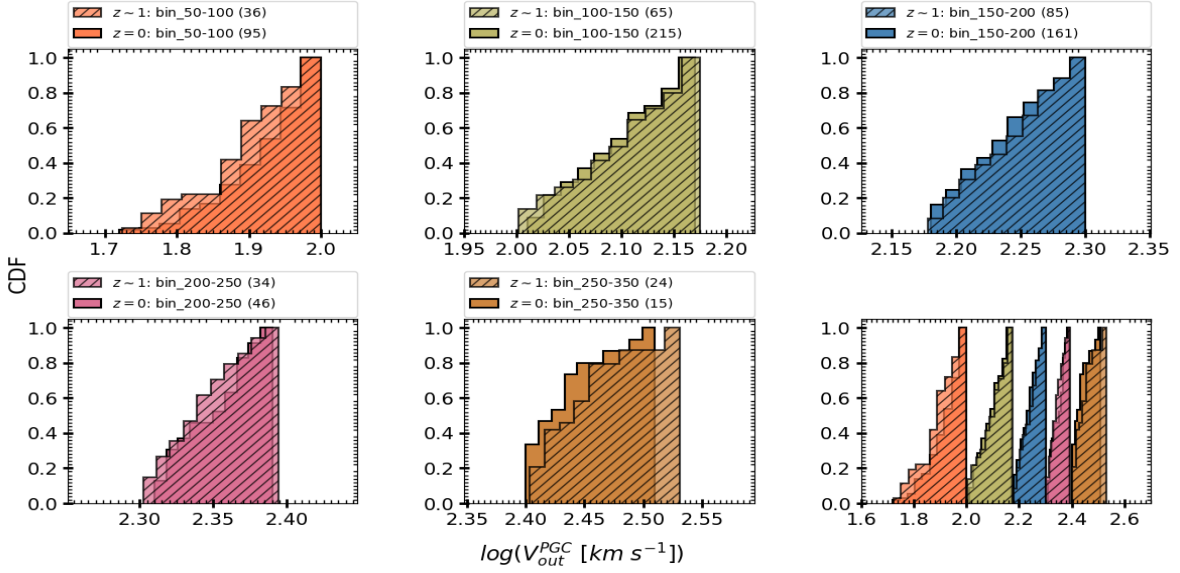


**Figure 4.6:** A comparison of cumulative density distribution of circular velocities of  $z \sim 1$  (hatched histograms) and  $z \approx 0$  (plane histograms) galaxies. The color code of each bin is same as Figure 4.4.

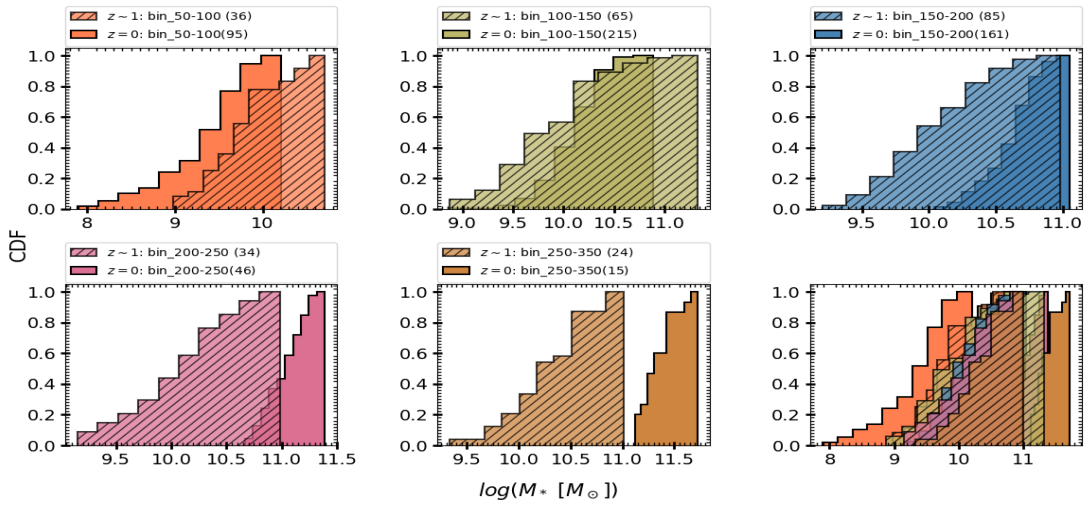


**Figure 4.7:** A comparison of cumulative density distribution of stellar masses of  $z \sim 1$  (hatched histograms) and  $z \approx 0$  (plane histograms) galaxies. The color code of each bin is same as Figure 4.4.

locals (except the lowest velocity bin). Therefore, we can state that both samples are indistinguishable in terms of *total mass* but differ in stellar masses, an outcome which is expected from *the empirical galaxy formation and evolution model* (c.f. [Moster et al., 2018](#), and references therein). This implies that we are comparing the local star-forming galaxies (disc-type systems), with galaxies at  $z \sim 1$  those are most likely their progenitors, in which gas is turning into stars keeping the *total mass* constant.

### 4.3 Presenting Flat Rotation Curves

Although we are limited by a few caveats mentioned in previous section, we proceed to interpret our results in the context of  $z \approx 0$  star-forming discs. In the Figure 4.8, we show the comparison of our binned rotation curves (PGC applied) of  $z \sim 1$  with the URCs of  $z \approx 0$ . For the purpose of clear and tidy comparison, we do not show the first radial bin of each binned rotation curves. The last radial bins contains the few data-points but we keep them in the analysis because they can be informative<sup>3</sup>. We notice that all the  $z \sim 1$  rotation curves coincide with the local rotation curves from optical radii ( $\sim 2R_e$ ) till the last point of observation. Except the lowest bin (*bin\_50 – 100*) which shows a gradual decline with increasing radius. In short Figure 4.8 is an explicit representation of  $z \sim 1$  flat rotation curves. In the Figure 4.5, we also show the co-added rotation curves in stellar mass bins. We yet again find the flat rotation curves with relatively large error in the amplitude. On this basis we conclude that the:

1. star-forming galaxies of  $z \sim 1$  manifest flat rotation curves from optical radii ( $\sim 2R_e$ ) till last point of observation.
2. Total potential ( $\phi(R)$ ) or total mass within the  $\sim 20$  *kpc* radii of  $z \sim 1$  and  $z \approx 0$  star-forming galaxies remains the same, i.e. it did not evolve in the past 6.5 *Gyr*, which suggests that the dark matter halo of star-forming galaxies most likely evolves slowly by accumulating the matter in the outermost regions of the galaxies. These results concord with the theoretical explanation of [Lapi et al. \(2020\)](#).

Furthermore, we notice a size-evolution in our sample relative to the local late-type galaxies. For the early and late-type galaxies, size-mass evolution has been already observed and reported in several studies (e.g. [van der Wel et al., 2014b](#); [Lapi et al., 2018a](#); [Tacconi et al., 2018](#), and references therein). For an example case, there is an extensive body of work done by [van der Wel et al. \(2014b\)](#) on the size evolution of late-type as a function of redshift, where they bin the galaxies in stellar masses and effective radii for redshift range  $0.25 \leq z \leq 1.75$ . They showed that the size evolution in late-type galaxies

<sup>3</sup>For example, rotation curves of the lowest velocity bin declines at the last (and second last) point of observation, it could be due to very few data points in the last radial bin. However, pay attention to the clear offset in stellar disc scale length in the lowest bin (see Figure 4.9), which apparently indicates high stellar-mass objects relative to  $z \approx 0$  galaxies (given that  $V_c^{z \sim 1} < V_c^{z \sim 0}$ ). Therefore, rotation curves can be declining in the lowest velocity bin. On the other hand, rotation curves of all the other velocity bins stays flat, even though they contain a few data points in the last radial bins (see Figure 4.8).

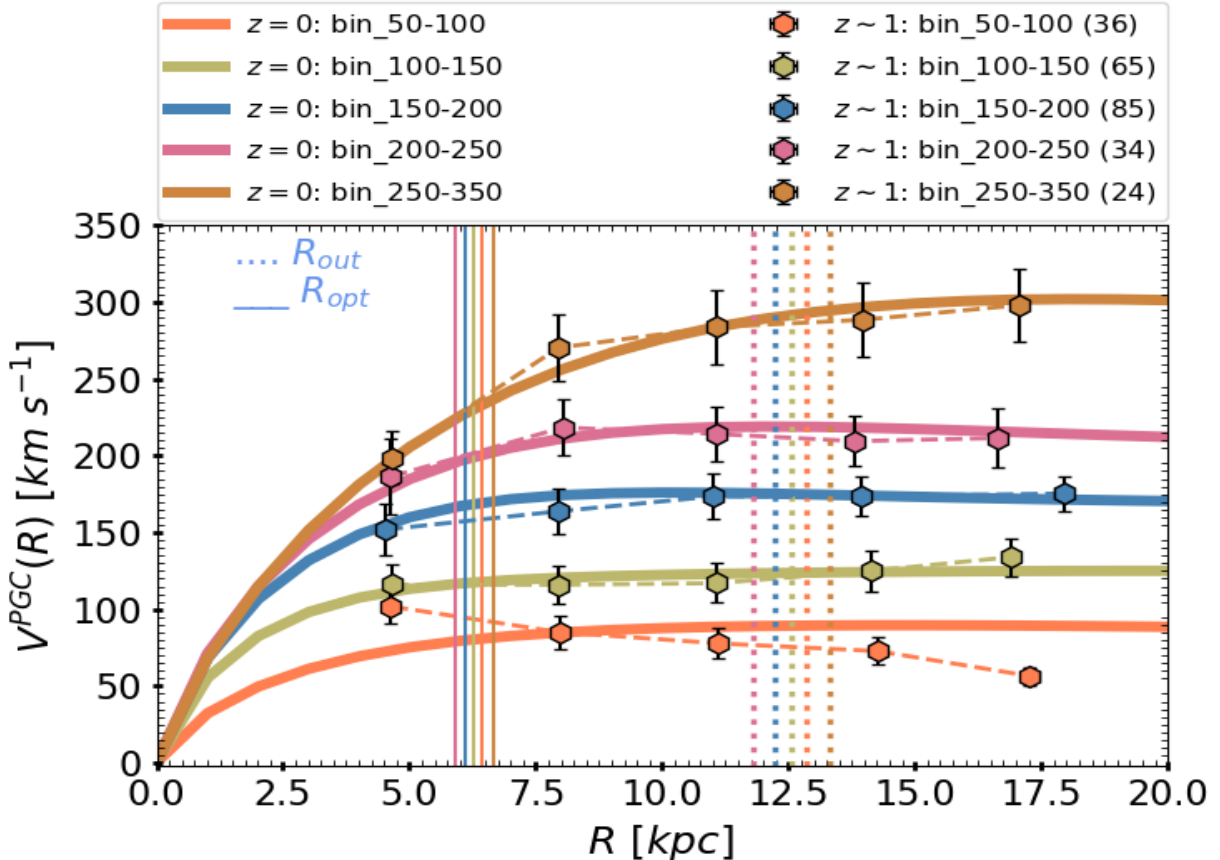


**Figure 4.8:** A comparison of  $z \sim 1$  co-added rotation curves of five velocity bins (dashed line connected hexagons) with local rotation curves (solid curves) of similar velocity bins derived from the URC sample (Persic et al. 1996; Salucci et al. 2007). The colour code of each velocity bin is the same as Figure 4.4. The digits in the bracket of the legend represent the number of rotation curves co-added in each bin. Dotted and solid vertical lines are showing the  $R_{out}$  and  $R_{opt}$  respectively for each rotation curve (colour coded same as velocity bins).

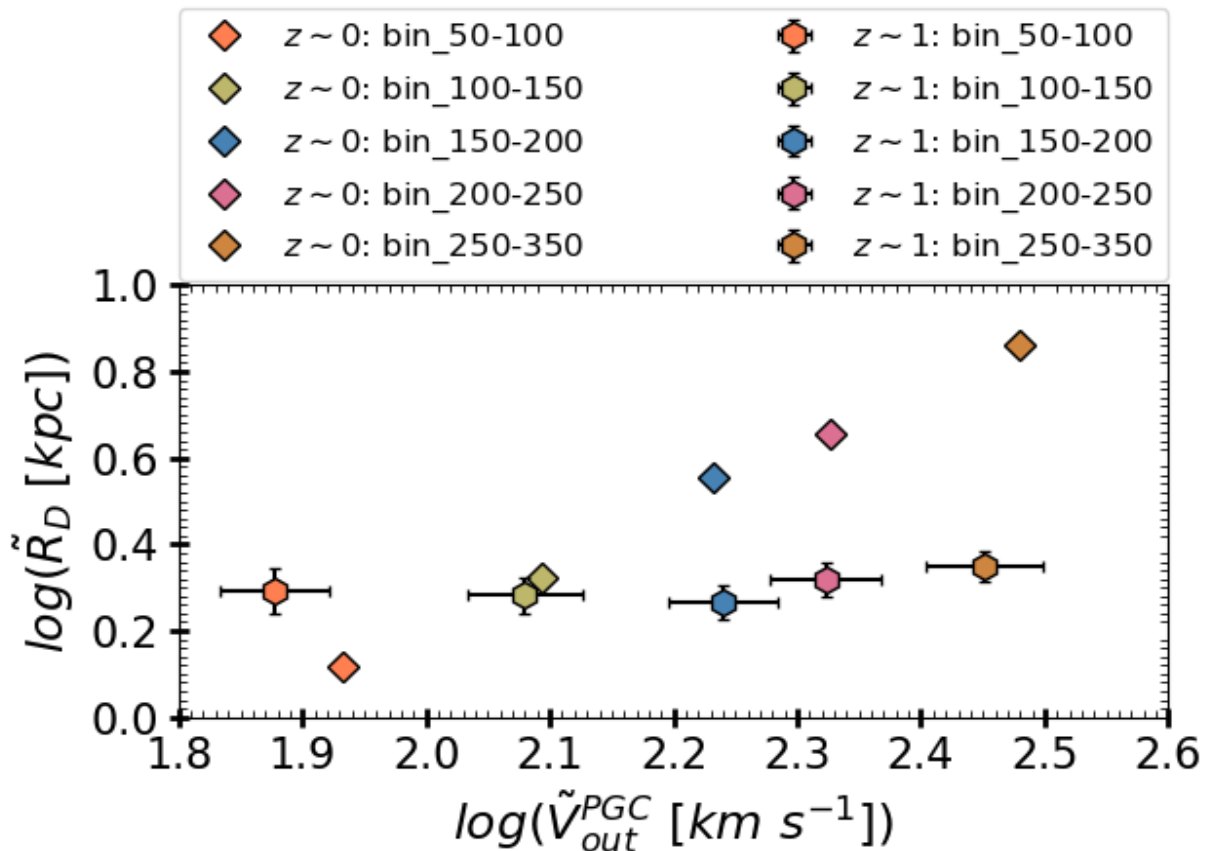


**Figure 4.9:** shows the median stellar disc radii ( $\tilde{R}_D$ ) of each velocity bin as a function of their median circular velocities  $\tilde{V}_{out}^{PGC}$ . The velocity bins are colour coded similarly as Figure 4.8. The hexagons with error bars represents the  $z \sim 1$  galaxies and diamonds are showing the local galaxies of similar velocity bin.

could be described as  $R_e \propto M_*^{0.22}(1+z)^{-1.48}$ , for details see Section 7.4.1. In this chapter, we are addressing the size evolution in the velocity plane of the  $z \sim 1$  galaxies and comparing it with locals, shown in Figure 4.9. In particular, we have binned the circular velocities and disc scale-length of galaxies for given velocity bins (same as the rotation curves in Figure 4.8), and plotted the stellar disc radii of each velocity bin ( $\tilde{R}_D$ ) as a function of their circular velocities ( $\tilde{V}_{out}^{PGC}$ ). We notice that stellar distribution does not depend on circular velocity. In particular, the lowest velocity bin is consistent with  $z \approx 0$  but at a *smaller* stellar disc-length than  $z \sim 1$  on average. On the other hand, we find that with increasing circular velocities, locals are consistent with  $z \sim 1$  but contain *larger* stellar disc-lengths. In short, for the high-redshift galaxies, the stellar disc radii remains constant as a function of the velocity while for locals it increase. This implies that at  $z \sim 1$  the stellar-disc component has not yet established a strong co-relation between the total mass or the total potential of the halo within  $\sim 20$  kpc as observed in the locals. It could be a consequence of underlying ‘complex’ astrophysics of the galaxy evolution. For example, most of the baryons are still gaseous at  $z \sim 1$ , i.e. gaseous-disc dominates. The latter comment has been already mentioned by [Glazebrook \(2013\)](#) and recently deeply investigated and favoured by [Tacconi et al. \(2018\)](#). Here, from the perspective of the dynamics, we emphasize that the stellar mass distribution evolves over cosmic time in the rotation-dominated system, whereas, a negligible evolution is noticed in the lower end of the velocities. Therefore, we suggest that the evolution of stellar light distribution is circular velocity dependent.

## 4.4 Summary

We have analysed the 256 rotation dominated galaxies. This sample covers the redshift range  $0.75 \leq z \leq 1.04$ , the effective radii  $-0.16 \leq \log(R_e [\text{kpc}]) \leq 0.89$ , the circular velocities  $1.42 \leq \log(V_{out}^{PGC} [\text{km s}^{-1}]) \leq 2.57$ , and the stellar masses  $8.83 \leq \log(M_* [\text{M}_\odot]) \leq 11.32$ . Using the technique of [Persic et al. \(1996\)](#), we have constructed the co-added and binned rotation curves of the five velocity bins out of 256 individual rotation curves and compared them with the rotation curves of local star-forming disc-type galaxies of same velocity bins (see: Section 4.3 and Figure 4.8). The main findings of this work are the following:

- The pressure gradient is more dominant effect in high-redshift galaxies than the beam smearing. It corrects the median rotation velocity more than the 50%, especially in the galaxies with  $v/\sigma < 5$ .
- A statistically robust method of co-adding and binning rotation curves shows that the  $z \sim 1$  outer rotation curves are very similar to the outer rotation curves of the local star-forming galaxies (see Figure 4.8) where dark matter dominates and flattens the rotation curves.
- We have noticed a significant evolution in the disc scale length over past 6.5 Gyrs (see Figure 4.9).

On the bases of above outcomes, we conclude that the *Total Matter* placed in a galactic halo within  $\sim 20$  kpc radius at  $z \sim 1$  remains same as  $z \approx 0$ . At the same time, stellar mass distribution (i.e. stellar disc) evolved over cosmic time (in past 6.5 Gyrs). This suggests a prolonged evolution of the star-forming galaxies (late-type systems).

# Chapter 5

## Dark Matter Fraction

***Preamble:*** *The majority of the work presented in this chapter has been published as a first author paper in [Sharma et al. \(2021c\)](#). To highlight certain aspects with more clarity, here, I have included some additional illustrations and descriptions.*

### 5.1 Introduction

It has been known for decades that the rotation curve (RC) of a galaxy can be used as a proxy for the enclosed mass and its underlying distribution ([Sofue & Rubin 2001](#) and [Salucci 2019](#)). In the local Universe, we see the rotation curves of late-type galaxies<sup>1</sup> rising steeply in the inner regions and then flattening far beyond the disc edge<sup>2</sup> ([Rubin et al., 1980](#); [Persic et al., 1996](#); [McGaugh, 2016](#), and references therein). The steep rise in the inner regions is caused by the combination of a baryon-dominated disc plus a cored halo ([Persic et al. 1996](#) and [Persic & Salucci 1988](#)), while the flattening in the outer regions of the stellar disc and beyond implies dark matter (DM) dominance ([Persic et al., 1996](#); [Persic & Salucci, 1988](#); [Kassin et al., 2006](#); [Martinsson et al., 2013](#); [Courteau & Dutton, 2015](#), and references therein).

As we mentioned in Chapter 2 (Section 2.3.2), the presence of dark matter in high-redshift star-forming galaxies is ambiguous due to their declining behaviour in the outskirts. In order to resolve the serious issues raised in the previous literature on high-redshift rotation curves, we derived the intrinsic shape of rotation curves in Chapter 3 by means of 344 main sequence star-forming galaxies. In Chapter 4, we have shown that a careful treatment of observational uncertainties and physical conditions of high-redshift galaxies provides us with the flat rotation curves from 5 kpc till the last point of observations. In particular, we have shown in Section 4.3 of Chapter 4, that the rotation curves of  $z \sim 1$  star-forming galaxies are very similar to their local counterparts. Now, that the shape of the rotation curves is established, in this chapter I analysed these rotation curves

---

<sup>1</sup>In the local Universe, most of the late-type galaxies are spiral systems hosting star-forming discs and are rotation-supported ( $v/\sigma > 1$ ).

<sup>2</sup>The disc edge is defined as  $3.2 R_D$  ( $= 1.89 R_e$ ), where the stellar surface luminosity  $\propto \exp(-r/R_D)$

to infer the dark matter fraction of  $z \sim 1$  star-forming galaxies. I begin with a brief recall of the dataset and analysis in Section 5.2, proceeded by estimating the total baryonic and dynamical masses of the sample in Section 5.2.1 and 5.2.3, respectively. Then the dark matter fraction of the sample is calculated for individual objects, as well as in terms of ensemble averages, see Section 5.3. The dark matter fraction obtained in both cases is then compared with local and high-redshift star-forming galaxies in Section 5.4. Finally, I provide the concluding remarks in Section 5.5.

## 5.2 Data Analysis

We utilize the KROSS dataset previously studied by [Stott et al. \(2016\)](#); [Harrison et al. \(2017\)](#); [Tiley et al. \(2019a,b\)](#) and [Johnson et al. \(2018\)](#). In particular, we studied a sub-sample of 344 KROSS star-forming galaxies in Chapter 3, where the kinematics of these objects were rederived from the original KROSS datacubes via the  $^3D$ Barolo code ([Teodoro & Fraternali 2015](#) and [Di Teodoro et al. 2016](#)). This code accounts for the beam-smearing correction in 3D space and provides the moment maps, stellar surface brightness profile, rotation curve, and dispersion curve along with the kinematic models. In addition, our rotation curves were corrected for pressure gradients that are likely to affect the kinematics of high-redshift galaxies. In the end, we analyzed only 256 rotation-dominated Quality 1 and 2 objects out of 344 KROSS objects, which we refer to as the Q12 sample, see Section 4.2 (Figure 4.1).

In this work, we use the Q12 sample to derive the dark matter fraction at various scale lengths (characteristic radii), defined in Section 3.2.1.3. For the accuracy and quality of the sample, we remove those galaxies that have  $R_{out} < 3.5$  kpc (below the resolution limit),  $z < 0.65$ , and  $M_* < 10^9 M_\odot$ ;<sup>3</sup> in total we removed 31 galaxies. Our final sample contains 225 galaxies that have the inclination range  $25^\circ < \theta_i \leq 75^\circ$ , the redshift range  $0.76 \leq z \leq 1.04$ , the effective radii  $0.08 \leq \log(R_e [\text{kpc}]) \leq 0.89$ , and circular velocities  $1.45 \leq \log(V_{out} [\text{km s}^{-1}]) \leq 2.83$ , where  $V_{out}$  is calculated at  $R_{out}$ .

In the section below section, I present the determination of baryonic and dynamical masses:

### 5.2.1 Baryonic Mass Estimates

In the Section 3.2.1.5, 3.2.1.7 & 3.2.1.8, we derived the total stellar, molecular, and atomic mass content of our galaxies, which lead us to estimate the total baryonic mass as follows:

$$M_{bar} = M_* + M_{H_2} + 1.33M_{HI}, \quad (5.1)$$

where factor 1.33 accounts for the helium abundance. As a result, the total gas and stellar mass fraction can be written as  $f_{star} = M_*/M_{bar}$ ,  $f_{H_2} = M_{H_2}/M_{bar}$ ,  $f_{HI} = M_{HI}/M_{bar}$ . In our sample of galaxies, we find the range  $0.03 \leq f_{star} \leq 0.94$  for the stellar mass fraction,

<sup>3</sup>To derive the gas mass, we used scaling relations that hold for  $9.0 \leq \log(M_\odot) \leq 11.8$ ; therefore, we excluded one galaxy ('U-HiZ\_z1\_201') with  $\log(M_\odot) < 9.0$ .

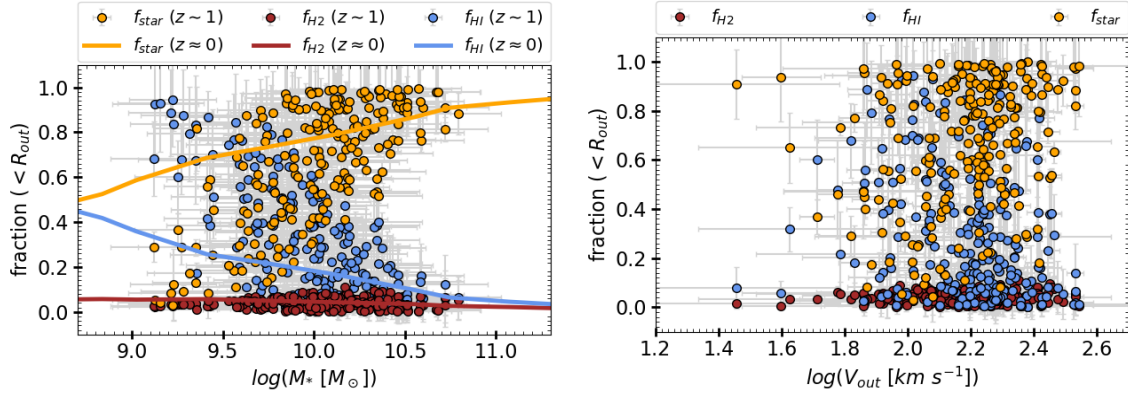


**Figure 5.1:** Stellar and gas mass fraction of our sample as a function of stellar mass and circular velocity (left and right panel, respectively) within the outer radius ( $R_{out}$ ; i.e. visible region). The color code in both panels is the same and given as follows: the brown filled circles represent the molecular gas mass fraction ( $f_{H2} = M_{H2}(< R_{out})/M_{bar}(< R_{out})$ ), the orange filled circles indicate the star mass fraction ( $f_{star} = M_*(< R_{out})/M_{bar}(< R_{out})$ ), and the blue filled circles represent the atomic gas mass fraction ( $f_{HI} = M_{HI}(< R_{out})/M_{bar}(< R_{out})$ ). A comparison study of local late-type galaxies from [Calette et al. \(2018\)](#) is drawn by solid lines; the color coding is same as the high-redshift objects.

$0.01 \leq f_{H2} \leq 0.05$  for the H2 (molecular gas) mass fraction, and  $0.04 \leq f_{HI} \leq 0.95$  for the HI (atomic gas) mass fraction. In Figure [5.1] these fractions are plotted as a function of stellar mass and circular velocity (left and right panels, respectively) of a galaxy. Firstly, we notice that the molecular gas fraction is small in the visible region ( $\sim 5\%$ ) and remains constant as a function of the stellar mass and the circular velocity. Therefore, we argue that at  $z \sim 1$  molecular gas does not play a significant role in the kinematics, as occurs in the local star-forming galaxies. Secondly, we observe a gradual decrease (increase) in the mass fraction of the atomic gas (stars) as a function of stellar mass. In particular, at the lower mass end ( $\leq 10^{9.5} M_{\odot}$ ) HI dominates, while at higher mass ( $\geq 10^{10.2} M_{\odot}$ ) stars dominate. At intermediate masses ( $10^{9.5-10.0} M_{\odot}$ ), the fraction of HI and stellar masses is almost 50-50% (see left panel Figure 5.1).

We compare our baryon mass fraction results with local late-type galaxies ([Calette et al., 2018](#)) shown by solid lines in the left panel of the Figure [5.1]. We note that the objects with  $M_* > 10^{10} M_{\odot}$  tend to have a similar gas and stellar mass fraction as local late-type galaxies, while low-mass  $M_* < 10^{10} M_{\odot}$  objects seem to have a higher HI fraction independent of the local objects. We note that the H2 fraction remains the same. From the comparison of  $z \sim 1$  and  $z \sim 0$  baryon fractions, a key feature of galaxy evolution emerges, suggesting that the galaxies in our sample are in the middle of their evolutionary path<sup>4</sup>. The brightest (most massive) galaxies appear to be depleting their gas reservoir faster than the faintest galaxies, and because they exhibit this behavior, they appear to be present-day spiral galaxies.

<sup>4</sup>Evolutionary path, a period in which a galaxy gradually accumulates mass and increases in size.

### 5.2.2 Baryonic Mass Within the Characteristic Radii

Our goal is to calculate the dark matter fraction of our galaxies within  $R_e$ ,  $R_{opt}$ , and  $R_{out}$ , and therefore we must first determine the baryonic masses within these radii. In our Chapter 4, we found that the kinematics of the Q12 sample is similar to local star-forming disc galaxies. This suggests that the radial distribution of stellar and molecular gas masses within these galaxies can be well approximated by the Freeman disc (Freeman, 1970b):

$$\begin{aligned} M_*( < R) &= M_*^{tot} \left[ 1 - \left( 1 + \frac{R}{R_*} \right) \exp\left(\frac{-R}{R_*}\right) \right] \\ M_{H2}(< R) &= M_{H2}^{tot} \left[ 1 - \left( 1 + \frac{R}{R_{H2}} \right) \exp\left(\frac{-R}{R_{H2}}\right) \right] \\ M_{HI}(< R) &= M_{HI}^{tot} \left[ 1 - \left( 1 + \frac{R}{R_{HI}} \right) \exp\left(\frac{-R}{R_{HI}}\right) \right] \end{aligned} \quad (5.2)$$

where stars are assumed to be distributed in the stellar disc ( $R_* = R_D$ ) known from photometry, discussed in Section 3.2.1.2. The molecular gas is generally distributed outward through the stellar disc (up to the length of the ionized gas  $R_{gas}$ ); therefore, we take  $R_{H2} \equiv R_{gas}$ . Here, we estimate the gas scale length  $R_{gas}$  by fitting the  $H_\alpha$  surface brightness. We assume molecular and atomic gas has a spatial distribution described by an exponential profile

$$\Sigma_{gas} = \Sigma_0 \exp\left(\frac{-R}{R_{gas}}\right), \quad (5.3)$$

where  $\Sigma_0$  is central surface density and  $R_{gas}$  is gaseous disc scale length. To estimate the value of  $R_{gas}$ , we fit the observed surface density of ionized gas<sup>5</sup> following Equation 5.3 using Markov Chain Monte Carlo (MCMC) sampling. During the fitting procedure  $\Sigma_0$  and  $R_{gas}$  are the free parameter defined in the range  $1 \leq \log(\Sigma_0) \leq 9$  and  $-0.5 \leq \log(R_{gas} [\text{kpc}]) \leq 1.77$ , respectively. An example of best fit and posterior distribution is shown in Figure 5.2.

Moreover, studies of local disc galaxies have shown that the surface brightness of the HI disc is much more extended than that of the H2 disc (Fu et al., 2010, see their Fig. 5); see also Leroy et al. (2008) and Cormier et al. (2016). Therefore, we assume  $R_{HI} = 2 \times R_{H2}$ , which is a rough estimate, but still reasonable considering that at high-redshift no information is available on the  $M_{HI}$  (or  $M_{H2}$ ) surface brightness distribution. Thus, the Equation [5.2] allows us to estimate  $M_*$ ,  $M_{HI}$ , and  $M_{H2}$  within different radii ( $R_e$ ,  $R_{opt}$ , and  $R_{out}$ ).

---

<sup>5</sup>In principle star formation is embedded in the molecular gas clouds; therefore, surface density of ionized gas can be used to trace the gas distribution.

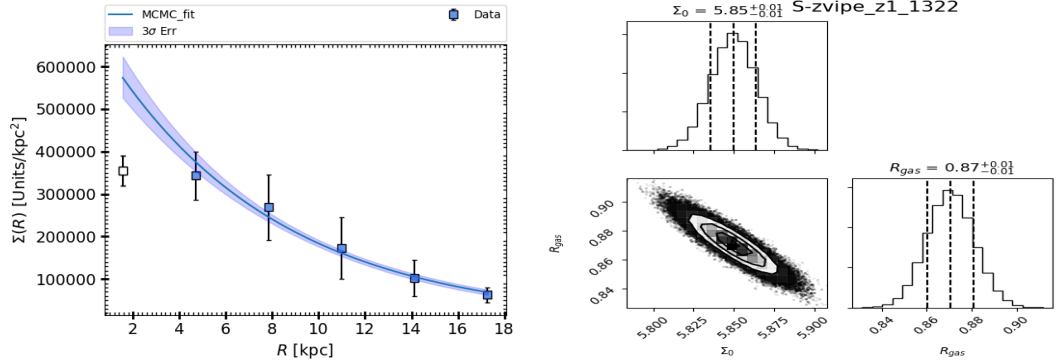


**Figure 5.2:** *Upper panel:* Observed surface brightness of  $H_{\alpha}$  gas. The MCMC fit is shown in blue accompanied by  $1\sigma$  error (blue shaded area). The first point (open square) is not used in fitting owing to the limitation assigned by 3DBarolo (discussed in Section 4.3). The value  $\Sigma_0$  keeps the dimension units/kpc $^2$ , where units = ergs $^1$ cm $^{-2}$  $\mu^{-1}$  1e + 17 km/s. *Lower panel:* Posterior distribution of  $\Sigma_0$  and  $R_{gas}$ , where vertical dashed lines show the 16, 50, 84 percentiles from left to right, respectively.

### 5.2.3 Dynamical Mass Estimates

The dynamical mass of a galaxy is defined as

$$M_{dyn}(< R) = \kappa(R) \frac{V^2(R) R}{G}, \quad (5.4)$$

where  $V(R)$  is the circular velocity computed at radius  $R$  and  $\kappa(R)$  is the geometric factor accounting for the presence of a stellar disc alongside the spherical bulge and halo (see (Persic & Salucci, 1990)). For  $R_e$ ,  $R_{opt}$ , and  $R_{out}$ , the values of  $\kappa$  are 1.2, 1.05, and 1.0, respectively. We favor a model-independent approach to determine the baryonic, dynamical, and dark matter masses at a given radius  $R$ , which differs from the standard rotation curve mass decomposition method, where  $M_{bar} + M_{DM} \simeq M_{dyn}$ . In Chapter 5, I will study the latter, while in this chapter we have investigated the former.

In Figure 5.3, we show the results of the dynamical mass within  $R_{out}$  as a function of stellar and baryonic mass in the left and right panels, respectively. We find that the baryonic masses generally do not exceed the dynamical masses, and a dark matter component occurs in all objects, as implied independently of their rotation curve profiles. Only a few galaxies are located in the forbidden region; however, they are consistent with  $M_{bar} \leq M_{dyn}$  within the  $1\sigma$  uncertainty intervals.<sup>6</sup>

The bulge mass contribution within 5 kpc is negligible for local spirals; therefore, we do not model it. However, we emphasize that the stellar masses derived from the absolute H-band magnitude (via their M/L ratio) include the bulge mass. Moreover, the geometric parameter  $\kappa(R)$  in the dynamical mass calculation takes into account the distribution of the mass located in the bulge and in the disc.

<sup>6</sup>In this work the stellar, gaseous ( $H_2$ ,  $HI$ ) and dynamical masses were calculated independently using different methods, which have their own errors (and systematic). Therefore, it is possible to encounter the situation where  $M_{dyn} < M_{bar}$ .

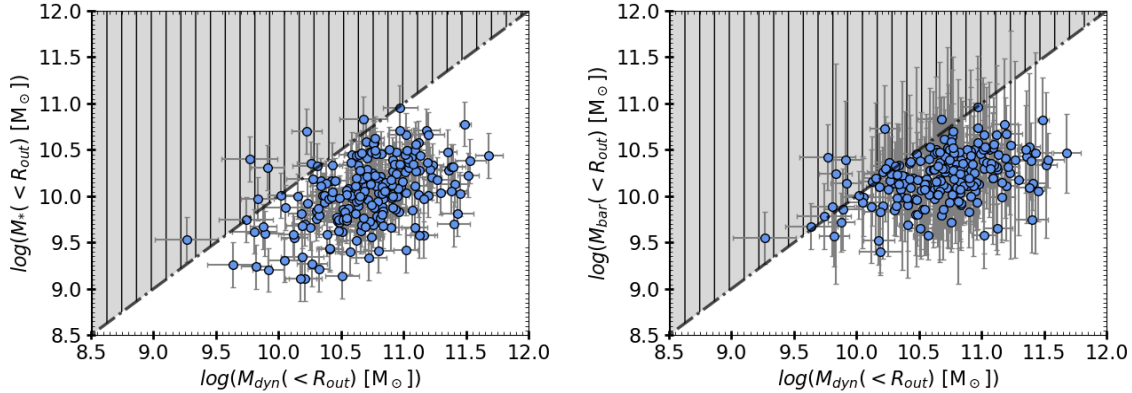


**Figure 5.3:** Stellar and baryonic masses as a function of dynamical mass (left and right panels, respectively), computed within  $R_{out}$ . The notations and color codes are the same in both panels and are given as follows: the blue filled circles represent the data, the dot-dashed black line shows the one-to-one plane, and the hatched-shaded gray area represents the forbidden region.

### 5.3 Dark Matter Fraction

Given the information on bayonic and dynamical masses, the dark matter fractions within radius  $R$  can be computed as

$$f_{DM}(< R) = 1 - \frac{M_{bar}(< R)}{M_{dyn}(< R)}. \quad (5.5)$$

Therefore, using Equation 5.5, we computed  $f_{DM}$  within  $R_e$ ,  $R_{opt}$ , and  $R_{out}$  for all galaxies. We note that owing to the limited spatial resolution in our rotation curves, the measurements of  $f_{DM}$  within  $R_e$  are less accurate than for  $R_{opt}$  and  $R_{out}$ . In the following subsection we demonstrate the dark matter fraction of individual objects as well as in terms of ensemble averages.

Individual galaxies: In the upper panel of Figure [5.4], the dark matter fractions within  $R_{out}$  are plotted as a function of stellar mass; objects are color coded according to the circular velocity computed at  $R_{out}$ . First, it is noticeable that for a given stellar mass, the dark matter fraction seems to increase with increasing circular velocity, whereas the dark matter fraction shows a (shallow) decrease with increasing stellar mass. It is important to stress that both the baryonic and dynamical masses are determined with independent methods that have non-negligible errors; this affects the determination of the dark matter fraction and its errors ( $\delta f_{DM}(< R_{out})$ ). A typical value of  $\delta f_{DM}(< R_{out})$  is  $\pm 0.2$ ; however, at inner radii the uncertainties on the dark matter fraction reaches 0.4. Second, at  $R_{out}$  only  $\sim 20\%$  of the objects have  $f_{DM}(R_{out}) < 0.5$ . Noticeably, the objects with a low dark matter fraction ( $f_{DM} < 0.5$ ) are not always the most massive but cover the broad stellar mass range  $\log(M_* [M_{\odot}]) \approx 9.2 - 10.7$ , irrespective of the local spirals (Salucci, 2019). Moreover, only 8% objects fall in the forbidden region. This is very likely due to i) the

Bin No.	$N_{Obj}$ [dpts]	$\log(\overline{M}_*)$ $[M_\odot]$	$\overline{z}$	$\overline{f_{DM}}(< R_{out})$	$\overline{f_{DM}}(< R_{opt})$	$\overline{f_{DM}}(< R_e)$
1	50	$9.59^{+0.11}_{-0.49}$	$0.84^{+0.00}_{-0.01}$	$0.79^{+0.05}_{-0.18}$	$0.73^{+0.06}_{-0.08}$	$0.71^{+0.08}_{-0.11}$
2	50	$9.89^{+0.13}_{-0.12}$	$0.84^{+0.01}_{-0.01}$	$0.76^{+0.01}_{-0.11}$	$0.70^{+0.03}_{-0.03}$	$0.75^{+0.03}_{-0.00}$
3	50	$10.12^{+0.07}_{-0.10}$	$0.84^{+0.02}_{-0.03}$	$0.73^{+0.01}_{-0.06}$	$0.66^{+0.03}_{-0.05}$	$0.66^{+0.01}_{-0.05}$
4	50	$10.35^{+0.12}_{-0.16}$	$0.86^{+0.02}_{-0.04}$	$0.65^{+0.04}_{-0.03}$	$0.65^{+0.07}_{-0.04}$	$0.62^{+0.06}_{-0.11}$
5	27	$10.59^{+0.37}_{-0.12}$	$0.90^{+0.03}_{-0.02}$	$0.43^{+0.11}_{-0.03}$	$0.30^{+0.2}_{-0.06}$	$0.40^{+0.07}_{-0.21}$

**Table 5.1:** Results of the binned dark matter fraction. For binning, the objects are first sorted into ascending stellar masses. Then affine binning is performed and 50 objects are allowed per bin. There are a total of 227 objects, so the final bin contains only 27 objects. To perform the binning, RMS statistics and the errors estimated from bootstrap iterations are used. *Col. 1:* Bin number; *Col. 2:* number of objects (or data points) per bin; *Col. 3:* binned stellar masses and their errors showing the minimum and maximum boundaries of each bin, lower and upper bounds respectively; *Col. 4:* binned redshift; *Cols.-5-7:* binned dark matter fraction within  $R_{out}$ ,  $R_{opt}$ , and  $R_e$ , respectively. Here  $1\sigma$  errors are given for each data point (except stellar masses). A catalogue of the individual quantities is published along with this table; see [Sharma \(2021, catalog\)](#).

measurement errors discussed above, ii) declining rotation curves, or iii) determination of the rotation curves themselves.

In the lower panel of Figure [5.4], we investigate the increase in the dark matter fraction from the optical to the outer radius by plotting  $f_{DM}(R_{opt})$  versus  $f_{DM}(R_{out})$ . As expected, 80% of the objects have  $f_{DM}(R_{out}) > f_{DM}(R_{opt})$ ; that is, in the majority of the objects dark matter fraction increases with radius. However, we note that the perturbed or declining rotation curves severely affect the 20% of objects showing  $f_{DM}(R_{out}) < f_{DM}(R_{opt})$ . We will address this problem in our follow-up work, in which we plan to mass model the individual rotation curves using the component separation method and then determine the dark matter fraction at various radii. In this work, we proceed by averaging the various dark matter fractions.

Ensemble averages : In our work, we focused primarily on the study of individual objects. However, to compare our results with previous studies, we average the dark matter fraction in a suitable number of stellar mass bins. In particular, we employ affine binning of our 225 objects, keeping 50 objects per bin, and the last bin contains 25 objects. To perform the binning, we use the root mean square statistic (RMS), and the errors are estimated from bootstrap iterations. For each bin, we iterate 500 times, and 50% samples are taken in each run. Then the errors are assigned for the 68th, 95th, and 99th percentiles (of the scatter). The binning details are further explained and tabulated in Table[5.1]. For simplicity, the averaged quantities are denoted by bar, for example,  $\overline{M}_*$

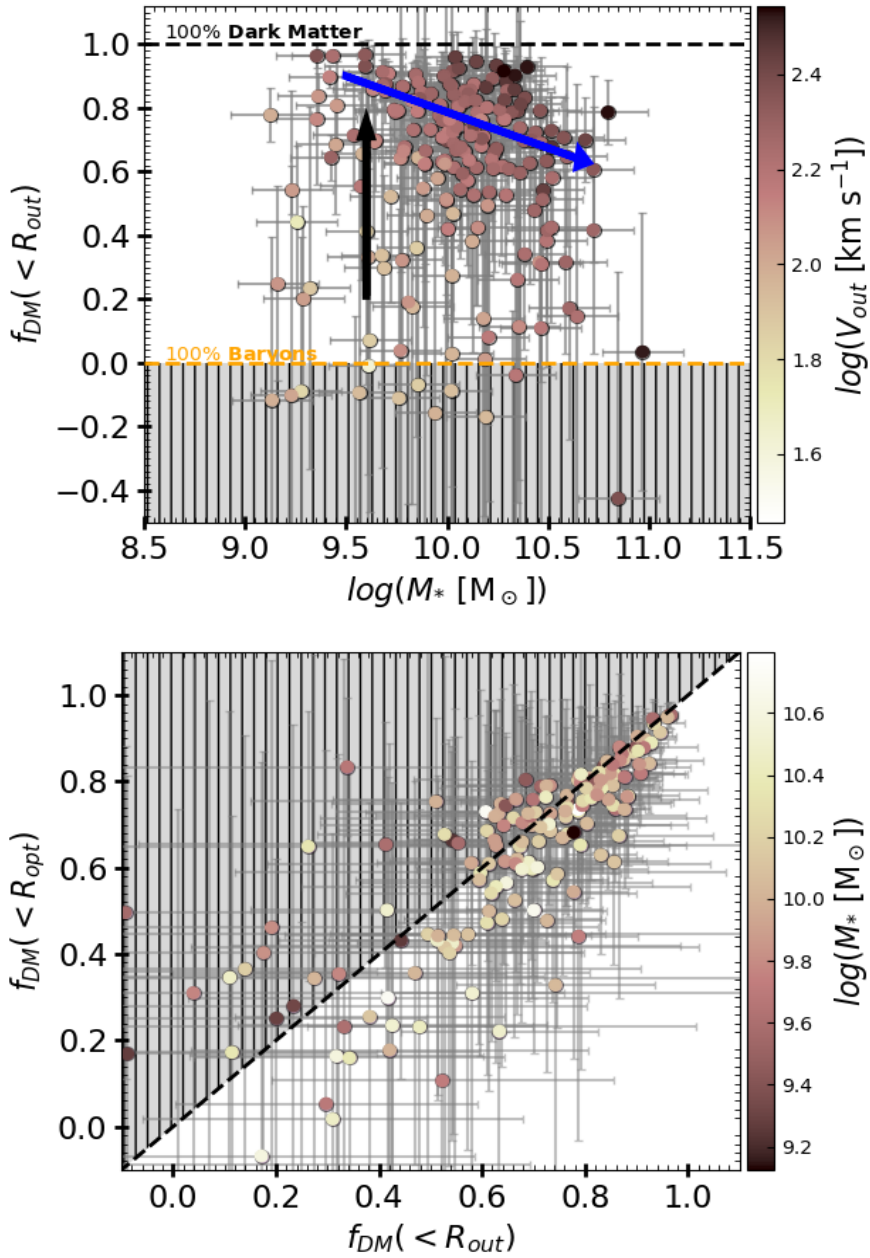


**Figure 5.4: DM fraction of individual galaxies.** *Upper panel:* Dark matter fraction within  $R_{out}$  as a function of stellar mass ( $M_*$ ), color coded by the circular velocity ( $V_{out}$ ) computed at  $R_{out}$ . The horizontal yellow and black dashed lines show the 100% baryon and dark matter regimes, respectively. The gray shaded area shows the forbidden region. The black arrow indicates that, for a given stellar mass, the fraction of dark matter in the galaxies increases with increasing circular velocity. The blue arrow shows a shallow decrease in the dark matter fraction with increasing stellar mass. *Lower panel:*  $f_{DM}(< R_{opt})$  vs.  $f_{DM}(< R_{out})$ , color coded by stellar mass. The gray shaded area represents the not allowed region (i.e.  $f_{DM}(< R_{out}) \neq f_{DM}(< R_{opt})$ ). The black dashed line shows the one-to-one relation. For the clarity of the figure (in the lower panel), objects below zero are not shown.

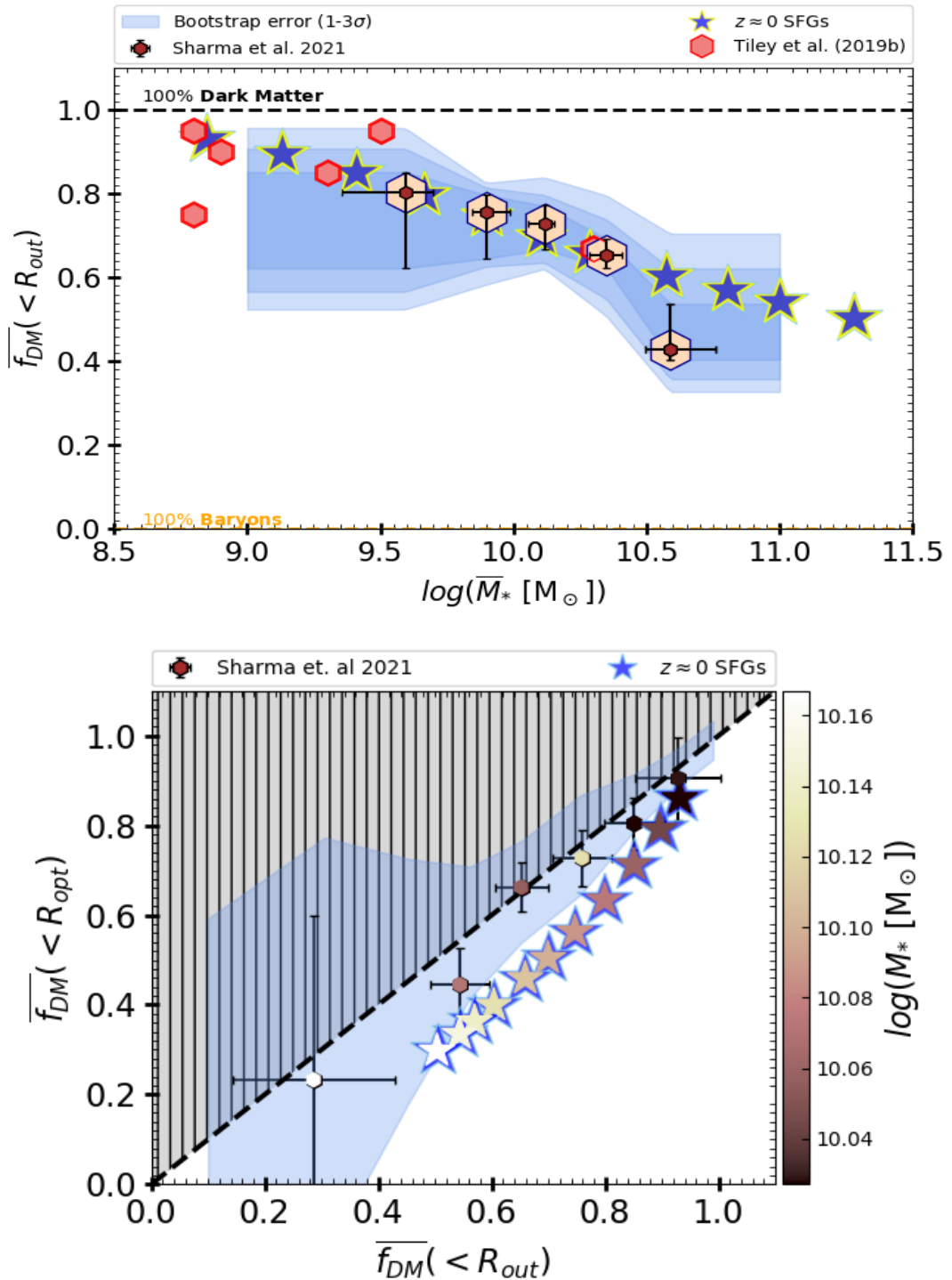


**Figure 5.5: dark matter fraction of ensemble averages.** *Upper panel:* Dark matter fraction within  $R_{out}$  as a function of stellar mass ( $\overline{M}_*$ ). The brown hexagons with error bars shielded by big light-peach hexagons represent our averaged data, and the blue shaded area shows the 1, 2, and  $3\sigma$  error at dark matter fraction. For comparison, we show the local star-forming disc galaxies (Persic et al., 1996) represented by the blue stars (in both panels), where the size of the marker represents the uncertainty in the values. The red hexagon represents the  $z \sim 1$  star-forming galaxies (Tiley et al., 2019b). *Lower panel:*  $\overline{f}_{DM}(< R_{opt})$  vs.  $\overline{f}_{DM}(< R_{out})$ , color coded by stellar mass. The gray shaded area represents the theoretically not allowed region (i.e.  $\overline{f}_{DM}(< R_{out}) \neq \overline{f}_{DM}(< R_{opt})$ ). The blue shaded area shows the maximum scatter in the relation. The lower panel interior of blue stars are color coded by stellar mass.

and  $\overline{f_{DM}}$ . We note that for the stacked data, we plot the  $1\sigma$  error on dark matter fraction and its maximum scatter ( $1 - 3\sigma$ ) is shown by the blue shaded regions. On the other hand, for stellar mass (being the running variable of the bin) we plot  $3\sigma$  errors, which directly shows the maximum deviation from the mean ( $\overline{M_*}$ ).

In upper panel of Figure 5.5, we show the same results as in the upper panel of Figure 5.4, but for the averaged dataset. From the upper panel, we can clearly see that the dark matter fraction weakly decreases with increasing stellar mass, and galaxies are dark matter dominated ( $\overline{f_{DM}}(< R_{out}) > 50\%$ ) at any stellar mass value ( $\log(\overline{M_*} [\text{M}_\odot]) \approx 9.5 - 10.0$ ). Similarly, in the lower panel of Figure 5.5 we show the same results as in lower panel of Figure 5.4, but for the averaged dataset. In detail, we binned the lower panel of Figure 5.4, in six  $f_{DM}(< R_{out})$  bins namely [0.0-0.5, 0.5-0.6, 0.6-0.7, 0.7-0.8, 0.8-0.9, 0.9-1.0], using RMS statistics and errors are  $\sqrt{\sigma_i^2/n}$  in each bin.<sup>7</sup> We can clearly see that the  $\overline{f_{DM}}(R_{out})$  is always larger than  $\overline{f_{DM}}(R_{opt})$ ; that is, the mass of dark matter increases with radius. Both panels of Figure 5.5 show that all of our ensemble averages have  $\overline{f_{DM}} \geq 50\%$  within  $R_{opt}$  till  $R_{out}$ , except for one data point at higher stellar mass. Nevertheless, ensemble averages of dark matter fraction in stellar mass bins, shown in Table 5.1, shows that  $\overline{f_{DM}}(< R_{out}) > \overline{f_{DM}}(< R_{opt}) > \overline{f_{DM}}(< R_e)$ , which validates our measurements.

## 5.4 Results & Discussion

In chapter 4 we showed that the outer rotation curves of  $z \sim 1$  star-forming galaxies (having  $v/\sigma > 1$ ) are similar to those of local ( $z \approx 0$ ) star-forming disc galaxies (Persic et al., 1996). In this work, we intend to compare the dark matter fraction of  $z \sim 1$  star-forming galaxies ( $v/\sigma > 1$ ) with those of  $z \approx 0$  star-forming discs. The results are shown in Figure 5.5. In the upper panel, we note that star-forming galaxies at  $z \sim 1$  and  $z \approx 0$  follow a similar trend in the  $f_{DM} - \overline{M_*}$  plane; these star-forming galaxies also seem to have almost the same fraction of dark matter in the outer radius. In the lower panel of Figure 5.5, we again observed a similar dark matter behavior as in the locals, but with a relatively higher dark matter fraction inside  $R_{opt}$ , which suggest that the radial profile of dark and luminous matter has evolved in the past 7 Gyrs. This could be because at  $z \sim 1$  the dark matter halo has already formed, while the stellar disc inside  $R_{opt}$  is still in the process of formation.

Our results are in fair agreement with those of Tiley et al. (2019b) of similar star-forming galaxies. In particular, their sample lies in the redshift range  $0.6 \lesssim z \lesssim 2.2$ ; therefore, we narrowed down their sample to the galaxies that lie between  $0.7 \lesssim z \lesssim 1.0$  and over-plotted them in Figure 5.5. As shown in the plot, there is a good agreement between the two studies. We note that Tiley et al. (2019b) computed  $\overline{f_{DM}}$  within  $6 R_D$ , while we compute within  $R_{out} = 5 R_D$ .

Next, we compared our work with Genzel et al. (2017); Drew et al. (2018), and Übler et al. (2018); see Figure 5.6. In these studies,  $f_{DM}$  is computed within  $R_e$ , where our

<sup>7</sup>where  $\sigma_i$  is standard deviation and  $n$  is the number of objects per bin.

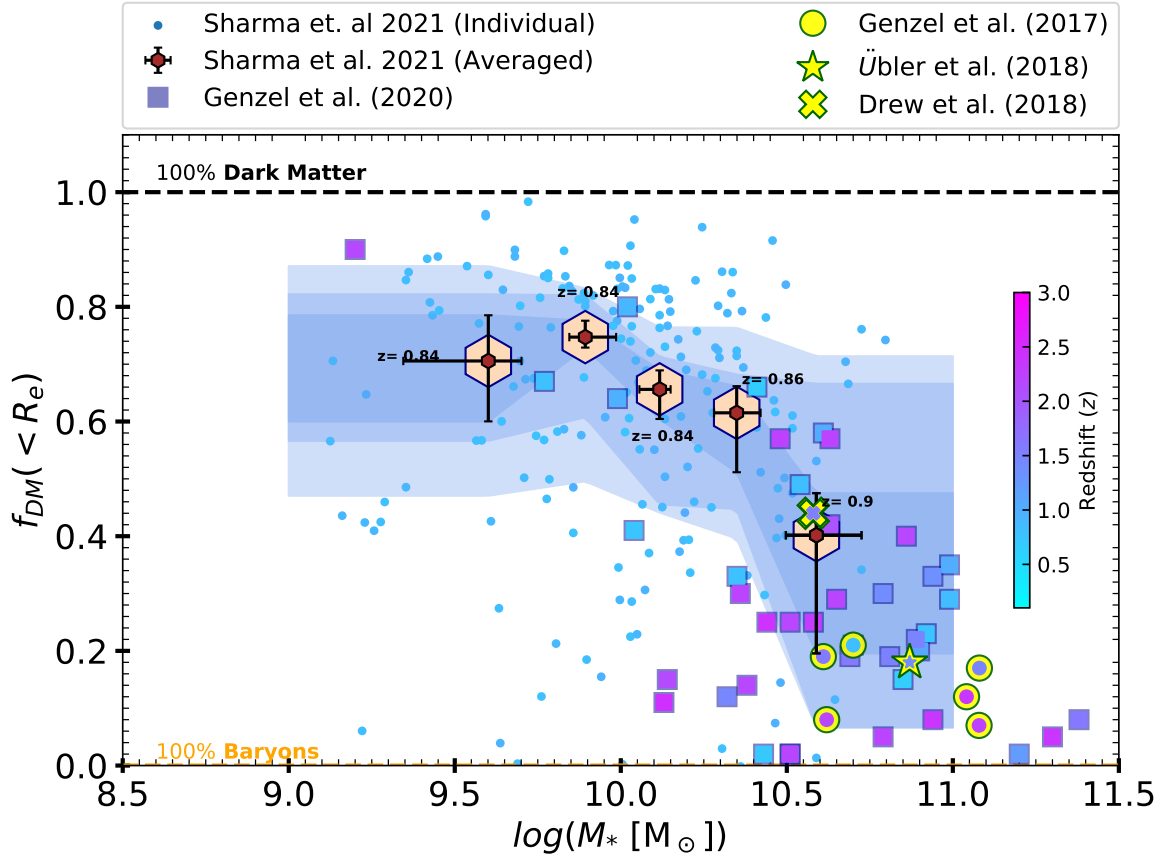


**Figure 5.6:** Comparison of averaged dark matter fraction (within  $R_e$ ) of our sample with previous high-redshift studies. We plot the dark matter fraction as a function of stellar mass, color coded by redshift. The brown hexagons with error bars shielded by big light-peach hexagons represent our averaged dataset, and individual galaxies are shown by small dots, color coded by redshift. The blue shaded area represents the  $1 - 3\sigma$  error on the dark matter fraction. Genzel et al. (2020) data are shown by filled squares. The measurements of Genzel et al. (2017), Drew et al. (2018), and Übler et al. (2018) are shown by yellow circles, a star and a cross, respectively, where the interior of each marker is color coded by redshift.

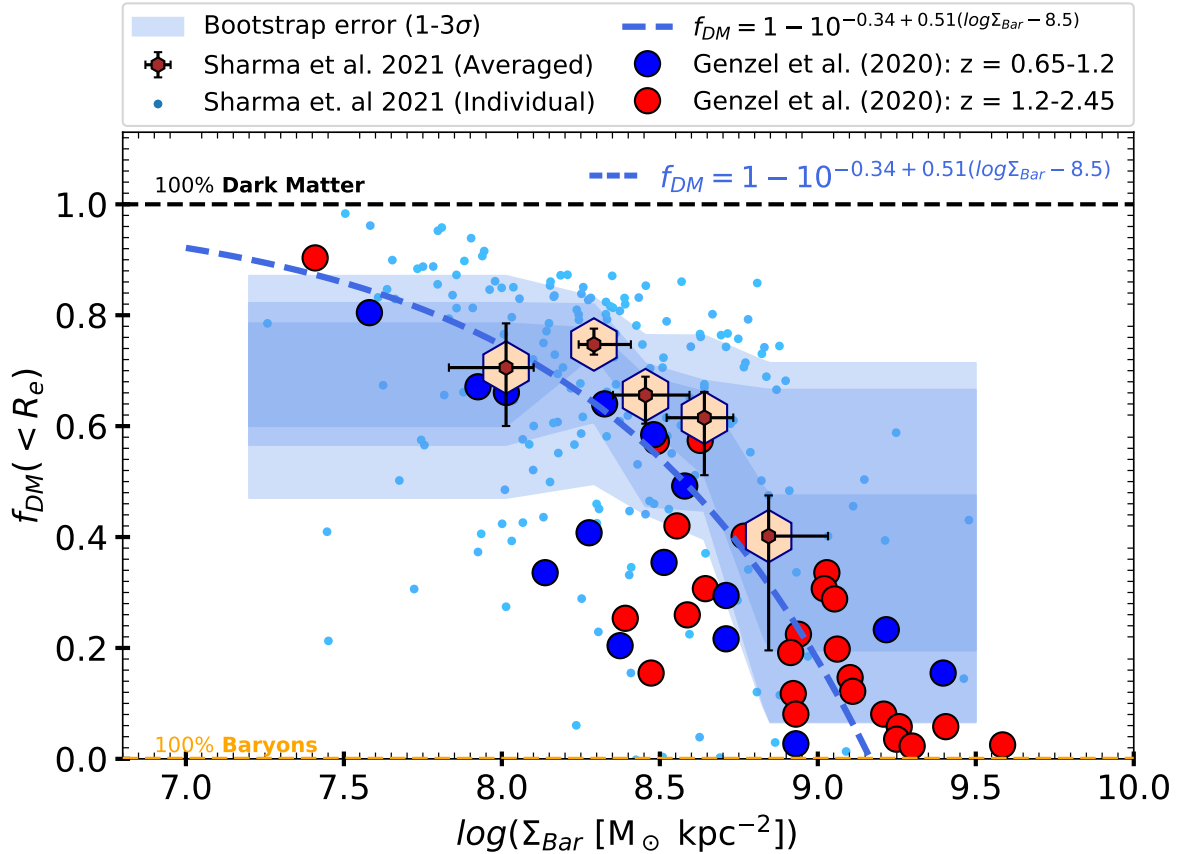


**Figure 5.7:** Dark matter fraction as a function of baryon surface density  $\Sigma_{Bar}(< R_e) = M_{bar}(< R_e)/\pi R_e^2$ . The brown hexagons with error bars shielded by big light-peach hexagons represent our averaged dataset, and individual galaxies are shown by small dots, color coded by redshift. The blue shaded area represents the  $1 - 3\sigma$  error on the dark matter fraction. The dashed blue line shows the relation  $f_{DM}(< R_e) = 1 - 10^{-0.34+0.51(\log \Sigma_{Bar} - 8.5)}$  given by Genzel et al. (2020) and their data are plotted in blue ( $z = 0.65 - 1.2$ ) and red ( $z = 1.2 - 2.45$ ) filled circles.

rotation curves are not spatially resolved and thus  $f_{DM}(< R_e)$  is subject to larger uncertainties than  $f_{DM}$  within  $R_{opt}$  and  $R_{out}$ . Even so our four massive ( $\log(M_*) \sim 10.5 - 10.9$ ) galaxies with  $f_{DM}(R_{out}) < 0.2$  are very close to the results of Genzel et al. (2017) and Übler et al. (2018). Moreover, we agree closely with Drew et al. (2018). We also compare our work with the recent work of Genzel et al. (2020) (squares color coded for redshift). Their sample has seven objects with  $9.0 \lesssim \log(M_*) \lesssim 10.5$  within the redshift range of  $0.5 < z \lesssim 1.0$  and have a dark matter fraction  $\geq 0.5$ ; these values agree well with our individual dark matter fraction within  $R_e$ . However, the ensemble mean of dark matter fraction within  $R_e$  is always greater than 40%, showing dissimilarity with the majority of Genzel et al. (2020) objects. In particular, the mean of the massive bins for which  $([\log(\bar{M}_*), \bar{f}_{DM}, \bar{z}] = [10.6, 0.53, 0.9])$  shows a much higher dark matter fraction than Genzel et al. (2020). We would like to emphasize that the majority of their sample<sup>8</sup> have high stellar masses ( $\log(M_*) > 10.5$ ) and a low dark matter fraction ( $f_{DM} < 35\%$ ), which is not the case for our sample.

Moreover, we also compared our results with the  $f_{DM}(< R_e)$  versus  $\Sigma_{Bar}(< R_e)$  relation put forward by Genzel et al. (2020) (see Figure 5.7), where  $\Sigma_{Bar}(< R) = M_{bar}(< R)/\pi R^2$ . This relationship can be pivotal for both the dark matter nature and evolution of disc galaxies. We note that for low surface brightness ( $\log(\Sigma_{Bar}(< R_e) \text{ M}_\odot \text{ kpc}^{-2}) < 8.7$ ) galaxies, their relation is in fair agreement with our data, but at high  $\Sigma_{Bar}$  it underestimates dark matter fractions. We suspect that the high bulge-to-total (B/T) disc ratio used in Genzel et al. (2020) artificially reduces the dark matter within the effective radius.

Furthermore, while the dark matter -fractions at  $z \sim 1$  and  $z \sim 0$  are roughly the same, the scatter in the  $f_{DM} - M_*$  relation suggests that these galaxies are still in the process of building (or acclimating) the distribution of baryons and dark matter that is, they are at different stages of their disc formation. However, it could also be due to the diversity in the dark matter halo properties (e.g. concentration and core radius or density), which are closely coupled to the properties of the baryonic matter (e.g. halo spin parameter and baryon fraction).

## 5.5 Summary

In this chapter, we have studied the fraction of dark matter in  $z \sim 1$  star-forming galaxies. We used our previous study of rotation curves (performed in Chapter 3) to compute accurate dynamical masses. In particular, we exploit 225 high-quality galaxies from the Q12 sample. This sample lies between redshift  $0.7 \lesssim z \lesssim 1.0$  with stellar masses  $\log(M_* [\text{M}_\odot]) = 9.0 - 11.0$  and circular velocities  $\log(V_{out} \text{ km s}^{-1}) = 1.45 - 2.83$ . We estimate the total baryonic masses using scaling relations of atomic and molecular gas masses given by Lagos et al. (2011) and Tacconi et al. (2018) respectively (see Section [3.2.1 & 5.2.1]). Subsequently, the dark matter fractions were computed using dynamical mass estimates from rotation curves. In Section [5.3], we showed that only  $\sim 6\%$  of objects have low dark matter fractions ( $0.0 < f_{DM} \leq 0.2$ ), but these objects are not

---

<sup>8</sup>We compare SED driven stellar masses of the Genzel et al. (2020) sample.

necessarily massive. That is, a low dark matter fraction can also be found in low-mass galaxies ( $\log(M_*/[\mathrm{M}_\odot]) < 9.5$ ); however, uncertainties are higher there. Nonetheless, the majority ( $\gtrsim 72\%$ ) of sample contains dark matter dominated ( $f_{DM} \gtrsim 0.5 - 0.99$ ) discs with a median radius  $\sim 9$  kpc (see Figure [5.4], [5.5] and [5.6]). These results are in agreement with a previous high-redshift study of the dark matter fraction of [Tiley et al. \(2019b\)](#) and are also consistent with local star-forming disc galaxies ([Persic et al., 1996](#)). Therefore, we conclude that:

1. The majority of star-forming disc-like galaxies ( $v/\sigma > 1$ ) at  $0.7 \lesssim z \lesssim 1.0$  have outer ( $\approx 5 - 9$  kpc) discs dominated by dark matter (see Figure 5.4 & 5.5).
2. Baryon-dominated galaxies exist at high-redshift similar to the local Universe, but they are very few (20%).
3. Star-forming galaxies at  $z \sim 1$  have similar or slightly higher ( $\sim 20\%$ ) dark matter fractions than the local ones within  $R_{opt}$  (see Figure 5.5).
4. The scattering in the dark matter fractions at given stellar masses and circular velocities is larger at  $z \sim 1$  than at  $z \sim 0$ . We interpret this as a consequence of ongoing galaxy formation or processes of evolution.

To gain a more fundamental understanding of the results presented in this chapter, as well as on the earlier findings, next, I worked on the mass decomposition of rotation curves (see Chapter 6), which sheds light on the structural properties of dark matter and its interplay with baryons.

# Chapter 6

## Structural Properties of Dark Matter Halos

In the late 1970s, Vera Rubin, showed that flat rotation curves are ubiquitous in local spiral galaxies and concluded that “*galaxies are surrounded by a dark matter halo which extends much further than their visible matter.*” These observational results were later supported by the theoretical models of structure formation (Ostriker & Peebles, 1973). Now, in the concordance cosmological models dark matter dominates the mass budget of galaxies, it is cold, collisionless and interacts with baryonic matter only via gravity. However, its nature has remained illusive. Recent studies of hundreds of galactic rotation curves in the local Universe suggest that dark matter halos contain a *core* with density profile:  $\rho_0 \propto r_0^0$  at their center (de Blok et al., 2001; Karukes & Salucci, 2017). This is at odds with the otherwise extremely successful predictions of cosmological N-body simulations, which result in central *cusps*:  $\rho_s \propto r_s^{-1}$  (Bullock et al., 2001), and is often referred to as the “*cusp-core problem*”. In the context of galaxy formation, the development of hydro-dynamical simulations (Schaye et al., 2015; Pillepich et al., 2018) have shown that baryonic processes (e.g. feedback from active galactic nucleic, dynamical friction) at galactic scale impact upon the distribution of dark matter over cosmic time-scales, i.e. dark matter cusps can be transformed into cores over several Gyrs. However, these results are strongly dependent on the assumptions and the implementation of the prescription used to describe the physics which occurs on the scales well below the resolution limit of the simulations (the so-called “sub-grid” physics). Therefore, I believe that ‘cusp to core transformation’ problem can be addressed through observations. Especially, now that we have data and techniques to deal with high-redshift observations. This is why, in this chapter, I present a pilot study to explore the structural properties of dark matter, i.e. inner dark matter density and radius over cosmic time, and conclude the results in the context of cusp to core transformation issue.

**Preamble:** *The majority of the work presented in this chapter has been accepted for publication in A&A (see Sharma et al., 2021a). To highlight certain aspects with more clarity, here, I may have included some additional illustrations and descriptions.*

## 6.1 Introduction

Dark Matter (DM) is a type of matter that astrophysicists have brought forward to account for the observational effects that appear to be due to the presence of an invisible massive component (öpik, 1915; Kapteyn, 1922; Jeans, 1922; Oort, 1932; Zwicky, 1933; Smith, 1936; Roberts & Rots, 1973; Rubin et al., 1978; Bosma, 1981; de Swart et al., 2017, and references therein). The astrophysical nature of such invisible matter can be inferred from its gravitational interaction on the luminous matter (Ostriker & Peebles, 1973; Persic & Salucci, 1988; Persic et al., 1996; Navarro et al., 1997; Sofue & Rubin, 2001; Salucci, 2019, and references therein) and the radiation emerges at different cosmological scales (Sunyaev & Zeldovich, 1969; Hu & Silk, 1993; Boehm & Schaeffer, 2005; Chluba & Sunyaev, 2011; Dvorkin et al., 2014; Slatyer & Wu, 2018; Ali-Haïmoud, 2019, and references therein). On the other hand, its particle nature, which is the centre of dark matter phenomenon is not yet characterized.

Recently, dark matter phenomenon was uniquely framed into the dark energy driven cold dark matter ( $\Lambda$ CDM) scenario (Steigman & Turner, 1985; Kolb & Turner, 1990b; Ellis, 2018), where non-relativistic dark matter can be described as a collision-less fluid, whose particle with cross-section of about  $10^{-26} \text{ cm}^2$ , only interact gravitationally and very weakly with standard model particles. This scenario emerges cosmologically very clearly (Peebles, 1993; Coles & Lucchin, 2002), has been confirmed by large scale observations (Einasto et al., 2017; Zaninetti, 2018, and references therein), can be investigated by appropriate simulations (Klypin, 1996; Vogelsberger et al., 2020, and references therein) and semi-analytical modelling (Kauffmann et al., 1993; Somerville & Primack, 1999; Lacey, 2001; Guo et al., 2011; Somerville & Davé, 2015, and references therein). As a consequence, a very well defined perturbation power law spectrum and lack of dependencies on the initial conditions, yields to a specific bottom-up formation and evolution of dark matter halos. However, two aspects in the progressive field of dark matter opposes the latter: 1) The search of dark matter particles, performed by various direct and indirect methods (e.g. Covi, 2013; Gaskins, 2016b), one of the major efforts of astro-particle physics, has been so far unsuccessful (Arcadi et al., 2018); 2) the main imprint of collision-less particle is a dark matter halo with cuspy central dark matter density ( $\rho \propto r^{-1}$ ), which is not present in the majority of local spirals, dwarf-discs and low surface brightness galaxies (e.g. Palunas & Williams, 2000; Salucci & Burkert, 2000a; de Blok et al., 2001; Karukes & Salucci, 2017; Di Paolo et al., 2019). Moreover, local galaxies show that the physical properties (e.g., luminosity and disc scale length) of luminous matter are deeply connected with the structural properties (e.g. dark matter core radius and core density) of dark matter (Salucci, 2019; Li et al., 2020, and references therein). This is very difficult to frame with collision-less particle, taking into account that most of the dark matter resides inside the galactic halo. These issues imply that in order to tackle the dark matter phenomenon, we need to refine the adopted dark matter scenario.

At this point, it is important to point-out that besides the structure of present-day dark matter halos, also the dark matter halo evolution through cosmic-time may reflect the nature of dark matter particle: in  $\Lambda$ CDM scenario, the collision-less nature of dark

particle is itself imprinted in the dark halo evolution with time (Ellis, 2018), which is well followed by hydrodynamical simulations (He, 2020). Also in the other scenarios of dark matter such as warm dark matter, Boson condensates, interacting dark matter ultra light axions etc., and alternative dark matter models such as Modified Newtonian Dynamics (MOND), one can find correspondence between properties of dark matter halos around local objects and those at high-redshift (hereafter high- $z$ ).

Along these lines of thought we must remind that, until recently, the determinations of high-redshift dark matter halo density profiles was impossible: the kinematical measurements lacked of sufficient sensitivity and spatial resolution. But, in the last decade, advanced use of integral field units (IFUs) in galaxy surveys has opened the several possibilities of studying the spatially resolved kinematics of high-redshift galaxies. For example, surveys with the Multi-Unit Spectroscopic Explorer (MUSE: Bacon et al. 2010), K-band Multi-Object Spectrograph (KMOS: Sharples 2014), the Spectrograph for INtegral Field Observations in the Near Infrared (SINFONI: Eisenhauer et al. 2003), and Atacama Large Millimeter/submillimeter Array (ALMA: Cox 2016).

In Chapter 3, I have used KMOS Redshift One Spectroscopic Survey (KROSS) data to derive the kinematics of large sample of  $z \sim 1$  star-forming disc-like galaxies. We have corrected such kinematics to proper rotation curves by correcting the issues related to high-redshift measurements, such as, beam-smearing and pressure-support conditions, see Section 2.4. In particular, we have used 3D-forward modelling of datacubes using  $3D$ Barolo (Teodoro & Fraternali, 2015), which provides somewhat better constraints on kinematics than 2D-kinematic modelling approaches, see Section 3.2.2. For pressure support, we employed the Pressure Gradient Correction (PGC) method, which make use of full information available in datacube and therefore provides better results than pressure support correction assuming isotropic and constant velocity dispersion, for details we refer reader to Section 3.2.3. These state-of-the-art techniques have provided us a large sample ( $> 200$ ) of accurate rotation curves of disc-like star-forming galaxies from  $z \sim 1$ , which I have individually (and statistically) analysed to determine the shape of the high-redshift rotation curves and dark matter content, as well as results are compared to local disc galaxies and previous high-redshift studies.

In Chapter 4, I showed that the outer rotation curves of  $z \sim 1$  star-forming galaxies are flat up to the last point of the observations, and they are very similar to local disc galaxies. However, due to the limited resolution, we could not say much about the inner rotation curves (below 5 kpc). We have also reported an evolution of the baryon distribution, which we expect from galaxy evolution models. In Chapter 5, I have employed a model-independent approach to determine the dark matter content of these galaxies. I clearly showed that the disc of star-forming galaxies is dominated by dark matter from 5 – 10 kpc, which is very similar to local disc galaxies. Now we know, that star-forming galaxies possess the flat rotation curves and dark matter dominated outer discs. Next, I have exploit the same rotation curve dataset to determine the structural properties of the dark matter, and compared them to the local disc galaxies.<sup>1</sup>

---

<sup>1</sup>The structural properties of dark matter are the functional parameters that define the density profile (or distribution) of dark matter in a halo. These can be either the inner/outer density and radius of the

In particular, I decompose the rotation curve of  $z \sim 1$  star-forming galaxies into their constituents that makes-up the rotation curve(stars, gas and dark matter), using dynamical mass modelling defined in Chapter 2 (Section 2.2.1). The latter approach allows us to determine the physical properties (e.g. stellar mass effective radius) dynamically, as well as structural properties of dark matter halo. In addition, dynamical modelling of rotation curves also provide us an alternative approach to determine the dark matter fraction. As mentioned earlier, in Chapter 5, I used a model-independent approach, which directly uses the galaxy kinematics to extract the dark matter content. Thus, studying these two approaches in parallel, have also allowed us to check the robustness of our dynamical models, which we show in this chapter. Through the mass-modelling techniques, we have also checked the scaling relations between dark and baryonic matter those emerged in local star-forming disc galaxies. Then, the phenomenologies of the dark matter at  $z \approx 0$  and  $\sim 1$  are compared with the aim that they provides us crucial information on the nature of dark matter. The chapter is organized as follows: Section 6.2 contains a brief summary of dynamical models and an approach to apply them on rotation curves. In Section 6.3, we show the results and critically analyse them. In Section 6.4.2, we compare our results with current state-of-art simulations. Finally in Section 6.5 and Section 6.6, we discuss the results and provide a summary.

## 6.2 Methodology

The technique of dynamical mass modeling used to decompose rotation curve into its constituents (stars, gas, and dark matter) is based on models defined by certain parameters that fit each constituent. For example, here I used the [Freeman \(1970b\)](#) disc to fit the stellar and gas components based on the following parameters: stellar disc radius  $R_D$ , stellar mass  $M_{\text{star}}$ , gas disc radius  $R_{\text{gas}}$ , gas mass  $M_{\text{gas}}$ . Note that stars are present in both the disc and the bulge; therefore, the stellar component is fitted twice, once for the bulge component having bulge of point mass  $M_{\text{bulge}}$ , and once for the stellar disc of mass  $M_D$ , i.e.  $M_{\text{star}} = M_{\text{bulge}} + M_D$ . The dark matter component is fitted with the NFW profile ([Navarro et al., 1996b](#)) and the Burkert profile ([Burkert, 1995](#)), defined by the inner density and the radius of the dark matter distribution  $(\rho_s, r_s)$  and  $(\rho_0, r_0)$ , respectively. The latter mass models are defined in great detail in Section 2.2.1, physical parameters are determined in Sections 3.2.1 & 5.2. A composite contribution of aforementioned component forms the rotation curve which can be described as a sum in quadrature of:

$$V_c^2(R) = V_D^2(R) + V_{\text{bulge}}^2(R) + V_{\text{H}_2}^2(R) + V_{\text{HI}}^2(R) + V_{\text{DM}}^2(R), \quad (6.1)$$

were  $V_D(R)$ ,  $V_{\text{bulge}}(R)$ ,  $V_{\text{H}_2}(R)$  and  $V_{\text{HI}}(R)$  are the circular velocity profiles of the stellar disc, bulge, molecular (H<sub>2</sub>) and atomic (HI) gas discs, together providing the baryon's contribution to the circular velocity and  $V_{\text{DM}}(R)$  gives the dark matter contribution. I have developed a technique which performs this complex modelling under Bayesian

---

dark matter or, the concentration of the halo. In some studies, the slope of the relation between inner dark matter density and radius is also considered as a structural parameter of dark matter.

inference and flexible models with realistic priors on baryonic components, and keeping dark matter structural parameters free. In the following sections, we present this technique to disentangle the aforementioned contributions from observed RCs. Note that we have corrected the observed RCs from inclination and pressure support, i.e. RCs are very close to being the circular velocity curves.

### 6.2.1 Rotation Curve Modelling

To perform the mass modelling of RCs, we define a  $\chi^2$  test-statistic on our observed kinematics  $V_o(R)$  and modelled kinematics  $V_m(R)$  as:

$$\mathcal{L}_{\text{kin}} \equiv \prod_{k=1}^N \frac{1}{\sqrt{2\pi} \Delta V_o(R_k)} \exp \left[ -\frac{1}{2} \left( \frac{V_o(R_k) - V_m(R_k)}{\Delta V_o(R_k)} \right)^2 \right], \quad (6.2)$$

For each bin  $k \leq N$ , we compare the theoretical prediction and observed dataset by including the observational uncertainty  $\Delta V_o(R_k)$  at each step. Our fitting procedure is based on Bayes' theorem:

$$\mathcal{P} \left( \text{Model}(\vec{\theta}) \mid \text{data} \right) \propto \mathcal{L}_{\text{kin}} \left( \text{data} \mid \text{Model}(\vec{\theta}) \right) \mathcal{P}_0 \left( \text{Model}(\vec{\theta}) \right), \quad (6.3)$$

where the posterior probability density function (p.d.f.) is sampled from the product of the prior probability distribution assigned to the set of model parameters  $\vec{\theta}$ , with the likelihood function reported in Equation 6.2, up to the overall normalization defining the so-called evidence of the model. The general model of RC under the Bayesian inference is defined by five parameters  $\vec{\theta} = \{M_D, R_D, M_{\text{bulge}}, r_{0/s}, \rho_{0/s}\}$ . Here, three parameters namely  $M_D, R_D, M_{\text{bulge}}$ , constrain the baryons, and two parameters namely  $r_{0/s}, \rho_{0/s}$  describe the dark matter halo<sup>2</sup>. The details of these parameters in various cases (studied in this work) of mass-modelling is given in Table 6.1. By employing Equation 6.2 & 6.3, we perform the Markov Chain Monte Carlo (MCMC) analysis exploiting RC dataset presented in Chapter 3. To perform the MCMC we make use of *emcee* package (Foreman-Mackey et al., 2013). For each object, we allow 100 walkers to evolve for 10,000 steps, which gives us  $10^6$  samples for analysis. We remove the first half of the sample to account for the burn-in period and the remaining are used in drawing the posteriors.

### 6.2.2 Fitting Details

Primarily, we performed mass modelling on individual RCs. We find that there are 28 perturbed RCs that we could not model, i.e. we mass-model 228 individual RCs. After the mass modelling of these RCs, we visually inspected each MCMC output (posteriors) and found that the 92 objects have hit the prior boundaries, either for dark matter parameters

<sup>2</sup>In  $\rho_{0/s}$  and  $r_{0/s}$ , subscript 0 gives the core radius and core density in case of Burkert halo, while subscript  $s$  defines the scale radius and characteristic density of NFW halo.

Parameter Range (log scale, Units)	Case-1 (Individual RCs)	Case-2 (Co-added RCs)
$8.0 \leq \log(M_D) \leq 12.5$	Gaussian Prior	Gaussian Prior
$-1.7 \leq \log(R_D) \leq 1.7$	Gaussian Prior	Gaussian Prior
$5.0 \leq \log(M_{\text{bulge}}) \leq 11.5$	Gaussian Prior	Flat Prior
$-2.0 \leq \log(r_{0/s}) \leq 2.0$	Flat Prior	Flat Prior
$-26 < \log(\rho_{0/s}) < -18$	Flat Prior	Flat Prior

**Table 6.1:** Mass modelling parameter range and their prior details. Note Gaussian prior keep 25% uncertainty around their central value, where central values are computed from the high-resolution photometric data (see [Harrison et al., 2017](#)) and Chapter 3. The units of physical quantities are as following:  $R_D$  [kpc],  $M_D$  [ $M_\odot$ ],  $M_{\text{bulge}}$  [ $M_\odot$ ],  $r_{0/s}$  [kpc] and  $\rho_{0/s}$  [gm cm $^{-3}$ ].

or for baryons (in particular  $M_D$ ). This tells us that the fitting of these 92 objects is prior-driven, so we have discarded them from the analysis. Thus, we end up analysing only 136 individual RCs.

To verify Case-1, in which we discard substantial amount of RC-fits, we also mass-modelled the co-added RCs. In the co-addition process, we take 228 RCs that are not perturbed. Then we divide the galaxies into 16 velocity bins, where each bin contains 15 RCs, except for the last bin, which contains only 3 RCs. We bin the co-added RCs using standard weighted mean statistics and errors on binned data are Root Mean Square (RMS). For details on co-addition and binning technique, we refer the reader to Chapter 4. In the Figure 6.1 we show co-added and binned RCs. While binning the RCs, we also bin the physical quantities (e.g.,  $M_D$ ,  $R_D$ ) associated with individual objects using RMS statistics and the errors are standard errors. These binned parameters are used in RC modelling either as initial guess (when the parameters have a flat prior) or as central values in the case of a Gaussian prior. In the following text, the binned parameters are represented by a tilde character (e.g.  $\tilde{M}_D$ ) and co-added plus binned RCs are referred to as *co-added RCs*.

As we briefly mentioned above, we have five free parameters in the fitting procedure, where three parameters, namely  $M_D$ ,  $R_D$ ,  $M_{\text{bulge}}$ , constrain the baryons and two parameters, namely  $r_{0/s}$ ,  $\rho_{0/s}$  describe the dark matter in case of Burkert and NFW halo. The exploration range of each parameter is motivated by mass modelling of local galaxies (see, [Persic et al., 1996](#); [Karukes & Salucci, 2017](#); [Lapi et al., 2018b](#); [Di Paolo et al., 2019](#)), given in Table 6.1. As mentioned above, we perform RC modelling in two cases: 1) individual RCs, 2) co-added RCs. The prior on the dark matter parameters are kept flat in both cases. The baryonic parameters, on the other hand, have different conditions on prior in different cases, each motivated by the need to treat the data robustly and without bias. Particularly, in *Case-1* we allow the Gaussian prior for  $M_D$ ,  $R_D$ , and  $M_{\text{bulge}}$  that yields an

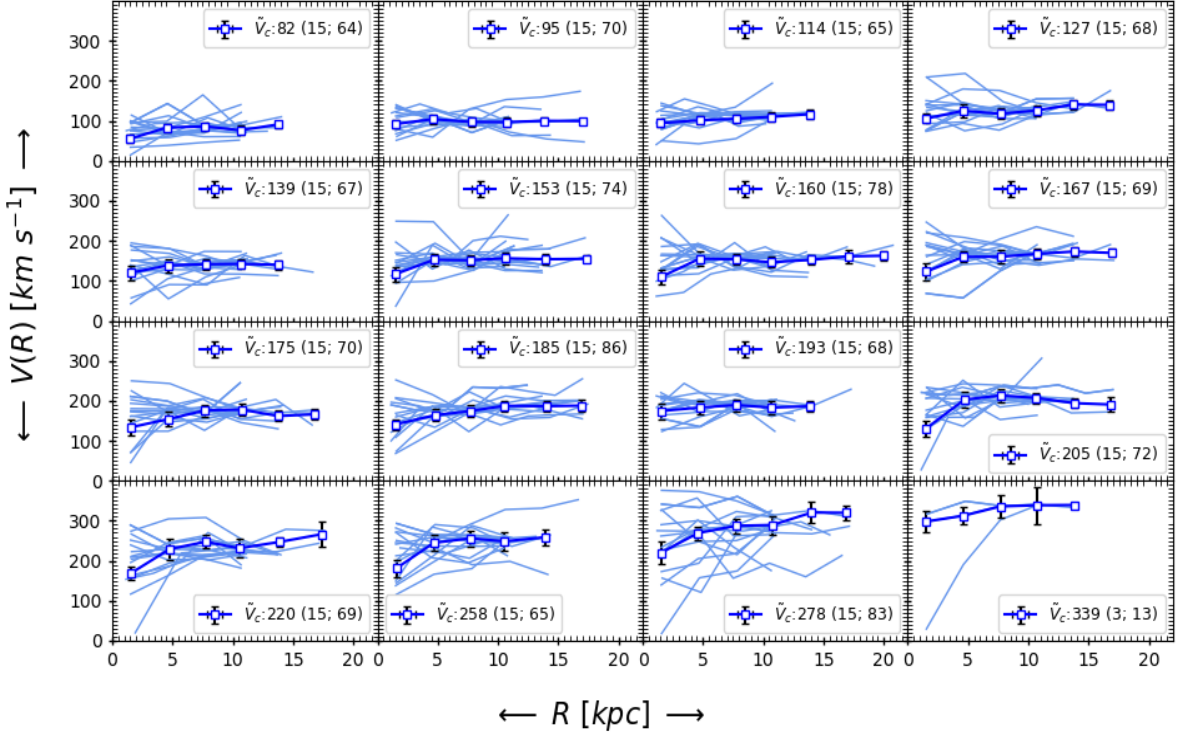


**Figure 6.1:** Coadded and binned Rotation Curves, so-called stacked RCs. Here, RCs are co-added according to their circular velocities  $V_c$ , keeping 15 RCs per bin, except for the highest  $V_c$  bin. Then, we bin the galaxies radially per  $2.5 \text{ kpc}$  corresponding to the binning scale of 3DBarolo, see Chapter 4. For the binning, we have used standard weighted mean statistic given by:  $\bar{X} = \frac{\sum_{i=1}^n x_i \times w_i}{\sum_{i=1}^n w_i}$ , where,  $x_i = \text{data}$ ;  $w_i = 1/\text{error}^2$ ;  $\bar{X} = \text{binned data}$ . The errors on binned data are root mean square error, computed as  $\delta_v^{ri} = \sqrt{\sum([( \delta_{v_i}^r )^2 + (\sigma_{v_i}^{ri})^2]) / N}$ , where  $\delta_{v_i}^r$  is the individual error on the velocities per radial bin and  $\sigma_{v_i}^{ri}$  scatter per radial bin. The individual and co-added RCs are shown by blue thin curves and hexagon connected with the dark blue line, respectively. The central velocity ( $\tilde{V}_c$ ) and the number of data points per bin are printed in the legend of each panel. For example, the notation  $\tilde{V}_c : 82 (15; 64)$  means that the central circular velocity of the bin is  $82 \text{ km s}^{-1}$ , contains 15 RCs and a total of 64 data-points.

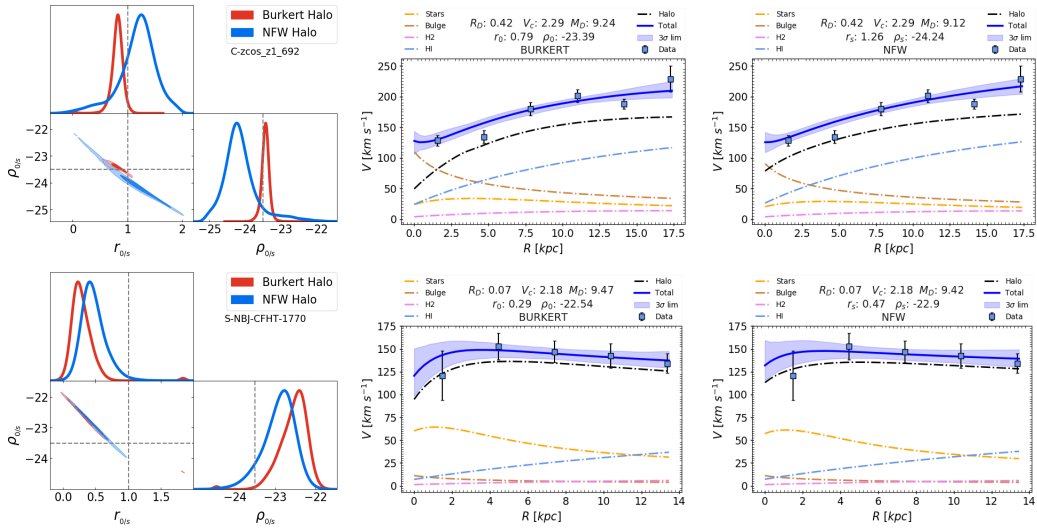


**Figure 6.2:** Individual RC mass modelling. *Column-1*: Posterior distributions (MCMC output) of the estimated parameters:  $r_{0/s}$  and  $\rho_{0/s}$ , for Burkert (red) and NFW (blue) halo. The vertical and horizontal gray dashed lines show the initial guess of parameters:  $r_{0/s}$  and  $\rho_{0/s}$ . *Column-2* & *3* shows the best fit to the RCs and their velocity decomposition for Burkert and NFW halos, respectively. In RC panels, the blue square with error bars represents the observed data, the blue solid line shows the best fit to the data, and the blue shaded area represents the  $3\sigma$  error in the fit. The decomposed velocity of stars, molecular gas, atomic gas, bulge, and dark matter is represented by yellow, violet, light blue, brown, and black dotted dashed lines, respectively. The best-fit value of parameter space  $\vec{\theta}$  are given in the legend of the figures. All the parameters are printed in log, with physical units as following:  $M_D$  [ $M_\odot$ ],  $R_D$  [kpc],  $M_{\text{bulge}}$  [ $M_\odot$ ],  $r_{0/s}$  [kpc] and  $\rho_{0/s}$  [ $\text{gm cm}^{-3}$ ].

uncertainty of 25% around the central value. The central value for  $M_D$  and  $R_D$  is taken from [Harrison et al. \(2017\)](#). The bulge mass  $M_{\text{bulge}}$  is  $1/10^{\text{th}}$  of the stellar disc mass  $M_D$ , motivated by local SFGs ([Bruce et al., 2014](#); [Morselli et al., 2017](#)). In *Case-2*, we allow the Gaussian prior only on  $R_D$ ,  $M_D$  and all other parameters keep a flat prior.

Note that our modelling approach also requires other parameters in the fitting process, namely  $M_{\text{H}_2}$ ,  $M_{\text{HI}}$ ,  $R_{\text{H}_2}$ , and  $R_{\text{HI}}$  (see Equation 6.1). In particular,  $M_{\text{H}_2}$  and  $M_{\text{HI}}$  are calculated in each MCMC run for a given star formation rate ( $M_{\text{H}_2,\text{HI}}(SFR, M_D, z)$ ) using the scaling relations given by [Tacconi et al. \(2018\)](#); [Lagos et al. \(2011\)](#), respectively. The molecular gas scale length  $R_{\text{H}_2}$  is determined from the  $H\alpha$  surface brightness distribution, since ionized gas around a star is surrounded by molecular gas clouds. For a detailed calculation of  $M_{\text{H}_2}$ ,  $M_{\text{HI}}$  and  $R_{\text{H}_2}$ , we refer the reader to Chapter 3 (Section 3.2.1.8 & 3.2.1.7). Moreover, studies of local disc galaxies have shown that the surface brightness of the HI disc is much more extended than that of the H<sub>2</sub> disc ([Fu et al., 2010](#), see their Fig. 5) see also ([Leroy et al., 2008](#); [Cormier et al., 2016](#)). Therefore, we assume  $R_{\text{HI}} = 2 \times R_{\text{H}_2}$ , which is a rough estimate and not effecting dark matter fraction. Notice that the aforementioned additional parameters are fixed in the modelling procedure to the best of our knowledge.

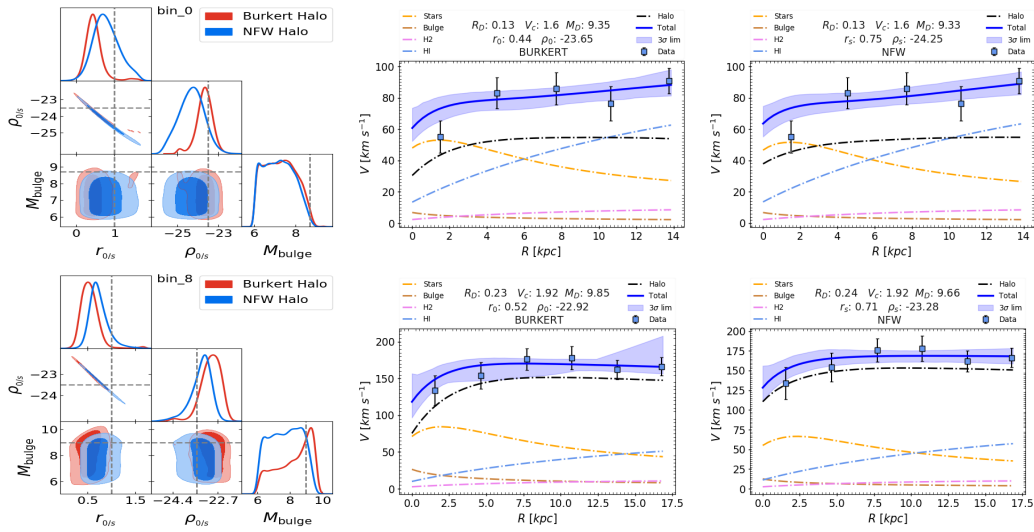


**Figure 6.3:** Co-added RC mass modelling. *Column-1*: Posterior distributions (MCMC output) of the estimated parameters:  $r_{0/s}$ ,  $\rho_{0/s}$  and  $M_{bulge}$ , for Burkert (red) and NFW (blue) halo. The vertical and horizontal gray dashed lines show the initial guess of parameters:  $r_{0/s}$ ,  $\rho_{0/s}$  and  $M_{bulge}$ . *Column-2 & 3* shows the best fit to the RCs and their velocity decomposition for Burkert and NFW halos, respectively. In RC panels, the blue square with error bars represents the observed data, the blue solid line shows the best fit to the data, and the blue shaded area represents the  $3\sigma$  error in the fit. The decomposed velocity of stars, molecular gas, atomic gas, bulge, and dark matter is represented by yellow, violet, light blue, brown, and black dotted dashed lines, respectively. The best-fit value of parameter space  $\vec{\theta}$  are given in the legend of the figures. All the parameters are printed in log, with physical units as following:  $M_D$  [ $M_\odot$ ],  $R_D$  [kpc],  $M_{bulge}$  [ $M_\odot$ ],  $r_{0/s}$  [kpc] and  $\rho_{0/s}$  [ $gm\ cm^{-3}$ ].

## 6.3 Results & Analysis

As described in Section 6.2.1, by inputting the individual RCs (Case-1) and the co-added RCs (Case-2), we constrain the parameter space  $\vec{\theta}$  and disentangle the various components for each RC. With this information, we have estimated the quantities  $R_{\text{vir}}$ ,  $M_{\text{vir}}$ ,  $c_{\text{vir}}$ , and  $f_{\text{DM}}$ . In particular, Table 6.2 provide the results of mass modelled best-fit parameters in Case-2, including dark matter fraction. In the following section, we discuss these results.

### 6.3.1 Mass Modelled rotation curves

Here, we present the results of mass modelling in Case-1 (individual RCs) and Case-2 (co-added RCs). Some examples of their MCMC outputs (posteriors) and best-fit to the RCs are shown in Figure 6.2 & 6.3, respectively. We note that in both cases the Burkert and NFW halo models provide a good and similar fit to the data. The rationale for this is that both halo models predict a similar dark matter density profile in the outskirts of the galaxies and differ only in the very inner region ( $< 2$  kpc), where our data are unresolved. Therefore, we cannot exclude one model over the other by just looking at the rotation curve fitting.

Next, we focused on comparing the physical properties of galaxies, such as total stellar and bulge masses. In particular, we compare the physical properties derived from Case-2 because this case gives us a smooth distribution of RCs that ignores the random fluctuations (perturbations) caused by bad data points, which makes the mass modelling more impeccable than Case-1. Therefore, in the upper panel Figure 6.4, we compare the dynamically derived stellar masses from Burkert and NFW halo of Case-2 with the photometric stellar masses. As we can see, the dynamical stellar masses from the Burkert halo agree with the photometric stellar masses with an intrinsic scatter of 0.3 dex. In contrast, the dynamical stellar masses derived from the NFW halo are a factor of 0.5 lower than the photometric stellar masses, with an intrinsic scatter of 0.43 dex. This suggests that the NFW halo most likely suppresses the baryon content, which could be problematic while deriving the dark matter fraction.

Moreover, in both cases (with both halo models) we have difficulty in constraining the bulge mass, and often end up with a very extended bulge mass distribution. However, the bulge is never heavier than  $0.3 \times M_{\text{star}}$  (see lower panel Figure 6.4), nor does it affect the dark matter fraction (see Figure 6.5). In fact, dark matter has emerged as a dominant quantity, especially in the outskirts, which is very similar to the local star-forming galaxies. We also find that for low-mass objects ( $M_{\text{D}} < 10^{9.5} M_{\odot}$ ), the atomic gas kinematics (HI) dominate the baryonic component, while for massive objects the stellar kinematics prevail.

### 6.3.2 Dark Matter Fraction

In Figure 6.5 we show the results of dark matter fraction of mass modeled RCs, in Case-1 and Case-2, for Burkert and NFW halo. Firstly, we notice that both halo models in both cases have shown that the majority ( $\sim 70\%$ ) of galaxies are dark matter dominated in

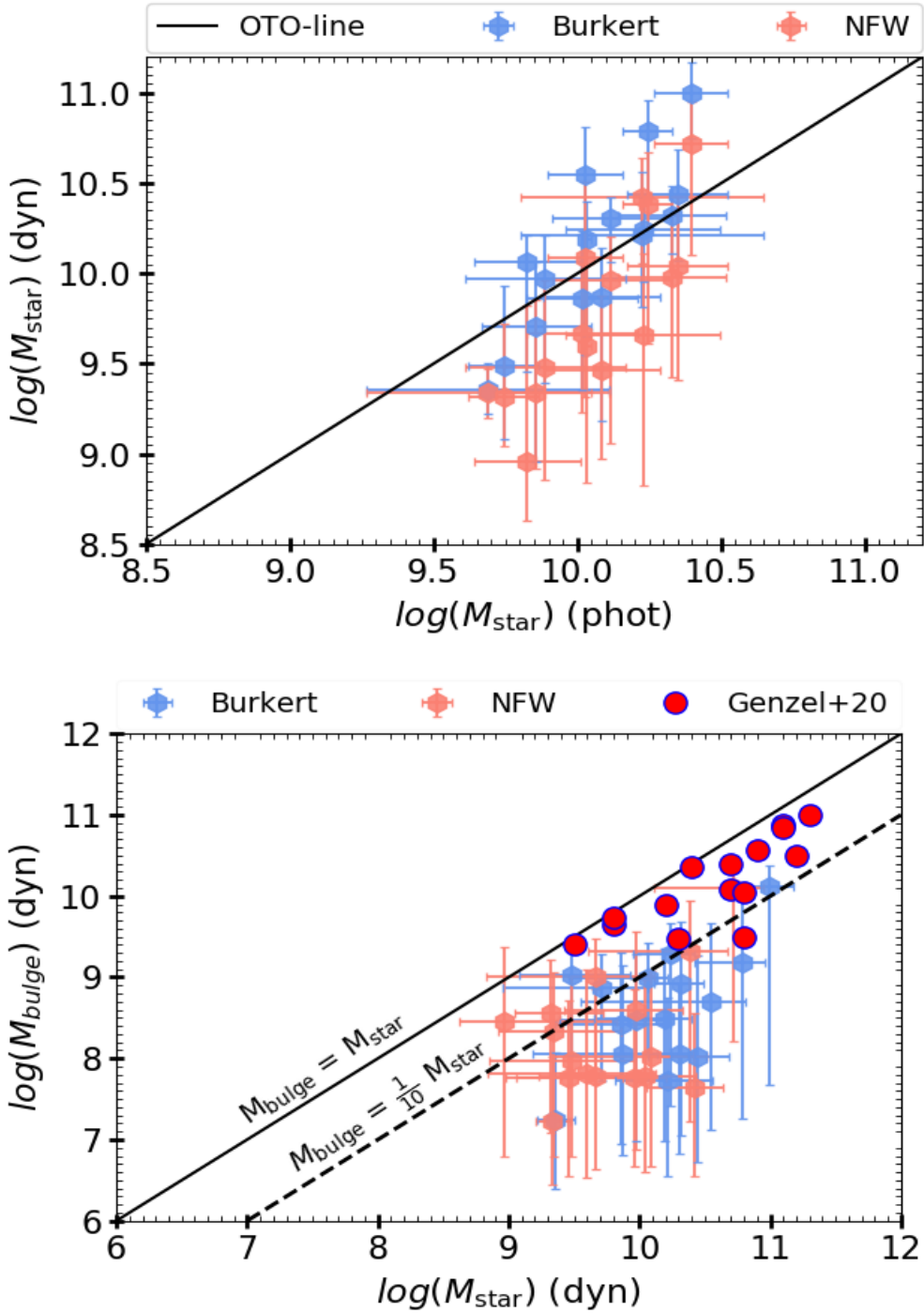


**Figure 6.4:** *Upper panel:* Comparison of the photometric and dynamical stellar masses in Burkert (blue) and NFW (pink) halo profiles for co-added RCs. The black solid line shows the one-to-one relations. We note that the dynamical stellar masses obtained in the possession of the Burkert halo agree very well with the photometric stellar masses. In contrast, the dynamical stellar masses obtained with the NFW halo are lower than the photometric stellar masses by a factor of 0.5. *Lower panel:* Dynamically derived bulge masses versus stellar masses, in the case of Burkert (blue) and NFW (pink) halo profiles for co-added RCs. We compare our results with a pioneering study in this field: Genzel et al. (2020, : red filled circles), and we find that in our sample  $B/T$  is never higher than  $\sim 0.3$ , which is different from what is reported by Genzel et al. (2020) for the same redshift range ( $z = 0.6 - 1.2$ ) and similar stellar mass sample.

the outskirts. Secondly, our current results are in very good agreement with our previous study done in Chapter 5, where we determine the dark matter fraction using a model-independent approach. This confirms that the majority of star-forming galaxies at  $z \sim 1$  have dark matter dominated discs.

In case of Individual RCs, there are nearly 20% objects those appear to be deficient in dark matter (in both halo models). We also note that the dark matter fraction derived from the individual RC modelling retains a higher uncertainty in both halo models, while it is significantly reduced in the case of the co-added RCs. This could be due to the low resolution in the data (non-smooth  $V(R)$ ), which is penalized by the large uncertainty. On the other hand, co-adding RCs statistically ignores the random fluctuations arising from the bad data points and provides us with a smooth RC, which can then be easily modelled dynamically, and hence keeps the relatively small uncertainty in the measurements. Besides the similarity in the  $f_{\text{DM}}$  measurements derived from co-added RCs (here) and Chapter 5, we also found that binning of individual  $f_{\text{DM}}$  in stellar mass range (keeping 10 points per bin) yields the dark matter fraction which overlaps the our previous results of Chapter 5.

As we have previously pointed-out in Section 6.3.1 that dynamical modelling in possession with NFW halo attempts to suppress stellar mass content, as shown in the upper panel of Figure 6.4. Therefore the dark matter fraction obtained in this case is higher in comparison to Burkert halo case, see lower panel of Figure 6.5. The latter argument is clearly visible from co-added RC (blue hexagons) analysis. This suggests that dynamical modelling with the NFW halo requires a precise baryon information, while the Burkert halo does not and is still able to constrain the physical properties of galaxies, for example stellar masses. This is the reason  $f_{\text{DM}}-M_*$  relation obtained with Burkert halo matches very well with the  $f_{\text{DM}}-M_*$  relation of the model-independent approach (blue shaded region). However, this can not be a piece of strong evidence to discard one model over the other because measurements from NFW models are still in good agreement within the  $1\sigma$  uncertainty.

### 6.3.3 Structural Properties of Dark Matter

With the information on the dark matter halo parameters:  $r_{0/s}$ ,  $\rho_{0/s}$ , we derived the physical properties of the galaxies, such as  $R_{\text{vir}}$ ,  $M_{\text{vir}}$  and the concentration in the case of the NFW halo. Using the latter quantities, we compared the  $c_{\text{vir}} - M_{\text{vir}}$  relation of our sample with dark matter only simulation (Bullock et al., 2001) and NIHAO hydrodynamical simulation (Wang et al., 2015), as shown in Figure 6.6. We find that the concentration at  $z \sim 1$  star-forming galaxies goes in the opposite direction, which challenges the simulations. In other words, both dark matter only and the hydro simulations predict that the halo concentration decreases with increasing redshift, (see red and blue dashed lines in Figure 6.6, while the observations show a higher concentration at  $z \sim 1$  compared to  $z \approx 0$ , but still consistent within the  $1\sigma$  uncertainty. We would like to notice the reader that the concentration is derived as  $c = R_{\text{vir}}/r_s$ , where the determination of  $R_{\text{vir}}$  requires a huge extrapolation. Therefore, the concentration in this work is not as accurate as can

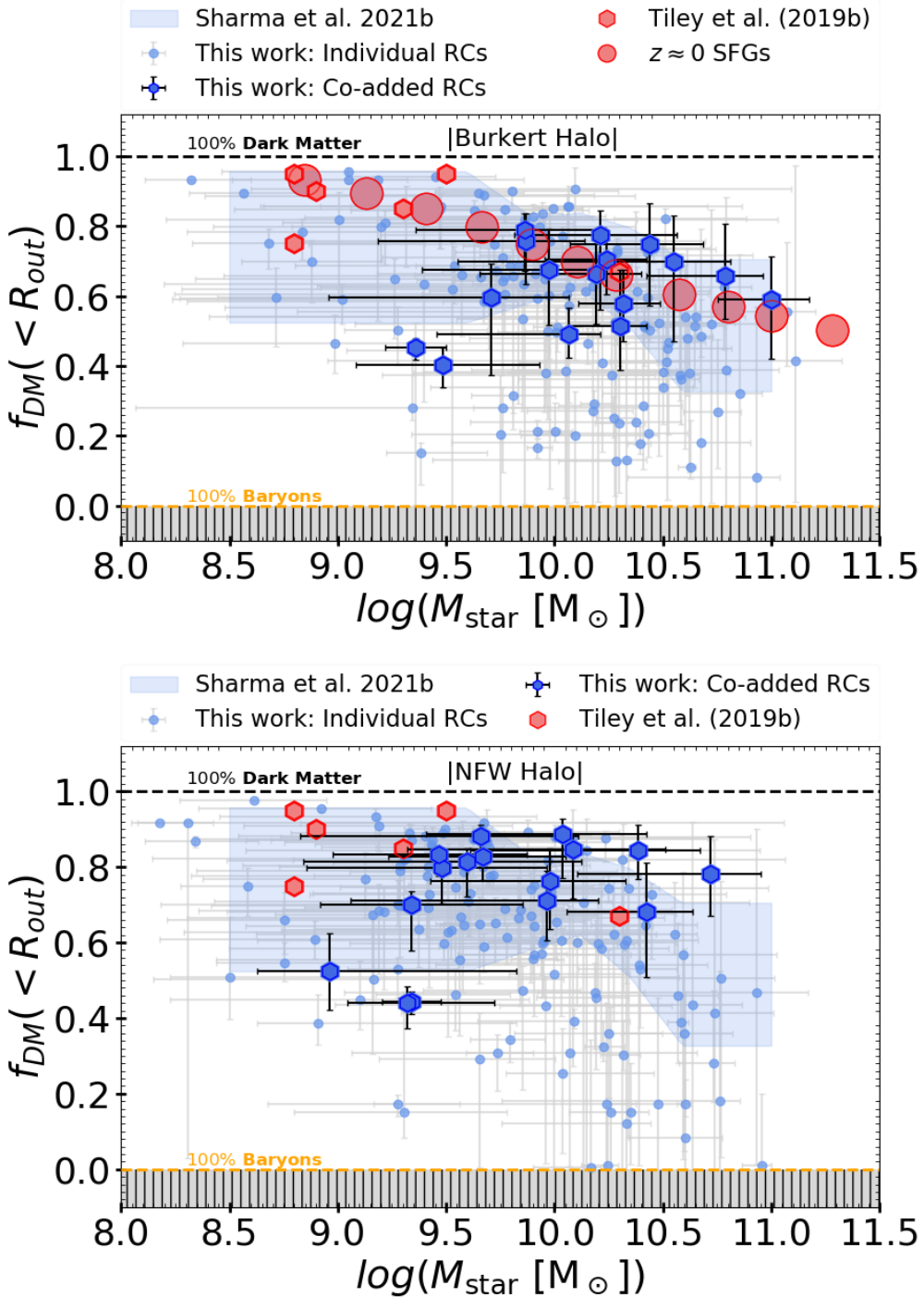


**Figure 6.5:** Dark matter fraction within  $R_{\text{out}}$  for the Burkert and NFW halos, left and right, respectively. The color coding in both panels are the same, individual RCs: blue filled circles, co-added RCs: blue hexagons, local star-forming galaxies: coral red circles, and high-redshift coral red hexagons. The size of the makers in locals star-forming galaxies includes their errors. The blue shaded area represents the model-independent dark matter fraction study that we previously conducted in Chapter 5.

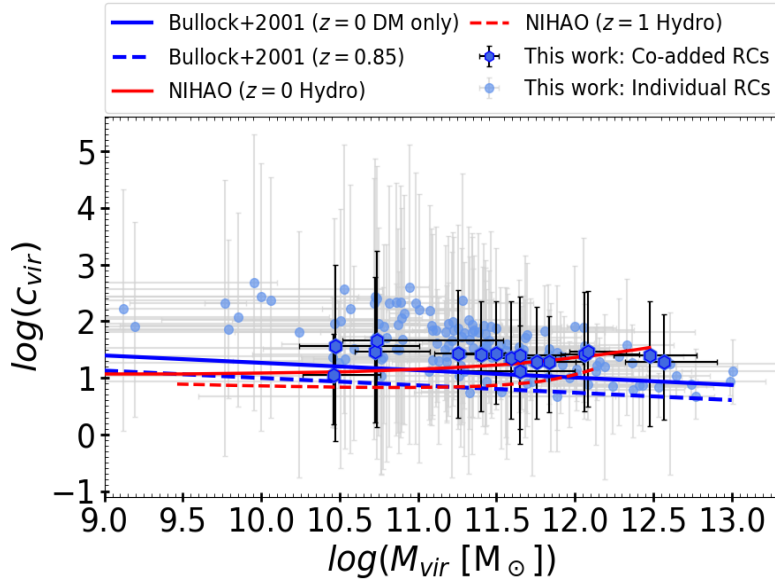


**Figure 6.6:** Concentration vs. virial mass relation for individual and co-added RCs (or galaxies), blue circles and hexagons, respectively. The blue and red, solid and dashed lines, represent the  $c - M_{vir}$  relation of dark matter only simulations (Bullock et al., 2001) and NIHAO suite of hydrodynamical cosmological simulations (Wang et al., 2015; Freundlich et al., 2020b), for  $z = 0$  and  $z \sim 1$ , respectively.

be derived from HI RCs, where data are available over more than 50 kpc radius. Thus, although the NFW halo gives conflicting results with respect to the simulations, we cannot falsify its presence in nature.

On the other hand, the relation between core density versus core radius, associate with the Burkert profile, emerge very similar to the local star-forming galaxies, with a similar slope, as shown in Figure 6.7. Moreover, we find that high-redshift galaxies have denser dark matter cores, as they lie above the local star-forming galaxies and low surface brightness galaxies (LSBs). At the same time, the size of their dark matter core is smaller with respect to local star-forming galaxies, but equivalent to the core of LSBs. This suggests that the structural properties (i.e. structure) of dark matter have evolved over cosmic time. In particular, dark matter cores at  $z \sim 1$  are smaller by a factor of 0.3, which makes them denser by  $\sim 1.5$  order of magnitude.

## 6.4 Point of View from Simulations

In this section, we compare the mass modelling results with the current state-of-the-art galaxy simulations: EAGLE, TNG100 and TNG50. For this purpose, I first selected the central galaxies with similar physical properties from the simulations; the details of the selection criteria can be found in Section 3.3. We then calculate the circular velocity of each halo (thanks to Dr. Kyle Oman for providing this data), and later co-add these

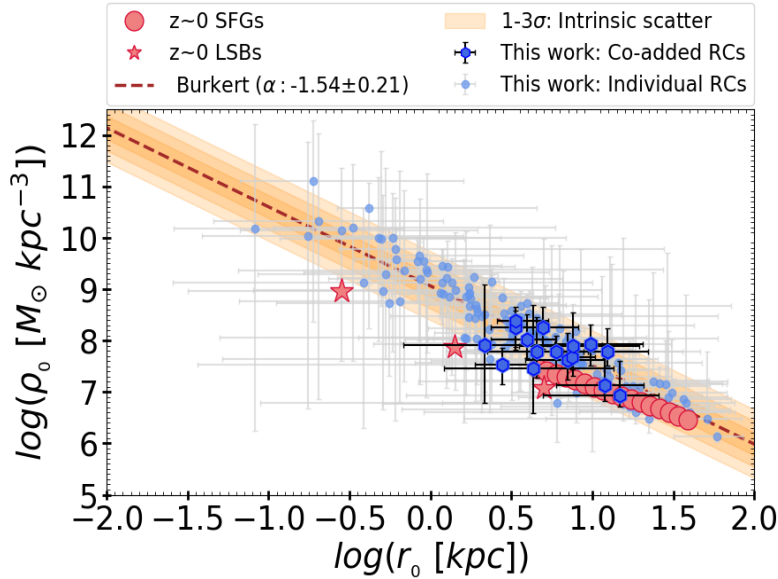


**Figure 6.7:** dark matter core density vs. core radius relation of local and high-redshift galaxies. The blue circles and hexagons represent the  $z \sim 1$  individual and co-added RCs, respectively. The coral circles and stars represent the local star-forming and low surface brightness galaxies (Persic et al., 1996; Di Paolo et al., 2019), respectively. The brown dashed line is the best fit  $\rho_0 \propto r_0^\alpha$  to  $z \sim 1$  data with slope  $\alpha = -1.54$ , and the orange shaded area represents the  $1 - 3\sigma$  intrinsic scatter in the relation.

circular velocity profiles to compare them with the observations. In the following section we briefly define this process and discuss the comparison.

#### 6.4.1 Rotation Curves of Galaxy Simulations

To compare the simulations with observations, we extract the mass profile of simulated galaxies expressed as circular velocity curve ( $V_c(R) = \sqrt{GM/R}$ ) and its constituent components (i.e. stars, gas and dark matter). We co-add and bin the simulated circular velocity curves using the similar approach as for observations; however using the RMS statistic, which works best for simulations. Briefly, we divide our simulated galaxies into 20 velocity bins between  $100-300 \text{ km s}^{-1}$  with a step-size of  $10 \text{ km s}^{-1}$ . Then each bin is co-added and binned to obtain a single circular velocity curve. We would like to note that in the simulations we know exactly the total velocity of the galaxy, as well as its different components (e.g. star:  $V_*$ , gas:  $V_{\text{gas}}$ ,  $V_{\text{HI}}$ , dark matter:  $V_{\text{DM}}$ ), so in the binning process we also bin these quantities. Moreover, we bin the physical quantities such as  $R_{\text{D}}$ ,  $M_*$ ,  $V_c$ , etc., associated to each galaxy. In Figure 6.8, we show an example case of co-adding, binning, and the final co-added circular velocity curves from all three simulations, and in Table 6.3, we tabulate all their relevant physical quantities. These circular velocity curve data are then used in the investigation of the DM fraction, see Section 6.3. We remark, TNG100 and TNG50 are similar same and only differs in terms of resolution.

However, we still notice a little dis-similarity in the shape of their circular velocity curves. Nevertheless, In this work, we avoid making any interpretations on the circular velocity curves derived from the simulations, as this is beyond the scope of this work and will be covered in our future work, where we plan to make the synthetic datacubes of simulated galaxies, and determining the RCs using the 3DBarolo, as suggested by [Oman \(2018\)](#) and [Oman et al. \(2019\)](#).

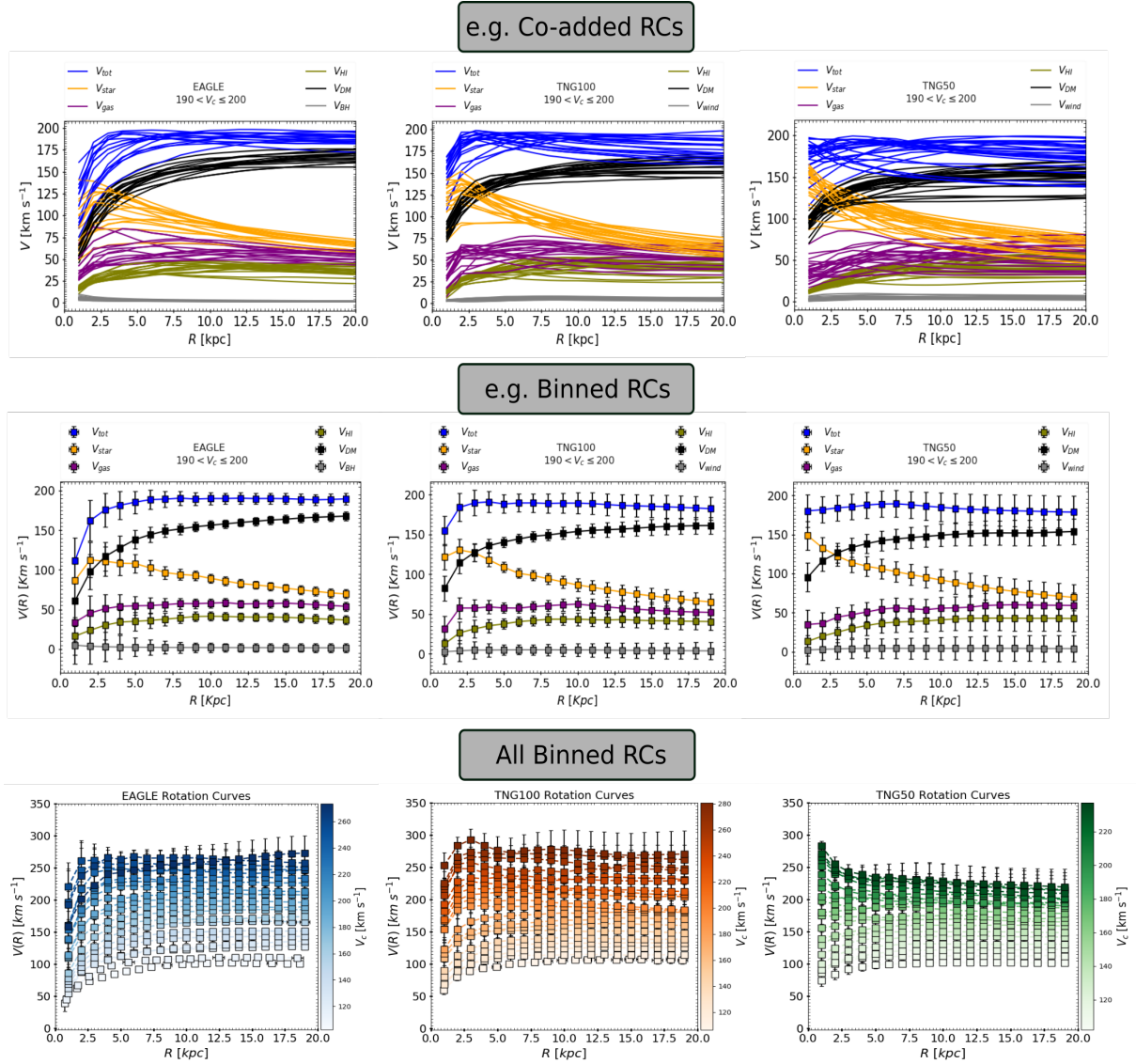


**Figure 6.8:** Circular velocity curves of galaxy simulations from left-to-right EAGLE, TNG100 and TNG50. *Upper panel:* An example of co-added RCs in bin `_11` ( $190 < V_c \leq 200$ ). *Middle panel:* An example of binned RC for the previous bin. *Bottom panel* Binned RCs of all velocity bins. The color code in the upper and the middle panel is the same and given as follows, blue: total circular velocity ( $V_c(R)$ ), black: dark matter contribution ( $V_{DM}(R)$ ), orange: stars ( $V_{star}$ ), violet: total gas, green: neutral hydrogen, and grey: black-hole in EAGLE and wind in TNG.

Binning Details		Photometric measurements										Physical Parameters: OBSERVATIONS										DM Fraction	
		$\tilde{R}_D$	$\tilde{V}_c$	$M_*$	SFR	$\tilde{R}_{H2}$	$\tilde{R}_D$	$\tilde{M}_D$	$\tilde{M}_{bul}$	$\tilde{r}_0$	$\tilde{\rho}_0$	$\tilde{R}_D$	$\tilde{M}_D$	$\tilde{M}_{bul}$	$\tilde{r}_0$	$\tilde{\rho}_0$	$\tilde{\rho}_s$	$f_{DM}^{BUR}$	$f_{DM}^{NFW}$				
No.	Dpts																						
0	15 (64)	0.11	1.92	9.69	0.92	1.02	0.13	9.35	7.24	0.44	4.52	0.13	9.33	7.23	0.75	3.92	0.45	0.44					
1	15 (70)	0.27	1.98	9.86	0.87	1.16	0.26	9.64	8.86	0.63	4.47	0.25	9.3	8.33	0.43	4.96	0.59	0.7					
2	15 (65)	0.22	2.06	9.75	1.02	0.93	0.22	9.3	9.03	0.34	4.92	0.22	9.24	8.56	0.25	5.21	0.4	0.44					
3	15 (68)	0.29	2.1	9.83	1.07	1	0.25	10.03	8.99	1.17	3.93	0.28	8.8	8.46	0.23	5.5	0.49	0.52					
4	15 (67)	0.19	2.14	9.89	0.98	1.11	0.19	9.96	8.48	0.65	4.79	0.2	9.46	7.97	0.63	4.88	0.67	0.8					
5	15 (74)	0.15	2.19	10.09	1.12	1.11	0.15	9.86	8.05	0.6	5.02	0.16	9.46	7.76	0.7	4.83	0.76	0.83					
6	15 (78)	0.26	2.2	10.12	0.99	1.03	0.28	10.3	8.05	1.07	4.14	0.26	9.96	7.76	1.07	4.09	0.51	0.71					
7	15 (69)	0.27	2.22	10.03	1.16	1.1	0.25	10.18	8.49	0.85	4.61	0.27	9.59	7.82	0.83	4.66	0.66	0.81					
8	15 (70)	0.21	2.24	10.02	1.02	1.04	0.23	9.85	8.43	0.52	5.25	0.24	9.66	7.78	0.71	4.89	0.79	0.83					
9	15 (86)	0.25	2.27	10.23	1.05	1.26	0.23	10.19	9.29	0.88	4.68	0.24	9.55	9.02	0.98	4.49	0.7	0.88					
10	15 (68)	0.16	2.29	10.33	1.08	1.05	0.15	10.3	8.92	0.78	4.79	0.15	9.96	8.59	0.81	4.77	0.58	0.76					
11	15 (72)	0.24	2.31	10.23	1.04	1	0.29	10.21	7.73	0.52	5.38	0.35	10.42	7.65	0.96	4.47	0.77	0.68					
12	15 (69)	0.28	2.34	10.03	1.3	1.02	0.3	10.54	8.69	0.88	4.89	0.3	10.08	8.03	0.92	4.81	0.7	0.85					
13	15 (65)	0.21	2.41	10.35	0.91	1.09	0.22	10.44	8.03	0.69	5.25	0.22	10.04	7.78	0.88	4.96	0.75	0.89					
14	15 (83)	0.33	2.44	10.25	0.99	0.99	0.31	10.78	9.19	1.09	4.79	0.29	10.35	9.32	1.22	4.5	0.66	0.84					
15	3 (13)	0.36	2.53	10.4	1.4	1.14	0.32	10.94	10.12	0.99	4.93	0.33	10.6	10.09	1.08	4.74	0.59	0.78					

**Table 6.2:** Structural (and physical) parameters of observed galaxies derived from their co-added RCs. *col.1-2* Bin number and total number of RCs, respectively. For example, the notation 15(67) tells that we have coadded 15 RCs those contain 67 data-points. *col.3-7* Photometric measurements of physical quantities  $\tilde{R}_D$ ,  $\tilde{V}_c$ ,  $\tilde{M}_D$ ,  $\tilde{SFR}$  and  $\tilde{R}_{H2}$ , respectively. The tilde  $\sim$  at the top of each quantity represents that it is a statistically measured quantity. *col.8-12* Modelled physical parameters ( $\tilde{R}_D$ ,  $\tilde{M}_D$ ,  $\tilde{M}_{bul}$ ,  $\tilde{r}_0$  and  $\tilde{\rho}_0$ , respectively) for Baryons and DM in case Burkert Halo. *col.13-17* Modelled physical parameters ( $\tilde{R}_D$ ,  $\tilde{M}_D$ ,  $\tilde{M}_{bul}$ ,  $\tilde{r}_s$  and  $\tilde{\rho}_s$ , respectively) for Baryons and DM in case NFW Halo. *col.18-19* DM fraction in case of Burkert and NFW halo, respectively. Here we provide each quantity in log and their physical units are as following:  $\tilde{R}_D$  [kpc],  $\tilde{V}_c$  [km s<sup>-1</sup>],  $\tilde{M}_D$  [M<sub>⊙</sub>],  $\tilde{SFR}$  [M<sub>⊙</sub> yr<sup>-1</sup>],  $\tilde{R}_{H2}$  [kpc],  $\tilde{M}_{bul}$  [M<sub>⊙</sub>],  $\tilde{r}_0$  [kpc] and  $\tilde{\rho}_0$  [M<sub>⊙</sub> kpc<sup>-3</sup>].

Bin No.	Number of RCs			$\tilde{R}_D$			$V_c$			$\frac{\dot{M}_*}{T_{100}}$			$\tilde{R}_{gas}$			$\tilde{f}_{DM}$			
	EAG	T100	T50	EAG	T100	T50	EAG	T100	T50	EAG	T100	T50	EAG	T100	T50	EAG	T100	T50	
0	1	4	38	0.43	0.34	2.01	9.15	9.28	0.97	1.37	1.45	0.88	0.78	0.74	0.74	0.82	0.74	0.74	
1	1	11	29	0.35	0.37	2.04	2.06	2.06	9.32	9.39	9.51	1.23	1.56	1.49	0.82	0.81	0.76	0.7	
2	3	9	35	0.43	0.41	0.36	2.1	2.1	9.61	9.53	9.66	1.54	1.55	1.5	0.81	0.81	0.76	0.7	
3	4	15	53	0.45	0.43	0.37	2.12	2.12	9.74	9.69	9.8	1.5	1.58	1.51	0.8	0.74	0.74	0.7	
4	4	11	37	0.51	0.36	0.39	2.16	2.15	9.81	9.84	9.94	1.62	1.71	1.58	0.81	0.72	0.68	0.68	
5	7	24	64	0.44	0.36	0.36	2.18	2.19	2.18	9.91	9.95	10.01	1.72	1.69	1.61	0.81	0.71	0.68	0.68
6	5	12	38	0.46	0.41	0.39	2.22	2.21	2.21	10.07	10.09	10.11	1.63	1.74	1.61	0.76	0.69	0.66	0.66
7	16	16	40	0.46	0.42	0.34	2.24	2.23	2.23	10.17	10.16	10.19	1.73	1.78	1.65	0.76	0.71	0.65	0.65
8	8	22	31	0.45	0.42	0.33	2.27	2.26	2.25	10.26	10.29	10.29	1.83	1.77	1.68	0.76	0.66	0.66	0.66
9	15	19	25	0.45	0.32	0.37	2.28	2.28	2.28	10.35	10.3	10.34	1.83	1.77	1.71	0.7	0.65	0.65	0.65
10	14	22	25	0.46	0.32	0.43	2.3	2.3	2.29	10.41	10.36	10.4	1.82	1.82	1.68	0.73	0.63	0.63	0.63
11	25	16	21	0.44	0.3	0.36	2.33	2.33	2.31	10.49	10.47	10.44	1.89	1.84	1.72	0.7	0.63	0.63	0.63
12	12	17	12	0.34	0.37	0.26	2.34	2.34	2.3	10.5	10.5	10.42	1.99	1.89	1.74	0.66	0.62	0.6	0.6
13	12	22	21	0.34	0.37	0.34	2.36	2.35	2.32	10.61	10.54	10.47	2	1.86	1.79	0.69	0.61	0.62	0.62
14	13	14	12	0.38	0.41	0.34	2.37	2.38	2.34	10.66	10.65	10.53	2.05	1.92	1.76	0.66	0.65	0.62	0.62
15	18	14	12	0.39	0.38	0.3	2.39	2.38	2.36	10.71	10.67	10.65	2.07	1.9	1.77	0.67	0.63	0.57	0.57
16	19	15	11	0.39	0.45	0.16	2.39	2.41	2.35	10.7	10.81	10.5	2.08	2.01	1.78	0.68	0.63	0.57	0.57
17	12	19	8	0.36	0.4	0.39	2.41	2.41	2.37	10.75	10.84	10.59	2.09	1.97	1.8	0.66	0.59	0.63	0.63
18	14	13	1	0.39	0.51	0.32	2.43	2.43	2.34	10.8	10.93	10.65	2.15	2.01	1.71	0.67	0.64	0.61	0.61
19	7	5	12	0.59	0.5	0.21	2.44	2.45	2.37	10.83	10.83	10.68	2.17	2.1	1.85	0.77	0.64	0.52	0.52

**Table 6.3:** Physical parameters of galaxies in simulations (EAGLE; EAGLE; TNG100; TNG50; T50). *col.1* Bin number. *col.2-4* Number of rotation curves in each bin. *col.5-7* Disc radius. *col.8-10* circular velocity computed at  $R_{\text{out}}$ . *col.11-13* stellar mass (includes bulge). *col. 14-16* gas disc length. *col.17-19* DM fraction. Here quantities are provided in log and their physical units are similar to the one given in Table 6.2.

### 6.4.2 Comparison with Simulations

The details of their sample selection and RC data can be found in the Sections 3.3.1 & 6.4.1. In particular, we compare our observed co-added RCs with the simulated co-added circular velocity curves. Briefly, in simulations we know exactly the total circular velocity of the galaxy as a function of radius ( $V_c(R)$ ), and its components such as stellar  $V_{\text{star}}(R)$ , dark matter  $V_{\text{DM}}(R)$ , gas  $V_{\text{gas}}(R)$  velocity profile etcetera. From observations we only know the  $V_c(R)$ , which we have mass modelled to disentangle its various components, see Section 6.2 (also see Section 2.2.1). That is, in both cases, observations and simulations, we know the  $V_c(R)$  and  $V_{\text{DM}}(R)$ . This allows us to compute dark matter fraction of galaxies as a function of radius using Equation 5.5. In Figure 6.9 we show the results of  $f_{\text{DM}}(R)$  in the aforementioned simulations. In particular, we show 12 velocity bins for which we have enough simulated data to bin and obtain the co-added RC, for details see Table 6.3. It is noticeable that all simulations show dark matter dominated galaxies from 5 kpc outwards. In other words, the simulated galaxies have 20% (minimum) to 50% dark matter within the effective radii, and they are dark matter dominated in the outskirts. These results are very similar to the observed star-forming galaxies at  $z \sim 1$ , reported previously in Chapter 5. We remind the reader that galaxies within effective radii are known to have less dark matter fraction because baryon dominates the inner region of galaxies. If one has to look for dark matter, it should be found in the outskirts ( $> 2 \times R_e$ ), as clearly shown in Figure 6.9.

To compare the simulations with the observations, we superimposed the  $f_{\text{DM}}(R)$  of the observed co-added RCs in Figure 6.9, in the case of the Burkert (black) and NFW (brown) halos. Since the observations in the inner region are not resolved, we mark the inner region (0-4 kpc) as a gray shaded area and avoid drawing any conclusions there. Notice that we compare observed and simulated co-added RCs only when  $V_c^{\text{SIM}} \approx V_c^{\text{OBS}}$ , shown at the top of each panel. First, we note that  $f_{\text{DM}}(R)$  in the Burkert halo case represents the simulations well within the  $1\sigma$  uncertainty. On the other hand, the NFW halo yields a higher dark matter fraction up to the outer edges in all velocity bins. Second, NFW and Burkert halo results are very similar in low velocity bins ( $V_c^{\text{SIM}} < 150 \text{ km s}^{-1}$ ) and agree with the simulations. However, when we go towards the higher velocity range, the NFW halo starts to show a deviation from the simulations, while the Burkert halo stays very close to the simulations. In particular, the Burkert halo and the simulations have almost the same dark matter fraction between 10-15 kpc radius, which is different from the NFW halo. In short, the Burkert profile seems to represent the simulations better and more accurately.

To obtain more quantitative difference, we emphasize to notice the dark matter fraction between 5-10 kpc radius in Figure 6.9. We can clearly notice that NFW halo allows more dark matter content than Burkert halo, which we do not even see in simulations. In other words, dark matter fraction derived from the Burkert halo model is close to the one seen in simulations for over all stellar mass (and circular velocity) range, while NFW yields a relatively high dark matter fraction. The latter could be a consequence of suppressing the stellar mass which we have already anticipated from the observations in

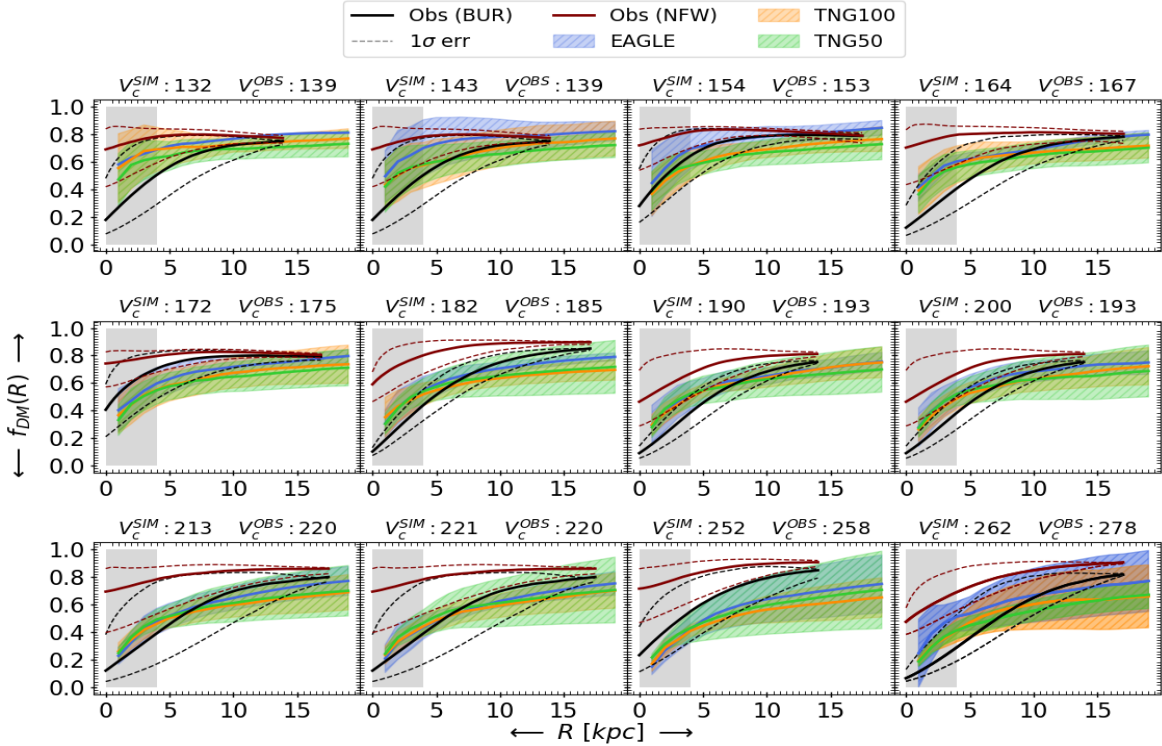


**Figure 6.9:** Dark matter fraction as a function of radius in various velocity bins of observed and simulated galaxies. The central value of  $f_{DM}(R)$  is shown by solid lines in each case. The color code is the same in all panels and is as follows: EAGLE : blue, TNG100: orange, TNG50: green, observations in the case of the Burkert halo: black, and NFW halo: brown. In the simulations, the  $1\sigma$  error in each measurement is represented by a shaded area, while in the observations it is a dashed line following the same color code. The grey shaded area in each panel represents the unresolved region in the observations. The central value of the circular velocity of each bin is printed at the top of each panel, where  $V_c^{SIM}$  and  $V_c^{OBS}$  specifies the simulations and observations, respectively.

Sections 6.3.1 & 6.3.2, and Figures 6.4 & 6.5. Besides this we notice to have three data points (at  $M_{\text{star}} \approx 9.2, 9.4, 10.0$ ) with low dark matter fraction (in observations) and the RCs associated with these data points have a gas-dominated outer disc, which we could not find in the simulations. Moreover, we recall that the dark matter fraction derived from the model-independent approach in Chapter 5, clearly overlaps with the dark matter fraction obtained with Burkert halo model, so the simulations. That is, these results are strengthening our previous finding as well as confirming the robustness of the current measurements and the quality of the KROSS data.

## 6.5 Discussion & Conclusions

To fit the individual RCs through mass modelling approach, one needs to use the informative prior on the baryons ( $M_D, M_{\text{bulge}}, R_D$ ) in advance, otherwise the parameter space

$\vec{\theta}$  is highly degenerate. In the case of co-added RCs, on the other hand, we could achieve a good fit only by specifying one or two baryonic parameter, which is stellar disc scale-length and stellar mass in this work. This case also allows us to adopt the flat prior on bulge mass, which is an unknown quantity (and un-resolved), so that we can determine it dynamically, see Section 6.3.1 and Table 6.1. Remark: when we use the NFW halo model for mass modelling of RCs, it gives a good fit to the data, but suppresses the baryon content and yields high dark matter fractions, which we do not see when using the Burkert halo, nor in the simulations (EAGLE, TNG100, TNG50). Based on RC fitting and structural properties of dark matter we can not include or exclude the NFW halo model but there exists the tension in constraining the stellar masses using NFW halo, see Figure 6.4. In principle, a galaxy can not have stellar mass more than the allowed by dynamics (e.g. Lyubenova et al., 2016). Providing the various results/comparisons of NFW and Burkert halo in the case of individual and co-added RCs, we found that our current sample favours the Burkert halo model and also agrees quite well with the simulations. Therefore, we focus on discussing the Burkert halo results in what follows.

We begin by referring to our earlier study of the dark matter fraction (Chapter 5), in which we used a model-independent approach to determine the  $f_{\text{DM}}$  from RCs. We found that our earlier finding agrees very well with our current results of the dark matter fraction obtained via mass modelling (see left panel Figure 6.5). Both the current and previous  $f_{\text{DM}}$  results also matches very well with the simulations (see Figure 6.9). Our current  $f_{\text{DM}}$  results are also consistent with the previously studied local and high-redshift star-forming galaxies, indicated by coral red circles and hexagons, respectively, in the Figure 6.5. Given the similarities between the observed data and the simulations mentioned above, we conclude that the current state-of-the-art simulations reproduce the observed Universe well. However, for small objects with low velocities and gas dominated system, there is still some work needed to be done.

In Chapter 4, we have shown that the progenitors of present-day star-forming galaxies at  $z \sim 1$  have similar rotation curves. Given the similarity in the RCs of  $z \sim 1$  and  $z = 0$ , and acknowledging the fact that the circular velocity is an indicator of the total mass of the system, we have concluded that the total mass within the optical extent of galaxies does not evolve from  $z \sim 1$  to  $z = 0$ , while the baryon distribution evolves. To bring our previous confirmation and the current finding on the same level, we compared our recent results on the structural properties of dark matter halo in the circular velocity plane, as shown in Figure 6.10. Let us remark that  $r_0 - V_c$  and  $\rho_0 - V_c$  relations of local galaxies are well fitted by second order polynomials, see Figure 6.10, which are given by:

$$\log r_0^{z \sim 0} = 1.63 \log V_c^2 - 5.24 \log V_c + 4.76 \quad (6.4)$$

$$\log \rho_0^{z \sim 0} = -1.99 \log V_c^2 + 6.67 \log V_c - 1.04 \quad (6.5)$$

Therefore, to visualize the differences in the structural properties of dark matter at different epochs, we used Equation 6.4 and 6.5 as a benchmark and have plotted the ratio:  $\frac{r_0^{z \sim 0}}{r_0^{z \sim 1}}$  and  $\frac{\rho_0^{z \sim 0}}{\rho_0^{z \sim 1}}$ , as a function of circular velocity in Figure 6.11. This immediately shows us

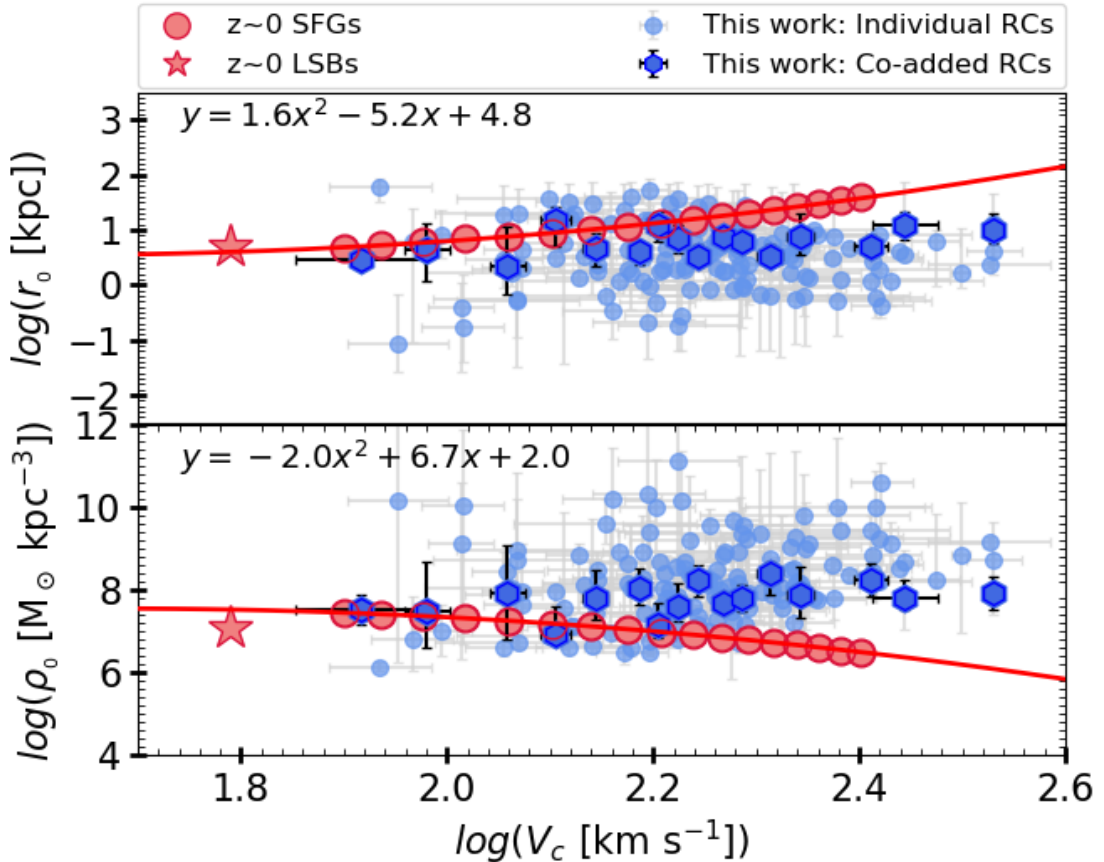


**Figure 6.10:** Structural properties of the dark matter halo at  $z \sim 1$ . dark matter core radius and core density as a function of circular velocity, upper and lower panels, respectively. The individual and co-added RCs measurements are represented by small blue circles and the hexagons, respectively. The comparison sample of local LSBs (Di Paolo et al., 2019) and star-forming galaxies (Persic et al., 1996; Lapi et al., 2018b) are represented by the coral red stars and circles, respectively. The best-fit line (second-order polynomial) of the local star-forming galaxies and LSBs is represented by a red line, and the equation is printed in the upper left corner of each panel. As we can notice the local star-forming galaxies lie above in the  $r_0 - V_c$  plane and below in the  $\rho_0 - V_c$  plane with respect to the  $z \sim 1$  star-forming galaxies. This is due to the fact that dark matter cores of  $z \sim 1$  star-forming galaxies are smaller and denser than their local counterparts, indicating an evolution in the structure of dark matter halos over cosmic time, that is fairly captured in the observations.

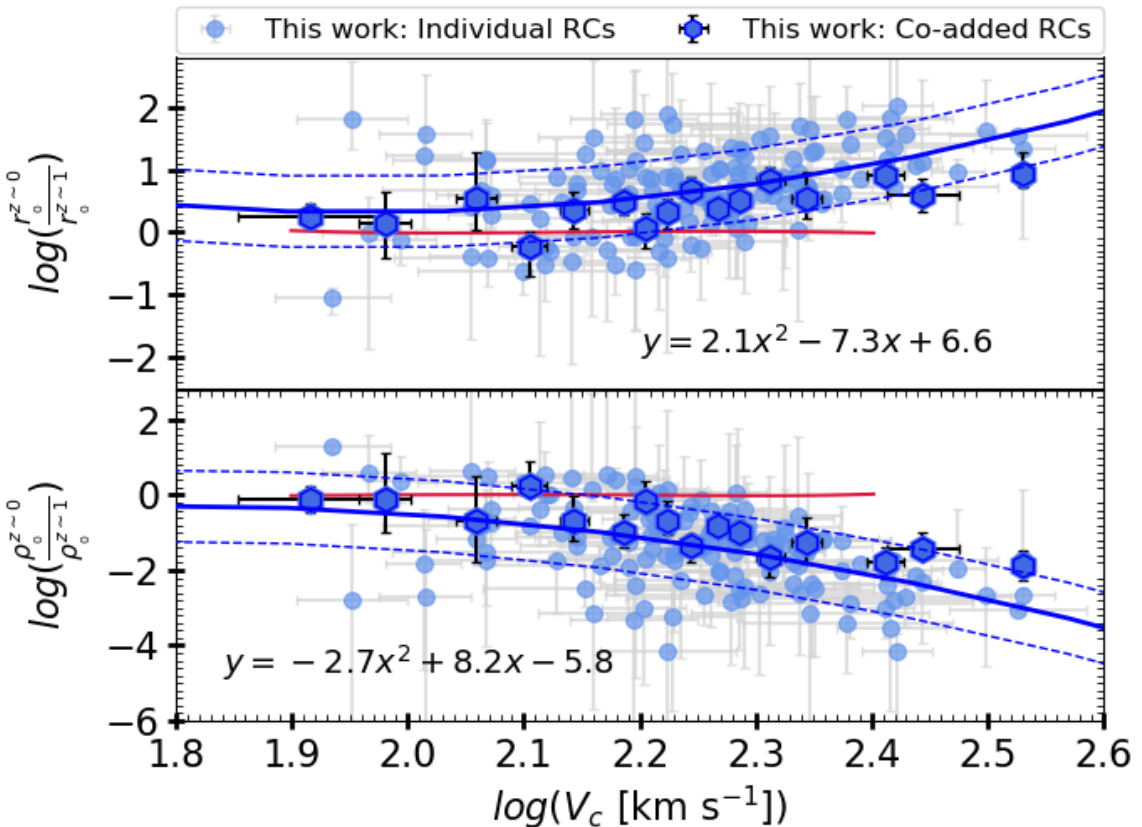


**Figure 6.11:** Normalized structural properties of the dark matter halo at  $z \sim 1$ . The ratio of dark matter core radius and density at  $z \approx 0$  to  $z \sim 1$  as a function of circular velocity. This plot shows the expansion factor of dark matter cores at  $z \sim 1$  with respect to local star-forming galaxies. The color codes for data points are similar to those in the left panel. The blue solid line shows the best-fit to the data, obtained by fitting the second order polynomial function printed in both panels. The dashed blue lines followed by solid line shows the  $1\sigma$  intrinsic scatter in the relations.

how the structural properties of dark matter differ at  $z \sim 1$  with respect to  $z \approx 0$ . First, we find that the dark matter cores at  $z \sim 1$  are smaller than their local counterparts by a median factor of 0.3. Second, the density of dark matter cores at  $z \sim 1$  is more than an order of magnitude higher than at  $z \approx 0$ . It is also very clear that these two ratios correlate very well with the circular velocity of the galaxies. Thus gives us the direct relation of expansion factor for core radius and density as a function of the circular velocity of a galaxy:

$$\log \left( \frac{r_0^{z \sim 0}}{r_0^{z \sim 1}} \right) = 2.1 \log V_c^2 - 7.3 \log V_c + 6.6 \quad [\pm 0.6 \text{ dex}] \quad (6.6)$$

$$\log \left( \frac{\rho_0^{z \sim 0}}{\rho_0^{z \sim 1}} \right) = -2.7 \log V_c^2 + 8.2 \log V_c - 5.8 \quad [\pm 0.9 \text{ dex}] \quad (6.7)$$

The Equation 6.6 & 6.7, are the efficacious in relating the structural properties of dark matter to baryonic matter. Plotting these relations in the right panel of Figure 6.11, clearly shows us that at  $z \sim 1$  objects those possessing higher circular velocity are denser in nature, i.e. more compact in size (in terms of dark matter cores), relative to  $z \approx 0$  star-forming galaxies. In other words, objects with higher circular velocity expand their dark matter cores larger over cosmic time, relative to objects with lower circular velocity. This means that the circular velocity plays a crucial role in the galaxy evolution process. We report that the intrinsic scatter in relation 6.6 & 6.7, is about 0.57 and 0.94 dex, respectively. Besides this, we also found that the galaxies in our sample have a typical dark matter core size of 3-10 kpc, which is a factor of 2.5 smaller than those reported in [Genzel et al. \(2020\)](#).

Moreover, the above discussion suggests that dark matter is most likely responding to the baryonic processes taking place in the inner region of galaxies throughout cosmic time. This also implies that early (say,  $z > 2$ ) dark matter halos are likely cuspy, which may have changed over cosmic time under the influence of galactic processes (e.g. AGN and supernova feedbacks, dynamical frictions), which has been previously suggested by many authors such as [Navarro et al. \(1996a\)](#); [Pontzen & Governato \(2012\)](#); [Nipoti & Binney \(2014\)](#); [Read et al. \(2016, 2018\)](#) and [Lazar et al. \(2020\)](#). Although, the difference in the size and density of the dark matter core between  $z \sim 1$  and  $z \approx 0$  is small, it is nevertheless remarkable and could have a very strong impact on the identification of the *Nature of Dark Matter*. In short, it shows a clear expansion in the structure of dark matter halos over cosmic timescales. Based on these results, one can easily interpret that if the dark matter cores are denser at  $z \sim 1$ , then the virialization scale (radius) of these systems should also be smaller with respect to the locals. The latter argument can be further tested using the forthcoming observations of neutral hydrogen in the outskirts of galaxies ([Baker et al., 2018](#)).

Furthermore, the results obtained with the Burkert halo model are consistent with the simulations. Therefore, so far we suggest that the rotation-dominated star-forming galaxies in the simulations and observations are very likely to have a dark matter core at the center of the halo. However, the inference of dark matter cores is very indirect in this study due to limited resolution in the inner region of galaxies. Therefore, to confirm the

our arguments, we still require high-resolution and good signal-to-noise data in the inner region of the galaxies. That can possibly be obtained with the upcoming James Webb Space Telescope (JWST) and in the future with the Extremely Large Telescope (ELT).

## 6.6 Summary

In this work, we have studied the structural properties of the dark matter in  $z \sim 1$  main sequence star-forming disc-like galaxies. We first mass-modelled the individual and co-added rotation curves, assuming that the baryons are distributed in the [Freeman \(1970a\)](#) disc and dark matter is modelled with the Burkert and NFW halo profiles. Then the mass modelling results in the Burkert and NFW cases are critically examined, interpreted, and compared with current state-of-the-art simulations. We found that the results obtained using the Burkert halo fits well with the observations and also mirror the simulations, see [Figure 6.2](#), [6.3](#), [6.4](#), [6.5](#), & [6.9](#). Therefore, in the end, we discussed and concluded the results obtained with the Burkert halo profile, we found that:

- Our mass modelling approach has proven robust to disentangle the various components of RCs, and being able to determine physical properties of baryons such as scale length, stellar and bulge mass, and dark matter structural properties such as core density and radius, as well as the fraction of dark matter.
- The dark matter fraction derived from the mass modelling outcomes (using [Equation 5.5](#)) agrees very well with the results of the model-independent dark matter fraction (obtained in [Chapter 5](#)). Moreover, it is also similar to those predicted by different simulations: EAGLE, TNG100 and TNG50.
- The results of the dark matter structural properties ( $r_0$  and  $\rho_0$ ) show that the dark matter cores at  $z \sim 1$  are on average a factor of 0.3 smaller and more than an order of magnitude denser than those of local star-forming galaxies. This suggests an expansion in the structure of dark matter halos over 6.5 Gyrs.
- We also report that the expansion of dark matter cores is a function of circular velocity. The objects with higher circular velocity expand their core more than those with low velocities. This suggests that the circular velocity plays a crucial role in deriving the galaxy evolution.

To sum-up, we have shown in our previous work that the progenitors of local star-forming galaxies at  $z \sim 1$  are similar in terms of total mass ( $V_c^2(R) \propto M_{\text{tot}}$ ), they are dark matter dominated objects and their baryon distribution evolves with time (see [Chapter 4](#) & [5](#)) . We have now shown that the dark matter distribution also changes over cosmic timescales. Therefore, we suggest that galactic processes that cause an evolution of the baryon distribution also have an impact on the dark matter. As a consequence, the dark matter distribution also changes through-out the cosmic time. In other words, dark matter responds to baryonic processes (e.g. AGN, supernova feedback, and dynamical

friction). If this work is confirmed by other observations, we will have the first observational evidence of *gravitational potential perturbations* in the inner region of galaxies. This study will have a strong implication on cross-checking simulations, as well as determining the astrophysical and particle nature of dark matter.



# Chapter 7

## Fundamental Scaling Relations

Although galactic processes are complex and show diversity from one galaxy type to another, there are some fundamental properties (in terms of kinematics and dynamics) that correlate over a large range (several orders of magnitude) of a galaxy type (late and early types). The correlation between the fundamental properties (mass, velocity, and scale-radius) of galaxies, often referred to as *scaling relations*, that are thought to play an important role in galaxy evolution. Indeed, they are the benchmark for current theoretical framework (and semi-analytical modelling) of galaxy formation and evolution. Therefore, the study of scaling relations and their cosmic evolution is an intriguing subject for both astrophysicists and cosmologists, and also one which always remains disputable. In this work, I have continued the long tradition of studying scaling relations, in particular, I have studied Tully-Fisher relation of disc galaxies and shown it's cosmic evolution since  $z \sim 1$ .

***Preamble:*** *The majority of the work has been submitted for publication in [Astronomy & Astrophysics](#) (see [Sharma & Salucci, 2021](#)). To highlight certain aspects with more clarity, here, I may have included some additional illustrations and descriptions.*

### 7.1 Introduction

The Tully-Fisher Relation (TFR) is the most fundamental empirical scaling relation which correlates the luminous matter properties with the dark halo. In the traditional TFR, which came from the seminal work of [Tully & Fisher \(in 1977\)](#), luminosity of the galaxies scales with their characteristic velocity (i.e. circular velocity  $V_c$ ) via power-law  $L \propto \beta V_c^\alpha$ , where  $\alpha$  is the slope, and  $\beta$  is intercept in the relation. Here, slope tells us the extent of circular velocity dependency on the luminosity, while quantity ( $\beta/\alpha$ ) is the zero-point which tells us the origin of this relation. In the local Universe, this relation is remarkably tight ( $\alpha \sim 4$ ;  $\beta/\alpha \sim 2$ ) for star-forming disc galaxies ([Tully & Fisher, 1977](#); [Feast, 1994](#); [Bell & de Jong, 2001](#); [Karachentsev et al., 2002](#); [Pizagno et al., 2007](#); [Toribio et al., 2011](#); [McGaugh et al., 2000](#); [Sorce et al., 2013](#)). Therefore, it is widely used in the

redshift independent distance measurements (Giovanelli et al., 1997a; Ferrarese et al., 2000; Freedman et al., 2011; Sorce et al., 2013; Neill et al., 2014). Since by knowing the luminosity one can relate the observed flux via  $L \propto F/4\pi D^2$  and infer the distance of the object. Moreover, TFR has also played an important role in determining the cosmological parameters, in particular by allowing the measurement of the Hubble constant  $H_0$  out to the local Universe (Giovanelli et al., 1997b; Tully & Pierce, 2000; Masters et al., 2006).

Beyond the distance indicator and cosmological needs, TFR is also widely discussed to understand the galaxy formation and evolution. In fact, it is one of the first scaling relations which explains the interplay of dark and luminous matter in the local Universe with a wide variety of data (Mathewson et al., 1992; McGaugh et al., 2000; McGaugh, 2005; Papastergis et al., 2016; Lapi et al., 2018b) and simulations (Mo & Mao, 2000; Steinmetz & Navarro, 1999). The rationale here is that the circular velocity is related to the total gravitational potential of the galaxy while luminosity traces the total stellar mass (Blumenthal et al., 1984; Mao et al., 1998; Girardi et al., 2002). This conception gives the birth to modified TFR:  $M \propto \beta V_c^\alpha$  (where  $M$  is the stellar or baryonic mass of the galaxy) which is well studied and proven remarkably tight in the local Universe (Verheijen & Sancisi, 2001; McGaugh, 2005; de Blok et al., 2008; Stark et al., 2009; Foreman & Scott, 2012; Lelli et al., 2016; Papastergis et al., 2016; Lapi et al., 2018b; Lelli et al., 2019). With the words of caution, in the optical and infra-red astronomy luminosity traces the stellar mass, which leads to stellar-TFR (STFR). Whereas, luminosity in the radio-wavelength traces the gas mass which in combination with stellar mass gives us nearly total baryonic mass ( $M_B = M_* + M_{gas}$ ) of the system and thus the relation is referred as baryonic-TFR (BTFR). Besides it, under the assumption that motion of baryons is circular in the Dark Matter (DM) halo, TFR also relates the total luminosity of galaxy via its total circular velocity, mass surface density ( $\Sigma$ ), and mass-to-light ratio ( $M/L = \Upsilon^*$ ) given by  $L \propto V_c/(\Sigma \Upsilon^*)$  (Binney & Tremaine, 2008). This relation gives us a simplistic way to infer the relative difference in mass-to-light ratio and surface-density of different subclasses of galaxies. Therefore, TFR is not only useful as distance indicator but also put the stringent constraints on the galaxy formation and evolution models and DM properties. The position of a galaxy on L-V or M-V plane gives us a direct indication of "how efficiently gas converted into stars and what is total mass distribution in the galaxy". In short, TFR is the foundation of galaxy formation and evolution models; therefore, it should be capable of explaining baryons and dark matter interplay at any epoch, and if not, then we have to understand why?

In this work, we are exploring the TFR at  $z \sim 1$  for star-forming galaxies (disc-like). Firstly, because a disc-type system form and evolve at  $z \leq 1.5$  and shows the homogeneous and controlled evolution (e.g. Lagos et al., 2017), therefore, can be used as a cosmic ladder to infer the cosmic evolution of baryons and dark matter. Second,  $z \sim 1$  is the epoch of transition where dark energy kicks-in and enforces the accelerated expansion of the Universe. It is known, nearly 50% of stellar mass in the Universe assembled in the galactic halos by  $z \approx 1$  (Pérez-González et al., 2008), and this is the time where cosmic star-formation density peaks (Madau & Dickinson, 2014, references therein). Therefore, it is crucial to compare the local baryonic and dark matter properties with the galaxies

at  $z \sim 1$ . It will allow us to understand: 1) how the disc-type system evolves after their formation at  $z \leq 1.5$ , and 2) what is the nature of the dark matter in these systems concerning the local Universe?

Some of the previous studies of star-forming galaxies (hereafter SFGs) in the cluster environment [Ziegler et al. \(2002\)](#); [Böhm et al. \(2004\)](#); [van Starkenburg et al. \(2006\)](#) have shown that the slope of TFR at intermediate redshift ( $z \sim 0.5$ ) is shallower in comparison to locals and lead the discussion of selection bias effect. However, other studies have shown that there is nearly no evolution in TFR slope since  $z \sim 1$  to  $z \approx 0$  ([Conselice et al., 2005](#); [Kassin et al., 2007](#); [Miller et al., 2011](#); [Miller et al., 2012](#)). Some recent studies of Integrated Field Unit (IFU) observations of isolated SFGs ([Puech et al., 2008](#); [Cresci et al., 2009](#); [Gnerucci et al., 2011](#); [Tiley et al., 2016](#); [Übler et al., 2017](#); [Harrison et al., 2017](#); [Tiley et al., 2019b](#)), claims that the zero-point of TFR varies while slope remains nearly the same. Therefore, currently, there is a chaos to reach on the conclusion of whether TFR has evolved over cosmic time (both in slope and zero-point) or it is just a selection effect. We would emphasize here that latter IFU studies have underlying uncertainties because: 1) Kinematics of datacubes has not been derived in 3D space, 2) There was a partial correction for beam smearing on the velocity profile, and 3) They have not accounted for the pressure gradient corrections which dominates at high- $z$  galaxies and suppress the circular velocity via radial-gradient. Notice, [Übler et al. \(2017\)](#) has accounted for the pressure gradient corrections but assuming constant and isotropic velocity dispersion, which overestimate the circular velocities (for details see Chapter 2, Section 2.4).

A quick recall, a telescope equipped with new generation spectrograph<sup>1</sup> can achieve only  $0.5 - 1.0$  arcsec spatial resolution, whereas, a galaxy from  $z \sim 1$  has a typical angular size of  $2 - 3$  arcsec. Therefore, a finite beam size causes the line emission to smeared on the adjacent pixels. As a consequence, the gradient in the velocity fields tend to become flattened, and line emission began to broad, which creates a degeneracy in the calculation of rotation velocity and velocity dispersion. This effect in the observations is referred to as ‘Beam Smearing’, which affects the kinematic properties of the galaxies, i.e. underestimated rotation velocity and overestimated velocity dispersion. *On average, beam smearing correction increases the circular velocity by 10 – 15%* (Chapter 3 and [Johnson et al. 2018](#)). On the other hand, at high- $z$  Inter-Stellar Medium (ISM) is highly turbulent ([Burkert et al., 2010](#); [Wellons et al., 2020](#)), this turbulence in the ISM induces a force against gravity in galactic disc via radial gradient which suppresses the rotation velocity of gas and stars. This effect generally referred to as ‘Asymmetric Drift (AD)’ for stellar component, and ‘Pressure Gradient (PG)’ for gas component. The latter effect is generally negligible in local rotation dominated galaxies (late-type galaxies) but significantly observed in the local dwarfs and early-type galaxies (e.g. [Valenzuela et al. \(2007\)](#); [Read et al. \(2016\)](#); [Weijmans et al. \(2008\)](#)). Highly turbulent ISM conditions at high- $z$  ([Burkert et al., 2010](#); [Turner et al., 2017](#); [Johnson et al., 2018](#); [Wellons et al., 2020](#)) make pressure gradient prominent to disentangle, specifically, in the case of circular velocity measurements, dynamical mass modelling and DM studies. Otherwise, one may lead to

---

<sup>1</sup>Integrated Field Units (IFUs)

underestimated circular velocity. *On average, AD or PG can suppress the rotation velocity by more than 50%*, see Chapter 3. Therefore, accurate Pressure Gradient Corrections (PGC) keeps more importance than the beam smearing correction.

Aforementioned physical and observational uncertainties have been disentangled by us in Chapter 3. In this work, we adopt the kinematic and photometric dataset established in latter work. We also employ the dynamically estimated stellar and halo masses determined in Chapter 6, thereby improves upon the understanding of TFR at high- $z$ . This chapter organized as follows, section 7.2 contains a brief description of data and its physical quantities, section 7.3 describes the numerical recipe of fitting TFR and section 7.4 & 7.5 focused on the results and detailed discussion between current results and previous studies. The main findings of the work are summarized in section 7.6. In this work, we have assumed a flat  $\Lambda$ CDM cosmology with  $\Omega_{m,0} = 0.27$ ,  $\Omega_{\Lambda,0} = 0.73$  and  $H_0 = 70 \text{ km s}^{-1}$ .

## 7.2 Ensemble Data

We are using the KROSS star-forming galaxy sample previously studied by Stott et al. (2016) and others (Harrison et al., 2017; Tiley et al., 2019a,b; Johnson et al., 2018), this data is publicly available at KROSS-website<sup>2</sup>. From publicly available KROSS sample, a sub-sample of 344 star-forming galaxies is deeply investigated by us in Chapter 3 (hereafter, GS20). In GS20, kinematics of the KROSS datacubes is derived from <sup>3D</sup>BAROLO (Teodoro & Fraternali, 2015; Di Teodoro et al., 2016). It takes into account the beam smearing correction in 3D-space and provides the moment maps, stellar surface brightness profile, rotation curve (RC), dispersion curve (DC) along with the kinematic models. Later RCs are corrected for pressure gradient, which seems to dominate the kinematics of high- $z$  galaxies, for details we refer the reader to Chapter 3. A two-step technique of handling datacubes in Chapter 3 yields the intrinsic velocity profile of an individual galaxy even in the low-resolution data. Therefore gives us a robust and reliable estimate of the circular velocity of the sample. Out of 344 KROSS sample, we choose to analyse only 256 Quality-1 & 2 objects, referred to as Q12 sample in GS20 work.

In this work we adopt this Q12 sample, which we have also used to study the dark matter fraction in Chapter 5. Let me remark, we adopt SED driven stellar masses (Tiley et al., 2019b), and total gas mass derived using Tacconi et al. (2018) and Lagos et al. (2011). Moreover, our sample is representative of *main-sequence* of star-forming galaxies. In Sharma et al. 2021c (under peer review), we further analyse the rotational curves (RCs) of Q12 and apply mass models to decompose the RCs into their constituents (stars gas and dark matter), thereby we study the structural properties of dark matter. In the latter work, we have also dynamically calculated the physical quantities (stellar mass & disc radius, virial mass & radius, and dark matter inner core density & radius) from individual and co- added RCs. Therefore, in this work, we use the photometric and kinematic data from Chapter 3, as well as the dynamically derived physical properties elaborated in Chapter 6.

---

<sup>2</sup><http://astro.dur.ac.uk/KROSS/data.html>

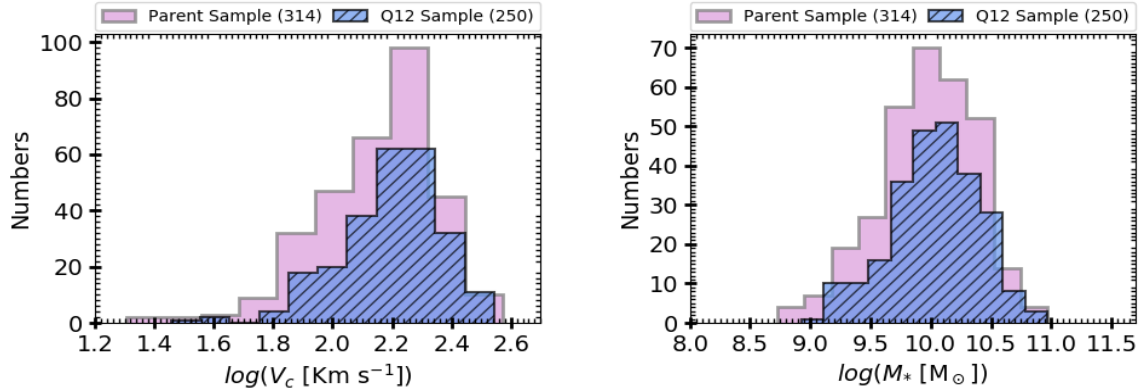


**Figure 7.1:** *Left Panel:* Distribution of circular velocities computed at  $R_{out}$ . *Right panel:* Distribution of stellar masses. The color code in both panels are same and given as following: parent Q12 sample in pink and analysed Q12 sample in blue. Notice Analysed Q12 sample is rotation dominated sample (i.e.  $V_{int}/\sigma > 1$ ) which contain 250 galaxies out of 256, where 6 galaxies are discarded due to huge asymmetry in their rotation curves.

Since this work is partly focused on individual study of RCs; therefore, we visually inspect each RC and remove them if huge asymmetry is noticed. In total we discard six RCs. To resume, our final sample contains 250 galaxies, which covers the inclination range:  $25^\circ \leq \theta_i \leq 75^\circ$ , the redshift range:  $0.75 \leq z \leq 1.04$ , the effective radii:  $0.12 \leq \log(R_e [\text{kpc}]) \leq 1.04$ , and circular velocities:  $1.49 \leq \log(V_{out} [\text{km s}^{-1}]) \leq 2.53$  computed at  $R_{out} (\sim 3R_e)$ . A distribution of circular velocities and stellar masses of Parent sample (established in Chapter 3) and Q12 sample used through-out in this thesis work is shown in Figure[7.1]. This implies that we cover the full velocity ranges of sample established in Chapter 3, so the KROSS parent Sample ([Stott et al., 2016](#); [Harrison et al., 2017](#)).

## 7.3 Methodology

In this section, we recall the circular velocities and stellar masses of the sample because they are the required quantities for Tully-Fisher relation. For the determination of other physical quantities, e.g. the radius of the stellar disc, we refer the reader to Section 3.2.1.5 and [Harrison et al. \(2017\)](#). Finally, we also describe the fitting method used in constraining the Tully-Fisher relation slope and zero-point.

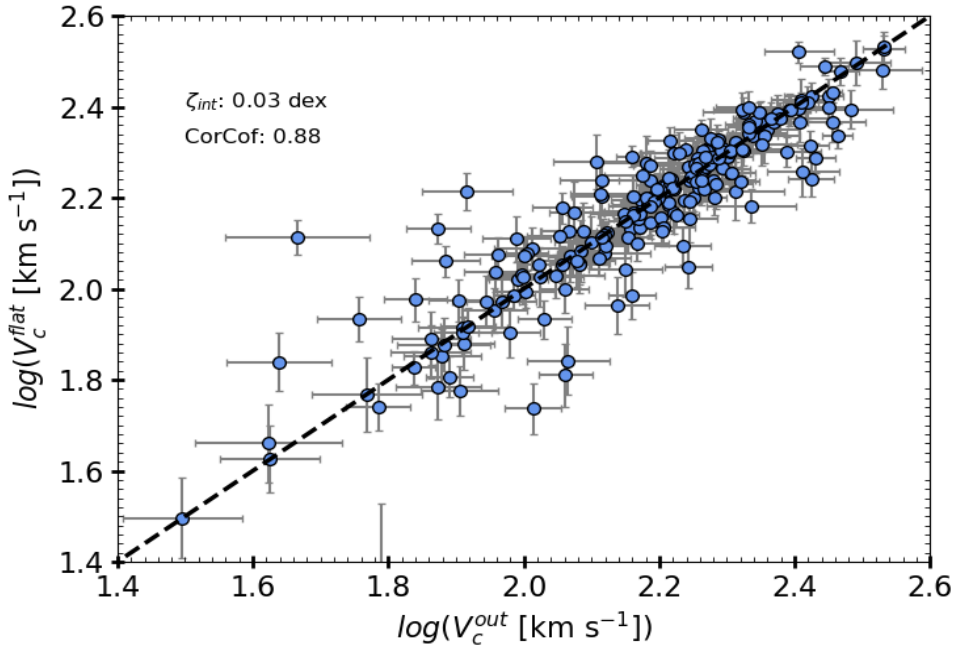


**Figure 7.2:** The comparison of circular velocities computed at  $R_{out}$  and  $R_{flat}$  ( $V_c^{out}$  and  $V_c^{flat}$  respectively). The black dashed line is showing the one-to-one plane. The intrinsic scatter ( $\zeta_{int}$ ) and Pearson co-relation coefficient ( $CorCof$ ) are printed on the upper left corner of the plot. In the analysis we refer  $V_c^{out} = V_c$  as a circular velocity of object.

### 7.3.1 Circular Velocity and Stellar Mass Measurements

We have investigated the circular velocity of rotation curves at four different scale lengths<sup>3</sup> (see Section 3.2.1.3)  $R_e$ ,  $R_{opt}$ ,  $R_{out}$  ( $= 5 R_D$ ) and  $R_{flat}$ <sup>4</sup> and referred to as  $V_c^{Re}$ ,  $V_c^{opt}$ ,  $V_c^{out}$  and  $V_c^{flat}$  respectively. Notice, effective radius for majority of sample falls below the resolution limit ( $\sim 4.0$  kpc with median seeing 0.5 arcsec at  $z \sim 0.9$ ), where as optical radius stays on the verge. To be conservative, we only rely on circular velocity measurements done at  $R_{out}$  and  $R_{flat}$ , those stays above the resolution limit in majority ( $\approx 99\%$ ) of sample. In Figure 7.2, we have shown the one-to-one comparison of  $V_c^{out} - V_c^{flat}$ . We notice that the  $V_c^{flat}$  and  $V_c^{out}$  correlates nearly 90% with an intrinsic scatter of 0.03 dex, i.e. for our sample one can either use  $V_c^{out}$  or  $V_c^{flat}$ . In our analysis, we have used  $V_c^{out}$  as a circular velocity and denoted it as  $V_c$ .

We adopt the stellar masses given by [Harrison et al. \(2017\)](#). These stellar masses are computed using fixed mass-to-light ratio in rest-frame H-band, following  $M_* = \Upsilon_H \times 10^{-0.4 \times (M_H - 4.71)}$ , where  $\Upsilon_H$  and  $M_H$  are mass-to-light ratio and absolute magnitude in

<sup>3</sup>For an exponential thin disc, stellar-disc radius is defined as  $R_D = 0.59R_e$ . Under the same assumption, scale length, which encloses the 80% of the stellar mass is referred to the optical radius and defined as  $R_{opt} = 3.2R_D$ . For details, we refer reader to [Persic et al. \(1996\)](#).

<sup>4</sup> $R_{flat}$  is estimated by taking the median of last three data points in the RCs (assuming RC is flat in the outskirts).

H-band respectively. For the details of photometric stellar mass determination, we refer the reader to Section 3.2.1.5. The stellar mass range covered by our sample employed in this chapter is shown in the right panel of Figure[7.1]. Note that in Chapter 6, we dynamically retrieve the stellar masses of individual and co-added (binned) data. In the same work (Figure 6.4) we have shown that the dynamically inferred stellar masses of binned data are in one-to-one relation with photometric stellar masses with relatively low intrinsic scatter. Therefore, in this chapter for individual galaxies we use photometric stellar masses and for binned dataset we use dynamically inferred stellar masses.

### 7.3.2 Fitting Method

We consider that the log-log distribution of stellar masses and circular velocities follows a power-law of slope ( $\alpha$ ) and intercept ( $\beta$ ). Which can mathematically defined as:

$$\log(Y) = \beta + \alpha \log(X) \quad (7.1)$$

Where,  $Y$  can be a list of stellar masses and  $X$  circular velocities ( $V_c$ ). To obtain the best-fit to the data, we use the Generalize Least-square Method (GLM). Which enables to include the uncertainties in the ordinate and abscissa, as well as takes into account the orthogonal scatter (see Press et al., 1992). For fiducial analysis, we assume maximum likelihood function such that 1) the uncertainties in abscissa and ordinate ( $\delta_x, \delta_y$ ) are independent of each other, 2) scatter ( $\sigma_x, \sigma_y$ ) in the data is Gaussian. Under this assumption log-likelihood function can be written as:

$$\ln(L) = - \sum_i^N \ln(\sqrt{2\pi\delta_{y,i}}) - \sum_i^N \frac{(Data - model)^2}{2\delta_{y,i}^2} \quad (7.2)$$

where  $\delta_{y,i} = \sqrt{\alpha^2\delta_{x,i}^2 + \delta_{y,i}^2 + \sigma_y^2}$ , and model is given by equation[7.1]. This method explores and optimizes the slope and intercept such that it allow minimum intrinsic scatter around the best-fit. We run the Markov Chain Monte Carlo (MCMC) simulation to obtain the posterior probability distribution of  $\alpha, \beta, \sigma_y$ . We initialize the chains with 70 random walkers, 10K steps with 5k burn-in. The initial guess are given in the range:  $[0 \leq \alpha \leq 5]$ ,  $[1 \leq \beta \leq 10]$ , and  $[0.01 \leq \sigma_y \leq 2.0]$ . This fitting is refer to as ‘MCMC-Fit’ in the analysis. This kind of method/technique has been previously used to infer the slope of TFR of local galaxies (Lelli et al., 2016), and proven robust to determine the accurate slope and zero-point.

Furthermore, the TFR fitting is performed on normalized data, where normalization is performed around pivot-point ( $pp$ ) of stellar/baryonic masses and circular velocities. Let us stress that this normalization doesn’t not make any change in the slope, but gives an offset on intercept ( $\beta_{pp}$ ). This offset is substantially taken-down by computing true intercept ( $\beta$ ) as:

$$\beta = -\alpha \times \log(V_c^{pp}) + \log(M^{pp}) - \beta_{pp} \quad (7.3)$$

where  $\log(V_c^{pp})$  and  $\log(M^{pp})$  are the pivot-point of circular velocities ( $\log(V_c^{pp} [\text{km s}^{-1}]) = 2.26$ ) and stellar/baryonic masses ( $\log(M_*^{pp} [\text{M}_\odot]) = 10.17$ ,  $\log(M_{Bar}^{pp} [\text{M}_\odot]) = 10.35$ ) respectively.

## 7.4 Results and Analysis

In this section, we first validate our sample with mass-size and angular momentum scaling relation, and then the new results of Tully-Fisher relation has been shown in comparison with previous high-redshift and local star-forming galaxies.

### 7.4.1 Mass-Size Relation

From the theoretical framework of galaxies, we know that the galaxies' halo accrete the hot gas during their evolution process, which cools down at the center of galaxy, as a consequence stars form. Over the time scale of galaxy evolution star-formation takes place in different regions of the galaxy, and from many regions stars eventually migrate. The rotation of galactic halo, which may occur due to tidal torque at the time of formation of halo or during a particular event, also help in migrating the stars [Binney & Tremaine \(2008\)](#). Therefore, the study of stellar-mass to size relation gives us the indirect evidence of assembly history of galaxies and their relationship with their dark matter halos.

The two main class of galaxies are early-type and late-type, recognized as red-sequence and blue-cloud in the local Universe ([Gavazzi et al., 2010](#)), they both show a different dependency between stellar-disc size and total stellar mass ([Shen et al., 2003](#)). However, for nearly a decade, cosmic evolution of mass-size relation of galaxies was an open question, (e.g. early-type: [Daddi et al. 2005](#); [van der Wel et al. 2008](#); [Saracco et al. 2011](#); [Carollo et al. 2013](#); late-type: [Mao et al. 1998](#); [Barden et al. 2005](#); [Mosleh et al. 2011](#)). Recently, with a large dataset of CANDELS survey [van der Wel et al. \(2014a\)](#) statistically studied the mass-size relation of early- and late-type galaxies through the cosmic time ( $0 < z < 3$ ). They shown that the early type galaxies have steep relation between mass-size, and they evolve faster with time. Whereas, late-type galaxies show a moderate evolution with time, as well as a shallow mass-size relationship, given as:

*Early – types :*

$$R_e \propto M_*^{0.75} \quad (\text{for } M_* > 2 \times 10^{10} \text{ M}_\odot), \quad (7.4)$$

$$R_e \propto (1 + z)^{-1.48} \quad (\text{fast evolution})$$

*Late – types :*

$$R_e \propto M_*^{0.22} \quad (\text{for } M_* > 3 \times 10^9 \text{ M}_\odot), \quad (7.5)$$

$$R_e \propto (1 + z)^{-0.75} \quad (\text{moderate evolution})$$

It is noteworthy that the intercept of the relation changes while the slope remains the same throughout cosmic time. This suggests that the different assembly mechanism acts

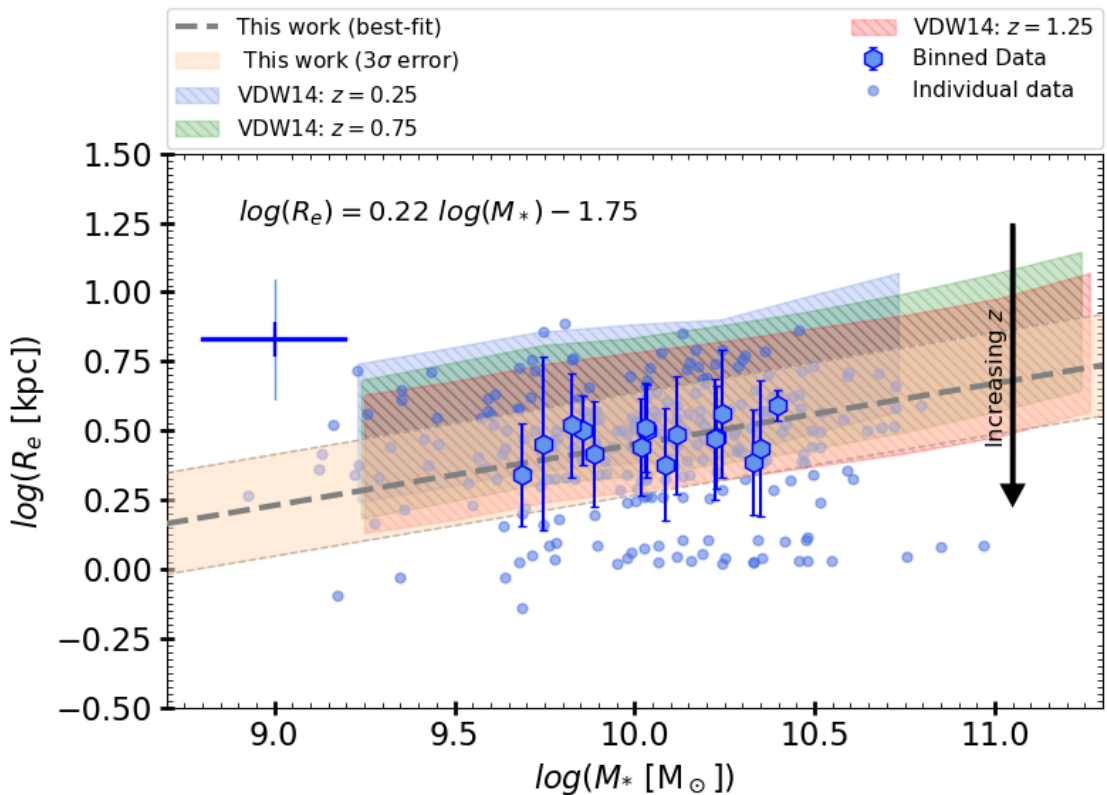


**Figure 7.3:** Mass-size relation of  $z \sim 1$  star-forming galaxies compared to [van der Wel et al. \(2014a\)](#) (CANDELS survey data). The blue small circles and hexagons represent the data used in this work. The grey dashed line and peach shaded area represent the best fit to the data and the  $3\sigma$  intrinsic scatter, respectively. The blue, green, and red shaded regions represent the mass-size relation of [van der Wel et al. \(2014a\)](#) at  $z = 0.25, 0.75$ , and  $1.25$ , respectively. The blue thin and thick plus markers represent the intrinsic scatter of one dex in the individual and binned datasets, respectively, around the grey best-fit line reported in this work.

similarly on both types of galaxies at different epochs (van der Wel et al., 2014a). Thus, we have an empirical evidence for one of the key processes that derive the galaxy evolution.

In this work, we checked our dataset of star-forming disc-like galaxies (i.e. late-types) with this benchmark relation. In Figure 7.3, we show the mass-size relation of our sample for individual galaxies and binned (derived from co-added RCs) dataset. We applied a liner-fit (using the least-square method) to individual (photometric) and binned (dynamical) quantities. In both cases, we have obtained a similar slope with different intrinsic scatter. In particular, we report a slope of 0.22 which is similar/equal to the one reported in van der Wel et al. (2014a), and an intrinsic scatter of 0.21 dex (individuals) and 0.06 dex (binned). This confirms the robustness of photometric and dynamically derived quantities of our sample, and allowed us to investigate the other seminal scaling relations. Furthermore, the authenticity of the mass-size relationship also verifies the robustness of our earlier results presented in Chapters 4, 5 & 6.

### 7.4.2 Specific Stellar Angular Momentum

The angular momentum is known to be a conserved and fundamental quantity of a galaxy. A galaxy halo acquires angular momentum at the time of its formation through large-scale tidal torques, and it remains approximately constant through-out the subsequent evolution. When the baryons fall into a halo, they can either gain or lose angular momentum (or both) depending on the surrounding conditions. The angular momentum gained by the baryons is generally small when they reach the halo (near the virial radius), but as they approach the centre of the halo (2-10 kpc), they can gain enough angular-momentum to form a centrifugally supported disc that follows an exponential profile (Athanassoula, 1983; Mo et al., 1998). From observations of local galaxies we know that in the latter processes the angular momentum seems to decay (re-distributed) weakly, i.e. a fraction ( $\sim 30\%$ ) of it is lost (transferred), either by viscous angular momentum redistribution (e.g. Courteau, 1997), or due to gas losses during disc formation (e.g. Burkert, 2009). Numerical framework of galaxy evolution suggest that angular momentum transfer occurs when the galactic disc is sufficiently centrifugally supported, roughly around  $z \sim 1$  (Lagos et al., 2017). However, it is currently a major challenge to provide observational evidence in favour of the latter. Recently, some IFU studies (e.g. Obreschkow et al., 2015; Burkert et al., 2016; Swinbank et al., 2017; Gillman et al., 2020) have shown that the stellar angular momentum scaling relation with stellar mass follow  $J_* = M_*^{2/3}(1+z)^{-\alpha}$  relation, where  $(1+z)^{-\alpha}$  gives the cosmic evolution (or angular momentum transfer over cosmic time) where  $\alpha$  lies between 0.5 – 1.5.

Given the moderate resolution in our sample (similar to previous high-redshift studies) but differently processed kinematics (relative to previous high-redshift studies). In this work, we attempted to verify the stellar angular momentum scaling with stellar (and halo) mass, relative to previously mentioned studies. Following Romanowsky & Fall (2012) we compute the stellar angular momentum normalized to stellar mass, i.e. specific stellar angular momentum, because it removes the implicit scaling between angular momentum

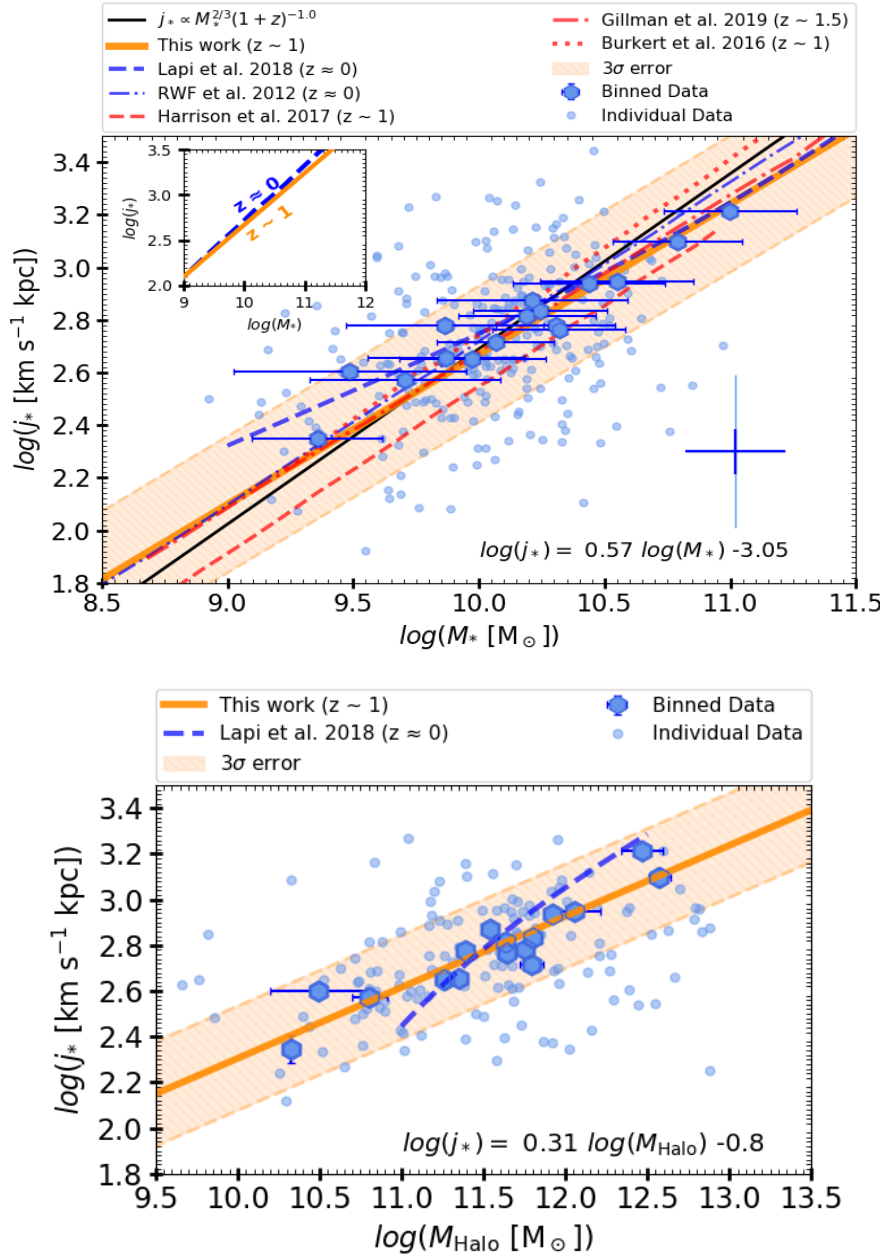


**Figure 7.4:** Specific stellar angular momentum as a function of stellar and halo mass, top and bottom panels, respectively. The blue circles and hexagons represent the individual and binned dataset. The orange solid line and peach shaded area represent the best fit to the data and the intrinsic scatter of  $3\sigma$ , respectively. The comparison studies of local star-forming galaxies are indicated by blue dotted-dashed and dashed lines, Romanowsky & Fall (2012) and Lapi et al. (2018b), respectively; high-redshift studies are represented by the red dotted, dotted-dashed, and dashed lines, Burkert et al. (2016); Harrison et al. (2017), and Gillman et al. (2020), respectively. The black solid line shows the relation  $J_* = M_*^{2/3}(1+z)^\alpha$  with  $\alpha = 1.0$  (Swinbank et al., 2017), which is very close to the data, and shows an intrinsic scatter of 0.06dex (for binned data). This shows that we are in good agreement with previous studies (Burkert et al., 2016; Swinbank et al., 2017). The blue thin and thick plus markers represent the intrinsic scatter of one dex in the individual and binned datasets, respectively, around the orange best-fit line. The inset-figure in the top panel shows a zoom of  $j_* - M_*$  fits at  $z \sim 1$  (this work) and  $z \approx 0$  (Romanowsky & Fall, 2012) within the stellar mass range  $9.0 \leq \log(M_* [M_\odot]) \leq 12.0$ .

and stellar mass:

$$j_*^n = k_n V_c R_e \quad (7.6)$$

where,  $V_c$  is the circular velocity of the galaxy,  $R_e$  is the effective radius, and  $k_n$  depends on the Sérsic index of galaxy which can be approximated by  $k_n = 1.15 + 0.029n + 0.062n^2$ .

To calculate the  $j_*$  of our sample, we use the circular velocity computed at  $2.95 R_e$ , and the Sérsic index of our sample ranges between  $0.65 \leq n \leq 1.25$ ; therefore, we approximated  $n=0.95 \pm 0.2$ . To fit the slope to the relation we use the same procedure defined for SFTR in Section 7.3.2. The results are shown in the upper panel of Figure 7.4. We note that the best-fit obtained in our work is equivalent to the fit obtained by [Swinbank et al. \(2017\)](#) and [Gillman et al. \(2020\)](#). Moreover, we matches the previous local and other high-redshift studies within  $3\sigma$  uncertainty.

A consistency check of the  $j_* - M_*$  best-fits for a typical range of stellar masses ( $9.0 \leq \log(M_*/[\mathrm{M}_\odot]) \leq 12.0$ ) of local disc galaxies is shown in the inset of the upper panel of Figure 7.4, for  $z \sim 1$  and  $z \approx 0$  galaxies. As we can see,  $j_* - M_*$  shows a very minimal (or no) change in the slope and zero-point of the relation. The similarity of the  $j_* - M_*$  plain of this work and other studies justifies the robustness of the kinematic and dynamical methods/techniques employed in Chapters 2 & 6. Therefore, now we can confidently use our sample to investigate the STFR over cosmic time-scales. On the other hand, the scaling of the specific angular momentum with the halo mass, lower panel Figure 7.4, shows a divergent evolution over cosmic time. This suggests that most-likely interplay (gravitational or collisional) between dark and luminous matter strongly depends on the environment of the galaxy.

### 7.4.3 Stellar Tully-Fisher Relation

Using the method described in Section 7.3.2, we obtained the best fit to the  $M_* - V_c$  plain of  $z \sim 1$  star-forming galaxies, the so-called ‘Stellar Tully-Fisher Relation (STFR).’ In Figure 7.5, we show the main results, while Figure 7.6 contains the posterior distribution of best fit slope, intercept, and vertical scatter obtained using MCMC-fit. We fitted both the individual galaxies (orange circles), and the binned dataset (orange hexagons). However, we have shown the best-fit corresponds to the binned dataset, as we rely on dynamically derived stellar masses more than the photometric stellar masses (see Chapter 6). We find that all individual data points fall within the  $3\sigma$  scatter of the best-fit (taking into account the 0.2 dex uncertainty of the individual stellar masses, see Section 3.2.1.5). We report STFR slope of  $\alpha_s = 2.43 \pm 0.85$  and zero-point  $\beta_s/\alpha_s = 2.00 \pm 0.44$ , with an intrinsic scatter of 0.4 dex (individuals) and 0.21 dex (binned).

To compare our results with local star-forming galaxies, we adopt the slope and intercept of the STFR relation given by [Reyes et al. 2011](#) and [Lapi et al. 2018b](#). One can note that our results are comparable to both local studies within  $3\sigma$  uncertainty. However, the intrinsic scatter reported around the best-fit of the comparison studies is a factor of 2 higher than the best-fit obtained in our work. Moreover, in this work we intend to investigate the small deviation between the slope and the zero-point of the STFR at two epochs ( $z \approx 0$  and  $z \sim 1$ ). Therefore, we decided to closely compare the

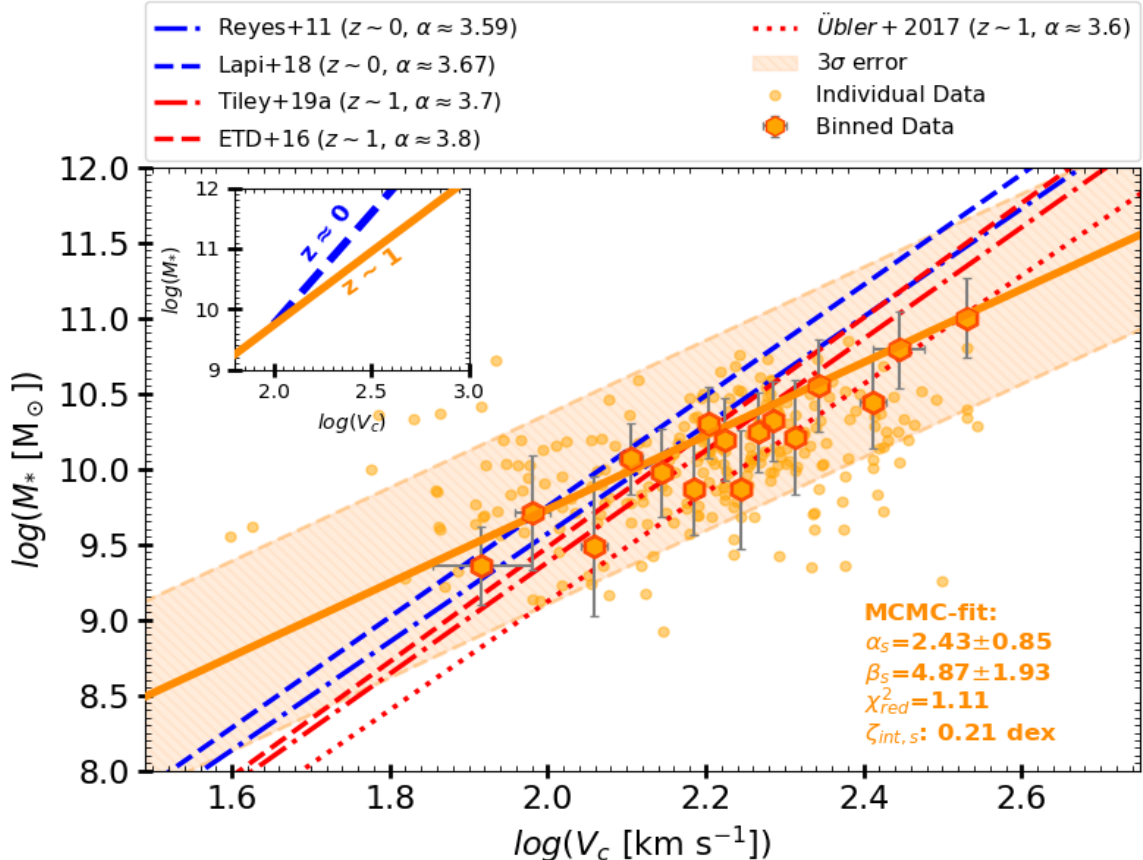


**Figure 7.5:** Stellar Tully-Fisher relation of  $z \sim 1$  star-forming galaxies. The orange circle, and hexagons represents the individual and binned data. The solid orange line shows the best-fit to the data generated using MCMC sampling, the dashed orange lines followed by the shaded area represents the  $3\sigma$  intrinsic scatter around the best fit line. The quality assessment parameters ( $\chi^2_{red}$ ,  $\zeta_{int,s}$ ) of MCMC-fit are printed on the lower-right side of the plot. For comparison purpose, we have plotted the local and high- $z$  STFRs by blue and red lines, respectively. Local STFR: The blue dotted-dashed line represents the Reyes et al. (2011) relation, and the blue dashed line shows the Lapi et al. (2018b) relation. High- $z$  STFR: the red dashed, dotted, and dotted-dashed lines show the Di Teodoro et al. (2016); Übler et al. (2017), and Tiley et al. (2019a), respectively. The inset-figure shows the zoom of STFR-fits at  $z \sim 1$  (this work) and  $z \approx 0$  (Lapi et al., 2018b) within the range  $1.8 \leq \log(V_c [\text{km s}^{-1}]) \leq 3.0$  and  $9.0 \leq \log(M_*) [\text{M}_\odot] \leq 12.0$ .

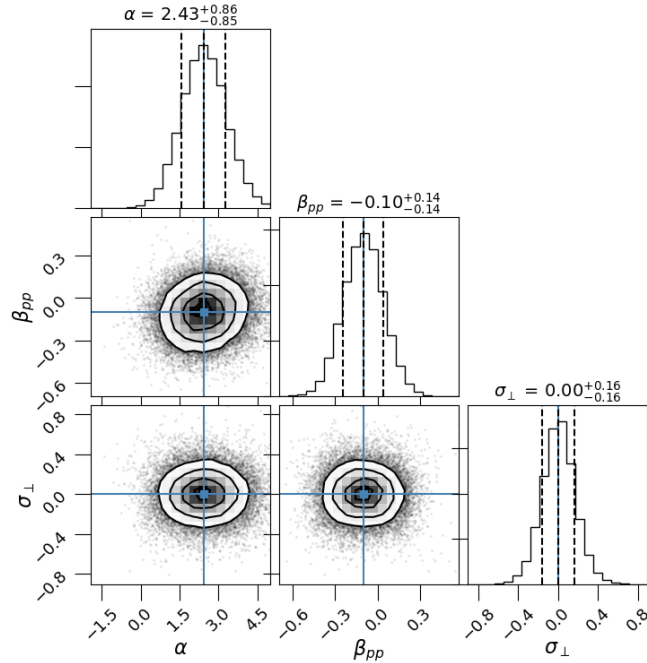


**Figure 7.6:** Posterior distribution of MCMC-fit,  $\alpha$  is the slope,  $\beta_{pp}$  is intercept (offset around pivot-point:  $pp$ ), and  $\sigma_{\perp}$  is the scatter on y-axis data. The blue crosses in the corner plots shows the final best-fit values, and they are printed on the top of each posterior distribution. Notice, in the main text (and plots) notation for slope, intercept and intrinsic scatter are referred to as  $\alpha_s$ ,  $\beta_s$ , and  $\zeta_{int,s}$  for STFR.

slope and zero-point obtained in this work with those obtained for the local population (in particular Lapi et al. 2018b) within the range  $1.8 \leq \log(Vc \text{ [km s}^{-1}\text{]}) \leq 3.0$  and  $9.0 \leq \log(M_* \text{ [M}_\odot\text{]}) \leq 12.0$ , shown in the inset of Figure 7.5.<sup>5</sup> We have found that the STFR shows a divergent evolution between  $z \sim 1$  and  $z \approx 0$  in the given mass and velocity range. That is, the zero-point of the relation does not change with cosmic time, while the slope shows a significant evolution.

To compare the results with those of high-redshift star-forming galaxies, we used the relations reported by Di Teodoro et al. (2016); Tiley et al. (2019a) and Übler et al.

<sup>5</sup>  $1.8 \leq \log(Vc \text{ [km s}^{-1}\text{]}) \leq 3.0$  and  $9.0 \leq \log(M_* \text{ [M}_\odot\text{]}) \leq 12.0$  are typical circular velocity and stellar mass ranges of local star-forming galaxies, respectively.

Author	Relation	Redshift	$\alpha_s$ [ $\log(km s^{-1})$ ]	$\beta_s$ [ $\log(M_\odot)$ ]	$\chi^2_{red}$	$\zeta_{int,s}$ (dex)
This work	STFR	$z \sim 1$	$2.43 \pm 0.85$	$2.00 \pm 0.44$	1.11	0.21
Reyes et al. (2011)	STFR	$z \sim 0$	$\approx 3.59 \pm 0.01$	$\approx 2.39 \pm 0.01$	2.34	0.34
Lapi et al. (2018b)	STFR	$z \sim 0$	$\approx 3.67 \pm 0.23$	$\approx 2.41 \pm 0.10$	2.79	0.51
Di Teodoro et al. (2016)	STFR	$z \sim 1$	$\approx 3.80 \pm 0.21$	$\approx 1.88 \pm 0.46$	2.34	0.33
Übler et al. (2017)	STFR	$z \sim 1$	$\approx 3.60 \pm 0.01$	$\approx 1.92 \pm 0.01$	2.38	0.32
Tiley et al. (2019a)	STFR	$z \sim 1$	$\approx 3.70 \pm 0.3$	$\approx 9.88 \pm 0.10$	2.22	0.27

**Table 7.1:** Stellar Tully Fisher Relation slope and zero-points obtained in this work and previous studies. Here  $\alpha_s$ ,  $\beta_s$ ,  $\chi^2_{red}$ , and  $\zeta_{int,s}$  columns gives the slope, zero-point, reduced  $\chi$ -square relative to data used in this work, and intrinsic scatter around the best-fit, respectively.

(2017), details are given in Table 7.1. We note that all of the aforementioned studies fairly accurately reflect our data. However, to assess the correctness of their best fit with respect to our data, we calculate the intrinsic scatter around their fits. We found that the intrinsic scatter with respect to other fits is at least a factor of 1 higher than the one obtained in our work, see Table 7.1. Therefore, we rely on the best fit, which we have obtained using a state-of-the-art technique. Moreover, small discrepancies in the slope and zero-point may result from differences in the determination of the circular velocities (kinematics), mentioned in Section 7.1.

## 7.5 Discussion and Conclusions

Recent studies of high-redshift galaxies, in particular Tiley et al. (2019a, KROSS) and Übler et al. (2017, KMOS3D), largely referred and compared in this entire work, report that the zero-point of the STFR varies with cosmic time, while the slope remains the same. In contrast to both studies, we report a significant evolution of the slope while the zero-point remains constant in the range of  $1.8 \leq \log(V_c [\text{km s}^{-1}]) \leq 3.0$  and  $9.0 \leq \log(M_* [\text{M}_\odot]) \leq 12.0$ , which is a similar range studied by Tiley et al. (2019a) and Übler et al. (2017). Hence, we report a divergent evolution in STFR from  $z \sim 1$  to  $z \approx 0$ , results are shown in Figure 7.5.

First of all, the evolution in the STFR and no evolution in mass-size and  $J_* - M_*$  relation of star-forming galaxies suggests that the baryonic assembly works in a similar way at all epochs in these systems. While, the dark matter response to the baryonic process is most likely different and time-dependent. Secondly, divergent evolution in the STFR (and also in  $J_* - M_{\text{Halo}}$  relation) may occur in response to environmental changes, for example, accretion and ejection of mass. Alternatively, divergent evolution may also takes place in response to the change/stabilisation of pressure conditions at high-redshift.

On the other hand, comparing our previous findings of Chapter 4 & 5 with current work, we found that:

$$\text{at } z \sim 1 : \quad M_* \propto V_c^{2.43} \rightarrow V_c \propto M_*^{0.41} \quad \& \quad V_c \propto R_D^0 \quad (7.7)$$

that is, circular velocity does not depend on stellar-disc radius, and it quickly grows with stellar mass. Whereas for locals:

$$\text{at } z \approx 0 : \quad M_* \propto V_c^4 \rightarrow V_c \propto M_*^{0.25} \quad \& \quad V_c \propto R_D^{0.67} \quad (7.8)$$

that is, circular velocity has nearly linear relation with stellar-disc radius of galaxies (Lapi et al., 2018b) and grows slowly with stellar mass. Alternatively, Equations 7.7 & 7.8 are suggesting that the for given a stellar mass gravitational potential ( $V_c^2 = rd\Phi/dr$ ) experienced by a galaxy at  $z \sim 1$  is higher than at  $z \approx 0$ , independent of its radius. This means that the galaxy with a same stellar masses have higher dark matter content within

stellar disc. The latter results have already been reported using a model independent dynamical studies of rotation curves in Chapter 5, where we show that dark matter fraction  $f_{\text{DM}}(< R_{\text{opt}} \text{ at } z \approx 0)$  is smaller than  $f_{\text{DM}}(< R_{\text{opt}} \text{ at } z \sim 1)$ .

Furthermore, if star-formation is always inside-out in disc-like systems (Moster et al., 2018), i.e. baryon ensembles and turns into stars in similar manner at  $z \sim 1$  and  $z \approx 0$ . On the other hand, Sharma et al. (2021c) we have already shown that the contribution of gas to the circular velocity is minimal, i.e.  $V_c^2 \approx V_{\text{star}}^2 + V_{\text{DM}}^2$ . Then, the evolution in the slope of STFR also suggest an evolution in the dark matter distribution. Surprisingly, the latter finding have also been reported in Chapter 6 using dynamical mass-modelling of rotation curves. These results can easily be favoured by phenomena, such as feedback scenarios and dynamical heating due to bursty star-formation which may transform dark matter *cusp* into *core* over the cosmic time (Navarro et al., 1996a; Pontzen & Governato, 2012; Nipoti & Binney, 2014; Read et al., 2016; Lazar et al., 2020). Moreover, we would like to point-out that the large scatter in the relation (in individual data-points) is possibly indicating the kinematic and morphological transition of high-z galaxies, which has also been reported by Kassin et al. (2007); Miller et al. (2014); Simons et al. (2016) and Übler et al. (2017).

## 7.6 Summary

In this chapter, we studied the seminal scaling relation, the ‘Tully-Fisher relation’, of star-forming galaxies since  $z \sim 1$ . We exploit the kinematic and photometric data obtained in Chapter 3 and Chapter 6. In particular we use 250 high-quality rotation dominated galaxies from the Q12 sample. This sample lies between redshift  $0.7 \lesssim z \lesssim 1.0$  with stellar masses  $\log(M_* [\text{M}_\odot]) = 9.0 - 11.0$  and circular velocities  $\log(V_{\text{out}} [\text{km s}^{-1}]) = 1.45 - 2.53$ . The rotation curves of the Q12 sample (individual and co-added) are dynamically modelled to decompose them into their constituents (stars, gas, and dark matter) allowing the study of structural properties of dark matter, see Chapter 6. The latter work also provides dynamically derived stellar and halo masses, which we have also employed in this work, especially in case of binned data.

In our earlier work, we have already demonstrated the robustness of circular velocities, which we compute using slightly different techniques than those employed in the recent high-redshift literature. In this work, we first showed the correctness of our photometric quantities: stellar mass and size, by plotting the mass-size relation of star-forming galaxies. We have demonstrated that our sample correctly reproduces the mass-size relation of  $z \sim 1$  star-forming galaxies given by van der Wel et al. (2014a), see Section 7.4.1. We have also shown that the scaling relation of stellar angular momentum with stellar mass emerges very similar to the previous studies of high-redshift star-forming galaxies (Burkert et al., 2016; Swinbank et al., 2017), see Section 7.4.2. Verification of both, mass-size and  $j_* - M_*$  relations, assure our kinematics and dynamical measurements. Therefore, we then exploited the stellar mass and circular velocity information to demonstrate the Stellar Tully-Fisher Relation (STFR), see Section 7.4.3. The fitting is performed using a

state-of-the-art method (Section 7.3.2), that has been proven to be robust for fitting the Tully-Fisher relation of local star-forming galaxies (e.g. [Lelli et al., 2016](#)). Furthermore, our results are compared with local and high-redshift STFR studies, see Section 7.4.3 & 7.5. We find that all previous studies fit the data fairly closely within the uncertainty of  $3\sigma$ . A large scatter in the relation (for individual data) is possibly indicative of the kinematic and morphological transition of high-redshift galaxies.

Although previous studies are largely consistent with our results, in this work, we intend to accurately measure the difference in slope and zero- point of STFR between  $z \approx 0$  and  $z \sim 1$ . Therefore, we compared the STFR fit obtained in our work with that of [Lapi et al. 2018b](#) (representing the local counterparts of  $z \sim 1$  star-forming galaxies). The results are shown in the inset of the Figure 7.5. We find that between  $1.8 \leq \log(Vc [\text{km s}^{-1}]) \leq 3.0$  and  $9.0 \leq \log(M_* [\text{M}_\odot]) \leq 12.0$  the zero- point remains the same, while the slope of the relation evolves. In particular, **we report a *divergent evolution in the STFR through cosmic time***. The latter suggests that the interplay of dark and luminous matter within the galaxies is strongly environment dependent process, i.e., galactic process do affect the distribution of dark matter in their subsequent evolution.



# Chapter 8

## Synopsis

*The main goal of this thesis has been to investigate the DARK MATTER imprints in the progenitors of local star-forming disc galaxies and, thereby, understand its astrophysical nature.*

The study of the kinematics and dynamics of galaxies is one of the most important methods to understand the structure of galaxies and the interplay between luminous (stars and gas called baryons) and dark matter. In particular, the rotation velocity profile of a galaxy,  $V_c(R)$ , extracted from the observed kinematics, is a powerful probe of its underlying mass distribution. Since disc (disc-like) galaxies are supported by their rotation velocity ( $V_c$ ), which can be easily related to the underlying gravitational potential ( $\Phi$ ) or enclosed dynamical mass ( $M_{\text{dyn}}$ : sum of baryons and dark matter) as:

$$R \frac{d\Phi}{dR} = V_c^2(R) = \frac{GM_{\text{dyn}}(< R)}{R}$$

where  $M_{\text{dyn}}(< R)$  is total gravitating matter within the radius  $R$ . Consequently, the circular velocity of a galaxy allows us to trace its fundamental properties, such as the enclosed mass and angular momentum. In addition, velocity dispersion also plays a key role in providing information about the "pressure conditions" of galaxies, which has direct implications for galaxy evolution. This is why, studying the kinematics and dynamics of a large number of galaxies over cosmic time will most-likely open a portal towards understanding their mass assembly, thus their formation and evolution.

In this thesis, I have examined the KMOS Redshift One Spectroscopic Survey (KROSS), which contains star-forming galaxies (SFGs). This survey was performed using Integrated Field Units (IFUs), the so-called second-generation spectrographs, which can provide the high-resolution spectrum of an entire galaxy, and of multiple galaxies, in one exposure and deliver the data in form of datacubes. The spectrum of a galaxy contains the stellar absorption and gas emission lines, which are crucial for studying its kinematics and dynamics – for details see Chapter 2. Here, I only exploit the star-forming disc like (i.e. rotation-dominated) systems, as their dynamics can be easily modelled under some simple assumptions, and provide robust constraints on the dark matter distribution (neatly worked-out in local galaxies).

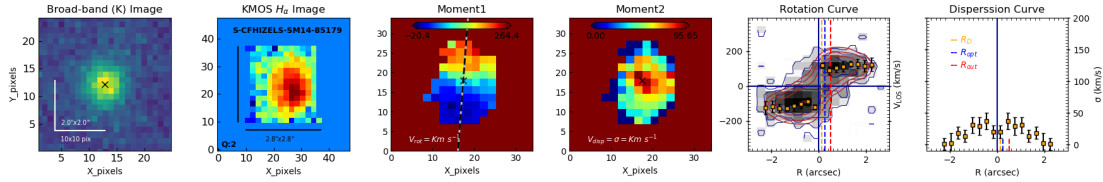


**Figure 8.1:** Barolo derived kinematics of  $z \sim 1$  star-forming galaxies, see Figure 3.6 (Chapter 3)

Although IFUs have proven remarkably good at observing individual galaxies and conducting large galaxy surveys in the local Universe, their high-redshift observations (surveys) still face challenges due to extreme distance and faintness of galaxies. The extreme distance of high-redshift galaxies leads to small angular size when observed with spectrograph of limited resolution, giving rise to ‘beam smearing’ which leads to a degeneracy between the rotation velocity and velocity dispersion (i.e. rotation and pressure). Due to the faintness of the object, we cannot observe the high signal-to-noise spectrum of stellar continuum. Therefore, so far we can only study the high-redshift galaxies from the gas emission. On the other hand, the interstellar medium is very turbulent in the early stages of galaxy formation, leading to a ‘pressure gradient’ that counteracts gravity by suppressing the rotation velocity. The aforementioned circumstances make the analysis and interpretation of the kinematics of high-redshift galaxies significantly more difficult compared to local galaxies. In this context, I have tested and applied state-of-the-art techniques capable of dealing with the observational and physical conditions and uncertainties encountered in high-redshift observations. This allowed me to obtain the intrinsic kinematics of  $z \sim 1$  star-forming galaxies, as presented in the Chapter 2 & 3.

The presented work is based on 344 star-forming galaxies from KROSS publicly available data. This sample contains 256 rotation dominated ( $V_{int}/\sigma > 1$ ) galaxies, that cover the redshift range  $0.70 \leq z \leq 1.04$ , effective radii  $0.69 \leq R_e [\text{kpc}] \leq 7.76$ , stellar masses  $8.7 \leq \log(M_* [\text{M}_\odot]) \leq 11.32$ , and star formation rates  $0.49 \leq \log(SFR [\text{M}_\odot \text{ yr}^{-1}]) \leq 1.77$ . Using  ${}^{3D}\text{BAROLO}$ , I have extracted the  $H\alpha$  kinematic maps and corresponding rotation curves. The main advantage of  ${}^{3D}\text{BAROLO}$  is that it incorporates the beam smearing in the 3D observational space, which provides us with the intrinsic rotation velocity even in the low spatial resolution data (see Chapter 3). I have corrected the obtained rotation curves for pressure support, which seems to be a more dominant effect than beam smearing in high- $z$  galaxies. My results demonstrate that only a combination of the three techniques (3D-kinematic modelling + 3D-beam smearing correction + pressure gradient correction) yields accurate rotation curves (RCs) of  $z \sim 1$  star-forming galaxies. Using this approach enabled me to study the following properties of  $z \sim 1$  star-forming galaxies:

- Rotation curves
- Dark matter content, and its structural properties
- Fundamental scaling relations

The main results of this work can be summarised as follows:

**Shape of the Rotation Curves:** I begin by examining the shape of rotation curves of  $z \sim 1$  star-forming galaxies by means of statistical analysis. The results are then compared with a similar study of local star-forming galaxies (Persic et al., 1996). In particular, the  $z \sim 1$  rotation curves are divided into five velocity bins and co-added together yielding a single rotation curve for each velocity bin. These five co-added rotation curves are then compared to their local counterparts (the Universal rotation curves of Persic et al. 1996). The physical properties of the galaxies associated with each velocity bin were also averaged during the binning process. When binning, the first thing that stands out is that galaxies whose circular velocities are similar at  $z \sim 1$  and  $z \approx 0$  have low stellar masses at  $z \sim 1$  (see Figures 4.6 & 4.7), which is a consequence of galaxy evolution processes, in which a galaxy converts gas into stars and consequently increases in stellar mass and size over cosmic time (c.f. Moster et al., 2018). This confirms our view that we are comparing the rotation curves of local star-forming galaxies with their progenitors. Secondly, it is surprising to see that:

1. Star-forming galaxies at  $z \sim 1$  manifest flat rotation curves from optical radii ( $\sim 2R_e$ ) till last point of observation ( $\sim 20$  kpc), and they are very similar to their local counterparts. We do not observe any change in the shape of rotation curves with respect to the local star-forming galaxies, except in the lowest velocity bin. For details, I refer the reader to Chapter 4, Figure 4.8.
2. Similarity in the shape of the rotation curves suggests that the total potential  $\Phi(R)$  or total mass within the  $\sim 20$  kpc radius of  $z \sim 1$  and  $z \approx 0$  star-forming galaxies remains approximately the same, i.e., it did not evolve in the past 6.5 Gyr. This suggests that the dark matter halo of star-forming galaxies most likely evolves slowly by accumulating the matter in the outermost regions of the galaxies.
3. I notice a significant evolution in the stellar-disc length ( $R_D$ ) of the galaxies as a function of their circular velocity. Therefore, I conclude that the stellar disc size of star-forming galaxies grows over cosmic time (since  $z \sim 1$ ) while the total mass stays constant (within  $\sim 20$  kpc), see Figure 4.9.

On the bases of above outcomes, we concluded that the *Total mass* within  $\sim 20$  kpc radius of  $z \sim 1$  star-forming galaxies remains the same as that of their  $z \approx 0$  counterparts. At the same time, stellar mass distribution (i.e., stellar disc) evolved over cosmic time (in past 6.5 Gyrs). This suggests a prolonged evolution of the star-forming galaxies (late-type systems).

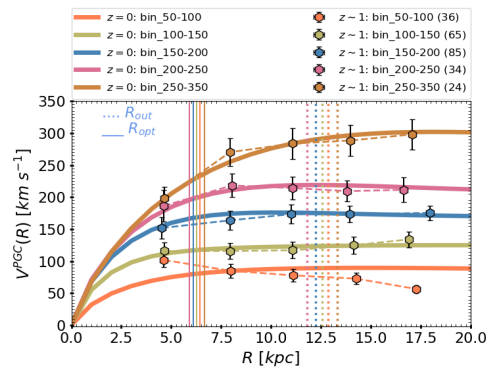


**Figure 8.2:** Shape of the RCs of  $z \sim 1$  and  $z \approx 0$  SFGs, see Figure 4.8 (Chapter 4).

When binning, the first thing that stands out is that galaxies whose circular velocities are similar at  $z \sim 1$  and  $z \approx 0$  have low stellar masses at  $z \sim 1$  (see Figures 4.6 & 4.7), which is a consequence of galaxy evolution processes, in which a galaxy converts gas into stars and consequently increases in stellar mass and size over cosmic time (c.f. Moster et al., 2018). This confirms our view that we are comparing the rotation curves of local star-forming galaxies with their progenitors. Secondly, it is surprising to see that:

**Dark Matter Fraction:** The study of dark matter on cosmological timescales is essential for understanding the formation and evolution of galaxies. Recent observational studies suggest that further back in time ( $z > 0.5$ ), rotation-supported star-forming galaxies (SFGs) begin to appear dark matter deficient compared to local star-forming galaxies. In contrast to the latter, we have just seen that the rotation curves of  $z \sim 1$  star-forming galaxies are flat from  $1.5\text{-}3 R_e$  ( $\sim 20$  kpc). The flattening of rotation curves indirectly suggests the sufficiency of dark matter, as reported in various studies of local star-forming galaxies (Rubin et al., 1978; Persic et al., 1996). However, we have no concrete evidence for the presence of dark matter from high-redshift, nor do we know how exactly it is distributed in high-redshift galaxies. Therefore, I closely investigate this issue in Chapter 5, where we computed the amount of dark matter from rotation curves at various radii using a model-independent approach. First, we calculate the total baryonic mass of the sample by estimating the stellar mass using high-resolution photometric data, and computing the gas (molecular and atomic) mass using scaling relations (Tacconi et al., 2018; Lagos et al., 2011). Under the common assumption of disc galaxies, in which the baryons are exponentially distributed, we were able to calculate the baryonic mass at each radius:  $M_{bar}(< R) = M_*(< R) + M_{H_2}(< R) + 1.33M_{HI}(< R)$ , where factor 1.33 accounts for the helium abundance. On the other hand, the total gravitating mass, i.e. dynamical mass, within the visible domain is computed directly from the rotation curves:  $M_{dyn}(< R) \propto V_c^2(R) R$  (see Section 5.2.3). The estimate of total baryonic and gravitating mass allowed us to compute the dark matter fraction ( $f_{DM}(< R) = 1 - \frac{M_{bar}(< R)}{M_{dyn}(< R)}$ ) of individual galaxies within various scale-lengths, namely  $R_e$ ,  $R_{opt}(\sim 2 R_e)$ , and  $R_{out}(\sim 2 R_e)$ . Note that in our work, we compute the stellar mass such that it also accounts for the stars in the galactic bulge, which is unresolved in our work. During the analysis, we notice that the baryonic masses generally do not exceed the dynamical masses, i.e.  $M_{bar}(< R) < M_{dyn}(< R)$ , and a dark matter component emerges in all objects, as implied independently by their rotation curve profiles. Only a few galaxies have  $M_{bar}(< R) > M_{dyn}(< R)$ ; however, they are consistent with  $M_{bar} \leq M_{dyn}$  within the  $1\sigma$  uncertainty. The main findings regarding dark matter fraction are:

1. At  $z \sim 1$  only a small fraction ( $\sim 5\%$ ) of our sample has a low ( $< 20\%$ ) dark matter fraction within  $\sim 2\text{-}3 R_e$ .
2. The majority ( $> 72\%$ ) of star-forming galaxies in our sample have dark matter-dominated outer discs ( $\sim 5 - 10$  kpc), which agrees well with local star-forming galaxies.

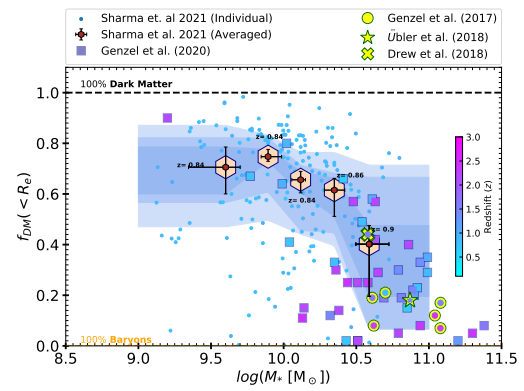


**Figure 8.3:** DM fraction within  $R_e$  at  $z \sim 1$ , see Figure 5.6 (Chapter 5).

However, we have no concrete evidence for the presence of dark matter from high-redshift, nor do we know how exactly it is distributed in high-redshift galaxies. Therefore, I closely investigate this issue in Chapter 5, where we computed the amount of dark matter from rotation curves at various radii using a model-independent approach. First, we calculate the total baryonic mass of the sample by estimating the stellar mass using high-resolution photometric data, and computing the gas (molecular and atomic) mass using scaling relations (Tacconi et al., 2018; Lagos et al., 2011). Under the common assumption of disc galaxies, in which the baryons are exponentially distributed, we were able to calculate the baryonic mass at each radius:  $M_{bar}(< R) = M_*(< R) + M_{H_2}(< R) + 1.33M_{HI}(< R)$ , where factor 1.33 accounts for the helium abundance. On the other hand, the total gravitating mass, i.e. dynamical mass, within the visible domain is computed directly from the rotation curves:  $M_{dyn}(< R) \propto V_c^2(R) R$  (see Section 5.2.3). The estimate of total baryonic and gravitating mass allowed us to compute the dark matter fraction ( $f_{DM}(< R) = 1 - \frac{M_{bar}(< R)}{M_{dyn}(< R)}$ ) of individual galaxies within various scale-lengths, namely  $R_e$ ,  $R_{opt}(\sim 2 R_e)$ , and  $R_{out}(\sim 2 R_e)$ . Note that in our work, we compute the stellar mass such that it also accounts for the stars in the galactic bulge, which is unresolved in our work. During the analysis, we notice that the baryonic masses generally do not exceed the dynamical masses, i.e.  $M_{bar}(< R) < M_{dyn}(< R)$ , and a dark matter component emerges in all objects, as implied independently by their rotation curve profiles. Only a few galaxies have  $M_{bar}(< R) > M_{dyn}(< R)$ ; however, they are consistent with  $M_{bar} \leq M_{dyn}$  within the  $1\sigma$  uncertainty. The main findings regarding dark matter fraction are:

1. At  $z \sim 1$  only a small fraction ( $\sim 5\%$ ) of our sample has a low ( $< 20\%$ ) dark matter fraction within  $\sim 2\text{-}3 R_e$ .
2. The majority ( $> 72\%$ ) of star-forming galaxies in our sample have dark matter-dominated outer discs ( $\sim 5 - 10$  kpc), which agrees well with local star-forming galaxies.

3. We find a large scatter in the fraction of dark matter at a given stellar mass (or circular velocity) with respect to local star-forming galaxies, suggesting that galaxies at  $z \sim 1$  span a wide range of stages in the formation of stellar discs and have diverse dark matter halo properties coupled with baryons.

**Structural properties of Dark Matter:** Recent hydrodynamical simulations are providing increasingly strong evidence that dark matter in galaxies responds to baryonic processes that can lead to changes in the structure of dark matter halos. Most likely, only the inner dark matter structure, i.e. the inner dark matter density slope, is affected, since most of the baryonic processes take place in the centre of the halo. The baryonic processes that affect the dark matter distribution can be detected by measuring the dynamics of the galaxy on the scales of a few kilo parsecs over cosmic time. This means that rotation curves can be a useful tool to study the response of dark matter to baryons. Moreover, we have just shown that star-forming galaxies are dark matter dominated systems at  $z \sim 1$  i.e. their kinematics can be useful to determine the structural properties of dark matter and its subsequent evolution by comparing the results with local star-forming galaxies.

In this context, I have shown a pilot study in Chapter 6, where I perform the mass modelling to disentangle the various mass component which make up the rotation curve (i.e.  $V_c(R)$ ). This technique is based on models that are defined by a few parameters to fit each component. In particular, I have used Freeman (1970a) disc to disentangle the stellar and gas components, which is based on the parameters  $R_D$ ,  $M_*$ ,  $M_{gas}$  and  $R_{gas}$ . The bulge is considered as point mass. Dark matter is disentangled using two halo profiles: NFW (Navarro et al., 1996b) and Burkert (Burkert, 1995), which are defined by the characteristic inner density and radius of the halo ( $\rho_{DM}^{inner}$ ,  $r_{DM}^{inner}$ ). I have developed a technique, which performs this complex modelling using Bayesian inference and flexible models with realistic priors on baryonic components, while keeping dark matter structural parameters ( $\rho_{DM}^{inner}$ ,  $r_{DM}^{inner}$ ) free. In my pilot study, I have successfully tested this mass modelling approach on individual and co-added rotation curves, which is capable of constraining  $\rho_{DM}^{inner}$ ,  $r_{DM}^{inner}$ . This method also provides us an alternative (but model-dependent way) to compute the dark matter fraction. Therefore, to check the robustness of our models, we first compared the dark matter fraction obtained from mass modelling with the one derived in Chapter 5. We report that dark matter fraction derived with Burkert halo profile matches very well with the model-independent approach, while NFW halo suppresses the stellar mass and overestimate the dark matter content, see Figure 6.5. To confirm the latter, we have compared dark matter fraction of our sample with state-of-the-art hydrodynamical simulations (EAGLE and TNG100, TNG50). We observed that

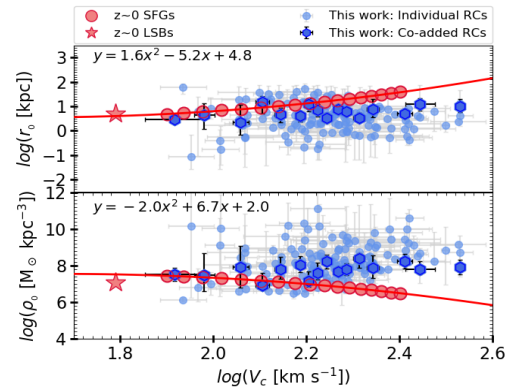


**Figure 8.4:** Evolving dark matter cores since  $z \sim 1$ , see Figure 6.10 (Chapter 6).

dark matter fraction derived using Burkert halo profile mirrors the simulations closely, see Figure 6.9. Using various results/comparisons of NFW and Burkert halo, in the case of individual and co-added RCs (see Chapter 6) I found that our current sample favours the Burkert halo model and also agrees quite well with the simulations. Therefore, I focus on discussing the Burkert halo results in what follows:

1. The dark matter structural properties (for Burkert halo  $r_0$  and  $\rho_0$ ) show that the dark matter cores at  $z \sim 1$  are on average  $\sim 3$  times smaller and more than an order of magnitude denser than those of local star-forming galaxies. This suggests an expansion of the DM halos over 6.5 Gyrs.
2. The expansion of dark matter cores is a function of circular velocity. The objects with higher circular velocity expand their core more than those with low circular velocities. This suggests that the circular velocity plays a crucial role in deriving the galaxy evolution.
3. The galactic processes that cause an evolution of the baryon distribution (reported in Chapter 4) may also have an impact on the dark matter. As a consequence, the dark matter distribution also changes through-out the cosmic time. In other words, dark matter most-likely responds to baryonic processes (e.g., AGN, supernova feedback, and dynamical friction).

If this pilot study is confirmed by high-quality observations, we will have the first concrete observational evidence of *gravitational potential perturbations* in the inner region of galaxies, which has been so far only implied by the cosmological simulations.

**Fundamental Scaling Relations:** The correlation between the fundamental properties (mass, velocity, and scale-radius) of galaxies are often referred to as *scaling relations*. These scaling relations make the foundation of current understanding of galaxies and their dynamical state, as well as play an important role in understanding the galaxy evolution. Therefore, the study of the scaling relations of galaxies across cosmic timescales is crucial to better understand the formation and evolution of galaxies. Moreover, recent observational studies show that as we go further back in time ( $z > 0.5$ ), rotation-supported star-forming galaxies (SFGs) exhibit a turbulent interstellar medium, in which pressure dominates and provides additional support to the stellar (or gas) disc against gravity, leading to lower rotational velocities, and we have also seen enclosed

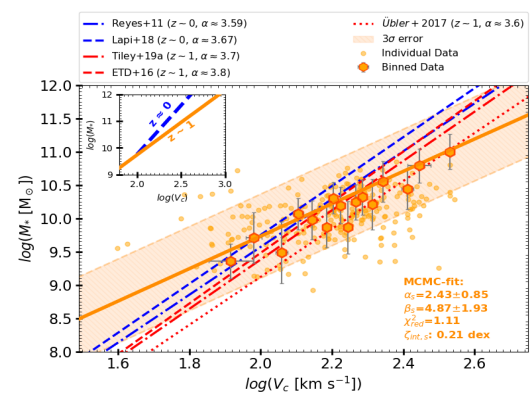


**Figure 8.5:** Stellar Tully-Fisher Relation at  $z \sim 1$ , see Figure 7.5 (Chapter 7).

dark matter responds to the baryonic processes. Under such peculiar conditions a very important question arises: what happens to the seminal scaling relations?

With this line of thought, I investigated several fundamental scaling relation, namely the mass-size relation, stellar angular momentum scaling with stellar mass, and stellar Tully-Fisher relation of star-forming galaxies at  $z \sim 1$  – see Chapter 7. We find that  $z \sim 1$  star-forming disc-like galaxies exhibit the same mass-size relations as local disc galaxies, as well as a similar scaling of the specific stellar angular momentum with stellar mass. This confirms the results of previous studies suggesting that the baryon assembly acts in a similar way at all epochs (e.g. [van der Wel et al., 2014a](#); [Burkert et al., 2016](#); [Swinbank et al., 2017](#)). On the other hand, we noticed a significant evolution in the slope of the stellar Tully-Fisher relation at  $z \sim 1$ , while its zero-point remains the same as local disc galaxies. Therefore, I report a divergent evolution of the stellar Tully-Fisher relation, suggesting that the interaction (gravitational or collisional) of baryons and dark matter is an environment- and time-dependent process.



# Chapter 9

## Conclusions & Future Perspectives

“Research is a skill of drawing sufficient conclusion from insufficient premises, in recognition of other free minds to utilize them in making their own decisions.”

---

### 9.1 Concluding Remarks

Firstly, to gain a new insights into the understanding of  $z \sim 1$  star-forming galaxies galaxies, in particular, their dark matter distribution, I have derived and analysed the kinematics and dynamics of a large sample of  $z \sim 1$  galaxies by employing the multiple state-of-the-art techniques, previous studies, and cosmological simulations. All the aforementioned results, which are briefly summarised in Chapter 8, show that dark matter is ubiquitous in disc-like galaxies at  $z \sim 1$ .

Secondly, our preliminary study of determining the internal distribution of dark matter in  $z \sim 1$  disc-like systems suggest that the size of their inner dark matter cores is smaller, and consequently they are denser than their local counterparts. This suggests that the predictions concerning the transformation of cusps into cores (Pontzen & Governato, 2014) are most likely correspond to the facts. That is, the dark matter responds to baryonic processes that dynamically heat-up the dark matter particles, leading to a disruption and displacement in its initial distribution. The latter can be interpreted as, transforming the original dense inner dark matter density (cusp) into a sparse distribution (core). Most importantly, this study attempted to gives us the first empirical evidence of *gravitational potential perturbations* in the inner region of galaxies, linking the dark and luminous matter properties, as well as constraining the dark matter structure. If my results are verified with high-quality data, they will have implications for theories of galaxy formation and evolution.

Furthermore, I believe that future observational facilities and missions will observe the high-redshift galaxies with unprecedented precision. Therefore, the techniques developed (and exploited) in my work can be used to exploit the upcoming data. That will provide us with a better understanding of astrophysical behaviour of dark matter and most likely help us to constrain its particle nature.

## 9.2 Future Prospects

Dark Matter dominates the mass budget of galaxies. However, there is growing evidence, both from observations and simulations, that dark matter in galaxies also responds to the baryonic processes that may lead to changes in the structure of dark matter halos, the so-called *cusp to core* transformation. ***Until now, the structure of dark matter halos and their evolution through cosmic time is one of the intriguing open questions of galaxy formation and evolution models, as well as cosmology.***

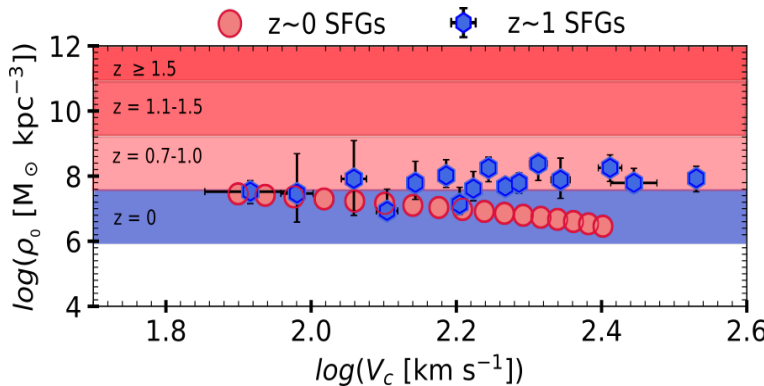


**Figure 9.1:** A preliminary study of  $z \sim 1$  rotation curve decomposition lead to the determination of the dark matter halo structure, studied in Chapter 6. This work shows that observations are capable of capturing the dark matter response to baryonic processes, which occur on cosmic time-scales (roughly 4-10 Gyrs).

below the resolution limit of the simulations (so-called “sub-grid” physics). Therefore, now that we have plenty of high-redshift observations over a wide redshift range, and we are capable of robustly analyse / interpret them. At the same time, the baryonic processes that impact the dark matter distribution occur on cosmic time-scales (roughly 4-10 Gyrs), thus these complex processes (and their evolution) can only be captured by measuring the dynamics of the galaxy on few kilo-parsec scales across cosmic-time. Therefore, I believe that we should now address this problem through observations. Indeed, one of my preliminary studies, in Chapter 6, have shown the evidence of evolving dark matter cores between  $z \approx 0$  and  $z \sim 1$ , i.e., the response of dark matter to the baryonic processes is possible to capture observationally, see Fig. 9.1. ***Providing this, the next straight forward step of my work is to measure the dark matter response to baryons***

Due to the lack of high-redshift data in the past and the complexity of the previous observations, until recently the scientific community has tried to solve this question using state-of-the-art simulations. However, the results based on simulations are strongly dependent on the assumptions and the implementation of the prescription used to describe the physics which occurs on the scales well

*in the inner regions of galaxies using a deep data (high signal-to-noise) over a wide redshift range ( $z = 0.2 - 3$ ).*

Besides this, in future, I plan to trace the cosmological evolution of dark matter in the context of galaxy evolution. This idea is so broad that it requires several intermediate steps (projects), each step itself being an independent scientific goal. For example, to trace the evolution of dark matter, I want to work towards:

- Constraining stellar kinematics of high-redshift galaxies: At present, the stellar kinematics of high- $z$  galaxies are poorly determined because it is extremely difficult to obtain spectra with high signal-to-noise ratios in the stellar continuum. However, we have relatively good knowledge of their ionized gas content, and these galaxies are likely to be gas rich systems [Förster Schreiber & Wuyts \(2020\)](#). The latter information can be used to identify analogous objects at low- $z$ . Therefore, I plan to study the counterparts of high- $z$  galaxies in the local Universe to infer (or bridge) their stellar continuum. This can be done by linking the gas metallicity of galaxies to their stellar kinematics (i.e. velocity dispersion). For this science case surveys like MAGPI, WEAVE -Apertif, and those of ALMA will be very useful.
- Halo intrinsic properties across the cosmic time: According to the tidal torque theory, the dark matter halo attains *angular momentum* at the time of its formation via tidal torques, which remains approximately conserved through-out its evolution. As the baryons collapse into the dark matter halo, both most likely exchange their angular momentum. In the literature, these terms are generally studied in form of halo and stellar spin parameters,  $\lambda_H$  and  $\lambda_r$ , respectively. The former indicates the conditions at the stage of galaxy formation, while the latter indicates the current dynamical state of a galaxy. Therefore, a statistical study of the correlation of these two quantities with each other and with the physical properties of galaxies (e.g.  $M_*$ ,  $\rho_c$ ) would certainly allows us to trace the evolutionary path of galaxies. Even more interestingly, these quantities are intrinsic and arise from the conserved quantities (stellar and halo angular momentum); therefore, I believe this will give us a new insight (or universality) into galaxy formation and evolution picture. Moreover, these kinds of studies are also very important to identify the analogous systems in the simulations, which will allow an identical comparison between observations and simulations. Here, I would like to emphasize that the calculation of the stellar spin parameter with IFU data is possible [Emsellem et al. \(2007\)](#), on the other hand, dynamical modelling of RCs can be used to infer the halo spin parameter using the methodology of [Romanowsky & Fall \(2012\)](#).
- Alternative to the Hubble sequence: A combination of dynamical and kinematical studies presented in this work and a practice to derive the intrinsic properties of the halo can provide us with an alternative to the Hubble sequence of galaxies ([Zhu et al., 2018](#)), i.e. we are no longer bound to morphological studies of galaxies to follow galaxy evolution (which are challenging at higher- $z$ ). Therefore, the exploration

(study) of point-2 via semi-analytical modelling, observations, and simulations over cosmic time will provide us with a way to study different classes of galaxies across the Hubble time and track their subsequent evolution.

- Impact of extinction on rotation curves: I plan to use multi-wavelength data to infer the evolution of extinction over cosmic time. This study is crucial for various aspects of galaxy evolution and also of great importance for the study of dark matter. As we know, dust is prominent in the inner region of galaxies; therefore, dust extinction suppresses the rotational velocity of galaxies within effective radii, leading to erroneous estimates of the structural properties of dark matter halos. In particular, this effect is of great importance in the context of the so-called ‘core vs. cusp’ problem, and thus for the questions related to the nature of the dark matter.
- Stellar-to-gas disc sizes: At present, we do not know the exact relationship between stellar, molecular, and atomic disc sizes (even in local galaxies). If we have latter information, it will allow us to constrain the dark matter fraction in the visible domain much more precisely, especially in high- $z$  galaxies where we extrapolate the atomic and molecular gas content using simulations (or scaling relations).

—\* ***The End*** \*—

# Bibliography

- Acevedo J. F., Bramante J., 2019, *Physics Review D*, **100**, 043020
- Alcock C., et al., 1993, *Nature*, **365**, 621
- Ali-Haïmoud Y., 2019, *Physics Review D*, **99**, 023523
- Allen S. W., Evrard A. E., Mantz A. B., 2011, *Annual Review of Astronomy and Astrophysics*, **49**, 409
- Aoki S., 1985, *Astronomy & Astrophysics*, **148**, 1
- Arbey A., Mahmoudi F., 2021, *Progress in Particle and Nuclear Physics*, **119**, 103865
- Arcadi G., Dutra M., Ghosh P., Lindner M., Mambrini Y., Pierre M., Profumo S., Queiroz F. S., 2018, *European Physical Journal C*, **78**, 203
- Arnouts S., Cristiani S., Moscardini L., Matarrese S., Lucchin F., Fontana A., Giallongo E., 1999, *Monthly Notices of the Royal Astronomical Society*, **310**, 540
- Asencio E., Banik I., Kroupa P., 2021, *Monthly Notices of the Royal Astronomical Society*, **500**, 5249
- Athanassoula E. E., ed. 1983, Internal kinematics and dynamics of galaxies 100 Vol. 100
- Aubourg E., et al., 1993, *Nature*, **365**, 623
- Babcock H. W., 1939, *Lick Observatory Bulletin*, **498**, 41
- Bacon R., et al., 1995, *AAPS*, **113**, 347
- Bacon R., et al., 2001a, *Monthly Notices of the Royal Astronomical Society*, **326**, 23
- Bacon R., et al., 2001b, *Monthly Notices of the Royal Astronomical Society*, **326**, 23
- Bacon R., et al., 2010, The MUSE second-generation VLT instrument. Society of Photo-Optical Instrumentation Engineers (SPIE) Conference Series, p. 773508, doi:10.1117/12.856027, <https://ui.adsabs.harvard.edu/abs/2010SPIE.7735E..08B>

- Bacon R., Brinchmann J., Richard J., Contini T., Drake A., Franx M. and Tacchella S., Vernet J., Wisotzki L., 2015, *Astronomy & Astrophysics*, **575**, A75
- Bahcall N. A., 1988, *Annual Review of Astronomy and Astrophysics*, **26**, 631
- Bailes M., et al., 2021, *Nature Reviews Physics*, **3**, 344
- Baker A. J., Blyth S., Holwerda B. W., LADUMA Team 2018, in American Astronomical Society Meeting Abstracts #231. p. 231.07
- Baldry I. K., Glazebrook K., Brinkmann J., Ivezić Ž., Lupton R. H., Nichol R. C., Szalay A. S., 2004, *Astrophysics Journal*, **600**, 681
- Banik N., Bertone G., Bovy J., Bozorgnia N., 2018, *Journal of Cosmology and Astroparticle Physics*, **2018**, 061
- Barden M., et al., 2005, *Astrophysics Journal*, **635**, 959
- Bartolo N., De Luca V., Franciolini G., Lewis A., Peloso M., Riotto A., 2019, *Phys. Rev. Lett.*, **122**, 211301
- Bashinsky S., Bertschinger E., 2002, *Physics Review D*, **65**, 123008
- Battinelli P., Demers S., Rossi C., Gigoyan K. S., 2013, *Astrophysics*, **56**, 68
- Begeman K., 1989, *Astronomy and Astrophysics*, **223**, 47
- Begeman K. G., Broeils A. H., Sanders R. H., 1991, *Monthly Notices of the Royal Astronomical Society*, **249**, 523
- Bell E. F., de Jong R. S., 2001, *The Astrophysical Journal*, **550**, 212
- Bellazzini M., Oosterloo T., Fraternali F., Beccari G., 2013, *Astronomy & astrophysics*, **559**
- Bergström L., 2012, *Annalen der Physik*, **524**, 479
- Bertone G., Hooper D., 2018, *Reviews of Modern Physics*, **90**, 045002
- Billard J., et al., 2021, arXiv e-prints, p. arXiv:2104.07634
- Binney J., Tremaine S., 2008, *Galactic Dynamics*: Second Edition. Princeton University Press
- Blandford R. D., Narayan R., 1992, *Annual Review of Astronomy and Astrophysics*, **30**, 311
- Blitz L., 1979, *Astrophysics Journal Letter*, **231**, L115
- Blumenthal G. R., Faber S., Primack J. R., Rees M. J., 1984, *Nature*, **311**, 517

- Boehm C., Schaeffer R., 2005, *Astronomy & Astrophysics*, 438, 419
- Böhm A., et al., 2004, *Astronomy & Astrophysics*, 420, 97
- Bolzonella M., Miralles J. M., Pelló R., 2000, *Astronomy & Astrophysics*, 363, 476
- Bonaldi A., et al., 2021, *Monthly Notices of the Royal Astronomical Society*, 500, 3821
- Bosma A., 1978, PhD thesis, University of Groniongen
- Bosma A., 1981, *The Astronomical Journal*, 86, 1791
- Bosma A., 1999, in Merritt D. R., Valluri M., Sellwood J. A., eds, Astronomical Society of the Pacific Conference Series Vol. 182, Galaxy Dynamics - A Rutgers Symposium. p. 339 ([arXiv:astro-ph/9812013](https://arxiv.org/abs/astro-ph/9812013))
- Bosma A., Van der Kruit P., 1979, *Astronomy and Astrophysics*, 79, 281
- Bouché N., Carfantan H., Schroetter I., Michel-Dansac L., Contini T., 2015, *The Astronomical Journal*, 150, 92
- Boylan-Kolchin M., Bullock J. S., Kaplinghat M., 2011, *Monthly Notices of the Royal Astronomical Society*, 415, L40
- Boylan-Kolchin M., Bullock J. S., Kaplinghat M., 2012, *Monthly Notices of the Royal Astronomical Society*, 422, 1203
- Bruce V. A., et al., 2014, *Monthly Notices of the Royal Astronomical Society*, 444, 1660
- Bruzual G., Charlot S., 2003, *Monthly Notices of the Royal Astronomical Society*, 344, 1000
- Bullock J. S., Kolatt T. S., Sigad Y., Somerville R. S., Kravtsov A. V., Klypin A. A., Primack J. R., Dekel A., 2001, *Monthly Notices of the Royal Astronomical Society*, 321, 559
- Burkert A., 1995, *Astrophysics Journal Letter*, 447, L25
- Burkert A., 2009, in Jogee S., Marinova I., Hao L., Blanc G. A., eds, Astronomical Society of the Pacific Conference Series Vol. 419, Galaxy Evolution: Emerging Insights and Future Challenges. p. 3 ([arXiv:0908.1409](https://arxiv.org/abs/0908.1409))
- Burkert A., et al., 2010, *The Astrophysical Journal*, 725, 2324
- Burkert A., et al., 2016, *The Astrophysical Journal*, 826, 214
- Calette A. R., Avila-Reese V., Rodríguez-Puebla A., Hernández-Toledo H., Papastergis E., 2018, *rmxaa*, 54, 443

- Calzetti D., Armus L., Bohlin R. C., Kinney A. L., Koornneef J., Storchi-Bergmann T., 2000, *Astrophysics Journal*, 533, 682
- Calzetti D., et al., 2007, *Astrophysics Journal*, 666, 870
- Capozziello S., Cardone V. F., Troisi A., 2007, *Monthly Notices of the Royal Astronomical Society*, 375, 1423
- Cappi A., 2015, *Frontiers in Astronomy and Space Sciences*, 2, 5
- Carollo C. M., et al., 2013, *Astrophysics Journal*, 773, 112
- Carr B., Kühnel F., 2020, *Annual Review of Nuclear and Particle Science*, 70, 355
- Carr B., Kohri K., Sendouda Y., Yokoyama J., 2020, arXiv e-prints, p. arXiv:2002.12778
- Casasola V., et al., 2020, *Astronomy & Astrophysics*, 633, A100
- Catena R., Ullio P., 2010, *Journal of Cosmology and Astroparticle Physics*, 2010, 004
- Catinella B., Giovanelli R., Haynes M. P., 2006, *The Astrophysical Journal*, 640, 751
- Chabrier G., 2003, *Publications of the Astronomical Society of the Pacific*, 115, 763
- Chan T. K., Kere D., Oñorbe J., Hopkins P. F., Muratov A. L., Faucher-Giguère C.-A., Quataert E., 2015, *Monthly Notices of the Royal Astronomical Society*, 454, 2981
- Chluba J., Sunyaev R. A., 2011, *Monthly Notices of the Royal Astronomical Society*, 419, 1294
- Claudi R. U., et al., 2008, in McLean I. S., Casali M. M., eds, Society of Photo-Optical Instrumentation Engineers (SPIE) Conference Series Vol. 7014, Ground-based and Air-borne Instrumentation for Astronomy II. p. 70143E, doi:10.1117/12.788366
- Clowe D., Bradač M., Gonzalez A. H., Markevitch M., Randall S. W., Jones C., Zaritsky D., 2006, *Astrophysics Journal Letter*, 648, L109
- Coles P., Lucchin F., 2002, Cosmology: The Origin and Evolution of Cosmic Structure, Second Edition. Wiley Press
- Conn A. R., et al., 2013, *Astrophysics Journal*, 766, 120
- Conselice C. J., Blackburne J. A., Papovich C., 2005, *The Astrophysical Journal*, 620, 564
- Cormier D., et al., 2016, *Monthly Notices of the Royal Astronomical Society*, 463, 1724
- Courteau S., 1997, *AJ*, 114, 2402
- Courteau S., Dutton A. A., 2015, *Astrophysics Journal Letter*, 801, L20

- Courtes G., 1982, An Integral Field Spectrograph (IFS) for Large Telescopes. Cambridge Press, p. 123, doi:10.1007/978-94-009-7787-7\_16
- Covi L., 2013, *Astronomische Nachrichten*, 334, 605
- Cox P., 2016, in Proceedings of the 2016 ALMA Conference. p. 2
- Cresci G., et al., 2009, *The Astrophysical Journal*, 697, 115
- Croon D., McKeen D., Raj N., 2020, *Physics Review D*, 101, 083013
- D'Onofrio M., Rummukainen K., 2016, *Physics Review D*, 93, 025003
- Daddi E., et al., 2005, *Astrophysics Journal*, 626, 680
- Dalal N., Kochanek C. S., 2002, *Astrophysics Journal*, 572, 25
- Dalcanton J. J., Stilp A. M., 2010a, *The Astrophysical Journal*, 721, 547
- Dalcanton J. J., Stilp A. M., 2010b, *Astrophysics Journal*, 721, 547
- Davies R., et al., 2013, *Astronomy & Astrophysics*, 558, A56
- Davis M., Efstathiou G., Frenk C. S., White S. D. M., 1985, *Astrophysics Journal*, 292, 371
- Dayal P., Ferrara A., 2018, *Physics Reports*, 780, 1
- DeRocco W., Graham P. W., Kasen D., Marques-Tavares G., Rajendran S., 2019, *Physics Review D*, 100, 075018
- Deason A. J., et al., 2011, *Monthly Notices of the Royal Astronomical Society*, 415, 2607
- Dehnen W., Binney J., 1998, *Monthly Notices of the Royal Astronomical Society*, 294, 429
- Dekker H., D'Odorico S., Kaufer A., Delabre B., Kotzlowski H., 2000, in Iye M., Moorwood A. F., eds, Society of Photo-Optical Instrumentation Engineers (SPIE) Conference Series Vol. 4008, Optical and IR Telescope Instrumentation and Detectors. pp 534–545, doi:10.1117/12.395512
- Del Popolo A., Le Delliou M., 2017, *Galaxies*, 5, 17
- Di Cintio A., Brook C. B., Dutton A. A., Macciò A. V., Stinson G. S., Knebe A., 2014, *Monthly Notices of the Royal Astronomical Society*, 441, 2986
- Di Paolo C., Salucci P., Erkurt A., 2019, *Monthly Notices of the Royal Astronomical Society*, 490, 5451
- Di Teodoro E., Fraternali F., Miller S., 2016, *Astronomy & Astrophysics*, 594, A77

- Di Valentino E., et al., 2021a, arXiv e-prints, p. [arXiv:2103.01183](https://arxiv.org/abs/2103.01183)
- Di Valentino E., et al., 2021b, *Astroparticle Physics*, 131, 102604
- Díaz-Sánchez A., Dannerbauer H., Sulzenauer N., Iglesias-Groth S., Rebolo R., 2021, arXiv e-prints, p. [arXiv:2106.14281](https://arxiv.org/abs/2106.14281)
- Ding W.-B., Yu Z., Xu Y., Liu C.-J., Bao T., 2019, *Chinese Physics Letters*, 36, 049701
- Dolag K., Borgani S., Murante G., Springel V., 2009, *Monthly Notices of the Royal Astronomical Society*, 399, 497
- Donnari M., et al., 2019, *Monthly Notices of the Royal Astronomical Society*, 489, 3036
- Drew P. M., Casey C. M., Burnham A. D., Hung C.-L., Kassin S. A., Simons R. C., Zavala J. A., 2018, *The Astrophysical Journal*, 869, 58
- Duc P.-A., Paudel S., McDermid R. M., Cuillandre J.-C., Serra P., Bournaud F., Cappellari M., Emsellem E., 2014, *Monthly Notices of the Royal Astronomical Society*, 440, 1458
- Durand S., Acker A., Zijlstra A., 1998, *AAPS*, 132, 13
- Dutta B., Strigari L. E., 2019, *Annual Review of Nuclear and Particle Science*, 69, 137
- Dutton A. A., Macciò A. V., Frings J., Wang L., Stinson G. S., Penzo C., Kang X., 2016, *Monthly Notices of the Royal Astronomical Society: Letters*, 457, L74
- Dvorkin C., Blum K., Kamionkowski M., 2014, *Physics Review D*, 89, 023519
- Einasto J., 1965, Trudy Astrofizicheskogo Instituta Alma-Ata, 5, 87
- Einasto M., et al., 2017, *Astronomy & Astrophysics*, 603, A5
- Eisenhauer F., et al., 2003, *Proc. SPIE Int. Soc. Opt. Eng.*, 4841, 1548
- Ellis G., 2018, *Foundations of Physics*, 48, 1226
- Emsellem E., et al., 2007, *mnras*, 379, 401
- Epinat B., Amram P., Balkowski C., Marcellin M., 2010, *Monthly Notices of the Royal Astronomical Society*, 401, 2113
- Erkal D., Belokurov V., 2015, *Monthly Notices of the Royal Astronomical Society*, 454, 3542
- Feast M. W., 1994, *Monthly Notices of the Royal Astronomical Society*, 266, 255
- Fedorova E., Sliusar V. M., Zhdanov V. I., Alexandrov A. N., Del Popolo A., Surdej J., 2016, *Monthly Notices of the Royal Astronomical Society*, 457, 4147

- Feng J. L., 2010, *Annual Review of Astronomy and Astrophysics*, 48, 495
- Ferrarese L., et al., 2000, *ApJS*, 128, 431
- Ferreira P. G., 2019, *Annual Review of Astronomy and Astrophysics*, 57, 335
- Ferrero I., Abadi M. G., Navarro J. F., Sales L. V., Gurovich S., 2012, *Monthly Notices of the Royal Astronomical Society*, 425, 2817
- Fields B. D., 2011, *Annual Review of Nuclear and Particle Science*, 61, 47
- Forbes D. A., Alabi A., Romanowsky A. J., Brodie J. P., Strader J., Usher C., Pota V., 2016, *Monthly Notices of the Royal Astronomical Society: Letters*, 458, L44
- Foreman S., Scott D., 2012, *Physics Review Letter*, 108, 141302
- Foreman-Mackey D., Hogg D. W., Goodman D. L. J., 2013, *Publications of the Astronomical Society of the Pacific*, 125, 306
- Förster Schreiber N. M., et al., 2009, *Astrophysics Journal*, 706, 1364
- Frampton P. H., 2019, *Modern Physics Letters A*, 34, 1950124
- Freedman W. L., Turner M. S., 2003, *Rev. Mod. Phys.*, 75, 1433
- Freedman W. L., et al., 2011, *AJ*, 142, 192
- Freeman K., 1970a, *The Astrophysical Journal*, 160, 811
- Freeman K., 1970b, *The Astrophysical Journal*, 160, 811
- Freundlich J., et al., 2020b, *Monthly Notices of the Royal Astronomical Society*, 499, 2912
- Freundlich J., et al., 2020a, *Monthly Notices of the Royal Astronomical Society*, 499, 2912
- Fu J., Guo Q., Kauffmann G., Krumholz M. R., 2010, *Monthly Notices of the Royal Astronomical Society*, 409, 515
- Förster Schreiber N. M., Wuyts S., 2020, *Annual Review of Astronomy and Astrophysics*, 58, null
- Gaitskell R. J., 2004, *Annual Review of Nuclear and Particle Science*, 54, 315
- Galianni P., Patat F., Higdon J. L., Mieske S., Kroupa P., 2010, *Astronomy & Astrophysics*, 521, A20
- Gaskins J. M., 2016a, *Contemporary Physics*, 57, 496
- Gaskins J. M., 2016b, *Contemporary Physics*, 57, 496

- Gates E. I., Gyuk G., Turner M. S., 1995, *Physics Review Letter*, **74**, 3724
- Gaudi B. S., 2012, *Annual Review of Astronomy and Astrophysics*, **50**, 411
- Gavazzi G., Fumagalli M., Cucciati O., Boselli A., 2010, *Astronomy & Astrophysics*, **517**, A73
- Gentile G., Salucci P., Klein U., Vergani D., Kalberla P., 2004, *Monthly Notices of the Royal Astronomical Society*, **351**, 903
- Genzel R., et al., 2008, *Astrophysics Journal*, **687**, 59
- Genzel R., et al., 2017, *Nature*, **543**, 397
- Genzel R., et al., 2020, *Astrophysics Journal*, **902**, 98
- Giacconi R., et al., 2001, *The Astrophysical Journal*, **551**, 624
- Gillman S., et al., 2020, *Monthly Notices of the Royal Astronomical Society*, **492**, 1492
- Giovanelli R., Haynes M. P., Herter T., Vogt N. P., da Costa L. N., Freudling W., Salzer J. J., Wegner G., 1997a, *AJ*, **113**, 53
- Giovanelli R., Haynes M. P., da Costa L. N., Freudling W., Salzer J. J., Wegner G., 1997b, *Astrophysics Journal Letter*, **477**, L1
- Girardi M., Manzato P., Mezzetti M., Giuricin G., Limboz F., 2002, *The Astrophysical Journal*, **569**, 720
- Glashow S. L., 1959, *Nuclear Physics*, **10**, 107
- Glazebrook K., 2013, *pasa*, **30**, e056
- Gnerucci A., et al., 2011, *Astronomy & Astrophysics*, **528**, A88
- Governato F., et al., 2010, *Nature*, **463**, 203
- Graham P. W., Janish R., Narayan V., Rajendran S., Riggins P., 2018, *Physics Review D*, **98**, 115027
- Green A. W., et al., 2010, *Nature*, **467**, 684
- Guimarães R., Petitjean P., de Carvalho R. R., Djorgovski S. G., Noterdaeme P., Castro S., Poppe P. C. D. R., Aghaee A., 2009, *Astronomy & Astrophysics*, **508**, 133
- Guo Q., et al., 2011, *Monthly Notices of the Royal Astronomical Society*, **413**, 101
- Guth A. H., 1981, *Physics Review D*, **23**, 347
- Harrison C., et al., 2017, *Monthly Notices of the Royal Astronomical Society*, **467**, 1965

- Hassani E., Milad Ghaffarpour Mousavi S., 2021, arXiv e-prints, p. arXiv:2106.03398
- Hayashi E., et al., 2004, *Monthly Notices of the Royal Astronomical Society*, 355, 794
- Hayashi K., Chiba M., Ishiyama T., 2020, *The Astrophysical Journal*, 904, 45
- He J.-h., 2020, *Monthly Notices of the Royal Astronomical Society*, 493, 4453
- Hildebrandt H., et al., 2017, *Monthly Notices of the Royal Astronomical Society*, 465, 1454
- Hoekstra H., Jain B., 2008, *Annual Review of Nuclear and Particle Science*, 58, 99
- Honma M., Sofue Y., 1997, *Publications of the Astronomical Society of Japan*, 49, 453
- Hou L. G., Han J. L., Shi W. B., 2009, *Astronomy & Astrophysics*, 499, 473
- Hu W., Dodelson S., 2002, *Annual Review of Astronomy and Astrophysics*, 40, 171
- Hu W., Silk J., 1993, *Physics Review D*, 48, 485
- Huang Y., et al., 2016, *Monthly Notices of the Royal Astronomical Society*, 463, 2623
- Hubble E. P., 1926, *Astrophysics Journal*, 64, 321
- Ibata R. A., et al., 2013, *Nature*, 493, 62
- Ilbert O., et al., 2006, *Astronomy & Astrophysics*, 457, 841
- Inomata K., Kawasaki M., Mukaida K., Tada Y., Yanagida T. T., 2017, *Physics Review D*, 96, 043504
- Iocco F., Pato M., Bertone G., 2015, *Nature Physics*, 11, 245
- Jeans J. H., 1915, *Monthly Notices of the Royal Astronomical Society*, 76, 70
- Jeans J. H., 1922, *Monthly Notices of the Royal Astronomical Society*, 82, 122
- Johnson H. L., et al., 2018, *Monthly Notices of the Royal Astronomical Society*, 474, 5076
- Johnston S., et al., 2008, *Experimental Astronomy*, 22, 151
- Jonas J., MeerKAT Team 2016, in MeerKAT Science: On the Pathway to the SKA. p. 1
- Joudaki S., et al., 2018, *Monthly Notices of the Royal Astronomical Society*, 474, 4894
- Kakkar R., 2015, *Atomic and Molecular Spectroscopy*. Springer press
- Kapteyn J. C., 1922, *Astrophysics Journal*, 55, 302

- Karachentsev I. D., Mitronova S. N., Karachentseva V. E., Kudrya Y. N., Jarrett T. H., 2002, *Astronomy & Astrophysics*, 396, 431
- Karachentsev I. D., Bautzmann D., Neyer F., Polzl R., Riepe P., Zilch T., Mattern B., 2014, arXiv e-prints, p. [arXiv:1401.2719](https://arxiv.org/abs/1401.2719)
- Karukes E. V., Salucci P., 2017, *Monthly Notices of the Royal Astronomical Society*, 465, 4703
- Kassin S. A., de Jong R. S., Weiner B. J., 2006, *Astrophysics Journal*, 643, 804
- Kassin S. A., et al., 2007, *Astrophysics Journal Letter*, 660, L35
- Kassin S. A., et al., 2012, *Astrophysics Journal*, 758, 106
- Kauffmann G., White S. D. M., Guiderdoni B., 1993, *Monthly Notices of the Royal Astronomical Society*, 264, 201
- Kawasaki M., Nakayama K., 2013, *Annual Review of Nuclear and Particle Science*, 63, 69
- Kelley T., Bullock J. S., Garrison-Kimmel S., Boylan-Kolchin M., Pawlowski M. S., Graus A. S., 2019, *Monthly Notices of the Royal Astronomical Society*, 487, 4409
- Kelvin B., 1904, Baltimore lectures
- Kennicutt R. C., Evans N. J., 2012, *Annual Review of Astronomy and Astrophysics*, 50, 531
- Kennicutt Jr R. C., 1998, *The Astrophysical Journal*, 498, 541
- Kent S. M., 1986, *AJ* , 91, 1301
- Kim S. Y., Peter A. H. G., 2021, arXiv e-prints, p. [arXiv:2106.09050](https://arxiv.org/abs/2106.09050)
- Kim S. Y., Peter A. H. G., Hargis J. R., 2018, *Physics Review Letter*, 121, 211302
- Kirby E. N., Bullock J. S., Boylan-Kolchin M., Kaplinghat M., Cohen J. G., 2014, *Monthly Notices of the Royal Astronomical Society*, 439, 1015
- Kleczek J., 1988, *solphys*, 115, 409
- Klypin A., 1996, in Bonometto S., Primack J. R., Provenzale A., eds, Dark Matter in the Universe. p. 419 ([arXiv:astro-ph/9605183](https://arxiv.org/abs/astro-ph/9605183))
- Klypin A., Kravtsov A. V., Valenzuela O., Prada F., 1999, *Astrophysics Journal*, 522, 82
- Kochanek C. S., 1995, in Holt S. S., Bennett C. L., eds, American Institute of Physics Conference Series Vol. 336, Dark Matter. pp 297–306, doi:10.1063/1.48349

- Kohler S., 2016, A Solution to “Too Big to Fail”, *AAS Nova Highlights*
- Kolb E. W., Turner M. S., 1990a, *The early universe*. 1 Vol. 69, CRC Press
- Kolb E. W., Turner M. S., 1990b, *The early universe*. 1 Vol. 69, CRCPress
- Konstantopoulos I., et al., 2013, in *American Astronomical Society Meeting Abstracts* #221. p. 215.01
- Korsaga M., Epinat B., Amram P., Carignan C., Adamczyk P., Sorgho A., 2019, *Monthly Notices of the Royal Astronomical Society*, **490**, 2977
- Kovetz E., et al., 2019, *baas*, **51**, 101
- Kretschmer M., Dekel A., Freundlich J., Lapiner S., Ceverino D., Primack J., 2020, Evaluating Galaxy Dynamical Masses From Kinematics and Jeans Equilibrium in Simulations ([arXiv:2010.04629](https://arxiv.org/abs/2010.04629))
- Krogager J.-K., et al., 2013, *Monthly Notices of the Royal Astronomical Society*, **433**, 3091
- Kroupa P., Theis C., Boily C. M., 2005, *Astronomy & Astrophysics*, **431**, 517
- Kuhlen M., Diemand J., Madau P., Zemp M., 2008, *Journal of Physics: Conference Series*, **125**, 012008
- Kuzio de Naray R., Kaufmann T., 2011, *Monthly Notices of the Royal Astronomical Society*, **414**, 3617
- Kuzio de Naray R., McGaugh S. S., de Blok W. J. G., 2008, *Astrophysics Journal*, **676**, 920
- Lacey C., 2001, in Umemura M., Susa H., eds, *Astronomical Society of the Pacific Conference Series* Vol. 222, *The Physics of Galaxy Formation*. p. 273
- Lagos C. D. P., Baugh C. M., Lacey C. G., Benson A. J., Kim H.-S., Power C., 2011, *Monthly Notices of the Royal Astronomical Society*, **418**, 1649
- Lagos C. d. P., Theuns T., Stevens A. R. H., Cortese L., Padilla N. D., Davis T. A., Contreras S., Croton D., 2017, *Monthly Notices of the Royal Astronomical Society*, **464**, 3850
- Lang P., et al., 2017, *The Astrophysical Journal*, **840**, 92
- Lapi A., et al., 2018a, *The Astrophysical Journal*, **857**, 22
- Lapi A., Salucci P., Danese L., 2018b, *The Astrophysical Journal*, **859**, 2
- Lapi A., Pantoni L., Boco L., Danese L., 2020, *Astrophysics Journal*, **897**, 81

- Law D. R., et al., 2015, *AJ*, 150, 19
- Lawrence A., et al., 2007, *Monthly Notices of the Royal Astronomical Society*, 379, 1599
- Lazar A., et al., 2020, arXiv e-prints, p. [arXiv:2004.10817](https://arxiv.org/abs/2004.10817)
- Lehmer B. D., et al., 2005, *The Astrophysical Journal Supplement Series*, 161, 21
- Lelli F., McGaugh S. S., Schombert J. M., 2016, *Astrophysics Journal Letter*, 816, L14
- Lelli F., McGaugh S. S., Schombert J. M., Desmond H., Katz H., 2019, *Monthly Notices of the Royal Astronomical Society*, 484, 3267
- Leroy A. K., Walter F., Brinks E., Bigiel F., de Blok W. J. G., Madore B., Thornley M. D., 2008, *AJ*, 136, 2782
- Li P., Lelli F., McGaugh S., Schombert J., 2020, *ApJS*, 247, 31
- Loiacono F., Talia M., Fraternali F., Cimatti A., Di Teodoro E. M., Caminha G. B., 2019, *Monthly Notices of the Royal Astronomical Society*, 489, 681
- Luna A., Bronfman L., Carrasco L., May J., 2006, *Astrophysics Journal*, 641, 938
- Lynden-Bell D., 1976, *Monthly Notices of the Royal Astronomical Society*, 174, 695
- Lyubenova M., et al., 2016, *Monthly Notices of the Royal Astronomical Society*, 463, 3220
- Ma C.-P., Bertschinger E., 1995, *Astrophysics Journal*, 455, 7
- Madau P., Dickinson M., 2014, *Annual Review of Astronomy and Astrophysics*, 52, 415
- Maddox N., et al., 2021, *Astronomy & Astrophysics*, 646, A35
- Mao S., Mo H. J., White S. D. M., 1998, *Monthly Notices of the Royal Astronomical Society*, 297, L71
- Martin A. M., Papastergis E., Giovanelli R., Haynes M. P., Springob C. M., Stierwalt S., 2010, *Astrophysics Journal*, 723, 1359
- Martinsson T. P., Verheijen M. A., Westfall K. B., Bershady M. A., Andersen D. R., Swaters R. A., 2013, *Astronomy & Astrophysics*, 557, A131
- Massey P., Hanson M. M., 2013, *Astronomical Spectroscopy. EOP Science*, p. 35, doi:10.1007/978-94-007-5618-2\_2
- Masters K. L., Springob C. M., Haynes M. P., Giovanelli R., 2006, *The Astrophysical Journal*, 653, 861
- Mathewson D. S., Ford V. L., Buchhorn M., 1992, *ApJS*, 81, 413

- McClure-Griffiths N. M., Dickey J. M., 2007, *Astrophysics Journal*, 671, 427
- McConnell D., et al., 2016, *pasa*, 33, e042
- McGaugh S. S., 2005, *Phys. Rev. Lett.*, 95, 171302
- McGaugh S. S., 2016, *Astrophysics Journal*, 816, 42
- McGaugh S., 2020, *Galaxies*, 8, 35
- McGaugh S. S., Schombert J. M., Bothun G. D., de Blok W. J. G., 2000, *The Astrophysical Journal*, 533, L99
- McQuinn M., 2016, *Annual Review of Astronomy and Astrophysics*, 54, 313
- Metz M., Kroupa P., Libeskind N. I., 2008, *The Astrophysical Journal*, 680, 287
- Milgrom M., 1983, *Astrophysics Journal*, 270, 365
- Miller M. C., Yunes N., 2019, *Nature*, 568, 469
- Miller S. H., Bundy K., Sullivan M., Ellis R. S., Treu T., 2011, *Astrophysics Journal*, 741, 115
- Miller S. H., Ellis R. S., Sullivan M., Bundy K., Newman A. B., Treu T., 2012, *The Astrophysical Journal*, 753, 74
- Miller S. H., Ellis R. S., Newman A. B., Benson A., 2014, *The Astrophysical Journal*, 782, 115
- Mo H. J., Mao S., 2000, *Monthly Notices of the Royal Astronomical Society*, 318, 163
- Mo H. J., Mao S., White S. D. M., 1998, *Monthly Notices of the Royal Astronomical Society*, 295, 319
- Moller P., et al., 2018, *Monthly Notices of the Royal Astronomical Society*, 474, 4039
- Moore B., Ghigna S., Governato F., Lake G., Quinn T., Stadel J., Tozzi P., 1999, *Astrophysics Journal Letter*, 524, L19
- More S., Miyatake H., Mandelbaum R., Takada M., Spergel D. N., Brownstein J. R., Schneider D. P., 2015, *Astrophysics Journal*, 806, 2
- Morselli L., Popesso P., Erfanianfar G., Concas A., 2017, *Astronomy & Astrophysics*, 597, A97
- Mosleh M., Williams R. J., Franx M., Kriek M., 2011, *Astrophysics Journal*, 727, 5
- Moster B. P., Naab T., White S. D. M., 2018, *Monthly Notices of the Royal Astronomical Society*, 477, 1822

- Navarro J. F., Eke V. R., Frenk C. S., 1996a, *Monthly Notices of the Royal Astronomical Society*, 283, L72
- Navarro J. F., Frenk C. S., White S. D. M., 1996b, *Astrophysics Journal*, 462, 563
- Navarro J. F., Frenk C. S., White S. D., 1997, *Astrophysics Journal*, 490, 493
- Neill J. D., Seibert M., Tully R. B., Courtois H., Sorce J. G., Jarrett T. H., Scowcroft V., Masci F. J., 2014, *Astrophysics Journal*, 792, 129
- Nesti F., Salucci P., 2013, *Journal of Cosmology and Astroparticle Physics*, 2013, 016
- Niikura H., et al., 2019, *Nature Astronomy*, 3, 524
- Nipoti C., Binney J., 2014, *Monthly Notices of the Royal Astronomical Society*, 446, 1820
- Noterdaeme P., Petitjean P., Ledoux C., Srianand R., 2009, *Astronomy & Astrophysics*, 505, 1087
- Noterdaeme P., et al., 2012, *Astronomy & Astrophysics*, 540, A63
- Obreschkow D., et al., 2015, *The Astrophysical Journal*, 815, 97
- Oh S.-H., de Blok W. J. G., Brinks E., Walter F., Kennicutt Robert C. J., 2011a, *AJ*, 141, 193
- Oh S.-H., Brook C., Governato F., Brinks E., Mayer L., de Blok W. J. G., Brooks A., Walter F., 2011b, *AJ*, 142, 24
- Oman K. A., 2018, in Chiappini C., Minchev I., Starkenburg E., Valentini M., eds, 213-218 Vol. 334, *Rediscovering Our Galaxy*. pp 213–218 ([arXiv:1712.02562](https://arxiv.org/abs/1712.02562)), doi:10.1017/S1743921317006615
- Oman K. A., et al., 2015a, *Monthly Notices of the Royal Astronomical Society*, 452, 3650
- Oman K. A., et al., 2015b, *Monthly Notices of the Royal Astronomical Society*, 452, 3650
- Oman K. A., Marasco A., Navarro J. F., Frenk C. S., Schaye J., Benítez-Llambay A., 2019, *Monthly Notices of the Royal Astronomical Society*, 482, 821
- Oort J. H., 1932, *bain*, 6, 249
- Oort J. H., 1940, *Astrophysics Journal*, 91, 273
- Ostriker J. P., Peebles P. J. E., 1973, *Astrophysics Journal*, 186, 467
- Ouchi M., Ono Y., Shibuya T., 2020, *Annual Review of Astronomy and Astrophysics*, 58, 617
- Paczynski B., 1986, *Astrophysics Journal*, 304, 1

- Padmanabhan T., 1993, Structure formation in the universe. Cambridge university press
- Palunas P., Williams T. B., 2000, *AJ* , **120**, 2884
- Pannella M., et al., 2015, *Astrophysics Journal*, **807**, 141
- Papastergis E., Giovanelli R., Haynes M. P., Shankar F., 2015, *Astronomy & Astrophysics*, **574**, A113
- Papastergis E., Adams E. A. K., van der Hulst J. M., 2016, *Astronomy & Astrophysics*, **593**, A39
- Pato M., Iocco F., Bertone G., 2015, *Journal of Cosmology and Astroparticle Physics* , **2015**, 001
- Pawlowski M. S., Kroupa P., 2013, *Monthly Notices of the Royal Astronomical Society*, **435**, 2116
- Pawlowski M. S., Kroupa P., 2019, *Monthly Notices of the Royal Astronomical Society*, **491**, 3042
- Pawlowski M. S., McGaugh S. S., 2014, *Monthly Notices of the Royal Astronomical Society*, **440**, 908
- Pawlowski M. S., Kroupa P., Jerjen H., 2013, *Monthly Notices of the Royal Astronomical Society*, **435**, 1928
- Pawlowski M. S., Famaey B., Merritt D., Kroupa P., 2015, *Astrophysics Journal*, **815**, 19
- Peñarrubia J., 2019, *Monthly Notices of the Royal Astronomical Society*, **484**, 5409
- Peebles P. J. E., 1993, Principles of Physical Cosmology . Princeton University Press
- Penzias A. A., Wilson R. W., 1965, *Astrophysics Journal*, **142**, 419
- Pérez-González P. G., et al., 2008, *The Astrophysical Journal*, **675**, 234
- Perivolaropoulos L., Skara F., 2021, arXiv e-prints, p. arXiv:2105.05208
- Péroux C., McMahon R. G., Storrie-Lombardi L. J., Irwin M. J., 2003, *Monthly Notices of the Royal Astronomical Society*, **346**, 1103
- Persic M., Salucci P., 1988, *Monthly Notices of the Royal Astronomical Society*, **234**, 131
- Persic M., Salucci P., 1990, *Monthly Notices of the Royal Astronomical Society*, **247**, 349
- Persic M., Salucci P., 1991, *The Astrophysical Journal*, **368**, 60
- Persic M., Salucci P., Stel F., 1996, *Monthly Notices of the Royal Astronomical Society*, **281**, 27

- Pillepich A., et al., 2018, *Monthly Notices of the Royal Astronomical Society*, **473**, 4077
- Pizagno J., et al., 2007, *AJ* , **134**, 945
- Planck Collaboration et al., 2016, *Astronomy & Astrophysics*, **594**, A13
- Planck Collaboration et al., 2020a, *Astronomy & Astrophysics*, **641**, A6
- Planck Collaboration et al., 2020b, *Astronomy & Astrophysics*, **641**, A7
- Poincare H., Vergne H., 1911, Lecons sur les hypotheses cosmogoniques professees a la Sorbonne. Paris observatorie
- Pont F., Queloz D., Bratschi P., Mayor M., 1997, *Astronomy & Astrophysics*, **318**, 416
- Pontzen A., Governato F., 2012, *Monthly Notices of the Royal Astronomical Society*, **421**, 3464
- Pontzen A., Governato F., 2014, *Nature*, **506**, 171
- Porter T. A., Johnson R. P., Graham P. W., 2011, *Annual Review of Astronomy and Astrophysics*, **49**, 155
- Press W. H., Teukolsky S. A., Vetterling W. T., Flannery B. P., 1992, Numerical recipes in FORTRAN. The art of scientific computing. Cambridge University Press
- Price S. H., et al., 2016, *Astrophysics Journal*, **819**, 80
- Pritchard J. R., Loeb A., 2012, *Reports on Progress in Physics*, **75**, 086901
- Prochaska J. X., Herbert-Fort S., Wolfe A. M., 2005, *Astrophysics Journal*, **635**, 123
- Profumo S., Giani L., Piattella O. F., 2019, *Universe*, **5**, 213
- Puech M., et al., 2008, *Astronomy & Astrophysics*, **484**, 173
- Rao S. M., Turnshek D. A., Nestor D. B., 2006, *Astrophysics Journal*, **636**, 610
- Read J., Iorio G., Agertz O., Fraternali F., 2016, *Monthly Notices of the Royal Astronomical Society*, **462**, 3628
- Read J. I., Walker M. G., Steger P., 2018, *Monthly Notices of the Royal Astronomical Society*, **481**, 860
- Refregier A., 2003, *Annual Review of Astronomy and Astrophysics*, **41**, 645
- Refsdal S., 1964, *Monthly Notices of the Royal Astronomical Society*, **128**, 295
- Reid M. J., et al., 2014, *Astrophysics Journal*, **783**, 130

- Reyes R., Mandelbaum R., Gunn J., Pizagno J., Lackner C., 2011, *Monthly Notices of the Royal Astronomical Society*, 417, 2347
- Roberts M. S., 2008, in Bridle A. H., Condon J. J., Hunt G. C., eds, Astronomical Society of the Pacific Conference Series Vol. 395, *Frontiers of Astrophysics: A Celebration of NRAO's 50th Anniversary*. p. 283
- Roberts M. S., Rots A. H., 1973, *Astronomy & Astrophysics*, 26, 483
- Romanowsky A. J., Fall S. M., 2012, *ApJS*, 203, 17
- Roszkowski L., Sessolo E. M., Trojanowski S., 2018, *Reports on Progress in Physics*, 81, 066201
- Rubin V. C., Ford W. Kent J., 1970, *Astrophysics Journal*, 159, 379
- Rubin V. C., Ford W. K. J., Thonnard N., 1978, *Astrophysics Journal Letter*, 225, L107
- Rubin V. C., Ford Jr W. K., Thonnard N., 1980, *The Astrophysical Journal*, 238, 471
- Salam A., Ward J. C., 1959, *Il Nuovo Cimento*, 11, 568
- Salpeter E. E., 1955, *Astrophysics Journal*, 121, 161
- Salucci P., 2019, *Astronomy & Astrophysics Rev.*, 27, 2
- Salucci P., Burkert A., 2000a, *The Astrophysical Journal Letters*, 537, L9
- Salucci P., Burkert A., 2000b, *Astrophysics Journal Letter*, 537, L9
- Salucci P., Lapi A., Tonini C., Gentile G., Yegorova I., Klein U., 2007, *Monthly Notices of the Royal Astronomical Society*, 378, 41
- Salucci P., Turini N., di Paolo C., 2020, *Universe*, 6
- Sánchez S. F., et al., 2012, *Astronomy & Astrophysics*, 538, A8
- Saracco P., Longhetti M., Gargiulo A., 2011, *Monthly Notices of the Royal Astronomical Society*, 412, 2707
- Sauer T., 2008, *Archive for History of Exact Sciences*, 62, 1
- Sawala T., et al., 2016, *Monthly Notices of the Royal Astronomical Society*, 457, 1931
- Schaye J., et al., 2015, *Monthly Notices of the Royal Astronomical Society*, 446, 521
- Scoville N., et al., 2007, *The Astrophysical Journal Supplement Series*, 172, 38
- Sersic J. L., 1968, *Atlas de Galaxias Australes*. Cambridge press

- Sharma G., 2021, Dark matter fraction in  $z \geq 1$  star-forming galaxies, doi:10.7910/DVN/O1KKIV, <https://doi.org/10.7910/DVN/O1KKIV>
- Sharma G., Salucci P., 2021,  $\text{\AA}$ , 000, 0000
- Sharma G., Salucci P., van de Ven G., 2021a, *Astronomy & Astrophysics*, 000, 0000
- Sharma G., Salucci P., van de Ven G., 2021c, *Astronomy & Astrophysics*, 503, 1753
- Sharma G., Salucci P., Harrison C. M., van de Ven G., Lapi A., 2021b, *Monthly Notices of the Royal Astronomical Society*, 503, 1753
- Sharples R., 2014, *Proceedings of the International Astronomical Union*, 10, 1116
- Sharples R. M., Bender R., Hofmann R., Genzel R., Ivison R. J., 2003, in Iye M., Moorwood A. F. M., eds, Society of Photo-Optical Instrumentation Engineers (SPIE) Conference Series Vol. 4841, Instrument Design and Performance for Optical/Infrared Ground-based Telescopes. pp 1562–1571, doi:10.1117/12.460985
- Shen S., Mo H. J., White S. D. M., Blanton M. R., Kauffmann G., Voges W., Brinkmann J., Csabai I., 2003, *Monthly Notices of the Royal Astronomical Society*, 343, 978
- Simon J. D., Bolatto A. D., Leroy A., Blitz L., Gates E. L., 2005, *Astrophysics Journal*, 621, 757
- Simons R. C., et al., 2016, *The Astrophysical Journal*, 830, 14
- Simons R. C., et al., 2017, *Astrophysics Journal*, 843, 46
- Slatyer T. R., Wu C.-L., 2018, *Phys. Rev. D*, 98, 023013
- Smith S., 1936, *Astrophysics Journal*, 83, 23
- Sobral D., et al., 2015, *Monthly Notices of the Royal Astronomical Society*, 451, 2303
- Sofue Y., 2016, *Publications of the Astronomical Society of Japan*, 69
- Sofue Y., 2020, *Galaxies*, 8, 37
- Sofue Y., Rubin V., 2001, *Annual Review of Astronomy and Astrophysics*, 39, 137
- Sofue Y., Honma M., Omodaka T., 2009, *Publications of the Astronomical Society of Japan*, 61, 227
- Somerville R. S., Davé R., 2015, *Annual Review of Astronomy and Astrophysics*, 53, 51
- Somerville R. S., Primack J. R., 1999, *Monthly Notices of the Royal Astronomical Society*, 310, 1087
- Sorce J. G., et al., 2013, *Astrophysics Journal*, 765, 94

- Speagle J. S., Steinhardt C. L., Capak P. L., Silverman J. D., 2014, *The Astrophysical Journal Supplement Series*, 214, 15
- Spitzer Lyman J., 1942, *Astrophysics Journal*, 95, 329
- Springel V., White S. D. M., Tormen G., Kauffmann G., 2001, *Monthly Notices of the Royal Astronomical Society*, 328, 726
- Springel V., et al., 2005, *nature*, 435, 629
- Springel V., et al., 2008, *Monthly Notices of the Royal Astronomical Society*, 391, 1685
- Stadel J., Potter D., Moore B., Diemand J., Madau P., Zemp M., Kuhlen M., Quilis V., 2009, *Monthly Notices of the Royal Astronomical Society*, 398, L21
- Stark D. V., McGaugh S. S., Swaters R. A., 2009, *AJ*, 138, 392
- Steidel C. C., Adelberger K. L., Dickinson M., Giavalisco M., Pettini M., Kellogg M., 1998, *The Astrophysical Journal*, 492, 428
- Steigman G., Turner M. S., 1985, *Nuclear Physics B*, 253, 375
- Steinmetz M., Navarro J. F., 1999, *Astrophysics Journal*, 513, 555
- Stott J. P., et al., 2016, *Monthly Notices of the Royal Astronomical Society*, 457, 1888
- Strateva I., et al., 2001, *AJ*, 122, 1861
- Subrahmanyan C., 1960, Principles of stellar dynamics. University of Chicago press Dover edition
- Sung A., Tu H., Wu M.-R., 2019, *Physics Review D*, 99, 121305
- Sunyaev R. A., Zeldovich Y. B., 1969, *Nature*, 223, 721
- Swaters R. A., F. M. B., van den Bosch Frank C. Balcells M., 2003, *Astrophysics Journal*, 583, 732
- Swinbank A. M., Sobral D., Smail I., Geach J. E., Best P. N., McCarthy I. G., Crain R. A., Theuns T., 2012, *Monthly Notices of the Royal Astronomical Society*, 426, 935
- Swinbank A. M., et al., 2017, *Monthly Notices of the Royal Astronomical Society*, 467, 3140
- Tacconi L. J., et al., 2010, *Nature*, 463, 781
- Tacconi L. J., et al., 2018, *Astrophysics Journal*, 853, 179
- Taillet R., Longaretti P.-Y., Salati P., 1995, *Astroparticle Physics*, 4, 87

- Tasca, L. A. M. et al., 2009, *A&A*, 503, 379
- Teodoro E. D., Fraternali F., 2015, *Monthly Notices of the Royal Astronomical Society*, 451, 3021
- Tiley A. L., et al., 2016, *Monthly Notices of the Royal Astronomical Society*, 460, 103
- Tiley A., et al., 2019a, *Monthly Notices of the Royal Astronomical Society*, 482, 2166
- Tiley A. L., et al., 2019b, *Monthly Notices of the Royal Astronomical Society*, 485, 934
- Tollerud E. J., Bullock J. S., Strigari L. E., Willman B., 2008, *Astrophysics Journal*, 688, 277
- Toribio M. C., Solanes J. M., Giovanelli R., Haynes M. P., Martin A. M., 2011, *Astrophysics Journal*, 732, 93
- Treu T., 2010, *Annual Review of Astronomy and Astrophysics*, 48, 87
- Tröster T., et al., 2020, *Astronomy & Astrophysics*, 633, L10
- Tully R. B., Fisher J. R., 1977, *Astronomy and Astrophysics*, 54, 661
- Tully R. B., Pierce M. J., 2000, *Astrophysics Journal*, 533, 744
- Turner O. J., Harrison C. M., Cirasuolo M., McLure R. J., Dunlop J., Swinbank A. M. and Tiley A. L., 2017, arXiv e-prints, p. [arXiv:1711.03604](https://arxiv.org/abs/1711.03604)
- Übler H., et al., 2017, *Astrophysics Journal*, 842, 121
- Übler H., et al., 2019, *The Astrophysical Journal*, 880, 48
- Umemura M., Ikeuchi S., 1985, *Astrophysics Journal*, 299, 583
- Valenzuela O., Rhee G., Klypin A., Governato F., Stinson G., Quinn T., Wadsley J., 2007, *The Astrophysical Journal*, 657, 773
- Valotto C., Giovanelli R., 2003, Boletin de la Asociacion Argentina de Astronomia La Plata Argentina, 46, 97
- Varidel M. R., et al., 2019, *Monthly Notices of the Royal Astronomical Society*, 485, 4024
- Vegetti S., Koopmans L. V. E., Auger M. W., Treu T., Bolton A. S., 2014, *Monthly Notices of the Royal Astronomical Society*, 442, 2017
- Verbeke R., Papastergis E., Ponomareva A. A., Rathi S., De Rijcke S., 2017, *Astronomy & Astrophysics*, 607, A13
- Verde L., Protopapas P., Jimenez R., 2013, *Physics of the Dark Universe*, 2, 166

- Verde L., Treu T., Riess A. G., 2019, *Nature Astronomy*, 3, 891
- Verheijen M. A. W., 1997, PhD thesis, University of Groningen
- Verheijen M. A. W., Sancisi R., 2001, *Astronomy & Astrophysics*, 370, 765
- Vittorio N., Silk J., 1984, *Astrophysics Journal Letter*, 285, L39
- Vogelsberger M., Marinacci F., Torrey P., Puchwein E., 2020, *Nature Reviews Physics*, 2, 42
- Walsh D., Carswell R. F., Weymann R. J., 1979, *Nature*, 279, 381
- Wang K., Huang Q.-G., 2020, *Journal of Cosmology and Astroparticle Physics*, 2020, 045
- Wang Y., Zhao G.-B., 2020, *Research in Astronomy and Astrophysics*, 20, 158
- Wang L., Dutton A. A., Stinson G. S., Macciò A. V., Penzo C., Kang X., Keller B. W., Wadsley J., 2015, *Monthly Notices of the Royal Astronomical Society*, 454, 83
- Wang W., Han J., Cautun M., Li Z., Ishigaki M. N., 2020, *Science China Physics, Mechanics, and Astronomy*, 63, 109801
- Weijmans A.-M., Krajnović D., Van De Ven G., Oosterloo T. A., Morganti R., De Zeeuw P., 2008, *Monthly Notices of the Royal Astronomical Society*, 383, 1343
- Weinberg S., 1967, *Physics Review Letter*, 19, 1264
- Weinberg D. H., Bullock J. S., Governato F., Kuzio de Naray R., Peter A. H. G., 2015, *Proceedings of the National Academy of Science*, 112, 12249
- Wellons S., Faucher-Giguère C.-A., Anglés-Alcázar D., Hayward C. C., Feldmann R., Hopkins P. F., Kere D., 2020, *Monthly Notices of the Royal Astronomical Society*, 497, 4051
- Westmoquette M., 2007, PhD thesis, University College London, <https://discovery.ucl.ac.uk/id/eprint/1446265>
- Whitaker K. E., et al., 2014, *Astrophysics Journal*, 795, 104
- Whiting M. T., 2012, *Monthly Notices of the Royal Astronomical Society*, 421, 3242
- Willman B., et al., 2005, *Astrophysics Journal Letter*, 626, L85
- Wirth H., Bekki K., Hayashi K., 2020, *Monthly Notices of the Royal Astronomical Society*, 496, L70
- Wisnioski E., et al., 2015, *Astrophysics Journal*, 799, 209
- Wisnioski E., et al., 2019, *Astrophysics Journal*, 886, 124

- Wong K. C., et al., 2014, *The Astrophysical Journal*, 789, L31
- Woodgate B. E., et al., 1998, *Publications of the Astronomical Society of the Pacific*, 110, 1183
- Wuyts S., et al., 2016, *Astrophysics Journal*, 831, 149
- Yegorova I. A., Babic A., Salucci P., Spekkens K., Pizzella A., 2011, *Astronomische Nachrichten*, 332, 846
- Zaninetti L., 2018, *International Journal of Astronomy and Astrophysics*, 8, 258
- Zhu L., et al., 2018, *Nature Astronomy*, 2, 233
- Ziegler B. L., et al., 2002, *The Astrophysical Journal*, 564, L69
- Zwaan M. A., Meyer M. J., Staveley-Smith L., Webster R. L., 2005, *Monthly Notices of the Royal Astronomical Society: Letters*, 359, L30
- Zwicky F., 1933, *Helvetica Physica Acta*, 6, 110
- de Blok W. J. G., McGaugh S. S., Bosma A., Rubin V. C., 2001, *Astrophysics Journal Letter*, 552, L23
- de Blok W. J. G., Bosma A., McGaugh S., 2003, *Monthly Notices of the Royal Astronomical Society*, 340, 657
- de Blok W. J. G., Walter F., Brinks E., Trachternach C., Oh S. H., Kennicutt R. C. J., 2008, *AJ*, 136, 2648
- de Swart J. G., Bertone G., van Dongen J., 2017, *Nature Astronomy*, 1, 0059
- de Vaucouleurs G., 1958, *Astrophysics Journal*, 128, 465
- van Starkenburg L., van der Werf P. P., Yan L., Moorwood A. F. M., 2006, arXiv e-prints, pp astro-ph/0601297
- van de Hulst H. C., Raimond E., van Woerden H., 1957, *bain*, 14, 1
- van den Bosch F. C., Swaters R. A., 2001, *Monthly Notices of the Royal Astronomical Society*, 325, 1017
- van der Wel A., Holden B. P., Zirm A. W., Franx M., Rettura A., Illingworth G. D., Ford H. C., 2008, *Astrophysics Journal*, 688, 48
- van der Wel A., et al., 2012, *The Astrophysical Journal Supplement Series*, 203, 24
- van der Wel A., et al., 2013, *The Astrophysical Journal*, 777, L17
- van der Wel A., et al., 2014a, *Astrophysics Journal*, 788, 28

van der Wel A., et al., 2014b, *Astrophysics Journal*, 788, 28

Übler H., et al., 2018, *The Astrophysical Journal*, 854, L24

öpik E., 1915, *Bull. de la Soc. Astr. de Russie*, 21